



Universiteit
Antwerpen

Faculteit Wetenschappen
Departement Fysica

Confined states in mono- and bi-layer graphene nanostructures

Ingeperkte toestanden in mono- en bi-gelaagde grafeen nanostructuren

Proefschrift voorgelegd tot het behalen van de graad van doctor in de wetenschappen aan
de Universiteit Antwerpen te verdedigen door

Mohammad Zarenia

Promotor
Prof. Dr. François Peeters

Antwerpen

May 2013

Members of the Jury:**Chairman**

Prof. Dr. Dirk Lamoen, Universiteit Antwerpen, Belgium

Supervisor

Prof. Dr. François Peeters, Universiteit Antwerpen, Belgium

Members

Prof. Dr. Nick Van Remortel, Universiteit Antwerpen, Belgium,

Prof. Dr. Bart Partoens, Universiteit Antwerpen, Belgium,

Prof. Dr. Tapash Chakraborty, University of Manitoba, Canada,

Prof. Dr. David Neilson, University of Camerino, Italy,

Prof. Dr. Andrey Chaves, Universidade Federal do Ceará, Brazil.

Contact Information

Mohammad Zarenia
G.U. 205
Groenenborgerlaan 171
2020 Antwerpen
Belgium
m.zarenia@gmail.com

Acknowledgement

I would like to express my deepest appreciation to my supervisor Prof. François Peeters for his guidance and continuous encouragement during my PhD study. I consider it an honor to be his student. Besides my supervisor, I would like to thank the rest of my thesis committee: Prof. Dirk Lamoen, Prof. Bart Partoens, Prof. Nick Van Remortel, Prof. David Neilson, Prof. Tapash Cahkraborty, and Prof. Andrey Chaves for reviewing my thesis and giving their insightful comments.

I am indebted to Prof. Milton Pereira Jr., Prof. Bart Partoens, and Prof. Panagiotis Vasilopoulos who kindly shared their knowledge on graphene with me.

The present thesis would not have been successful without the help of my collaborators. I thank Prof. Tapash Cahkraborty, Prof. Andrey Chaves, Prof. Gil de Aquino Farias, Prof. Milan Tadić, Dr. Ortwin Leenaerts and Marko Grujić for their fruitful discussions we had throughout our research.

I would like to thank all my colleagues in CMT group for making a lively and friendly environment during these years. My special thanks go to Dr. Massoud Ramezani Masir, Dr. Michael Barbier and Davoud Nasr Esfahani, who I benefited from discussion with them. I must thank Christophe De Beule who did a great favor for me by translating the summary of my thesis in Dutch.

Last and most importantly, I give my heartfelt thanks to my wife Samira for her continuous love and her strong support.

Mohammad Zarenia
Antwerp, May 2013.

This work was supported by the Flemish Science Foundation (FWO-VI), the Belgian Science Policy (IAP), the European Science Foundation (ESF) under the EUROCORES program EuroGRAPHENE (project CONGRAN), the Methusalem foundation of the Flemish Government, the bilateral projects between Flanders and Brazil and the collaboration project FWO-CNPq.

Contents

List of Abbreviations	1
1 Introduction	3
1.1 Graphene: A 2D material	3
1.2 Applications	4
1.2.1 Graphene-based solar cells	4
1.2.2 High-speed graphene transistors	5
1.2.3 Flexible graphene-based display	6
1.3 Motivation of the thesis	6
1.4 Contribution of the thesis	7
1.5 Organization of the thesis	9
2 Theoretical aspects of graphene	11
2.1 Electronic properties of graphene	11
2.1.1 Crystal structure	11
2.1.2 Band structure	12
2.1.3 From tight binding approach to continuum model	14
2.1.4 Experimental observation of graphene bandstructure	15
2.1.5 Chirality in graphene	16
2.2 Bilayer graphene	17
2.3 Influence of a perpendicular magnetic field	20
2.3.1 Landau levels in monolayer graphene	21
2.3.2 Landau levels in bilayer graphene	22

2.4	Confinement in graphene	23
2.4.1	Klein paradox problem	23
2.4.2	Graphene quantum dots	26
2.4.3	Bilayer graphene quantum dots	28
3	Energy levels of triangular and hexagonal graphene quantum dots	29
3.1	Introduction	29
3.2	Tight-binding model	31
3.3	Continuum model: Dirac-Weyl equation	32
3.3.1	Zigzag boundary conditions	34
3.3.2	Armchair boundary conditions	34
3.3.3	Infinite-mass boundary condition	34
3.4	Numerical results	35
3.4.1	Zero magnetic field	35
3.4.2	Magnetic field dependence	45
3.5	Conclusion	51
4	Energy spectrum of a circular graphene quantum dot	53
4.1	Introduction	53
4.2	The continuum approach	54
4.2.1	Zero energy solutions	56
4.2.2	Non-zero energy solutions: zero magnetic field	57
4.2.3	Non-zero energy solutions with magnetic field	57
4.2.4	Energy spectrum	58
4.3	The tight-binding model	60
4.4	Conclusion	66
5	Snake states in graphene quantum dots in the presence of a p-n junction	69
5.1	Introduction	69
5.2	Model	71
5.3	p-n junction: zero magnetic field	71
5.4	snake states: influence of a perpendicular magnetic field	76
5.4.1	p-n junction	76
5.4.2	p-n-p junction	87
5.5	Triangular shaped p-n junction	89
5.6	Conclusion	91

6	Electron-electron interaction in bilayer graphene quantum dots	93
6.1	Introduction	93
6.2	Continuum model	95
6.3	Single-particle energy levels	96
6.4	Two-electron energy spectrum	97
6.5	Conclusion	103
7	Gate defined quantum rings in bilayer graphene	105
7.1	Introduction	105
7.2	Continuum model	107
7.3	Numerical results	109
7.4	Conclusion	113
8	Energy levels of an ideal quantum ring in monolayer and bilayer graphene	115
8.1	Introduction	115
8.2	Single layer graphene	116
8.2.1	Model	116
8.2.2	Results	118
8.3	Bilayer graphene	122
8.3.1	Model	122
8.3.2	Results	125
8.4	Conclusion	130
9	Chiral states in monolayer graphene	133
9.1	Introduction	133
9.2	Kink-shaped mass profile	135
9.3	Effect of a small gap between two mass regions	137
9.4	Superlattice	139
9.4.1	Ab-initio verification	141
9.5	Conclusion	142
10	Chiral states in bilayer graphene	143
10.1	Introduction	143
10.2	Model	145
10.3	Single kink	148
10.3.1	Influence of the smoothness of the kink profile	148
10.3.2	Magnetic field dependence	155
10.4	Kink-antikink	161
10.4.1	Zero magnetic field	161

10.4.2 Magnetic field dependence	167
10.5 Conclusion	171
11 Summary and future prospects	173
11.1 Concluding remarks of the thesis	173
11.2 Future prospects	176
12 Overzicht en toekomstperspectieven	177
12.1 Overzicht van de thesis	177
Bibliography	181

List of Abbreviations

0D	zero dimensional
1D	one dimensional
2D	two dimensional
3D	three dimensional
2DEG	two dimensional electron gas
ARPES	Angle-resolved photoemission spectroscopy
BLG	Bilayer graphene
BZ	Brillouin zone
CI	Configuration Interaction
CVD	Chemical vapor deposition
DFT	Density functional theory
DOS	Density of states
FET	Field effect transistor
GQD(s)	Graphene quantum dot(s)
GQR(s)	Graphene quantum ring(s)
h-BN	hexagonal boron-nitride
IMBC	Infinite-mass boundary condition
LDA	Local density approximation
OLED(s)	Organic light emitting diode(s)
LL(s)	Landau level(s)
LDOS	Local density of states
QD(s)	Quantum dot(s)
QH	Quantum Hall

QR(s)	Quantum ring(s)
STM	Scanning tunneling microscopy
TB(M)	Tight binding (model)
ZBC	Zigzag boundary condition

CHAPTER 1

Introduction

1.1 Graphene: A 2D material

Since 2004 a sheet of carbon atoms, graphene, that is packed in a hexagonal lattice has been one of the most intensively studied materials for a wide range of basic and applied sciences. This two-dimensional (2D) material, with a thickness of a single atom, has resulted in rich physics in its transport, electronic and optical properties. The theoretical study of graphene was initiated in the late 1940s, when a 2D sheet of sp^2 -bonded carbon atoms was studied by Wallace [1] in order to understand the band structure of graphite. The source of graphene, i.e. graphite, has been used since ancient times. Early reports on graphene dates back to 1962 when a graphene sheet was fabricated by the chemical reduction of exfoliated graphite [2]. At the end of the 60s, a graphene sheet was observed as a *disordered structure* on platinum surfaces that was heated in ultrahigh vacuum [3]. Despite these early attempts one had to wait till 2004 for the first publication on the experimental measurement of the electrical properties of graphene by K. Novoselov and A. Geim at the University of Manchester [4]. With the discovery of 2D graphene, scientists now have access to all dimensionalities of carbon-based materials including 3D (diamond and graphite), 2D (graphene), 1D (carbon nanotubes), and 0D (fullerene). These different allotropes of carbon are shown in Fig. 1.1.

To fabricate graphene, A. Geim and his coworkers used the mechanical cleavage method where graphene sheets were pulled off graphite by using the scotch tape method. By repeated peeling graphite, i.e. multiple-layer graphene, is cleaved into graphene flakes with

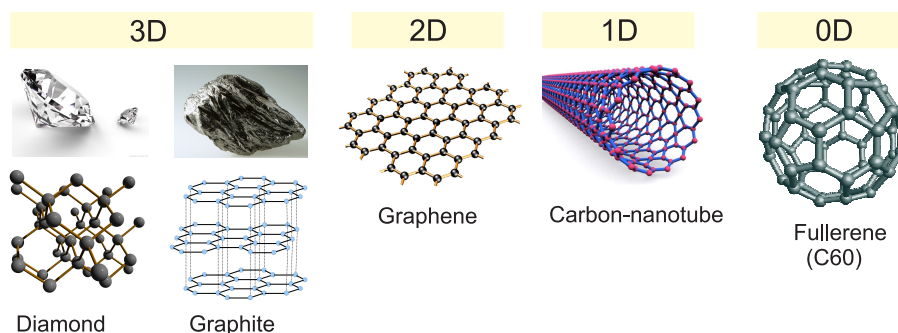


Figure 1.1: Different allotropes of carbon in three-, two-, one- and zero-dimension (the idea is taken from Ref. [5]).

different thicknesses. These flakes were deposited on a thick film of silicon oxide substrate. Some of these flakes were only one-atom thick. These monolayers of graphene could be detected using a standard optical microscope where the flakes have different color depending on their thickness. A diagrammatic picture of the above procedure is shown in Fig. 1.2.

During the last decade the interest in graphene increased tremendously. From 2004 up to now more than 4×10^4 publications on graphene have been published [6]. In 2010, Konstantin Novoselov and Andre Geim were awarded the Nobel Prize in Physics for their *groundbreaking experiments regarding the two-dimensional material graphene* [7]. For in-depth review on graphene, I would like to mention the recent book by M. Katsnelson which focuses on the theoretical aspects of graphene [8].

1.2 Applications

Graphene, is one of the strongest materials found in nature. It is flexible and transparent, and conducts both electricity and heat very well [9]. Because of these unique electronic properties, graphene is one of the most promising materials to bring about a revolution to electronics, sensors, and optical devices. In the following I mention a few examples of possible applications for graphene.

1.2.1 Graphene-based solar cells

A solar cell consists of a layer that absorbs sunlight. This layer is sandwiched between two electrodes. The electrodes are typically made of a conductive transparent metal indium tin oxide (ITO) which is a very expensive material. Recently, a new class of solar cells have

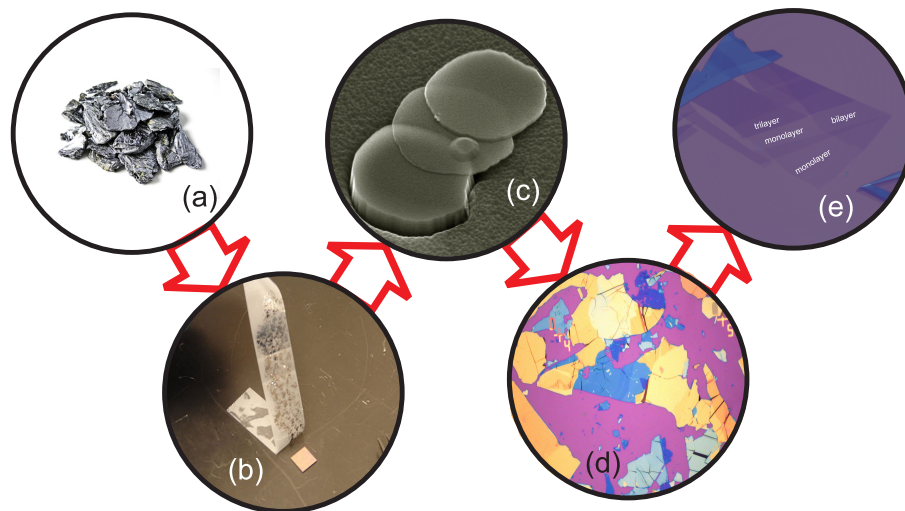


Figure 1.2: mechanical cleavage method : (a) starting from graphite (b) using an adhesive tape to peel off layers in graphite and to put graphite flakes on a silicon oxide wafer (c) SEM image of 30 layers thick (adopted from Ref. [7]) (d) An optical microscope view of graphite pieces on a silicon oxide wafer (e) An enlarged region of the optical image where we distinguish graphene flakes (adopted from Ref. [9]).

been proposed and demonstrated based on graphene [10]. In this new solar cells graphene is used as a electrode while using fullerene and carbon nanotubes to absorb light and generate electrons and holes. The entire device is made of carbon which is stable in a wide range of temperatures.

1.2.2 High-speed graphene transistors

Pristine graphene has a linear energy-momentum spectrum with zero gap which gives the possibility of electron-hole crossover at the Fermi energy. It has a remarkable carrier mobility of about $4 \times 10^4 \text{ cm}^2/(\text{V.s})$ [11] at room temperature which is even higher, i.e. $2 \times 10^5 - 10^6 \text{ cm}^2/(\text{V.s})$, at low temperature [12, 13]. Such a large mobility makes graphene a promising material for high-mobility nanoelectronic applications. The high mobility of the carriers is essential for achieving high-speed and high-performance transistors. After the discovery of graphene, notable efforts have been made to fabricate a graphene Field Effect Transistor (FET) [14, 15]. One of the successful experimental realization of graphene-based FET has been carried out by researchers at IBM, USA [15]. They demonstrated that the frequency performance of the graphene device already exceeds the cut-off frequency of state-of-the-art silicon transistors for the same gate length. Fig. 1.3 shows an array

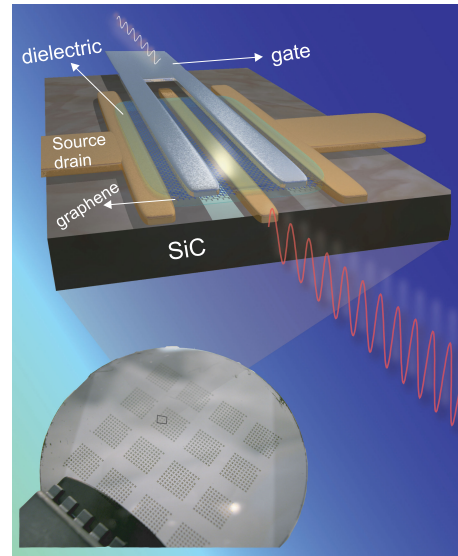


Figure 1.3: An array of graphene transistors and a cross-sectional view of a top-gated graphene FET deposited on a SiC wafer made by IBM [15].

of graphene transistors with a schematic picture of a cross-sectional view of a top-gated graphene FET deposited on a SiC wafer made by IBM.

1.2.3 Flexible graphene-based display

It is recognized that graphene can be used as a very thin transparent sheet in addition to its high conductivity [16]. Because of this advantage, graphene can be a very good candidate to be used in organic light-emitting diodes (OLED)¹. These diodes are used in electronic device display screens which require low power consumption. The conventional material used in the OLED films is based on indium that is expensive and toxic. Replacing graphene with indium not only reduces the cost but also has the added advantage for possible fabrication of flexible screens [17] (Fig. 1.4(b)). Moreover graphene-based OLEDs are pure organic and can be fabricated in even large sizes (see Fig. 1.4(a)).

1.3 Motivation of the thesis

Among the various interesting physical properties of graphene [18–20], the present work concerns its electronic properties. One of the main challenges to utilize graphene-based devices is the electrical confinement of carriers within quantum structures. Confinement

¹OLEDs have an electroluminescent layer between two charge-injecting electrodes, at least one of which is transparent.

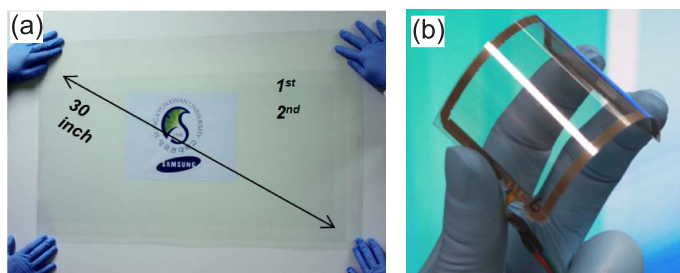


Figure 1.4: (a) A large continuous display based on few-layer graphene deposited on a polymer substrate, fabricated by Samsung company (Taken from Ref. [17]). (b) A flexible graphene screen.

of the carriers in graphene by electrostatic potentials, in contrast to semiconductors, is extremely difficult due to the *Klein tunneling* effect in graphene [21]. The Klein tunneling is a consequence of the zero band gap in conjunction with the chiral nature of the charge carriers which prevents electrostatic induced quantum confinement in graphene structures. The goal of this thesis is the study of quantum systems in which the carriers can be confined in graphene. We want to propose: *How to confine electrons in different monolayer and bilayer graphene structures and to learn which aspects of graphene-based quantum systems are different from those made of conventional semiconductors.*

1.4 Contribution of the thesis

In order to answer the questions, mentioned in the previous section, we studied two main classes of graphene quantum structures which have different type of confinement: **I**) those where an energy gap opens, and **II**) those that exhibit zero modes (chiral states) in the energy gap of their energy spectrum. For the first class we study graphene quantum dots and quantum rings in both monolayer and bilayer graphene. For the second class, we investigate chiral states in monolayer and bilayer graphene nanostructures. Below, we give an overview of the state-of-the-art of the studied systems and present our contribution to the problem.

IA. Graphene quantum dots: To open a gap in graphene, one has to apply a different potential on the two sublattice atoms. However, we should notice that these atoms are separated by ~ 0.142 nm, thus techniques such as lithographic surface modification are not possible. A different approach is based on the reduction of the dimensionality of 2D graphene to 1D *graphene nanoribbon* and 0D *graphene flakes*, so called *graphene quantum dots* (GQDs). Of particular interest in this thesis are GQDs in which quantum

confinement was experimentally observed [22–24]. Isolation of GQDs offers the possibility to utilize the unique electronic properties of graphene to investigate novel physics and to use it for applications. In this thesis, a detailed theoretical study will be carried out on the electronic properties of GQDs. The results on GQDs in this thesis, will be obtained using both tight-binding and continuum models. Within our study, we want to answer the following questions: How do the edges and shape of the GQDs influence the electronic properties? Can the Dirac-Weyl equation describe properly the energy states of nano scale graphene flakes?

Recent studies on graphene p-n junctions demonstrate the existence of snake states at the p-n interface in the presence of external magnetic field which is a consequence of the Klein tunneling in graphene [25, 26]. In this thesis a detailed study of GQDs with a p-n and p-n-p junction is presented for the first time. The goal of this study is to learn *how the different confined states, e.g. edge states, Landau levels and snake states, interplay and influence the electronic properties of GQDs*. The presented results are very important for the experimental realization of electronic devices based on graphene p-n junctions.

IB. Bilayer graphene quantum dots: After the discovery of graphene, attention was also given to bilayer graphene (BLG). Similar to monolayer graphene, BLG has a gapless spectrum at the Fermi level but applying a perpendicular electric field opens a tunable gap [27, 28]. Using nanostructuring the gate, this tunable gap can be used to electrostatically confined QDs [29, 30]. Such gate defined QDs in BLG were recently fabricated by two different groups [31, 32]. One important issue in accurately describing the electronic properties of nanostructures is by including the Coulomb interaction between the confined electrons in such systems. Here, we extend the previous work on BLG quantum dots [29, 30] by including the Coulomb interaction for the two-electron problem as the simplest case. We will show that the competition between the valley-index and the spin of the electrons leads to new transitions of the ground state energy of bilayer graphene QDs as function of an external perpendicular magnetic field.

IC. Quantum rings in graphene: The tunable gap in BLG can be exploited for the confinement of electrons and holes of BLG nanostructures. We propose for the first time an electrostatically confined quantum ring in BLG. Quantum rings are a very important class of quantum nanostructures which have generated a lot of interest, especially because the phase coherence results in the observation of Aharonov-Bohm oscillations. We also examine a toy model consisting of an ideal ring (with zero width) in both monolayer and bilayer graphene. This toy model has the advantage that it allows for an analytical solution of the problem. In monolayer graphene the ring structure is modeled by applying a finite *mass* term, which might be realized by the interaction with the underlying substrate [11].

IIA. Chiral states in graphene: It was recently found that the presence of appropriate substrates can break the sublattice symmetry and induce a gap in the graphene spectrum

[11,33]. Hexagonal boron-nitride (h-BN) is such a substrate, and recent magnetotransport measurement of graphene on top of h-BN were very promising for high quality electronic devices [11]. In this thesis we propose that the existence of a line defect in the h-BN substrate induces unidirectional chiral states in the graphene band structure.

IIB. Chiral states in bilayer graphene: It was recently recognized that, one can find 1D chiral states in BLG in the presence of an asymmetric gate potential profile (e.g. kink profile) [34]. The presence of 1D chiral states in graphene are important for the new area of *valleytronics* [35] which attempts to use the valley degree of freedom for novel applications of graphene similar to spintronics. In this thesis we extend the previous works by studying the influence of an external magnetic field, the smoothness of the kink interface and kink-antikink potential profiles on the chiral states in BLG.

1.5 Organization of the thesis

The thesis is organized as follows:

In **chapter 2**, we give a brief introduction of the electronic properties of graphene. We focus on those theoretical aspects of single layer and bilayer graphene that are relevant for the calculations in this thesis. In particular the tight binding and continuum models for graphene are described.

Chapter 3 presents a comparative study of the energy levels in QDs within the tight binding and the continuum model. In contrast to the previous studies, in which only a special geometry and boundary is studied using the continuum model [36], our study covers triangular and hexagonal QDs with armchair, zigzag and infinite-mass boundary conditions. The influence of a perpendicular magnetic field is also investigated.

In **chapter 4**, the energy levels of a circular QD is studied analytically. Here by solving the Dirac equation we calculate the energy levels in the presence of different boundary conditions. The results are compared with those obtained using a tight binding approach.

In **chapter 5**, we investigate the magnetic interface states of graphene quantum dots that contain different shaped p-n junctions or a p-n-p junction. In this chapter, the interplay between the edge states and the quantum Hall states in QDs is studied in detail for the first time.

In **chapter 6**, we investigate the energy levels of a parabolic quantum dot in bilayer graphene in the presence of Coulomb interaction and an external magnetic field. We obtain the interacting spectrum for a dot containing two electrons within a continuum model.

In **chapter 7**, a gate defined quantum ring in bilayer graphene is proposed. The energy spectrum in the presence of an external magnetic field is investigated. We show that the energy spectrum displays a magnetic field dependence that is quite distinct from that of

semiconductor quantum rings.

Our results in chapter 7 for electrostatically confined quantum rings with finite width can be modeled using a toy model where the ring has zero-width. In **chapter 8**, we propose an analytical approach to obtain the energy levels of such ideal quantum rings in both monolayer and bilayer graphene.

Chapter 9 investigates the presence of chiral states (zero modes) in bilayer graphene in the presence of asymmetric gate potentials. The effect of a perpendicular magnetic field on such chiral states is considered.

In **chapter 10**, we propose the appearance of chiral states in single layer graphene when it is deposited on top of a hexagonal boron-nitride substrate with a line defect. Our results in this chapter are obtained analytically and are supported by density functional theory (DFT) simulations.

Finally we conclude with highlighting the remarkable results of the thesis in **chapter 11**.

Theoretical aspects of graphene

2.1 Electronic properties of graphene

2.1.1 Crystal structure

The carbon atoms in graphene are arranged in a honeycomb lattice due to their sp^2 hybridisation. The honeycomb lattice is not a Bravais lattice. Therefore two neighboring sites are inequivalent (see Fig. 2.1(a) which defines the triangular sublattices A and B). These A and B sublattices have triangular Bravais lattices, and thus the honeycomb lattice can be defined as a triangular Bravais lattice with two atoms per unit cell. The yellow region in Fig. 2.1(a) indicates the unit cell. The lattice vectors are

$$\mathbf{a}_1 = \frac{a}{2}(3, \sqrt{3}), \quad \mathbf{a}_2 = \frac{a}{2}(3, -\sqrt{3}) \quad (2.1)$$

where $a = 0.142$ nm denotes the carbon-carbon distance [18]. The vectors δ_1 , δ_2 and δ_3 shown in Fig. 2.1(a) indicate the three nearest neighbors in real space that connect the carbon atoms belonging to the same sublattice

$$\delta_1 = \frac{a}{2}(1, \sqrt{3}), \quad \delta_2 = \frac{a}{2}(1, -\sqrt{3}), \quad \delta_3 = \frac{a}{2}(-1, 0). \quad (2.2)$$

Using $\mathbf{a}_i \cdot \mathbf{b}_j = 2\pi\delta_{ij}$ (\mathbf{a}_i and \mathbf{b}_j are respectively vectors in the direct and reciprocal lattices) we obtain the reciprocal lattice vectors

$$\mathbf{b}_1 = \frac{2\pi}{3a}(1, \sqrt{3}), \quad \mathbf{b}_2 = \frac{2\pi}{3a}(1, -\sqrt{3}). \quad (2.3)$$

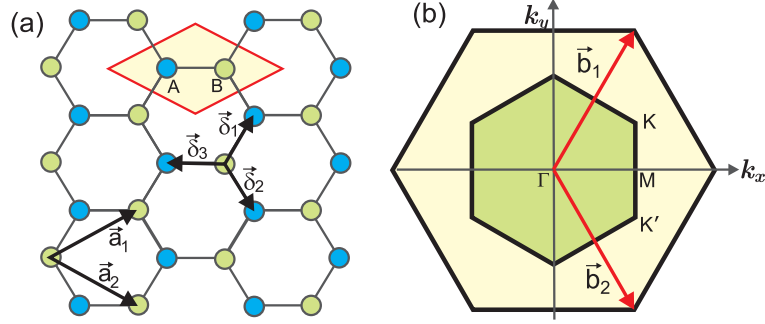


Figure 2.1: (a) Graphene lattice consisting of A and B sublattices. The yellow region shows the unit cell. \vec{a}_1 , \vec{a}_2 are basis vectors while $\vec{\delta}_1$, $\vec{\delta}_2$, and $\vec{\delta}_3$ are translation vectors between the neighboring atoms. (b) The reciprocal lattice with the hexagonal first BZ shown in green and the second BZ shown in yellow. \vec{b}_1 and \vec{b}_2 are the reciprocal lattice vectors. Two nonequivalent K and K' points are indicated in the figure.

These vectors define the corresponding first and second Brillouin zones (BZ) as shown in Fig. 2.1(b). The first BZ (green hexagon) represents a set of inequivalent points in reciprocal space, i.e. points which may not be connected to another by a reciprocal lattice vector. Of particular interest in the physics of graphene are the six corners of the first BZ, which consist of three pairs of inequivalent points K and K' . The position of these points in momentum space is given by

$$K = \left(\frac{2\pi}{3a}, \frac{2\pi}{3\sqrt{3}a} \right), \quad K' = \left(\frac{2\pi}{3a}, -\frac{2\pi}{3\sqrt{3}a} \right). \quad (2.4)$$

Note that the four remaining corners can be connected to one of these points via a translation by a reciprocal lattice vector. In the following section we will show that the interesting physics occurs for low-energy of graphene around these points and therefore these points play an essential role in the electronic properties of graphene. It is worth mentioning that the inequivalent K and K' points are not related to different sublattices A and B in the graphene lattice, but are a consequence of the two-dimensional lattice structure.

2.1.2 Band structure

The electronic band structure of graphene was derived already in 1940 [1] within a tight-binding model (TBM). Here, we present a brief overview of the derivation of the energy spectrum within a nearest-neighbor model. The Schrödinger equation for electrons on each of the sublattices is

$$H\psi_A(\mathbf{r}_n) = E\psi_A(\mathbf{r}_n), \quad H\psi_B(\mathbf{r}_n) = E\psi_B(\mathbf{r}_n) \quad (2.5)$$

where E is the energy, $\psi_A(\mathbf{r}_n)$ and $\psi_B(\mathbf{r}_n)$ represent the wave functions respectively at site A_n and B_n . Now we consider H as a TBM Hamiltonian where we take into account only the nearest neighbors corresponding to each sublattice (see Fig. 2.1(a)) and we obtain

$$E\psi_A(\mathbf{r}_n) = -t[\psi_B(\mathbf{r}_n + \boldsymbol{\delta}_1) + \psi_B(\mathbf{r}_n + \boldsymbol{\delta}_2) + \psi_B(\mathbf{r}_n + \boldsymbol{\delta}_3)], \quad (2.6)$$

$$E\psi_B(\mathbf{r}_n) = -t[\psi_A(\mathbf{r}_n - \boldsymbol{\delta}_1) + \psi_A(\mathbf{r}_n - \boldsymbol{\delta}_2) + \psi_A(\mathbf{r}_n - \boldsymbol{\delta}_3)], \quad (2.7)$$

where $t \approx 3$ eV is the nearest-neighbor hopping parameter. In the tight binding approximation, $\psi_{A,B}$ can be expanded in Bloch functions which satisfy $\psi_{A,B}(\mathbf{r}_n + \boldsymbol{\delta}_i) = \exp(i\mathbf{q}\cdot\boldsymbol{\delta}_i)\psi_{A,B}(\mathbf{r}_n)$ where $\mathbf{q} = (q_x, q_y)$ is the momentum. Then we have

$$E\psi_A(\mathbf{r}_n) = -t[e^{i\mathbf{q}\cdot\boldsymbol{\delta}_1} + e^{i\mathbf{q}\cdot\boldsymbol{\delta}_2} + e^{i\mathbf{q}\cdot\boldsymbol{\delta}_3}]\psi_B(\mathbf{r}_n), \quad (2.8)$$

$$E\psi_B(\mathbf{r}_n) = -t[e^{-i\mathbf{q}\cdot\boldsymbol{\delta}_1} + e^{-i\mathbf{q}\cdot\boldsymbol{\delta}_2} + e^{-i\mathbf{q}\cdot\boldsymbol{\delta}_3}]\psi_A(\mathbf{r}_n). \quad (2.9)$$

The above equations can be rewritten in matrix form

$$\begin{pmatrix} E & -tf(\mathbf{q}) \\ -tf^*(\mathbf{q}) & E \end{pmatrix} \begin{pmatrix} \psi_A \\ \psi_B \end{pmatrix} = 0, \quad (2.10)$$

where

$$f(\mathbf{q}) = [e^{i\mathbf{q}\cdot\boldsymbol{\delta}_1} + e^{i\mathbf{q}\cdot\boldsymbol{\delta}_2} + e^{i\mathbf{q}\cdot\boldsymbol{\delta}_3}]. \quad (2.11)$$

Calculating the eigenvalues of the above equations we obtain the dispersion relation,

$$E = \pm t \sqrt{1 + 4 \cos^2(\sqrt{3}aq_y/2) + 4 \cos(\sqrt{3}aq_y/2) \cos(3aq_x/2)}. \quad (2.12)$$

where (+) denotes the conduction and (−) the valence band. The corresponding band structure is shown in Fig. 2.2. Neglecting the electron spin, there are two bands due to the two orbitals per unit cell. The conduction (top) and valence (bottom) bands touch each other at the corners of the first Brillouin zone, i.e. K and K' points. For the reason that will be clear in the next section these points are also called *Dirac* points. In the absence of any external potential the Fermi energy is located exactly at the Dirac points which makes graphene a zero-gap semiconductor. The energy bands in Eq. (2.12) fulfill *time-reversal* symmetry which implies $E(k) = -E(-k)$. At the Dirac points we find a doubly degenerate zero-energy solution, i.e. corresponding to K and K' , that is the so called *valley* degeneracy. The energy dispersion is enlarged around one of the K points in the right panel of Fig. 2.2. The energy spectrum is linear for small values of wavevector \mathbf{q} around the K (or K') points (that is verified in the next section by expanding Eq. (2.12) around the Dirac points). This linearity leads to several unique electronic properties.

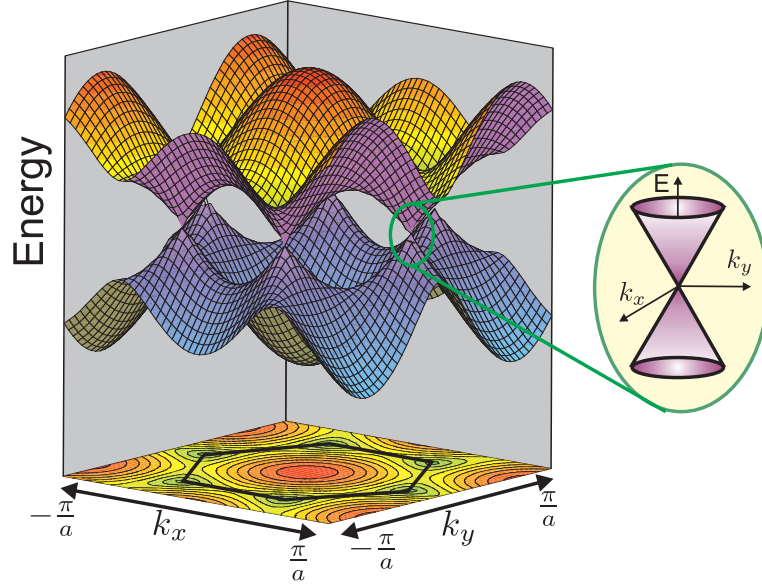


Figure 2.2: Graphene band structure

2.1.3 From tight binding approach to continuum model

In order to describe the low-energy limit, i.e. the energy region which is much smaller than the band width t , we introduce the effective Hamiltonian as

$$H_{eff} = \begin{pmatrix} 0 & tf^*(\mathbf{k}) \\ tf(\mathbf{k}) & 0 \end{pmatrix} \quad (2.13)$$

where we obtain $f(\mathbf{k})$ by expanding $f(\mathbf{q})$ around the K point $\mathbf{q} = \mathbf{k} + \mathbf{K}$ ($|\mathbf{k}| \ll |\mathbf{K}|$) that results in

$$f(\mathbf{k}) = e^{i\pi/6} \left[\frac{3}{2} a (k_x - ik_y) \right]. \quad (2.14)$$

The phase appearing in Eq. (2.14) is a consequence of the arbitrary choice of the relative phase between the two sublattice components and does not affect the dispersion relation (2.12) which depends only on the modulus of the phase factor. This yields the effective low-energy Hamiltonian around the K point as

$$H^K = \hbar v_F [\sigma_x k_x + \sigma_y k_y] \quad (2.15)$$

where we have defined the Fermi velocity of the carriers $v_F = 3at/2\hbar \approx 10^6$ m/s, and σ_x and σ_y are Pauli matrices.

Similarly, one can expand $f(\mathbf{q})$ around the K' point which gives

$$H^{K'} = -\hbar v_F [\sigma_x k_x - \sigma_y k_y]. \quad (2.16)$$

Expanding the energy spectrum (2.12) around the K (or K') with help of

$$\cos \frac{3aq_x}{2} \approx -1, \quad \cos \frac{\sqrt{3}aq_y}{2} \approx \frac{1}{2} - \frac{3}{4}ak_y, \quad \cos^2 \frac{\sqrt{3}aq_y}{2} \approx \frac{1}{4} - \frac{3}{4}ak_y \quad (2.17)$$

we obtain the dispersion energy around the K (or K') point as

$$E = \pm \hbar v_F |\mathbf{k}| \quad (2.18)$$

which is independent of K and K' . Eq. (2.18) is often called the Dirac-Weyl equation in analogy to the Dirac-Weyl equation [37] for neutrinos where now the velocity of light is replaced with the Fermi velocity v_F of graphene. From Eqs. (2.15) and (2.16) the full effective Hamiltonian is given by

$$H_{eff} = \begin{pmatrix} H_K & 0 \\ 0 & H_{K'} \end{pmatrix} \quad (2.19)$$

where the eigenstates are the four-component wavefunction

$$\Psi_K = \frac{1}{\sqrt{2}} \begin{pmatrix} 1 \\ e^{i\varphi_k} \\ 0 \\ 0 \end{pmatrix}, \quad \Psi_{K'} = \frac{1}{\sqrt{2}} \begin{pmatrix} 0 \\ 0 \\ 1 \\ e^{-i\varphi_k} \end{pmatrix} \quad (2.20)$$

with $\varphi_k = \arctan(k_y/k_x)$. It should be noticed that the Pauli matrices in H_K and $H_{K'}$ distinguish the A and B components in each valley, i.e. *sublattice pseudospin*, while H_K and $H_{K'}$ in Eq. (2.19) which correspond respectively to the K and K' valley are linked to the *valley pseudospin*. If one should include also the real spin of the electrons the effective Hamiltonian becomes a 8×8 matrix.

2.1.4 Experimental observation of graphene bandstructure

The band structure of solids can be observed experimentally using the angle resolved photoemission spectroscopy (ARPES) technique. In this technique an electron analyzer detects the energy of the photo-emitted electrons from the sample and the working principle is based on the conservation of the momentum and energy in the photon-electron scattering,

$$\hbar\nu = E_f - E_i, \quad \mathbf{k} = \mathbf{k}_f - \mathbf{k}_i \quad (2.21)$$

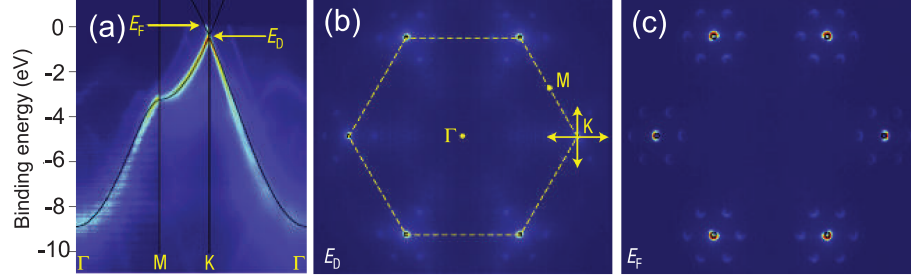


Figure 2.3: ARPES measurement of the dispersion relation of epitaxial graphene (from Ref. [38]).

where ν is the frequency of the incident photon. $E_i(\mathbf{k}_i)$ and $E_f(\mathbf{k}_f)$ are, respectively, the energy (momentum) of the incident and final electron states. The direction of the final momentum \mathbf{k}_f , gives information on the momentum-dependence of the energy and thus the electronic bandstructure.

Figure 2.3 shows the first ARPES results on epitaxial graphene that was reported by A. Bostwick *et al* [38]. The energy dispersion of the π band (see Fig. 2.3(a)) exhibits a linear behavior around the K (or K') points which is in agreement with the theoretical dispersion relation obtained within the TBM. The form of the first BZ of graphene is shown in Fig. 2.3(b) where an energy map corresponding to $E_D = 0$ is plotted. The energy cut at the Fermi level E_F is shown in Fig. 2.3(c) which demonstrates the circular Fermi surface around the K and the K' points (notice that due to the substrate effect, i.e. SiC in this experiment, $E_F \neq E_D$).

2.1.5 Chirality in graphene

The *helicity* operator, is a well-known operator in the field of high-energy physics. The helicity of a particle is defined as the projection of spin onto the direction of its motion. Based on this definition the helicity operator is given by

$$h_k = \boldsymbol{\sigma} \cdot \mathbf{k} / |\mathbf{k}| \quad (2.22)$$

where $\boldsymbol{\sigma}$, i.e. Pauli matrices, represents the spin of the particles. Notice that h_k is a Hermitian and unitary operator. When the spin projection of the particle is parallel to the direction of its motion (e.g. neutrinos) the eigenvalue of h_k is $\eta = +1$ and when it is anti-parallel (e.g. anti-neutrinos) it results in the eigenvalue $\eta = -1$.

For graphene, since the charged particles are described by the Dirac Hamiltonian, we can use the same definition as Eq. (2.22) for the helicity operator where now the *sublattice pseudospin* replaces the real spin. Because of this correspondence h_k is referred to

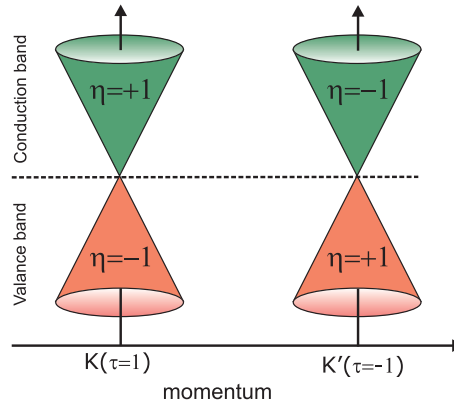


Figure 2.4: Relation between the valence and conduction bands, valley isospin τ , and chirality η in graphene.

as *chirality*. This operator commutes with H_K and $H_{K'}$ of Eqs. (2.15) and (2.16), i.e. $[H_{K,K'}, h_k] = 0$. It is possible to express the Dirac Hamiltonian in terms of the chirality operator in the valley isotropic form

$$H = \tau h_k |\mathbf{k}| \quad (2.23)$$

where $\tau = +1$ ($\tau = -1$) corresponds to the Hamiltonian for the K (K') valley. The chirality eigenvalue η is depicted in Fig. 2.4 for the conduction and valence bands at the different valleys.

2.2 Bilayer graphene

Bilayer graphene (BLG) consists of two coupled sheets of graphene that are located on top of each other. Figure 2.5 shows the crystal structure of bilayer graphene, in AB stacking formation, where the layers are arranged so that one of the atoms from the lower layer A_2 is directly below an atom from the upper layer B_1 . The hopping parameter between the carbon atoms in each layer is $t \approx 3$ eV and the strongest coupling parameter between the layers occurs between A_2 and B_1 sublattices $\gamma = 0.4$ eV (the other interlayer coupling parameters are negligible) [39]. Now we consider BLG as a system of two coupled layers of monolayer which are connected via A_1 and B_2 atoms (see Fig. 2.5). Our description

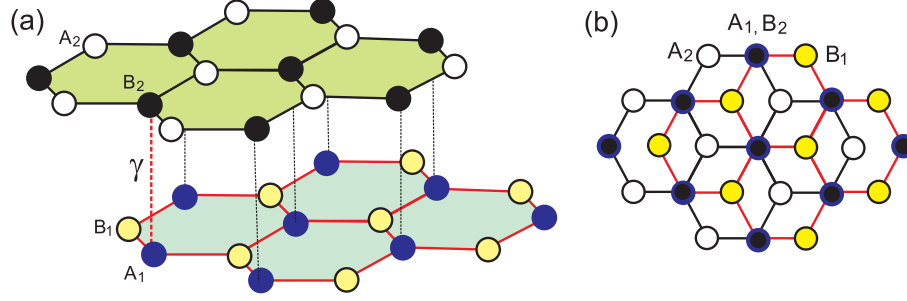


Figure 2.5: (a) Bilayer graphene lattice consisting of two layers in AB stacking. $t \approx 3$ eV is the hopping parameter between the carbon atoms in each layer, i.e. between A_1 - B_1 (or A_2 - B_2). $\gamma \approx 0.4$ eV is the hopping parameter between A_1 and B_2 . (b) Top view of bilayer graphene lattice depicted in (a).

can be formulated in a 4×4 Hamiltonian

$$H = \begin{pmatrix} 0 & tf(\mathbf{q}) & 0 & \gamma \\ tf^*(\mathbf{q}) & 0 & 0 & 0 \\ 0 & 0 & 0 & tf(\mathbf{q}) \\ \gamma & 0 & tf^*(\mathbf{q}) & 0 \end{pmatrix} \quad (2.24)$$

where $f(\mathbf{q})$ is given by Eq. (2.11). In analogy with single layer graphene we obtain an effective Hamiltonian for BLG around the K or K' points

$$H_{BLG} = \begin{pmatrix} 0 & \hbar v_F(\tau p_x + ip_y) & 0 & \gamma \\ \hbar v_F(\tau p_x - ip_y) & 0 & 0 & 0 \\ 0 & 0 & 0 & \hbar v_F(\tau p_x + ip_y) \\ \gamma & 0 & \hbar v_F(\tau p_x - ip_y) & 0 \end{pmatrix} \quad (2.25)$$

where $p_{x,y} = -i\hbar\partial_{x,y}$ and $\tau = +1$ ($\tau = -1$) denotes the Hamiltonian corresponding to K (K'). The corresponding wavefunction of the Hamiltonian (2.25) are

$$\psi_K = [\varphi_{A_1}, \varphi_{B_1}, \varphi_{A_2}, \varphi_{B_2}]^T, \quad \psi_{K'} = [\varphi_{B_1}, \varphi_{A_1}, \varphi_{B_2}, \varphi_{A_2}]^T, \quad (2.26)$$

The corresponding energy spectrum of Hamiltonian (2.25) consists of four valley degenerate bands

$$E_{\pm}^{\pm} = \pm \frac{\gamma}{2} \pm \sqrt{\frac{\gamma^2}{4} + (\hbar v_F k)^2} \quad (2.27)$$

where $k = \sqrt{k_x^2 + k_y^2}$ is the wavevector. The spectrum is plotted in Fig. 2.6(a). The lowest energy bands touch each other at the K point while the two upper bands which result from the strong coupling between the layers γ , have the energies $E_+^+ \geq \gamma$ and $E_-^- \leq -\gamma$.

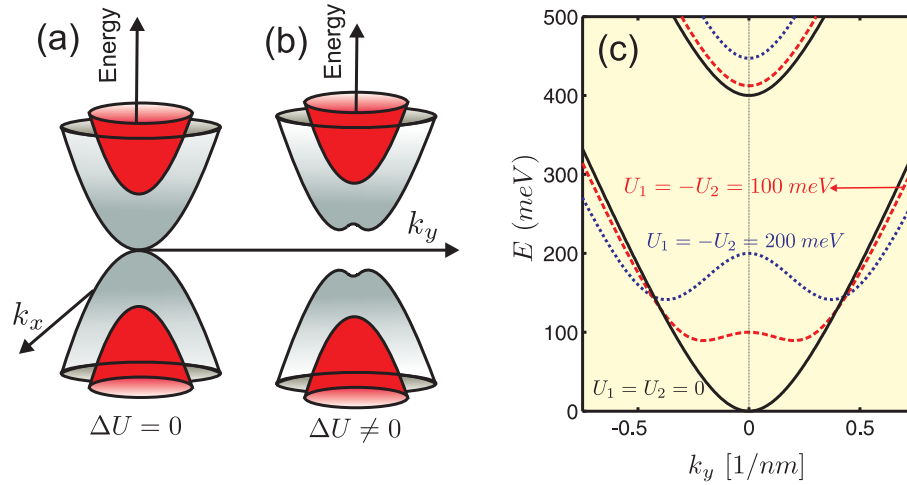


Figure 2.6: Low energy spectrum of (a) unbiased $\Delta U = 0$ and (b) biased bilayer graphene $\Delta U \neq 0$. (c) Energy spectrum of bilayer graphene for $U_1 = U_2 = 0$ (black solid curve), $U_1 = -U_2 = 100$ meV (red dashed curve) and $U_1 = -U_2 = 200$ meV (blue dotted curve).

It was recently found that the application of a perpendicular electric field as e.g. produced by external gates deposited on the BLG surface can induce a gap in the spectrum (see Fig. 2.6(b)) by creating a charge imbalance between the two graphene layers [28,40]. In the experiment of Ref. [40], the authors demonstrated that they can arbitrarily change the band gap in BLG from zero to 250 meV at room temperature. The existence of such a tunable gap is remarkable and shows the potential of BLG for nanoelectronics. In order to study the effect of the gate potential on the energy spectrum of BLG we apply the electrostatic potentials U_1 and U_2 receptively to the upper and lower layers of BLG. Then the Hamiltonian is given by $H = H_{BLG} + V$ where

$$V = \begin{pmatrix} U_1 \mathbf{I} & 0 \\ 0 & U_2 \mathbf{I} \end{pmatrix} \quad (2.28)$$

and \mathbf{I} represents a 2×2 unity matrix. The solutions for the energy spectrum yield,

$$E_{\pm}^{\pm} = \frac{1}{2} [U_1 + U_2 \pm \sqrt{(\gamma \pm \Gamma)^2 + \Omega}] \quad (2.29)$$

where $\Gamma = \sqrt{\gamma^2 + 4s^2 + 4(s^2/\gamma^2)\Delta U^2}$, $\Omega = [1 - 4(s/\gamma)^2]\Delta U^2$, $\Delta U = U_1 - U_2$, and $s = \hbar v_F k$. When $U_1 = U_2 = U$ the spectrum results in Eq. (2.27) which is only shifted by U . Figure 2.6(c) shows the spectrum for $U_1 = U_2 = 0$ (black solid curve), $U_1 = -U_2 = 100$ meV (dashed red curve) and $U_1 = -U_2 = 200$ meV. Note that the spectrum is increasingly

deformed when ΔU increases, with the appearance of energy minima at nonzero values of k ,

$$k_y^{min} = \pm \frac{\Delta U}{2\hbar v_F} \sqrt{\frac{\Delta U^2 + 2\gamma^2}{\Delta U^2 + \gamma^2}}. \quad (2.30)$$

Except for the Hamiltonian (2.25) corresponding to BLG, another effective 2×2 Hamiltonian, the so called *two-band Hamiltonian*, is often used in the literature. This Hamiltonian describes the low energy limit $E \ll \gamma$ where the upper bands in Fig. 2.6 are neglected. Because of $E \ll \gamma$, we assume that the occupation of the sites which are connected via γ is zero. Now we write the eigenproblem for the Hamiltonian 2.25 as

$$\begin{pmatrix} \tau U_1 & \pi & 0 & \gamma \\ \pi^\dagger & \tau U_1 & 0 & 0 \\ 0 & 0 & \tau U_2 & \pi \\ \gamma & 0 & \pi^\dagger & \tau U_2 \end{pmatrix} \begin{pmatrix} \phi_A \\ \phi_B \\ \phi_C \\ \phi_D \end{pmatrix} = E \begin{pmatrix} 0 \\ \phi_B \\ \phi_C \\ 0 \end{pmatrix} \quad (2.31)$$

where $\pi = v_F(p_x + ip_y)$ and $\pi^\dagger = v_F(p_x - ip_y)$ and $[\phi_A, \phi_B, \phi_C, \phi_D]^T$ denotes the four-component wave function. Let us use the first and the last rows of Eq. (2.31) to express ϕ_A and ϕ_D in terms of the other components

$$\phi_A = \frac{\tau U_2 \pi \phi_B - \gamma \pi^\dagger \phi_C}{\gamma^2 - U_1 U_2}, \quad \phi_D = \frac{\tau U_1 \pi^\dagger \phi_C - \gamma \pi \phi_B}{\gamma^2 - U_1 U_2} \quad (2.32)$$

Noting $U_{1,2} \ll \gamma$ (because we are in low energy limit), we substitute the above relations into the second and third rows of Eq. (2.31) and obtain

$$\frac{\tau \pi^\dagger U_2 \pi}{\gamma^2} \phi_B - \frac{(\pi^\dagger)^2}{\gamma} \phi_C + \tau U_1 \phi_B = E \phi_B, \quad (2.33)$$

$$\frac{\tau \pi U_1 \pi^\dagger}{\gamma^2} \phi_C - \frac{\pi^2}{\gamma} \phi_B + \tau U_2 \phi_C = E \phi_C. \quad (2.34)$$

Rewriting the above equations in matrix form one can obtain the 2×2 Hamiltonian as

$$H = -\frac{1}{\gamma} \begin{pmatrix} 0 & (\pi^\dagger)^2 \\ \pi^2 & 0 \end{pmatrix} + \tau \left[\begin{pmatrix} U_1 & 0 \\ 0 & U_2 \end{pmatrix} - \frac{1}{\gamma^2} \begin{pmatrix} U_2 \pi^\dagger \pi & 0 \\ 0 & U_1 \pi^\dagger \pi \end{pmatrix} \right] \quad (2.35)$$

For a detailed discussion of this effective two-band approximation, see Refs. [39, 41].

2.3 Influence of a perpendicular magnetic field

Here we will investigate the energy levels of monolayer and bilayer graphene in the presence of a perpendicular magnetic field. The energy levels of a quantum system in the presence of an external magnetic field are the so called *Landau levels* (LLs).

2.3.1 Landau levels in monolayer graphene

The Hamiltonian of graphene in the presence of an external magnetic field is given by

$$H = \begin{pmatrix} 0 & -i\hbar v_F[(\partial_x + eA_x) - i(\partial_y + eA_y)] \\ -i\hbar v_F[(\partial_x + eA_x) - i(\partial_y + eA_y)] & 0 \end{pmatrix} \quad (2.36)$$

where A_x, A_y are the vector potential components. Notice that the Hamiltonian (2.36) is obtained using the transformation $\mathbf{p} \rightarrow \mathbf{p} + e\mathbf{A}$ in Eq. (2.15). This transformation is valid as long as the lattice spacing a is much smaller than the magnetic length $l_B = \sqrt{\hbar/eB}$. We will understand later that the LLs are independent of valley index. Considering the Landau gauge $\mathbf{A} = (0, Bx, 0)$, the Hamiltonian commutes with p_y , i.e. $[H, p_y] = 0$. This allows us to take $\psi(x, y) = e^{ik_y y} [\varphi_a(x), \varphi_b(x)]^T$ as the two-component wavefunction where k_y is the wavevector along the y -direction. Solving $H\psi = E\psi$ results in two coupled differential equations

$$-i\hbar v_F \left[\frac{d}{dx} + (k_y + x/l_B) \right] \varphi_b = E\varphi_a, \quad (2.37)$$

$$-i\hbar v_F \left[\frac{d}{dx} - (k_y + x/l_B) \right] \varphi_a = E\varphi_b. \quad (2.38)$$

The above equations can be solved analytically where the solutions are Hermite polynomials [42] and the LLs are given by,

$$E_n = \pm \frac{\hbar v_F}{l_B} \sqrt{2n} = \pm \hbar \omega_D \sqrt{n}, \quad n = 0, 1, 2, \dots \quad (2.39)$$

where $\omega_D = \sqrt{2}v_F/l_B$. The corresponding LLs of graphene are shown in Fig. 2.7(a). One important point of the above spectrum, is the difference between the LLs in graphene and those for standard electrons obtained within the Schrödinger equation where the LLs depend linearly on magnetic field $E_n \propto (n+1/2)B$. Notice that Eq. (2.39) is independent of the valley index. Another important aspect is the existence of a zeroth LL $E_0 = 0$ which is a direct consequence of the zero gap Dirac fermions in graphene. The zeroth LL has four-fold degeneracy: two-fold because of electron-hole symmetry and two-fold because of valley symmetry. Refs. [43–45] are examples where the zeroth LL was experimentally observed in graphene.

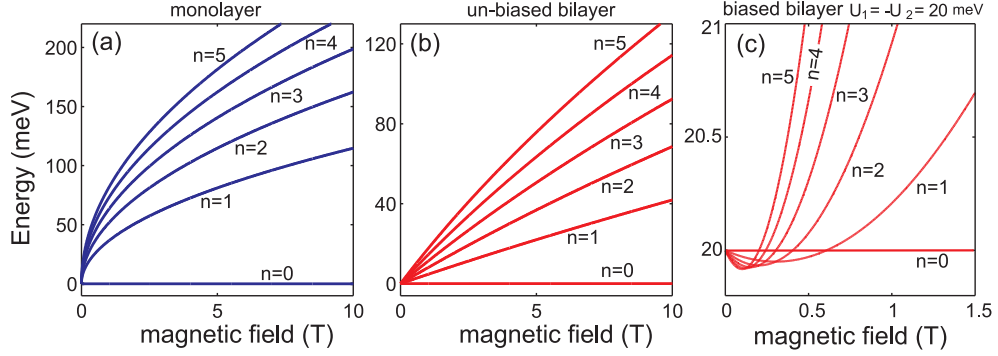


Figure 2.7: Landau levels as function of magnetic field in (a) single layer, (b) unbiased bilayer, and (c) biased bilayer graphene.

2.3.2 Landau levels in bilayer graphene

The Hamiltonian (2.25) for bilayer graphene around the K point and in the presence of gate potentials applied to the upper U_1 and lower U_2 layer yields

$$H = \begin{pmatrix} U_1 & 0 & 0 & \pi^\dagger \\ 0 & U_1 & \pi & 0 \\ 0 & \pi^\dagger & U_2 & \gamma \\ \pi & 0 & \gamma & U_2 \end{pmatrix}. \quad (2.40)$$

In the presence of a perpendicular magnetic field $\pi = -i\hbar v_F[\partial_x + i(\partial_y + (eB/\hbar)x)]$ in which we used the Landau gauge for the vector potential.

Taking $\psi(x, y) = e^{ik_y y}[\varphi_a(x), i\varphi_b(x), \varphi_c(x), i\varphi_d(x)]^T$, we solve $H\psi = E\psi$ and obtain

$$(d/d\xi + \xi)\varphi_d = (\epsilon - u_1)\varphi_a, \quad (2.41)$$

$$-(d/d\xi - \xi)\varphi_c = (\epsilon - u_1)\varphi_b, \quad (2.42)$$

$$(d/d\xi + \xi)\varphi_b = (\epsilon - u_2)\varphi_c - \gamma\varphi_d, \quad (2.43)$$

$$-(d/d\xi - \xi)\varphi_a = (\epsilon - u_2)\varphi_d - \gamma\varphi_c \quad (2.44)$$

where $\xi = l_B k_y + x/l_B$, $\epsilon = El_B/\hbar v_F$, $u_{1,2} = U_{1,2}l_B/\hbar v_F$ and $\gamma' = \gamma l_B/\hbar v_F$. Equations (2.41)-(2.44) can be reduced to a single differential equation

$$[d^2/d\xi^2 + \alpha^2 + \delta^2 - \xi^2]\varphi_d = [(\alpha^2 - \delta^2)\gamma'^2 + (1 - 2\alpha\delta)^2]\varphi_d, \quad (2.45)$$

where $\alpha = \epsilon + (u_1 + u_2)/2$ and $\delta = (u_1 - u_2)/2$. We note that the solution of the following equation can also satisfy Eq. (2.45)

$$[-d^2/d\xi^2 + \xi^2]\varphi_d = s_\pm \varphi_d, \quad (2.46)$$

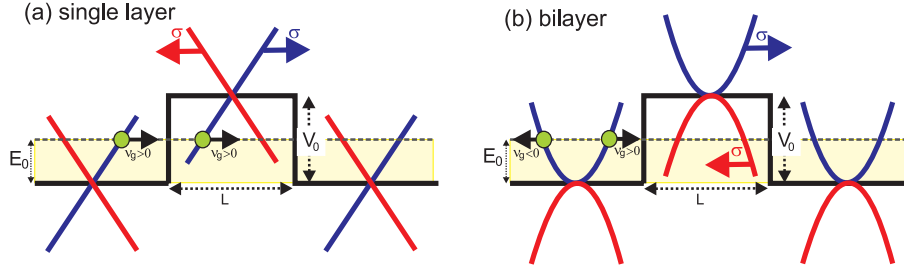


Figure 2.8: Schematic illustration of Klein tunneling in (a) single layer and (b) bilayer graphene. In both cases σ denotes the pseudospin direction corresponding to the conduction (blue curves) and valence (red curves) bands.

where $s_{\pm} = \alpha^2 + \delta^2 + \pm[(\alpha^2 - \delta^2)\gamma'^2 + (1 - 2\alpha\delta)^2]^{1/2}$. To solve Eq. (2.46) we set $\varphi_d(\xi) = f(\xi)e^{-\xi^2/2}$; this eliminates the ξ^2 term and gives

$$\frac{d^2 f}{d\xi^2} - 2\xi \frac{df}{d\xi} - (s_{\pm} + 1)f = 0. \quad (2.47)$$

This is the equation satisfied by the Hermite polynomials $H_n(\xi)$ for $1 + s_{\pm} = -2n$. The LL spectrum is given by the solutions α_n of the fourth-order algebraic equation

$$[(\alpha + \delta)^2 - 2(n + 1)][(\alpha - \delta)^2 - 2n] - (\alpha^2 - \delta^2)\gamma'^2 = 0, \quad n = 0, 1, 2, \dots \quad (2.48)$$

For $U_{1,2} = 0$, Eq. (2.48) results in the LLs for an unbiased bilayer graphene

$$E = \pm \left\{ \gamma^2/2 + (2n + 1)E_0^2 \pm \sqrt{\gamma^4/4 + (2n + 1)\gamma^2 E_0^2 + E_0^4} \right\}^{1/2}, \quad n = 0, 1, 2, \dots \quad (2.49)$$

where $E_0 = \hbar v_F/l_B$. For $\gamma \rightarrow 0$, Eq. (2.49) reduces to that of two uncoupled layers of graphene $E = \pm(\hbar v_F/l_B)\sqrt{2n + 1 \pm 1}$. Figs. 2.7(a) and 2.7(b) show the Landau levels respectively for unbiased BLG and in the presence of the gate potentials $U_1 = -U_2 = 20$ meV.

2.4 Confinement in graphene

2.4.1 Klein paradox problem

The so called Klein paradox, i.e. unimpeded transmission of relativistic particles through high and wide potential barriers, is a well-known phenomenon in quantum electrodynamics for about more than 80 years [46]. Graphene is the first condensed matter system in

which the Klein paradox (it is also known as *Klein tunneling*) through a potential barrier was observed experimentally [47]. Observation of the Klein paradox in graphene is due to the chiral nature of massless Dirac fermions. In order to present this problem in more detail we consider a massless Dirac fermion with energy E_0 and momentum k_1 approaching a 1D potential barrier¹. The Dirac equation for this system is

$$H_s = (-i\hbar v_F \partial_x \sigma_x + V)\psi = E_0 \psi, \quad V = \begin{cases} 0, & x < 0, x > L \\ V_0, & 0 \leq x \leq L \end{cases} \quad (2.50)$$

where ψ denotes the two-component wave function and for the regions *I* (before the barrier), *II* (inside the barrier), and *III* (after the barrier) is given by,

$$\psi_I = e^{ik_1 x} \begin{pmatrix} 1 \\ 1 \end{pmatrix} + R e^{-ik_1 x} \begin{pmatrix} 1 \\ -1 \end{pmatrix}, \quad E_0 = \hbar v_F |k_1| \quad (2.51)$$

$$\psi_{II} = A e^{ik_2 x} \begin{pmatrix} 1 \\ 1 \end{pmatrix} + B e^{-ik_2 x} \begin{pmatrix} 1 \\ -1 \end{pmatrix}, \quad V_0 - E_0 = \hbar v_F |k_2| \quad (2.52)$$

$$\psi_{III} = T e^{ik_3 x} \begin{pmatrix} 1 \\ 1 \end{pmatrix}, \quad E_0 = \hbar v_F |k_3|. \quad (2.53)$$

We now want to calculate the transmission (T) and reflection (R) coefficients. Continuity of the wave function at $x = 0$ and $x = L$ yields a set of four algebraic equations $A \pm B = T$, $1 + R = A + B$ and $1 - R = A - B$ which results in $T = 1$ and $R = 0$. A schematic illustration of the dispersion relation at the different regions of the potential barrier problem is shown in Fig. 2.8(a). The Klein tunneling is a consequence of the fact that the potential barrier can not reverse the direction of the group velocity of a massless fermions in graphene (notice that the group velocity of Dirac fermions before and inside the barrier is indicated in Fig. 2.8(a)). In monolayer graphene the pseudospin is conserved since $[\sigma_x, H_s] = 0$ and thus the velocity operator $v_x^s = -i[x, H_s] = \hbar v_F \sigma_x$ is also a conserved quantity.

Similarly, one can consider the tunneling problem through a 1D barrier in bilayer graphene. We use the two-band Hamiltonian, Eq. (2.35), in 1D that is given by $H_b =$

¹The potential barrier should be smooth over the graphene lattice constant ~ 0.24 nm in order to ensure that there is no inter-valley scattering (the distance between valleys in reciprocal space is $|K - K'| \sim 1/a$).

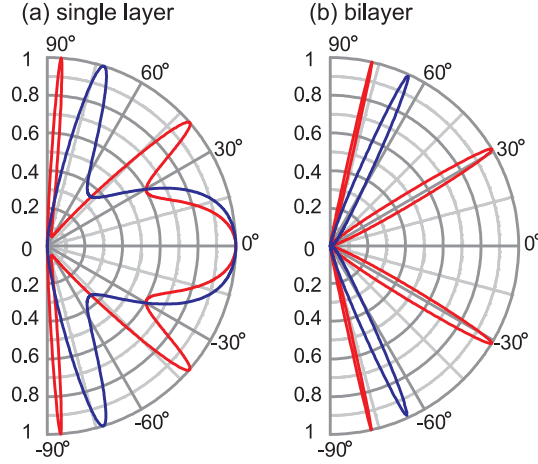


Figure 2.9: Transmission probability through a $L = 100$ nm wide barrier as a function of the incident angle for (a) single layer and (b) bilayer graphene. The Fermi energy for the incident electrons is $E_0 = 80$ meV for single layer and $E_0 = 17$ meV for bilayer. The barrier heights are (a) $V_0 = 200$ meV and (b) $V_0 = 50$ meV (red curves), and (a) $V_0 = 285$ meV and (b) $V_0 = 100$ meV (blue curves). The picture is adapted from Ref. [21].

$[(\hbar v_F)^2/\gamma]\partial_x^2 + V$. Now the wave functions outside and inside the barrier are

$$\psi_I = e^{k_1 x} + R e^{-k_1 x} \begin{pmatrix} 1 \\ 1 \end{pmatrix}, \quad \sqrt{\gamma E_0} = \hbar v_F |k_1| \quad (2.54)$$

$$\psi_{II} = A e^{ik_2 x} + B e^{-ik_2 x} \begin{pmatrix} 1 \\ 1 \end{pmatrix}, \quad \sqrt{\gamma(V_0 - E_0)} = \hbar v_F |k_2| \quad (2.55)$$

$$\psi_{III} = T e^{k_3 x} \begin{pmatrix} 1 \\ 1 \end{pmatrix}, \quad \sqrt{\gamma E_0} = \hbar v_F |k_3|. \quad (2.56)$$

Matching the solutions at $x = 0$ and $x = L$ yields $A = -B$, $R = -1$ and $T = 0$. This is in sharp contrast with single layer graphene. Although the pseudospin σ_x is still conserved but the velocity operator is not, i.e. $v_x^b = -i[x, H_b] = -2i(\hbar v_F)^2 \partial_x / \gamma$ (see Fig. 2.8(b)). A more general study of the Klein paradox in single layer and bilayer graphene is presented in Ref. [21] for a 2D barrier and arbitrary angle of the incident wave. In Fig. 2.9 the transmission probability T is shown as function of the incident angle for (a) single layer and (b) bilayer graphene. Although in BLG, the transmission is zero for a normally incident wave, however there are *magic angles*, e.g. at the angle $\sim 30^\circ$ for $V_0 = 50$ meV in Fig. 2.9(b), where the electrons can penetrate the barrier perfectly with unit transmission probability.

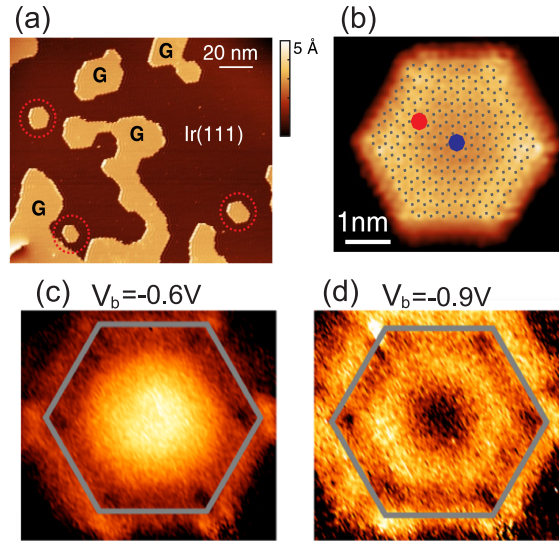


Figure 2.10: (a) Large scale STM image of GQDs grown by CVD on Ir(111). (b) STM topography of a small GQD (c) Measured LDOS maps corresponding to the bias voltages $V_b = -0.6$ V and $V_b = -0.9$ V. The gray line in (c) denotes the edges of the GQD. The figures are adopted from Ref. [52].

Despite the Klein tunneling problem in graphene, confinement of carriers in graphene-based nanostructures is an essential requirement to realize graphene electronic devices. In the following we discuss *graphene quantum dots* in which Dirac fermions are confined.

2.4.2 Graphene quantum dots

Quantum dots (QDs) are small structures in which the carriers are confined in all three spatial dimensions (i.e. zero-dimensional (0D) confinement). Because of the quantized energy in the QDs (that is a consequence of 0D confinement), they have been regarded as *artificial atoms* [48]. In addition to the interesting theoretical aspects, QDs are very promising candidates for spin qubits and thus for future quantum information technology. In conventional semiconductor QDs, based on GaAs, the spin-orbit and electron spin-nuclear spin interactions limit the spin coherence time and thus the functionality of the device. Therefore, to overcome this issue, an alternative material for QDs is needed.

Graphene-based QDs can be exceptional systems for spintronics applications due to their long spin coherence time which is a consequence of the very weak spin-orbit interaction in graphene. However, as we mentioned before, the Klein tunneling effect prevents the confinement of the carriers in graphene structures. Therefore, fabricating graphene

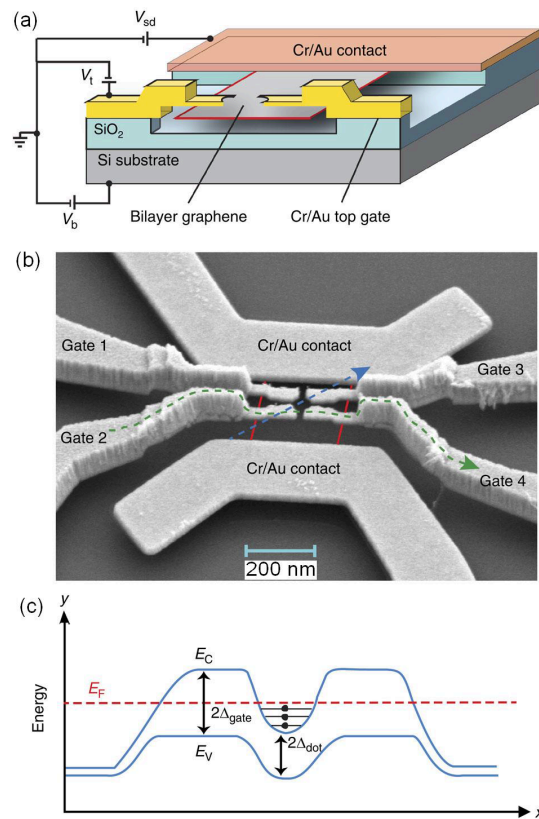


Figure 2.11: (a) Schematic cross-section of the experimental setup performed in Ref. [31] for (a) gate-defined bilayer graphene quantum dot. (b) Scanning electron micrograph of a QD device. (c) Potential profile across the sample illustrating quantum dot formation. E_C and E_V indicate the edges of the conduction and valence bands.

QDs with gate potential techniques, that is well-known for semiconductor QDs [49], will become impossible to be implemented.

Soon after the discovery of graphene a new class of QDs, i.e. graphene flakes, were realized [50]. Graphene flakes are disk-like materials with finite size on the scale of nanometer. Because of the finite size of the flake, the energy levels are quantized and therefore these flakes are also referred to as graphene quantum dots (GQDs). GQDs can be fabricated by etching graphene into small flakes [51]. Another method to isolate GQDs is growing GQDs by chemical vapor deposition (CVD) on an Ir(111) substrate [52–54]. Fig. 2.10 shows the experimental results of Ref. [52]. In this experiment the local density of states of GQDs are measured for different size (reported up to 20 nm) and shapes using scanning tunneling microscopy and spectroscopy. Theoretical [55–58] and experimen-

tal [23] studies on GQDs demonstrate that the electronic properties of GQDs are highly depended on the size, geometry and type of the edges (i.e. armchair and zigzag) of the dot. There are also different chemical methods to grow very small graphene flakes. They are based on various chemical reactions that result in different shapes of graphene flakes [59].

2.4.3 Bilayer graphene quantum dots

The existence of a tunable energy gap in biased bilayer graphene has opened a new route to create quantum structures. In particular, the possibility of tailoring the energy gap in BLG has raised the prospect of the creation of electrostatically defined QDs in BLG. The energy levels of gated defined QDs have been investigated theoretically in the absence [29] and the presence [30] of a perpendicular magnetic field. Soon after these theoretical studies, such gate defined quantum dots in bilayer (and few-layer) graphene were realized experimentally [31, 32]. In Fig. 2.11 we show the experimental setup of gate defined bilayer graphene quantum dot as fabricated in Ref. [31].

The QDs in monolayer graphene which has been realized through direct etching of the graphene layer, have inherently the problem of edge disorder. The preparation of a specific type of edge is important and a challenging issue which has not yet been completely mastered experimentally. Both problems are not present in gated BLG quantum dots. A further advantage of this approach is that the confinement can be tuned by varying the gate profile and the depth of the confining potential by the strength of the gate voltage, thereby eliminating both edge and substrate disorder.

CHAPTER 3

Energy levels of triangular and hexagonal graphene quantum dots

The Dirac equation is solved for triangular and hexagonal graphene quantum dots for different boundary conditions in the presence of a perpendicular magnetic field. We analyze the influence of the dot size and its geometry on their energy spectrum. A comparison between the results obtained for graphene dots with zigzag and armchair edges, as well as for infinite-mass boundary condition, is presented and our results show that the type of graphene dot edge and the choice of the appropriate boundary conditions have a very important influence on the energy spectrum. The single particle energy levels are calculated as function of an external perpendicular magnetic field which lifts degeneracies. Comparing the energy spectra obtained from the tight-binding approximation to those obtained from the continuum Dirac equation approach, we verify that the behavior of the energies as function of the dot size or the applied magnetic field are qualitatively similar, but in some cases quantitative differences can exist.

3.1 Introduction

Recent improvements of different fabrication techniques made possible cutting and manufacturing of single layer graphene flakes, with different shapes and sizes [52–54, 60],

The results of this chapter were published as
M. Zarenia, A. Chaves, G. A. Farias, and F. M. Peeters, Phys. Rev. B **84**, 245403 (2011).

where the lateral confinement naturally occurs. Using the tight-binding model (TBM), remarkable effects have been reported as a consequence of the type of the edges and the geometry of these flakes [55–58, 61–63]: *i*) zero-energy states are predicted for triangular graphene flakes with zigzag boundaries, *ii*) for very small flakes a gap opens (the energy gap of different graphene flakes was recently investigated experimentally [23]) and the density of states (DOS) strongly depends on the type of the edges for any dot geometry, and *iii*) the energy levels of graphene quantum dots in the presence of a magnetic field approach the Landau levels with increasing magnetic field.

Recently, analytical results were reported for electrostatically defined circular quantum dots [64–68], for circular graphene disks with infinite mass boundary conditions [69], for triangular flakes with armchair edges [36] and zigzag edges [57] and for square graphene quantum dots [70]. However, it is not always clear how the complicated boundary conditions describing the zigzag and armchair edges can be invoked in the continuum model. Furthermore, the geometry of the triangular and hexagonal graphene flakes, make such systems harder to be studied by analytical means. One has to rely on, either a tight-binding model or a numerical solution of coupled differential equations in case of the continuum model.

The continuum model describes very well the low energy states in an infinite graphene sheet, but it is not clear if this is still the case for small graphene flakes. Therefore, it is important to learn if there is a minimum size beyond which the continuum model no longer gives reliable predictions. Furthermore, because of the large influence of the type of edges on the energy spectrum, and since it is not always clear which boundary conditions should be invoked in the Dirac equation for each possible geometry of the flake, a comparison between the results obtained with the different possible boundary conditions and a link with the TBM is an interesting issue which requires a detailed study.

In this chapter, by solving the Dirac equation numerically, we present a theoretical study of the energy spectra of triangular and hexagonal graphene quantum dots, where three types of boundary conditions are invoked, namely, zigzag, armchair and infinite mass boundary condition. The influence of an external magnetic field, perpendicular to the graphene layer, on the energy spectrum of the quantum dots is also analyzed. A comparison between the results obtained with the continuum model and those obtained from the tight-binding approach will be made.

3.2 Tight-binding model

The tight-binding Hamiltonian within the nearest neighbor approximation is

$$H = \sum_n E_n c_n c_n^\dagger + \sum_{\langle n,m \rangle} (t_{n,m} c_n^\dagger c_m + h.c.), \quad (3.1)$$

where E_n is the energy of the n -th site, $t_{n,m}$ is the hopping energy and c_n^\dagger (c_n) is the creation (annihilation) operator of the π electron at site n . Note that, for each site n , the summation is taken over all nearest neighboring sites m . In the presence of a magnetic field, the transfer energy becomes $t \rightarrow t e^{i2\pi\Phi_{n,m}}$, where $\Phi_{n,m} = (1/\Phi_0) \int_{r_n}^{r_m} \mathbf{A} \cdot d\mathbf{l}$ is the Peierls phase, with $\Phi_0 = h/e$ the magnetic quantum flux and \mathbf{A} the vector potential.

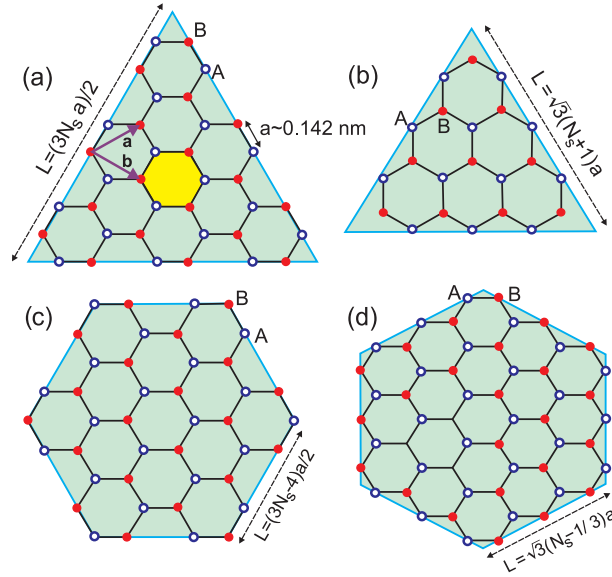


Figure 3.1: The lattice structure of triangular (upper panels) and hexagonal (lower panels) graphene quantum dots with (a,c) armchair edges and (b,d) zigzag edges. $a = 0.142$ nm is the C-C distance and the primitive lattice vectors are denoted by \mathbf{a} and \mathbf{b} . The atoms of the two sublattices are represented by blue circles and red dots. The yellow region indicates the area of one carbon hexagon. N_s is the number of C-atoms in each side of the dot.

Triangular and hexagonal quantum dots with zigzag and armchair edges are illustrated in Fig. 3.1, where the vectors $\mathbf{a} = a(3/2, \sqrt{3}/2)$ and $\mathbf{b} = a(3/2, -\sqrt{3}/2)$, with $a = 0.142$ nm the lattice parameter (or the C-C distance), are introduced as primitive lattice vectors. In the present work, we will consider only the interaction between each atom n and its three

first nearest neighbors. In the case of graphene, this interaction has the hopping energy $t = 2.7$ eV. The vector potential corresponding to the external magnetic field $\mathbf{B} = (0, 0, B)$ perpendicular to the layer is chosen as the Landau gauge $\mathbf{A} = (0, Bx, 0)$. With this choice of gauge, the Peierls phase for a transition between two sites n and m is $\Phi_{n,m} = 0$ in the x direction and $\Phi_{n,m} = \pm(x/3a)\Phi_c/\Phi_0$ along the $\pm y$ direction, where $\Phi_c = 3\sqrt{3}a^2 B/2$ is the magnetic flux threading one carbon hexagon (the area of one carbon hexagon is shown in Fig. 3.1(a) by the yellow region). An external potential is represented by a variation in the on-site energies E_n , and a vacancy or defect can be represented by setting the energy of the vacant site to a larger value and the hopping terms to these atoms as zero [71]. The Hamiltonian H in Eq. (3.1) can be represented in matrix form and the eigenvalues and eigenfunctions of a graphene flake can be obtained by diagonalization of the matrix. We emphasize that the hexagonal lattice presented in Fig. 3.1 is not a Bravais lattice, but a combination of two triangular lattices composed by atoms labeled as type A (blue) and type B (red). Accordingly, the tight-binding Hamiltonian of Eq. (3.1) can be rewritten as

$$H = \sum_n E_n^A a_n^\dagger a_n + \sum_n E_n^B b_n^\dagger b_n + \sum_{\langle n,m \rangle} (t_{n,m} a_n^\dagger b_m + h.c.) \quad (3.2)$$

where the operators a_n^\dagger (a_n) and b_n^\dagger (b_n) create (annihilate) an electron in site n of lattice A and B, respectively.

3.3 Continuum model: Dirac-Weyl equation

The first Brillouin zone in reciprocal space is a hexagon with six Dirac points, where only two of them are inequivalent. From the primitive vectors, we can find the position of these as $K = (2\pi/3a, 2\pi/3\sqrt{3}a)$ and $K' = (2\pi/3a, -2\pi/3\sqrt{3}a)$. The states near these points have approximately a linear dispersion and can be described as massless Dirac fermions by the Hamiltonian

$$H = \begin{pmatrix} H_K & \mathbf{0} \\ \mathbf{0} & H_{K'} \end{pmatrix}, \quad (3.3)$$

where H_K ($H_{K'}$) is the Hamiltonian in the K (K') point, which are given by

$$H_K = v_F \boldsymbol{\sigma} \cdot \mathbf{p}, \quad (3.4a)$$

$$H_{K'} = v_F \boldsymbol{\sigma}^* \cdot \mathbf{p}, \quad (3.4b)$$

where $\boldsymbol{\sigma} = (\sigma_x, \sigma_y)$ are Pauli matrices and $\boldsymbol{\sigma}^* = (\sigma_x, -\sigma_y)$ denotes the complex conjugate of the matrix $\boldsymbol{\sigma}$. In the presence of a magnetic field B perpendicular to the graphene layer

and using the Landau gauge, one can simply rewrite Eq. (3.3) in the following form:

$$H = \begin{pmatrix} 0 & \Pi_- & 0 & 0 \\ \Pi_+ & 0 & 0 & 0 \\ 0 & 0 & 0 & \Pi_+ \\ 0 & 0 & \Pi_- & 0 \end{pmatrix}, \quad (3.5)$$

where,

$$\Pi_{\pm} = -i\hbar v_F \left[\frac{\partial}{\partial x} \pm i \frac{\partial}{\partial y} \mp \frac{2\pi B}{\Phi_0} x \right]. \quad (3.6)$$

The wave function in real space for the sublattice A is

$$\psi_A(\mathbf{r}) = e^{i\mathbf{K}\cdot\mathbf{r}} \varphi_A(r) + e^{i\mathbf{K}'\cdot\mathbf{r}} \varphi_{A'}(r), \quad (3.7a)$$

and for sublattice B it is given by,

$$\psi_B(\mathbf{r}) = e^{i\mathbf{K}\cdot\mathbf{r}} \varphi_B(r) + e^{i\mathbf{K}'\cdot\mathbf{r}} \varphi_{B'}(r). \quad (3.7b)$$

The Hamiltonian of Eq. (3.5) acts on the four-component wave function

$\Psi = [\varphi_A, \varphi_B, \varphi_{A'}, \varphi_{B'}]^T$, which leads to the four coupled first-order differential equations:

$$-i \left[\frac{\partial}{\partial x'} - i \frac{\partial}{\partial y'} + \beta x' \right] \varphi_B = \epsilon \varphi_A, \quad (3.8a)$$

$$-i \left[\frac{\partial}{\partial x'} + i \frac{\partial}{\partial y'} - \beta x' \right] \varphi_A = \epsilon \varphi_B, \quad (3.8b)$$

$$-i \left[\frac{\partial}{\partial x'} + i \frac{\partial}{\partial y'} - \beta x' \right] \varphi_{B'} = \epsilon \varphi_{A'}, \quad (3.8c)$$

$$-i \left[\frac{\partial}{\partial x'} - i \frac{\partial}{\partial y'} + \beta x' \right] \varphi_{A'} = \epsilon \varphi_{B'}. \quad (3.8d)$$

In the above equations, we used the following dimensionless units: $x' = x/\sqrt{S}$, $y' = y/\sqrt{S}$, $\beta = 2\pi BS/\Phi_0 = 2\pi\Phi/\Phi_0$, $\epsilon = E/E_0$, with $E_0 = \hbar v_F/\sqrt{S}$, where $S \propto L^2$ is the area of the dot with L being the length of the side of the dot. In this section, we solve Eqs. (3.8) numerically, using the finite elements method, for the triangular and hexagonal graphene flakes shown in Fig. 3.1, considering zigzag, armchair and infinite mass boundary conditions. The numerical calculations are performed by using the standard finite element package COMSOL Multiphysics [72], which discretizes the two-dimensional flake in a finite-sized mesh and allows the implementation of the appropriate boundary conditions. The way the boundary conditions are implemented in the continuum model is the subject of the following three subsections.

3.3.1 Zigzag boundary conditions

The geometry of the hexagonal and triangular graphene quantum dots with zigzag edges are illustrated in Figs. 3.1(b,d). The length of one side of the hexagonal and triangular dots, respectively, are given by $L = \sqrt{3}(N_s - 1/3)a$ and $L = \sqrt{3}(N_s + 1)a$, with N_s being the number of atoms in each side of the dot and $a = 0.142$ nm is the C-C distance. The total number of C-atoms in the triangular dot is $N = [(N_s + 2)^2 - 3]$ and $N = 6N_s^2$ for the hexagonal dot. The zigzag-type boundary condition was previously studied by Akhmerov *et al.* [73], who presented a model which is generically applicable to any honeycomb lattice. For a graphene dot with zigzag edges and if the last atoms at the boundary are from sublattice A (blue circles in Fig. 3.1), the boundary conditions are given by $\varphi_A = \varphi_{A'} = 0$, whereas φ_B and $\varphi_{B'}$ are not determined, and similarly, when the zigzag edges are terminated by the B atoms (red dots in Fig. 3.1), $\varphi_B = \varphi_{B'} = 0$, while φ_A and $\varphi_{A'}$ are not determined.

3.3.2 Armchair boundary conditions

The geometry of a hexagonal and triangular graphene quantum dot with armchair edges is illustrated in Figs. 3.1(a,c). Here, the length of one of the edges of the hexagon dot is $L = (3N_s - 4)a/2$ and for the triangular dot is $L = 3N_s a/2$. For an armchair hexagonal graphene dot the total number of C-atoms is $N = [9N_s(N_s/2 - 1) + 6]$ and for the triangular dot is given by $N = (N_s + 2)3N_s/4$. Note that in the case of armchair boundaries the number of C-atoms in each side is an even number (see Figs. 3.1(a,c)). From Figs. 3.1(a,c), we notice that the edge atoms consist of a line of A-B dimers, where the wave function should be zero. From Eqs. (3.7a) and (3.7b), these boundary conditions become [74]

$$\varphi_A(\mathbf{r}) = -e^{i(\mathbf{K}' - \mathbf{K}) \cdot \mathbf{r}} \varphi_{A'}(\mathbf{r}), \quad (3.9a)$$

$$\varphi_B(\mathbf{r}) = -e^{i(\mathbf{K}' - \mathbf{K}) \cdot \mathbf{r}} \varphi_{B'}(\mathbf{r}), \quad (3.9b)$$

where \mathbf{r} is taken at the position of the edge. Notice that these armchair boundary conditions mix the wave functions of the K and K' points.

3.3.3 Infinite-mass boundary condition

A mass-related potential energy $V(x, y)$ can be coupled to the Hamiltonian via the σ_z Pauli matrix,

$$H = v_F \boldsymbol{\sigma} \cdot \mathbf{p} + \tau \sigma_z V(x, y), \quad (3.10)$$

where the parameter $\tau = \pm 1$ distinguishes the two K and K' valleys. It is straightfor-

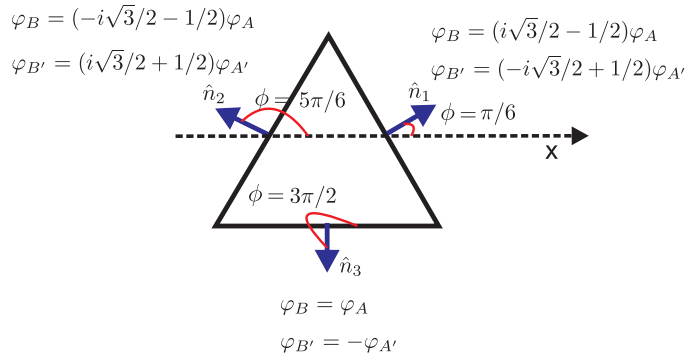


Figure 3.2: The infinite-mass boundary conditions implemented on the edges of a triangular dot. $\hat{n}_1, \hat{n}_2, \hat{n}_3$ are the outward unit vectors at each edge of the dot.

wardly verified that the presence of a mass term in the Hamiltonian of Eq. (3.10) induces a gap in the energy spectrum of graphene. However, if the mass-related potential $V(x, y)$ is defined as zero inside the dot and infinity at its edge, the Klein tunneling effect at the interface between the internal and external regions of the dot can be avoided and, consequently, the charge carriers will be confined. This infinite-mass boundary condition can be introduced in the Dirac equation by defining $\varphi_B(x, y)/\varphi_A(x, y) = ie^{i\phi}$ and $\varphi_{B'}(x, y)/\varphi_{A'}(x, y) = -ie^{i\phi}$ (which, respectively, correspond to the K -point and the K' -point wave spinors) at the boundary, where ϕ is the angle between the outward unit vector at the edges and the x -axis. [75] Due to its simplicity, this type of boundary condition has been used in the study of circular graphene dots [69] and rings [76, 114] in the presence of a perpendicularly magnetic field, where analytical solutions can be found. For the hexagonal and triangular geometries the angle ϕ has a fixed value at each side of the dot that simplifies the boundary conditions to $\varphi_B = \alpha\varphi_A$ (for the K valley) and $\varphi_{B'} = -\alpha\varphi_{A'}$ (for the K' valley) where $\alpha = ie^{i\phi}$ is a complex number. The infinite-mass boundary conditions are shown explicitly in Fig. 3.2 for a triangular dot.

3.4 Numerical results

3.4.1 Zero magnetic field

The energy levels of hexagonal (upper panels) and triangular (lower panels) graphene flakes, as calculated within the continuum model, are shown in Fig. 3.3 as function of the square root of the dot area. The results are shown for zigzag (a,b), armchair (c,d) and infinite-mass (e,f) boundary conditions and are qualitatively and quantitatively very

different. As the dot area increases, the energy levels tend to a gapless spectrum, which is expected, since the energy spectrum of an infinite graphene sheet does not exhibit a gap. A peculiar spectrum is observed for zigzag triangular dots (Fig. 3.3(b)): zero energy states are found for all sizes of such a dot. These zero energy states are separated from the remaining positive and negative energy states by an energy gap which decreases as the dot becomes larger. The presence of such zero energy states in triangular and trapezoidal graphene flakes have been previously reported in the literature [55,57,61], where the TBM was applied. In the case of zigzag triangular dots, it has been shown analytically [57] that

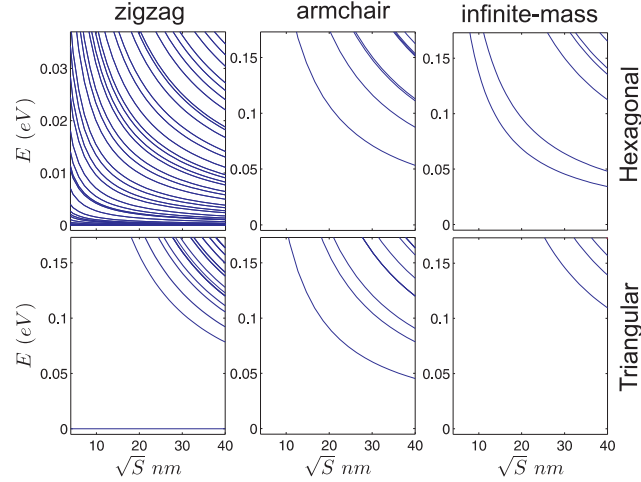


Figure 3.3: Energy levels of hexagonal (a, c, e) and triangular (b, d, f) graphene quantum dots with zigzag (a, b), armchair (c, d) edges and infinite mass boundary condition (e, f) as function of the square root of the dot area S in the absence of a magnetic field.

the equation $H\Psi = 0$ for the TBM Hamiltonian in Eq. (3.2) leads to $N_s - 1$ linearly independent states, namely, $N_s - 1$ degenerate states with $E = 0$, for any number N_s of C-atoms in one of the edges of the flake. Thus, Fig. 3.3(b) demonstrates that the existence of zero energy states, which is observed in the TBM, is qualitatively captured by the approximations of the continuum model as well. The results in Fig. 3.3 also show that the energy levels for a dot with armchair and infinite-mass boundary conditions are qualitative more similar to each other than the spectra for zigzag edges, where carriers are predominantly confined at the edge of the dot. In fact, for the triangular geometry, the infinite mass boundary condition describes very well the armchair states, specially for lower energy states. However, for the hexagonal geometry, the results for armchair and infinite mass boundary conditions are only qualitatively similar where, the hexagonal dots with infinite mass boundary condition exhibit more energy states in comparison with the

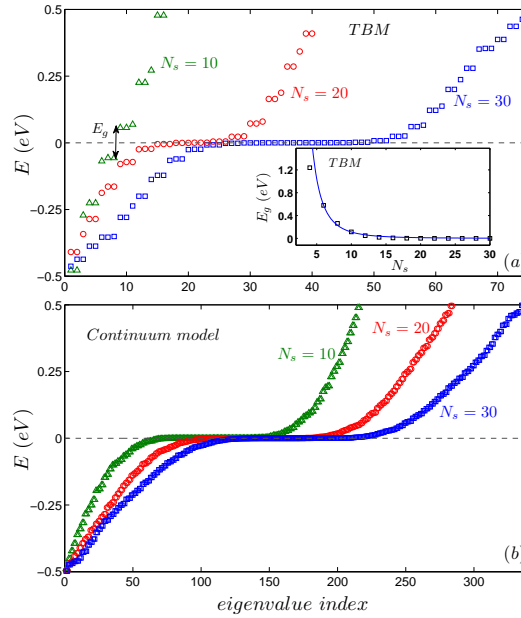


Figure 3.4: Energy levels of a zigzag hexagonal graphene dot as function of the eigenvalue index obtained by (a) the TBM and (b) the continuum model, for three different sizes of the dot with $N_s = 10, 20, 30$, having respectively surface area $S = 14.68, 60.78, 138.32 \text{ nm}^2$. The inset in panel (a) shows the energy gap E_g as function of N_s obtained, by the TBM.

armchair case. Notice that the energy spectra shown in Fig. 3.3 exhibits degenerate states. These degeneracies, which will be evidenced in the following figures, where we plot the energy spectra as a function of the eigenvalue index, are related to the symmetries of the triangular and hexagonal dots, as we will explain in further detail later on, when we discuss about the electron probability densities.

A comparison between the energy spectra obtained using the TBM (a) and the Dirac equation (b) for zigzag hexagonal dots is shown in Fig. 3.4, for three sizes of the dot, defined by the number of C-atoms in each side of the hexagon N_s . The energies E_i are plotted as a function of the eigenvalue index i . Although the results are quantitatively different, they are qualitatively similar, e.g. as the size of the dot increases, they start to exhibit an almost flat energy spectrum as a function of the eigenvalue index around the Dirac point. Such a flat spectrum leads to a peak in the DOS close to the Dirac point, which was recently reported in the literature [58] for graphene dots with zigzag edges within the TBM. The curves for $N_s = 30$ obtained by the TBM and continuum models are very similar, except for the fact that many more states are found in the latter, whereas

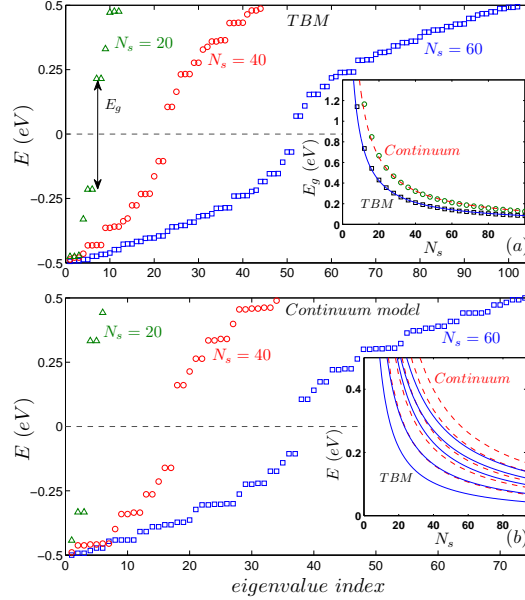


Figure 3.5: Energy levels of an armchair hexagonal graphene dot as function of the eigenvalue index obtained by (a) the TBM and (b) the continuum model for three different sizes of the dot with $N_s = 20, 40, 60$ having respectively surface area $S=41.07, 176.23, 405.68 \text{ nm}^2$. The inset in panel (a) shows the energy gap obtained from both TBM (black squares) and continuum model (green circles). The inset in panel (b) shows the lowest electron energy levels as function of N_s for both TBM (blue solid curves) and continuum model (red dashed curves).

the discrete character of the spectrum in the former is much more clear. For smaller dots, the agreement between these two models becomes clearly worse. For instance, an energy gap E_g is found for very small hexagons (i.e. $N_s \leq 10$) within TBM, whereas in the case of the continuum model such a gap is extremely small. As a consequence, the continuum model overestimates the DOS at $E = 0$ as the dot size decreases, since it exhibits a plateau in the energy as a function of the eigenstate index in the vicinity of $E = 0$ even for smaller N_s , where TBM results show a gap in the energy spectrum. Notice that the $E = 0$ states in zigzag dots are edge states, so that the number of zero-energy states depends on the number of edge atoms in the TBM and, similarly, to the number of mesh elements at the edge in the continuum model. Therefore, in the continuum model for $E = 0$, the finite elements problem is ill-defined, where the constructed matrix of the finite mesh elements in this case is singular (zero inverse), leading to spurious solutions around $E = 0$. As the size of the dot increases, the gap in the TBM results quickly reduces to zero and a

zero energy level for the hexagonal flakes with zigzag edges appears. [77] In the inset of Fig. 3.4(a), the energy gap values obtained by TBM are shown as function of N_s . These results can be fitted to $E_g = \alpha(1/N_s)^\gamma$ (blue solid curve in the inset of Fig. 3.4(a)), where $\alpha = 94.6$ eV and $\gamma = 3.23$ are fitting parameters.

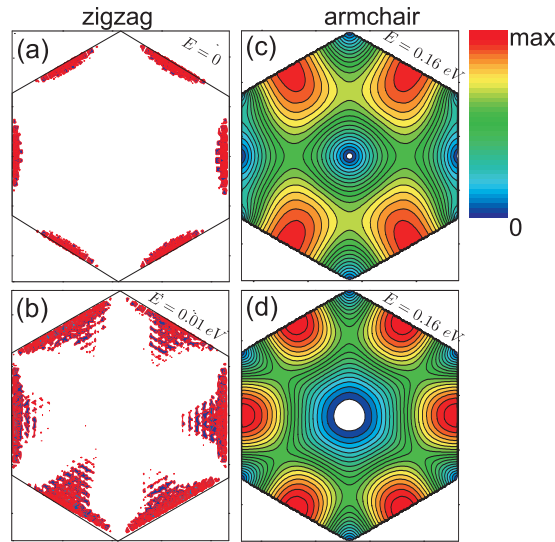


Figure 3.6: Electron probability densities corresponding to the two lowest energy levels of hexagonal graphene flakes, obtained by the continuum model, for (a,b) zigzag ($N_s = 20$) and (c,d) armchair ($N_s = 40$) edges.

The energy states of armchair hexagonal dots are shown as a function of the eigenvalue index in Fig. 3.5 within the TBM approach (Fig. 3.5(a)) and the Dirac-Weyl equations (Fig. 3.5(b)), for three different sizes of the dot. The energy spectrum in both cases approach the prolonged S-shape curve predicted by Ezawa [56] as the size of the dot increases and the spectrum exhibits an energy gap E_g at the Dirac point. The energy gap as function of N_s is shown in the inset of Fig. 3.5(a) which decreases rapidly as the size of the dot increases. Our numerical results can be fitted to $E_g = \alpha/N_s$ with $\alpha = 8.5$ eV for the TBM (blue solid curve) and $\alpha = 13$ eV for the continuum model (red dashed curve) results. Notice that E_g obtained from the continuum model is larger than the one from the TBM results in particular for small N_s and both curves can not be made to coincide by a simple shift in N_s . This is clearly a consequence of the increased importance of corrections to the linear spectrum used in the continuum model for small sizes of the system. The inset of Fig. 3.5(b) shows the five lowest electron states for both TBM (blue solid curves) and the continuum model (dashed red curves). Our results show that the continuum model

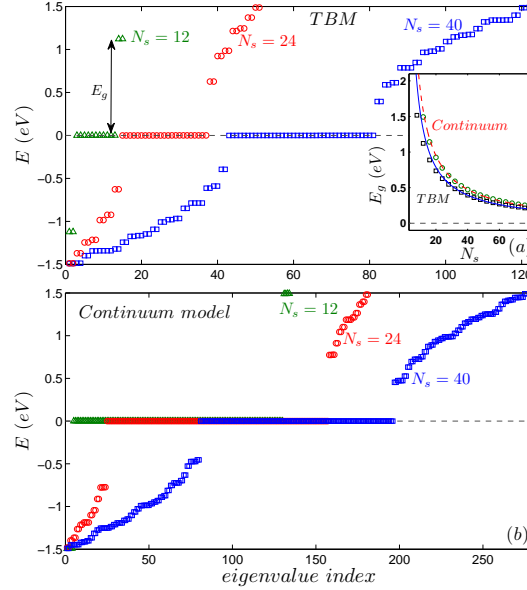


Figure 3.7: Energy levels of a zigzag triangular graphene dot as function of the eigenvalue index obtained by (a) the TBM and (b) the continuum model for three different sizes of the dot with $N_s = 12, 24, 40$ having respectively surface area $S=4.42, 16.37, 44.03 \text{ nm}^2$. The inset in panel (a) shows the energy gap obtained from both TBM (black squares) and continuum model (green circles).

overestimates the energy values also for the upper energy levels in comparison with the TBM energy levels. In fact, the energy dispersion in the continuum model is given by a linear curve, which coincides with the TBM energy spectrum for low energies, but as the energy goes further away from $E = 0$, this linear dispersion overestimates the energy as compared to the real band structure of graphene, which starts to bend down from the linear spectrum as the energy increases. This emphasizes once again the importance of the higher order corrections to the linear dispersion, especially for high energy states and smaller dot sizes.

Figure 3.6 shows the probability density (using the continuum model) corresponding to the first two energy levels of hexagonal flakes. The probability density for the zigzag case with $N_s = 20$ is presented in panels (a) and (b), respectively, for $E = 0$ and $E = 0.01 \text{ eV}$. The results clearly demonstrate that the zero energy states in the zigzag case are due to edge effects and, accordingly, are confined at the edges while the carriers confine towards the center of the flake with increasing energy (see Fig. 3.6(b)). The probability densities of the armchair edged graphene flake with $N_s = 40$ are very different as seen in Figs.

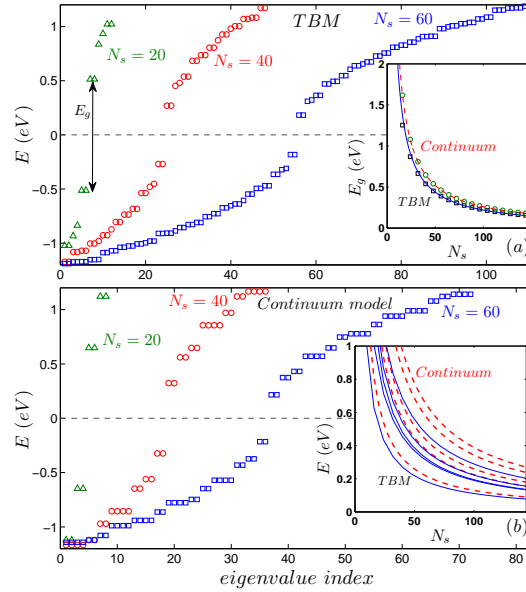


Figure 3.8: Energy levels of an armchair triangular graphene dot as function of the eigenvalue index obtained by (a) the TBM and (b) the continuum model for three different sizes of the dot with $N_s = 20, 40, 60$ having respectively surface area $S=7.85, 31.43, 70.72 \text{ nm}^2$. The inset in panel (a) shows the energy gap obtained from both TBM (black squares) and continuum model (green circles). The inset in panel (b) shows the lowest electron energy levels as function of N_s for both TBM (blue solid curves) and continuum model (red dashed curves).

3.6(c,d) for the lowest degenerate states with $E = 0.16 \text{ eV}$. The electron wavefunction is spread out over the whole sample, but different from the usual quantum dots with parabolic energy-momentum spectrum, it has a local minimum in the center of the dot. Note that Fig. 3.6(c) has only two-fold symmetry while Fig. 3.6(d) is six-fold symmetric. Both densities are zero in the center, while Fig. 3.6(c) has two extra zeros at the sides along $y = 0$. These results are comparable to the TBM results obtained in Ref. [58].

The energy spectrum for triangular dots with zigzag edges, obtained by the TBM and the Dirac-Weyl equation are shown as a function of the eigenvalue index in Figs. 3.7(a) and 3.7(b), respectively. Notice that both energy spectra exhibit zero energy states. As we mentioned before, the number of degenerate states with zero energy is a well defined quantity in the tight-binding approach, namely, $N_s - 1$, where N_s is the number of C-atoms in one side of the triangle [57]. On the other hand, the result in Fig. 3.7(b) for the continuum model exhibits many more zero energy states. Therefore, while the continuum model captures qualitatively the existence of zero energy states, it does not provide the

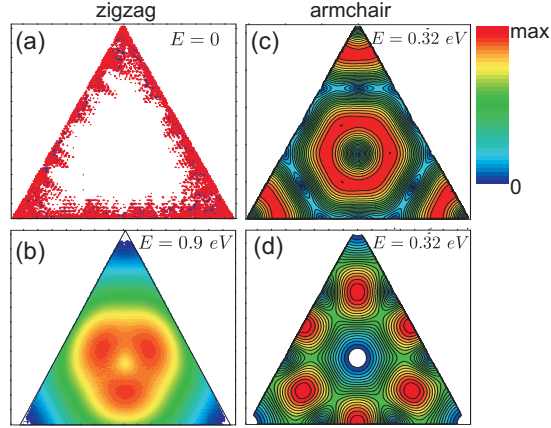


Figure 3.9: Electron probability densities corresponding to the lowest energy levels of the triangular graphene flakes, obtained by the continuum model, for (a,b) zigzag ($N_s = 20$) and (c,d) armchair ($N_s = 40$) edges.

appropriate number of degenerate states as calculated by the TBM. These zero energy levels are related to the edge states of zigzag graphene flakes [57, 58]. The energy gap (between the zero energy level and the first non-zero eigenvalue) is shown in the inset of Fig. 3.7(a) as function of the size of the dot, where E_g obtained by both models are comparable and the difference between the TBM (red dashed curve) and continuum (blue solid curve) results tends to zero for large graphene flakes. These results can be fitted to $E_g = \alpha/N_s$ with $\alpha = 15.75$ eV for the TBM gap and $\alpha = 18.9$ eV for the continuum model.

The energy spectra of triangular dots with armchair edges obtained by the TBM and the continuum model are shown in Fig. 3.8. No zero energy states are found and the energy gap at the Dirac point for both models is comparable. The gap can be fitted to $E_g = \alpha/N_s$ ($\alpha = 21.9$ eV for TBM and $\alpha = 25.9$ eV for the continuum model) as shown respectively by the blue solid and dashed red curves in the inset of Fig. 3.8(a). The lowest electron energy levels, obtained by the TBM (blue solid curves) and the continuum model (red dashed curves), are shown in the inset of Fig. 3.8(b) as function of N_s . The results show a larger difference between the TBM and continuum energy values for the upper energy levels (e.g. $|E_1^T - E_1^C| < |E_2^T - E_2^C|$).

Notice that the energy gaps found for all the systems that we investigated were fitted to $E_g = \alpha/N_s$ for different values of α , except for the case of zigzag hexagonal dots, where the gap is fitted to $E_g = \alpha/N_s^\gamma$, with $\gamma = 3.23$. This is a consequence of the fact that the corners of the zigzag hexagonal dot structure are not terminated by a single atom, as in

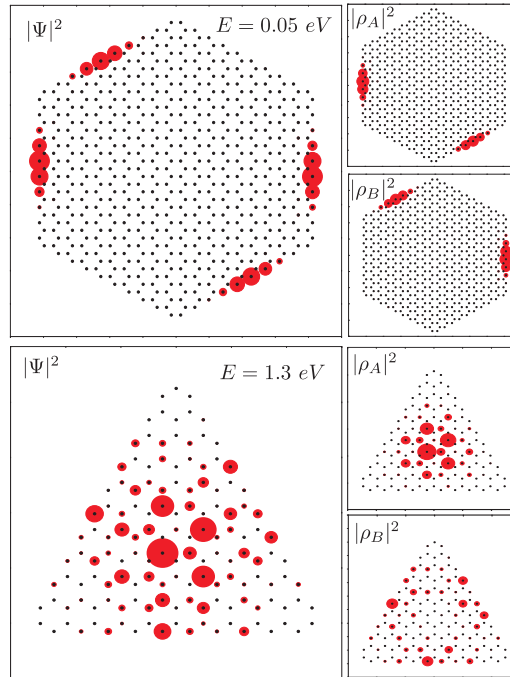


Figure 3.10: Electron densities for the first energy level of the triangular and hexagonal graphene flakes (using TBM) with $N_s = 10$ and zigzag edges. Left panels show the total electron density $|\Psi|^2$ and the right panels present the electron densities associated with A and B sublattices. The gray dots are the positions of C-atoms.

the case of zigzag triangular dots, but by a pair of C-atoms corresponding to two different sublattices, forming a A-B dimer (see Fig. 3.1). These A-B dimers are responsible for a vanishing wave function in the corners of the zigzag hexagonal dots, as observed in Fig. 3.6. As explained in Sec. III A, the zigzag boundary condition for each side of the dot is implemented in the Dirac-Weyl equations by setting to zero the component of the pseudo-spinor corresponding to the sublattice that forms that side. As the sublattice types of adjacent sides of a zigzag hexagonal dot are different, connected by the A-B dimers in the corners, the whole wave function must vanish at these corners, since these points are composed of both A and B sublattices. The vanishing wave function at the corners reduce the effective confinement area and, consequently, increases the energy gap, especially for smaller dots, where the influence of the corners is more significant. As the size of the dot increases, the role of the corners in the energy gap becomes less important and is eventually suppressed by the influence of the zigzag edges, leading to the zero energy states that form the plateau in Fig. 3.4, explaining the faster decay of the energy gap ($\gamma = 3.23$) in zigzag

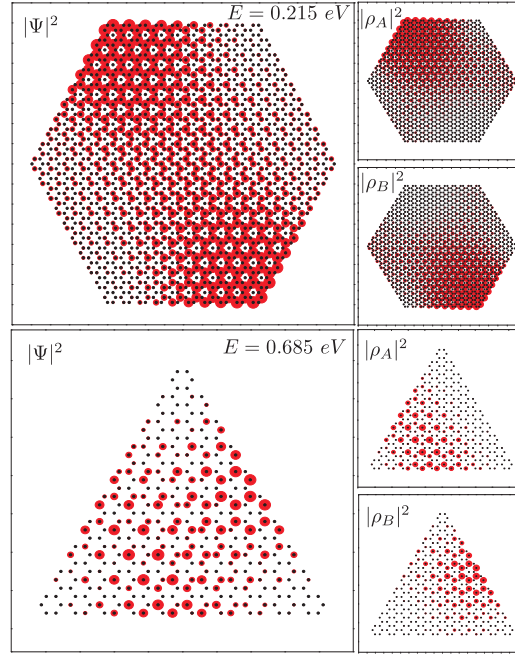


Figure 3.11: The same as Fig. 3.10 but for the dots with armchair boundaries and $N_s = 20$.

hexagonal dots, as compared to the other cases ($\gamma = 1$).

The probability density corresponding to the first two energy levels of triangular graphene flakes, obtained by the continuum model, is shown in Fig. 3.9. The probability density for the zigzag edged dot with $N_s = 20$ is presented in panels (a) and (b), respectively, for $E = 0$ and for the first non-zero eigenvalue (i.e. $E = 0.92$ eV). For the degenerate zero energy states the carriers are confined at the edges of the triangular flake which is typical for zigzag boundaries. States corresponding to large energy values are confined in the center of the triangle (Fig. 3.9(b)). For armchair triangular flakes, as in the hexagonal case, the electron state is spread out over the whole flake (Figs. 3.9(c,d) display the different probability densities for $N_s = 40$ corresponding to the first degenerate eigenvalues with $E = 0.32$ eV). Both wavefunctions have three-fold symmetry and the inner part is even six-fold symmetric. Note that the electron density in Fig. 3.9(d) is zero at the three corners and in the center of the triangle which is different from Fig. 3.9(c) where zero's are found at the corners of the inner hexagon and at the center of the sides of this hexagon.

The TBM electron densities of the zigzag graphene dots with $N_s = 10$ is shown in Fig. 3.10 for the first energy level of the triangular and hexagonal graphene flake. Left panels present the total electron density $|\Psi|^2$ and the electron densities associated with A and B

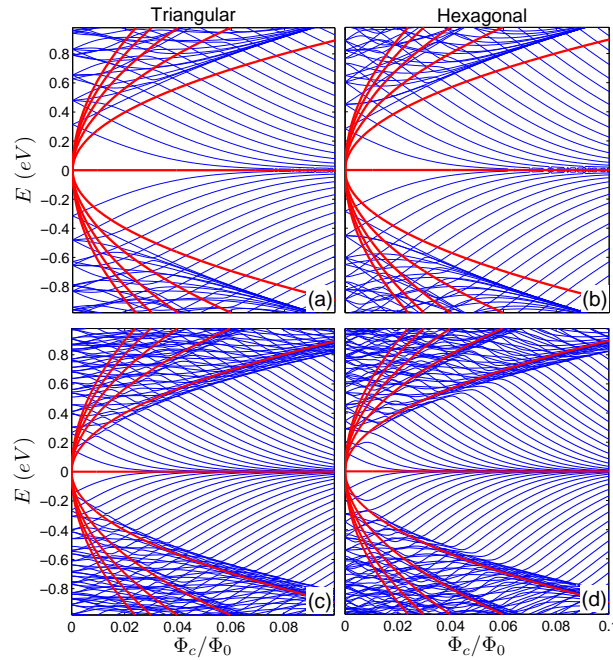


Figure 3.12: Energy levels of (a,c) triangular and (b,d) hexagonal graphene dots with armchair boundary as function of the magnetic flux threading one carbon hexagon Φ_c . The results in panels (a,b) are obtained using the continuum model while panels (c,d) display the TBM results. The quantum dots have an area S such that $\sqrt{S} = 10$ nm.

sublattices ($|\rho_{A,B}|^2$) are shown in the right panels. We found that the wavefunctions of the two-fold degenerate states are related to each other by a 60° rotation. The sum of the densities of the degenerate states results in a six-fold (three-fold) symmetric wavefunction for the hexagonal (triangular) flakes. As seen in Fig. 3.10 the total electron density is related to the densities of A and B sublattices by $|\Psi|^2 = |\rho_A|^2 + |\rho_B|^2$. Figure 3.11 describes the density distributions of the lowest energy levels for armchair graphene flakes. For the armchair hexagonal dots the electron densities corresponding to the A and B sublattices (right panels) can be transformed to each other by a 180° rotation whereas the density of the triangular wavespinors can not be linked to each other by a rotational transformation.

3.4.2 Magnetic field dependence

The dependence of the energy levels of triangular (a) and hexagonal (b) graphene flakes on the magnetic flux through one carbon hexagon $\Phi_c = BS_c$ is shown in Figs. 3.12 and 3.13, respectively for flakes with armchair and zigzag edges. The results in panels (a),(b)

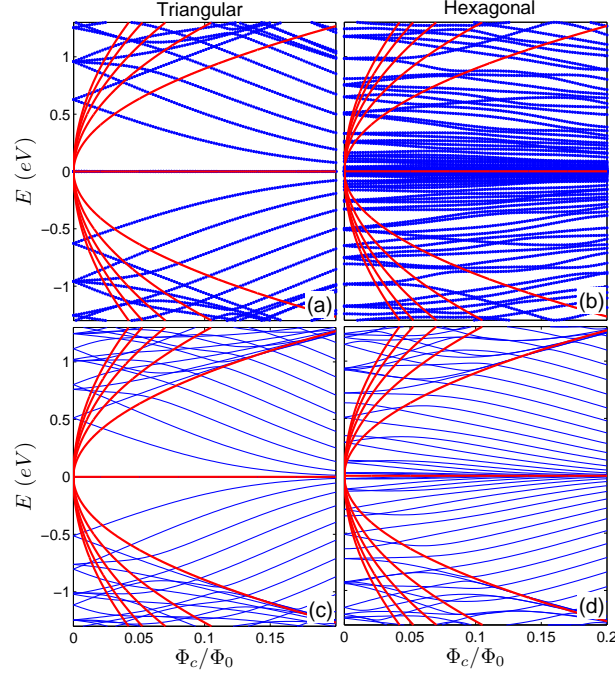


Figure 3.13: The same as Fig. 3.12 but for dots with zigzag boundaries and the dots have an area S such that $\sqrt{S} = 5$ nm.

are obtained using the continuum model and the results in panels (c),(d) show the TBM energy spectrum. $S_c = (3\sqrt{3}/2)a^2$ is the area of a carbon hexagon which is indicated by the yellow region in Fig. 3.1(a). The results are obtained for dots with an area of $S = 100$ nm² and $S = 25$ nm² respectively for armchair and zigzag edges. The continuum and TBM results are qualitatively similar to each other in the sense that as the magnetic flux increases, the energy levels converge to the Landau levels of a graphene sheet E_n (see red solid curves), which are given by

$$E_n = \text{sgn}(n) \frac{3at}{2l_B} \sqrt{2|n|}, \quad (3.11)$$

where, $l_B = \sqrt{\hbar/eB}$ is the magnetic length and n is an integer. The interplay between the quantum dot confinement and the magnetic field confinement is responsible for the appearance of a series of (anti)-crossings in the energy spectrum. As explained earlier, armchair graphene dots do not exhibit zero energy states for $B = 0$. However, as the magnetic field increases, some of the excited energy levels approach the zero energy Landau level $n = 0$ in both armchair and zigzag graphene flakes, which naturally produces (anti)-crossings between the excited states. Lifting the degeneracy of the energy levels by

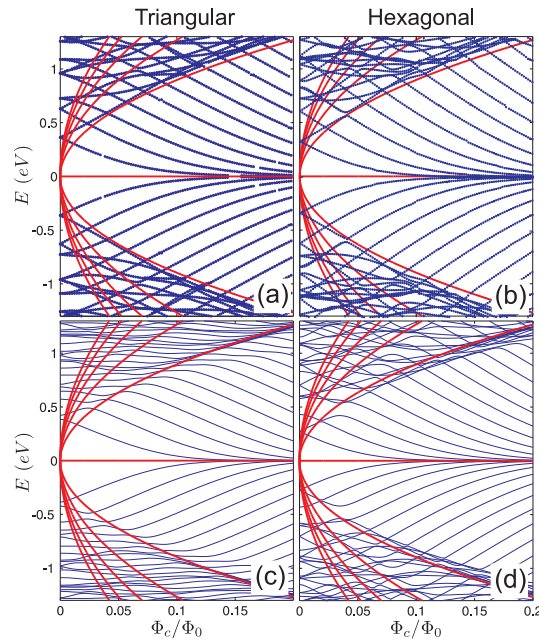


Figure 3.14: The same as Fig. 3.12, but for dots with infinite-mass boundary conditions. The dots have an area S such that $\sqrt{S} = 5$ nm. In panels (c,d), the infinite-mass boundary condition is applied within the TBM model, where we imposed a +10(-10) eV on-site potential for sublattice A(B) around the dot geometry.

the magnetic field results in a closing of the energy gap with increasing magnetic field. Notice that the zero energy states of zigzag triangular dots (Fig. 3.13(a)) are not affected by the magnetic field because they are strongly confined at the edges of the dot. All these features are qualitatively similar to those obtained by the TBM (see the lower panels in Figs. 3.12,3.13). In the case of hexagonal zigzag graphene dots (see Fig. 3.13(b)), the continuum model exhibits a plethora of additional lines as compared to the well known energy spectrum obtained by the TBM (compare Figs. 3.13(b) and 3.13(c)).

For the infinite-mass boundary condition, the energy spectrum of triangular (a) and hexagonal (b) dots as a function of the magnetic field is shown in Fig. 3.14 for the dot with area $S = 25$ nm². The energy spectrum in this case differs from both obtained for zigzag and armchair boundary conditions. The spectra exhibit no zero energy state at $B = 0$ and show crossings and anti-crossings between the higher energy levels which resemble the TBM results (see Figs. 3.14(c),(d) respectively for triangular and hexagonal dots). In the TBM model, the infinite-mass boundary conditions can be realized as a graphene dot structure surrounded by an infinite mass media, where we applied a staggered potential (i.e. +10(-10) eV on-site potential for sublattice A(B)) around the dot geometry.

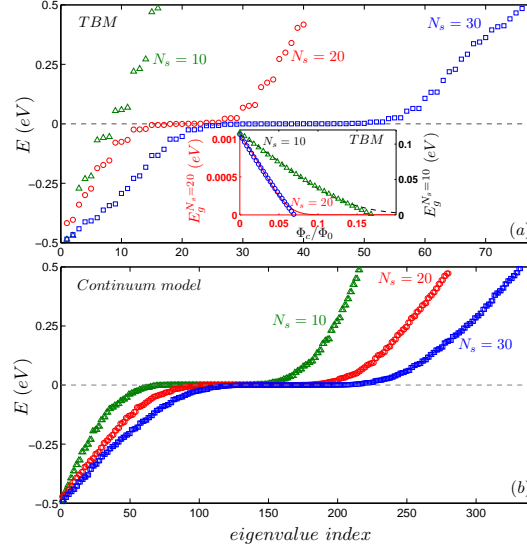


Figure 3.15: The same as Fig. 3.4 but in the presence of an external magnetic field of $B = 50$ T. The inset shows the energy gap as function of the magnetic flux obtained by the TBM for two values of N_s . The triangle and circle symbols display Eq. (3.12) which is fitted to the numerical results.

The energy levels obtained by the TBM (a) and the continuum model (b) for hexagonal graphene flakes under a $B = 50$ T external magnetic field are shown in Figs. 3.15 and 3.16 for zigzag and armchair edges, respectively, as function of the eigenvalue index. The energy spectra of such systems in the absence of magnetic field, which are shown in Figs. 3.4 and 3.5, are composed of a series of degenerate states for $|E| > 0$. The magnetic field lifts the degeneracy of such states and reduces the gap between the states. The energy gap as function of the magnetic flux through a single carbon hexagon Φ_c is shown in the insets of Fig. 3.15(a) and Fig. 3.16(a) respectively for zigzag (with $N_s = 10, 20$) and armchair (with $N_s = 20, 40$) hexagonal dots. These results can be fitted to

$$E_g(\Phi_c/\Phi_0) = E_g^0 + E_g^1(\Phi_c/\Phi_0) + E_g^2(\Phi_c/\Phi_0)^2 \quad (3.12)$$

where $E_g^{0,1,2}$ (eV) are the fitting parameters. In the inset of Figs. 3.15(a) and 3.16(a), the fitted results are shown by symbols. The fitting parameters for the TBM results of a zigzag hexagonal dot with $N_s = 10$ (for the range of $0 \leq \Phi_c/\Phi_0 \leq 0.17$) are $E_g^{0,1,2} = (0.12, -0.91, 1.36)$ eV (see triangles in the inset of Fig. 3.15(a)) and $E_g^{0,1,2} = (0.86, -26, 210)$ eV, $E_g^{0,1,2} = (0.88, -12.5, 46.5)$ eV are the fitting parameters of an armchair hexagonal dot with $N_s = 20$ respectively for TBM and continuum results (triangles

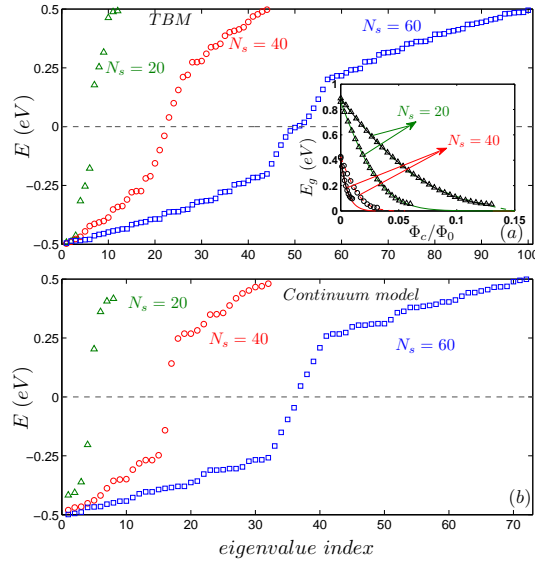


Figure 3.16: The same as Fig. 3.5 but in the presence of an external magnetic field of $B = 50$ T. The inset shows the energy gap as function of the magnetic flux obtained by the TBM (solid curves) and continuum model (dashed curves) for two values of N_s . The triangle and circle symbols display Eq. (3.12) which is fitted to the numerical results.

in the inset of Fig. 3.16(a)). The fittings are done for the range of $0 \leq \Phi_c/\Phi_0 \leq 0.06$ and $0 \leq \Phi_c/\Phi_0 \leq 0.13$ respectively for TBM and continuum results.

For the zigzag case and for $N_s = 20$, the energy gap is already negligible, whereas for $N_s = 10$, the $E_g \approx 0.12$ eV gap at $B = 0$ decays as the magnetic flux increases and approach zero in the limit of large magnetic flux (i.e. $\Phi_c/\Phi_0 > 0.2$). Due to the lifting of the degeneracies, the energy spectrum of an armchair hexagonal dot exhibits an almost linear behavior around $E = 0$ as function of eigenvalue index where, both TBM and continuum models approximately display the same slope for the linear regime.

For triangular graphene flakes under a $B = 50$ T (i.e. $\Phi_c/\Phi_0 = 0.0063$) magnetic field, the energy spectra obtained by the TBM (a) and the continuum model (b) are shown in Fig. 3.17, considering zigzag edges, and Fig. 3.18, considering armchair edges. As mentioned earlier, the presence of a magnetic field does not affect the $E = 0$ edge states in the triangular zigzag flakes, but lifts the degeneracy of the $E \neq 0$ states. The energy gap E_g around $E = 0$ of triangular flakes is shown as function of magnetic flux Φ_c in the insets of Fig. 3.17(a) and Fig. 3.18(a) respectively for zigzag (with $N_s = 12, 24$) and armchair (with $N_s = 20, 40$) edges (circle and triangle symbols present the fitted results). $E_g^{0,1,2} = (1.12, -1.32, -0.028)$ and $E_g^{0,1,2} = (1.5, -1.77, 0.4)$ are the fitting parameters

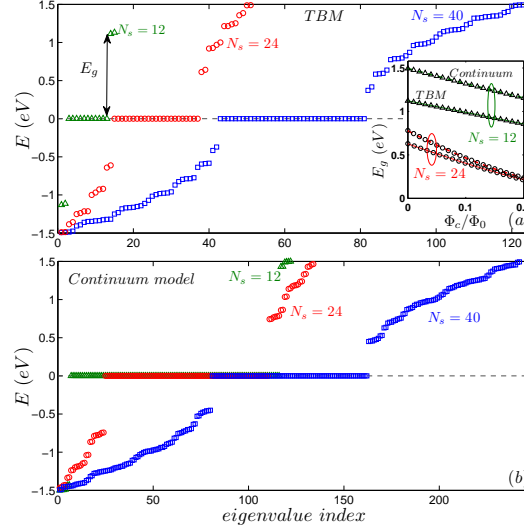


Figure 3.17: The same as Fig. 3.7 but in the presence of an external magnetic field of $B = 50$ T. The inset shows the energy gap as function of the magnetic flux obtained by the TBM (solid curves) and continuum model (dashed curves) for two values of N_s . The triangle and circle symbols display Eq. (3.12) which is fitted to the numerical results.

of a zigzag triangular dot with $N_s = 12$ respectively for TBM and continuum results (see inset of Fig. 3.17(a)). The fitting parameters for an armchair dot with $N_s = 20$ (see inset of Fig. 3.18(a)) obtained by TBM and continuum models are respectively $E_g^{0,1,2} = (1.02, -3.87, 3.83)$ and $E_g^{0,1,2} = (1.12, -2.41, 1.2)$. In both zigzag (with $N_s = 12$ and armchair ($N_s = 20$) triangular dots the fittings are done for the range of $0 \leq \Phi_c/\Phi_0 \leq 0.2$). In contrast with hexagonal dots the energy gap of the triangular dots reduces smoothly (i.e. almost linearly) with increasing the magnetic flux. Therefore the energy gap is weakly affected by a low magnetic field in triangular graphene dots. In the inset of Fig. 3.18(b) the energy gap is shown as function of N_s . As in the case of zero magnetic field E_g can be fitted to $E_g = \alpha/N_s$ as function of N_s (see blue solid and red dashed curves in Fig. 3.18(b)). The fitting parameter for $B = 50$ T are $\alpha \approx 21.87$ eV for TBM and $\alpha \approx 25.9$ eV for the continuum model which is almost the same as for zero magnetic field (see Fig. 3.8), i.e. because of the linear magnetic field dependence of the energy gap for low magnetic field it does not affect significantly the dependence of the energy gap on the size of the armchair triangular graphene dot.

As a matter of fact, tuning the energy gap by adjusting the external magnetic field is more useful for smaller sizes of the dot, since the energy gap decays to zero as the size of the dot increases. On the other hand, due to the small size of the dots considered in Figs.

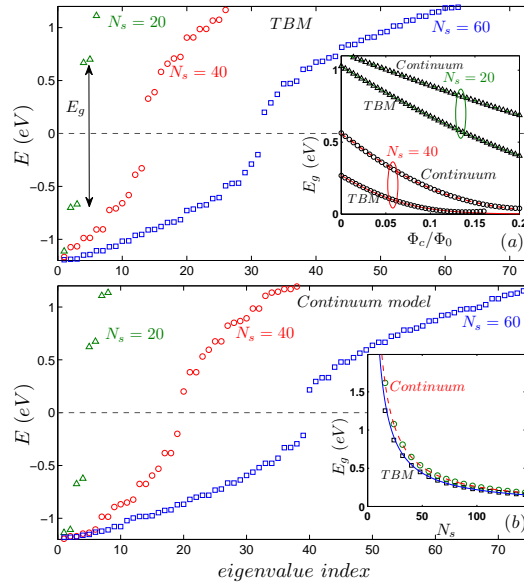


Figure 3.18: The same as Fig. 3.8 but in the presence of an external magnetic field $B = 50$ T. The inset in panel (a) shows the energy gap E_g , obtained by the TBM (solid curves) and continuum model (dashed curves), as function of the magnetic flux through one carbon ring Φ_c for $N_s = 20$ and $N_s = 40$. The triangle and circle symbols display Eq. (3.12) which is fitted to the numerical results. In the inset of panel (b) E_g is shown as function N_s for both TBM (black squares) and continuum models (green circles) in the presence of an external magnetic field $B = 50$ T.

3.15 - 3.18, we need large magnetic field values (e.g. $B = 50$ T) in order to see its effect on the energy spectrum. Nevertheless, as the influence of the magnetic field scales with the magnetic flux through the dot area, similar results will be obtained for lower magnetic fields in case of a larger graphene dot.

3.5 Conclusion

We have presented a theoretical study of triangular and hexagonal graphene quantum dots, using the two well known models of graphene: the tight-binding model and the continuum model. For the continuum model, the Dirac-Weyl equations are solved numerically, considering armchair, zigzag and infinite mass boundary conditions. A comparison between the results obtained from the TBM and the Dirac-Weyl equations show the importance of boundary conditions in finite size graphene systems, which affects their energy spectra.

The results obtained by the TBM for graphene flakes are only qualitatively similar to the results from the Dirac-Weyl equation for such systems considering zigzag and armchair boundary conditions, which shows that energy values obtained from the continuum model for small graphene dots may not always be quantitatively reliable.

More specifically, for zigzag hexagonal and triangular dots, the DOS at $E = 0$ in the absence of a magnetic field is overestimated in the continuum approach. Similarly, the continuum model also overestimates the energy gap around $E = 0$ in the armchair case for both geometries. A good agreement between both models is only observed for very large dots, as expected, and such agreement is always better for the triangular case, as compared to the hexagonal case. The energy spectrum obtained using the continuum model with infinite mass boundary condition for GQDs do not exhibit the same properties as the results obtained with the armchair or zigzag boundaries (in both TBM and continuum models), which shows that this type of boundary condition may not give a good description of finite size graphene flakes.

In the presence of an external magnetic field, the energy levels obtained by the continuum model with zigzag and armchair boundary conditions converge to the Landau levels of graphene as the magnetic field increases, as observed in the TBM. However, many additional artifact states appear in the continuum model, which do not match with any TBM result and do not approach any Landau level. Besides, the influence of an external magnetic field on the gap in the energy spectra of graphene flakes is particularly different for triangular and hexagonal dots. As the magnetic flux increases the energy gap of the hexagonal flakes (with $N_s \leq 10$ for zigzag edges) decreases quickly compared to the energy gap of the triangular flakes. This feature is observed in both TBM and continuum model, and suggests that the energy gaps of hexagonal flakes are more easily controllable by an applied external field, as compared to the triangular graphene dots.

Energy spectrum of a circular graphene quantum dot

An analytical approach, using the Dirac-Weyl equation, is implemented to obtain the energy spectrum of a circular graphene quantum dot in the presence of an external magnetic field. Results are obtained for the infinite-mass and zigzag boundary conditions. We found that the energy spectrum of a dot with zigzag boundary condition exhibits a zero energy band regardless of the value of the magnetic field, while for the infinite mass boundary condition, an energy gap opens. The analytical results are compared to those obtained from the tight-binding model: 1) we show the validity range of the continuum model, and 2) we found that the continuum model with infinite mass boundary condition describes rather well its tight binding analogue, which can partially be attributed to the blurring of the mixed edges by the staggered potential.

4.1 Introduction

The energy levels of circular graphene quantum dots (GQDs) in the presence of a perpendicular magnetic field was recently investigated analytically in Ref. [69], for the special case of infinite-mass boundary condition (IMBC). On the other hand, the energy levels in graphene nanostructures depend sensitively on the edge topology. For instance, for a

The results of this chapter were published as
M. Grujić, M. Zarenia, A. Chaves, M. Tadić, G. A. Farias, and F. M. Peeters, Phys. Rev. B **84**, 205441 (2011), and M. Grujić, M. Zarenia, M. Tadić, and F. M. Peeters, Phys. Scr. **T149**, 014056 (2012).

zigzag termination in graphene nanoribbons and graphene flakes, such as triangular and hexagonal GQDs, a band of zero-energy edge-localized states is found [55, 78, 79]. Except for the case where all the edges of the graphene flake are armchair, the appearance of the zero energy states seems to be robust with respect to edge roughness, as demonstrated by the persistent finite density of these states observed in realistic quasi-circular GQDs [80]. In the presence of an IMBC, the single-particle energy spectrum of a GQD exhibits already a gap around zero energy for low magnetic fields [69]. Therefore, it is important to determine what notable differences in the energy spectra may arise from the application of different boundary conditions.

In this chapter, we analytically solve the Dirac-Weyl equation for a circular graphene quantum dot in the presence of a perpendicular magnetic field, for both infinite-mass and zigzag boundary conditions. To validate the continuum model we present here also the results obtained within the tight binding model (TBM), where there is no ambiguity as far as the boundary conditions is concerned [58]. Two kinds of dots are considered in the TBM: i) a circular dot cut out from a graphene honeycomb lattice, and ii) a circular confinement region delimited by an infinite-mass barrier. The former case has an admixture of zigzag and armchair edges and, due to the zigzag parts, a band of quasi-zero energy levels is found. In the latter case, no zero energy states are present. We critically examine how the continuum model results compare to the TBM results, and which microscopical details in the latter are not captured by the approximations made in the former.

4.2 The continuum approach

The Dirac-Weyl Hamiltonian for low-energy electron states in graphene, in the presence of a perpendicular magnetic field and a mass-related potential, reads

$$H = v_F(\mathbf{p} + e\mathbf{A}) \cdot \boldsymbol{\sigma} + V(r)\sigma_z. \quad (4.1)$$

Here $\mathbf{A} = (0, B\rho/2, 0)$ is the vector potential in symmetric gauge and $\boldsymbol{\sigma}$ denotes the Pauli matrices, which takes into account contributions of two different graphene sublattices. This equation holds for the K valley states, and $\boldsymbol{\sigma}$ in this equation should be replaced by its complex conjugate $\boldsymbol{\sigma}^*$ when considering states in the K' valley. We assume that the carriers are confined in a circular area of radius R , which is modeled by an infinite mass outside the dot, i.e. $V(r) = 0$ for $r < R$, and $V(r) \rightarrow \infty$ for $r \geq R$, where r is the radial coordinate of the cylindrical coordinates system. In the case of the adopted ZBC, the two Dirac cones are labeled by the quantum number k , which has the value $+1$ in the K valley, and -1 in the K' valley. For the IMBC, however, we use the so called valley-isotropic form of the Hamiltonian, with fixed $k = +1$, and the valleys are

differentiated by another quantum number τ , which appears in the boundary condition itself (To simplify the calculations we use k for ZBC and τ for IMBC). Furthermore, we introduce the dimensionless variables $\rho = r/R$, $\beta = R^2/2l_B^2 = eBR^2/2\hbar$ and $\varepsilon = E/E_0 = ER/\hbar v_F$, where E is the carrier energy, $v_F = 10^6$ m/s is the Fermi velocity, and $l_B = \sqrt{\hbar/eB}$ is the magnetic length. The Dirac equation (4.1) in these dimensionless units reduces to the form

$$\begin{bmatrix} 0 & \pi_- \\ \pi_+ & 0 \end{bmatrix} \begin{bmatrix} \psi_1(\rho, \phi) \\ \psi_2(\rho, \phi) \end{bmatrix} = \varepsilon \begin{bmatrix} \psi_1(\rho, \phi) \\ \psi_2(\rho, \phi) \end{bmatrix}, \quad (4.2)$$

where, $\pi_{\pm} = -ie^{\pm ik\phi} \left[\partial_{\rho} \pm \frac{ik}{\rho} \partial_{\phi} \mp k\beta\rho \right]$. Because of the coupling between the orbital angular momentum L_z and pseudospin $\hbar\sigma_z/2$ we define the total momentum $J_z = L_z + \hbar\sigma_z/2$. We have $[H, J_z] = 0$, i.e. the total angular momentum is a conserved quantity, and thus the two-component wave function has the form:

$$\psi(\rho, \phi) = e^{im\phi} \begin{pmatrix} \chi_1(\rho) \\ e^{ik\phi} \chi_2(\rho) \end{pmatrix}. \quad (4.3)$$

where $m = 0, \pm 1, \pm 2, \dots$ is the total angular momentum quantum number. The two components of the wave function correspond to different sublattices, say χ_1 corresponds to the sublattice A , and χ_2 corresponds to the sublattice B .

Eq. (4.2) is solved with the boundary condition that expresses that the outward current at the graphene edge is zero. This leads to the following relation at the dot edge [75]

$$\tan(\phi) = -\Re[\psi_1^*(1, \phi)\psi_2(1, \phi)]/\Im[\psi_1^*(1, \phi)\psi_2(1, \phi)]. \quad (4.4)$$

where $\Re(\Im)$ is the real (imaginary) part. The following two boundary conditions

$$\frac{\psi_2(1, \phi)}{\psi_1(1, \phi)} = i\tau e^{i\phi} \rightarrow \frac{\chi_2(1)}{\chi_1(1)} = i\tau, \quad (4.5a)$$

$$\psi_1(1, \phi) = 0 \rightarrow \chi_1(1) = 0, \quad (4.5b)$$

both satisfy Eq. (4.4). The condition given by Eq. (4.5a) is called the infinite mass boundary condition (IMBC) [75] and imposes the requirement that the region outside the dot is forbidden for particles [81]. $\tau = +1(-1)$ is used for the $K(K')$ states. The condition Eq. (4.5b) requires that one of the wave function components is zero at the dot edge, which is called the zigzag boundary condition (ZBC) [73]. Note that a graphene quantum dot with circular geometry in principle includes both armchair and zigzag edges at the boundary which will be considered in section 4.3 within the TBM. Here, within the continuum

model, we consider for definiteness only ZBC at the edges. In the case of armchair edges the boundary condition includes the wavelspinors corresponding to both K and K' points which is given by

$$\psi_1^K e^{i\mathbf{K}\cdot\mathbf{r}} + \psi_1^{K'} e^{i\mathbf{K}'\cdot\mathbf{r}} = 0, \quad (4.6a)$$

$$\psi_2^K e^{i\mathbf{K}\cdot\mathbf{r}} + \psi_2^{K'} e^{i\mathbf{K}'\cdot\mathbf{r}} = 0. \quad (4.6b)$$

In addition to k and τ , we show below that the states in the analyzed circular GQD are labeled by the total angular quantum number m and the principal quantum number n . Therefore, it is convenient to denote them by the symbol (m, n) . The symbol n is also identified as the Landau level number. In discussing the various properties of the spectrum in the continuum model we use the notation $\varepsilon_{k,m,n}^p$, where $p \in e, h$ denotes electron(hole) eigenvalues, k is the valley index, and it equals to k or τ if considering ZBC or IMBC spectrum respectively. Furthermore n is omitted in zero field discussions.

4.2.1 Zero energy solutions

When $\varepsilon = 0$, the differential equations (4.2) are decoupled,

$$\frac{d\chi_1(\rho)}{d\rho} - \frac{mk}{\rho}\chi_1(\rho) - k\beta\rho\chi_1(\rho) = 0, \quad (4.7a)$$

$$\frac{d\chi_2(\rho)}{d\rho} + \frac{(mk+1)}{\rho}\chi_2(\rho) + k\beta\rho\chi_2(\rho) = 0. \quad (4.7b)$$

which offers straightforward solutions of the form $\chi_1(\rho) = C_1\rho^{mk}e^{k\beta\rho^2/2}$ and $\chi_2(\rho) = C_2\rho^{-(mk+1)}e^{-k\beta\rho^2/2}$.

These solutions can not simultaneously satisfy the IMBC of Eq. (4.5a) and be normalisable. Namely, if the normalization condition is imposed, either C_1 or C_2 , depending on the sign of m , should vanish, which prevents Eq. (4.5a) from being satisfied. Thus, we conclude that there are no zero energy states in the IMBC spectrum.

If the ZBC, Eq. (4.5b) is employed, it is possible to find normalisable zero energy solutions in both valleys. Those solutions are constructed by assuming $C_1 = 0$, and $C_2 \neq 0$ for both the $m < 0$ states in the K valley and the $m > 0$ states in the K' valley. Therefore, adopting the ZBC allows the appearance of a zero energy band. Those wave function components have the form $\chi_1(\rho) = 0$ and $\chi_2(\rho) = C\rho^{-(mk+1)}e^{-k\beta\rho^2/2}$, with $mk = -1, -2, -3, \dots$. Obviously, these states are completely pseudo-spin polarized, and reside on the B sublattice sites. The form of the wave function indicates that all states, except $mk = -1$, are edge localized, as is expected for zero energy zigzag states. Furthermore, states with larger $|m|$ are localized closer to the edge.

4.2.2 Non-zero energy solutions: zero magnetic field

When $\varepsilon \neq 0$ and when the magnetic field is zero, i.e. $\beta = 0$, Eqs. (4.2) are coupled. Substitution of χ_2 from the second into the first differential equation leads to the Bessel differential equation

$$\rho^2 \frac{d^2 \chi_1(\rho)}{d\rho^2} + \rho \frac{d\chi_1(\rho)}{d\rho} + (\varepsilon^2 \rho^2 - m^2) \chi_1(\rho) = 0, \quad (4.8)$$

with solution

$$\chi_1(\rho) = C_1 J_m(\varepsilon \rho). \quad (4.9)$$

From Eq. (4.2), the relation between the first and the second component of the wave function follows

$$\psi_2(\rho, \phi) = \frac{e^{ik\phi}}{\varepsilon} \left(-i\partial_\rho + \frac{k}{\rho} \partial_\phi + ik\beta\rho \right) \psi_1(\rho, \phi), \quad (4.10)$$

and thus

$$\chi_2(\rho) = ikC_1 J_{m+k}(\varepsilon \rho). \quad (4.11)$$

The boundary condition (4.5a) leads to the equation $\tau J_m(\varepsilon) = J_{m+1}(\varepsilon)$, while the boundary condition (4.5b) gives $J_m(\varepsilon) = 0$. Recalling that the Bessel functions obey the properties $J_m(\varepsilon) = (-1)^m J_{-m}(\varepsilon)$ and $J_m(\varepsilon) = (-1)^m J_m(-\varepsilon)$, several interesting properties of the zero-field energy spectra are derived: i) there is electron-hole symmetry in both valleys for ZBC, which is reflected via expression $\varepsilon_{\pm 1, m}^e = -\varepsilon_{\pm 1, m}^h$. Unlike ZBC, IMBC is known to break electron-hole symmetry [73], so the former relations do not hold. However there is a similar symmetry property for the IMBC, for which the expression $\varepsilon_{\pm 1, m}^e = -\varepsilon_{\pm 1, -(m+1)}^h$ holds. ii) Intervalley spectrum symmetry is present for the ZBC: $\varepsilon_{+1, m}^{e, h} = \varepsilon_{-1, m}^{e, h}$, whereas for the IMBC $\varepsilon_{+1, m}^{e, h} = \varepsilon_{-1, -(m+1)}^{e, h}$. The latter two properties for IMBC further indicate intervalley electron-hole symmetry between states of the same m , i.e. $\varepsilon_{\pm 1, m}^e = -\varepsilon_{\mp 1, m}^h$. iii) Finally we may deduce that the energy spectrum within each valley is either doubly degenerate (for $m \neq 0$, $\varepsilon_{\pm 1, +m}^{e, h} = \varepsilon_{\pm 1, -m}^{e, h}$) or non-degenerate (for $m = 0$) if ZBC is adopted where this is not the case for IMBC.

4.2.3 Non-zero energy solutions with magnetic field

For the general case $\varepsilon \neq 0$ and $\beta \neq 0$, we obtain the differential equation for χ_1

$$\left(\frac{d^2}{d\rho^2} + \frac{1}{\rho} \frac{d}{d\rho} - [2\beta(m+k) + \frac{m^2}{\rho^2} + \beta^2 \rho^2 - \varepsilon^2] \right) \chi_1(\rho) = 0, \quad (4.12)$$

where the symmetric gauge is used for the magnetic field. This equation has the normalisable solution

$$\psi_1(\rho, \phi) = C e^{im\phi} \rho^m e^{-\beta\rho^2/2} {}_1\tilde{F}_1\left(\frac{2m+k+1}{2} - \frac{\varepsilon^2}{4\beta}, m+1, \beta\rho^2\right), \quad (4.13)$$

where we used the relation $\psi_1(\rho, \phi) = e^{im\phi} \chi_1(\rho)$, obtained from Eqs. (4.2) and (4.3), and ${}_1\tilde{F}_1(a, b, z)$ is the regularized confluent hypergeometric function. The second component of the wave function is extracted from Eq. (4.10), and for the $K(k=1)$ and $K'(k=-1)$ valleys read

$$\begin{aligned} \psi_2(\rho, \phi) = ikC e^{i(m+k)\phi} \frac{2\rho^{m+k}}{\varepsilon} \left[\frac{(1-k)}{2} + \frac{(1+k)\varepsilon^2}{4} \right] \times \\ e^{-\beta\rho^2/2} {}_1\tilde{F}_1\left(\frac{2m+k+1}{2} - \frac{\varepsilon^2}{4\beta}, m+k+1, \beta\rho^2\right). \end{aligned} \quad (4.14)$$

The IMBC leads to the following eigenvalue equation:

$$\frac{\tau\varepsilon}{2} {}_1\tilde{F}_1\left(m+1 - \frac{\varepsilon^2}{4\beta}, m+2, \beta\right) - {}_1\tilde{F}_1\left(m+1 - \frac{\varepsilon^2}{4\beta}, m+1, \beta\right) = 0, \quad (4.15)$$

while for the ZBC we obtain

$${}_1\tilde{F}_1\left(\frac{2m+k+1}{2} - \frac{\varepsilon^2}{4\beta}, m+1, \beta\right) = 0. \quad (4.16)$$

4.2.4 Energy spectrum

Figure 4.1 shows the energy levels of a circular dot with radius $R = 70$ nm and $-4 \leq m \leq 4$ for both (a) IMBC and (b) ZBC cases as function of magnetic field. Energy states corresponding to the K and K' valleys are respectively drawn with blue solid and red dashed curves. The IMBC leads to an energy gap in the spectrum, as evident in Fig. 4.1(a) while the zigzag boundary conditions exhibit a zero energy state (the black solid line in Fig. 4.1(b)). Notice that when the magnetic field increases the lowest non-zero electron energy levels in both IMBC and ZBC decrease. This is in contrast with semiconductor QDs in which the Fock-Drawin states always increase with magnetic field [48]. We fitted the lowest energy level to a Gaussian function $\varepsilon(\beta) = a \exp(-([\beta - b]/c)^2)$ (see green solid curves in Fig. 4.1(a,b)) where $(a, b, c)_{IMBC} = (3, -3.9, 4.55)$ and $(a, b, c)_{ZBC} = (4.47, -7.1, 9)$ are the fitting parameters, respectively, for the IMBC and ZBC. We found a relation between the parameter c of the different energy levels: $c_{IMBC}^i \approx 1.15 c_{IMBC}^{i-1}$ and $c_{ZBC}^i \approx c_{ZBC}^{i-1}$ (with i being the eigenstate index) respectively for IMBC and ZBC.

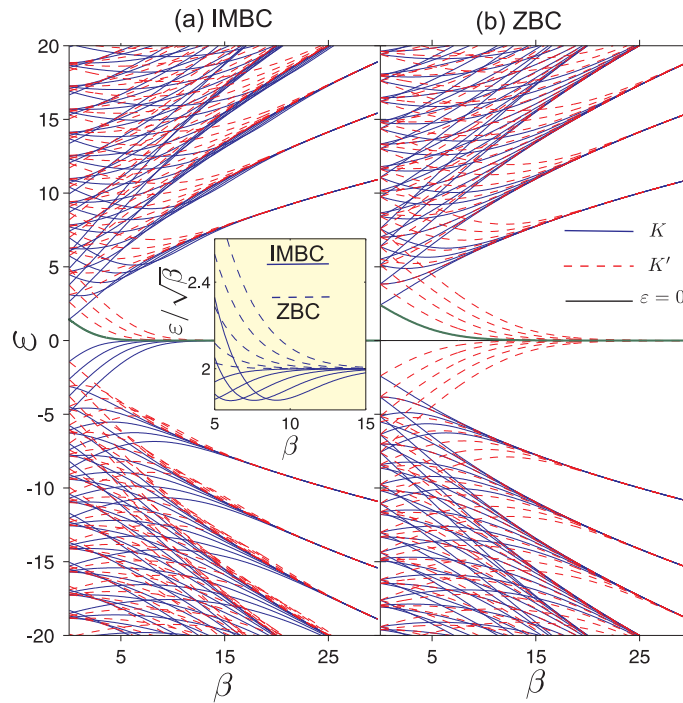


Figure 4.1: Energy spectrum of a circular graphene quantum dot with $R = 70$ nm in a perpendicular magnetic field for: (a) the IMBC, and (b) ZBC. The energy levels corresponding to the K and K' valleys are shown respectively by the blue solid curves and red dashed curves. The zigzag zero energy state is shown by the black solid line. The green solid curves display the fitted function to the first energy levels. Only the six lowest electron and hole energy levels are shown for $-4 \leq m \leq 4$. The inset of panel (a) shows an enlargement of the energy levels, corresponding to the K valley, around the region where the quantum dot states merge to form the first LL for both IMBC (solid curves) and ZBC (dashed curves).

From (4.15) and (4.16) we may deduce that for each boundary condition the magnetic field breaks all but one symmetry property, which were stated in previous section. Thus from Eq. (4.15) one may notice that the energy levels of the K and K' valleys are symmetric as $\varepsilon_{\pm 1, m}^e = -\varepsilon_{\mp 1, m}^h$. On the other hand, when the ZBC is adopted, Eq. (4.16) depends on ε^2 , and consequently the electron and hole states in each valley are symmetric with respect to each other.

With increasing magnetic field, the quantum-dot states merge to form the Landau levels (LLs) of graphene. In contrast with semiconductors, the LLs in graphene are non-equidistant and exhibit square-root dependence on the magnetic field [82]. The asymptotic

dependence of the energy spectrum at large magnetic field and for both K and K' valleys is given by

$$\varepsilon_{\pm 1, m, n}^{e, h}(\beta) = \pm \sqrt{4\beta \left(n_\rho + \frac{|m| + m}{2} \right)} \quad (4.17)$$

where $n_\rho = 0, 1, 2, \dots$ gives the energy levels in the presence of the ZBC and $n_\rho = 1, 2, 3, \dots$ corresponds to the IMBC.

4.3 The tight-binding model

It is clear that the advantage of using the continuum model lies in the fact that it provides analytical solutions which are easy to handle. However, the continuum model was derived from the tight-binding model (TBM) [18] for an infinite graphene sheet, under the restriction of low energy charge carriers around the Dirac cones in K and K' . Therefore, it is of interest to investigate the validity range of the continuum model for GQDs.

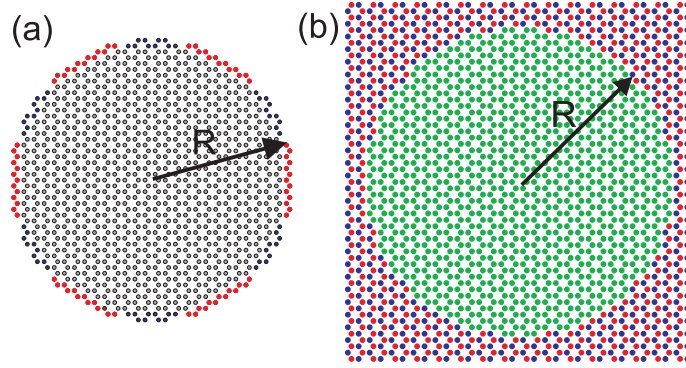


Figure 4.2: Sketch of the two circular graphene dots of radius R considered in our TB calculations: (a) A circular dot cut out from the graphene honeycomb lattice, where the red (blue) sites refer to zigzag (armchair) boundaries. (b) A circular region (green) surrounded by an infinite mass media, which is obtained by considering a staggered potential, i.e. a +10 (-10) eV on-site potential for lattice A (B) sites, represented by red (blue) atoms. In both cases, the dot is made out of all the atomic sites which are inside a circle of radius R and which have at least two nearest-neighbors sites inside the circle.

Actual dot structures are normally cut out from a graphene honeycomb lattice, instead of being surrounded by an infinite mass media, and therefore cannot have only one type of edges, as illustrated in Fig. 4.2. However, we intend to demonstrate that the simple boundary conditions described above still provide some agreement with the tight-binding

(TB) results. The results in this section are obtained from a first nearest-neighbors tight binding Hamiltonian which is given by

$$H = \sum_n E_n c_n^\dagger c_n + \sum_{nm} t e^{2\pi i \Phi_{nm}} c_n^\dagger c_m \quad (4.18)$$

where E_n is the on-site energy and $c_i(c_i^\dagger)$ is the annihilation (creation) operator, $t = 2.7$ eV is the zero magnetic field hopping term where the C-C distance is $a_0 = 0.142$ nm, $\Phi_{nm} = \frac{1}{\phi_0} \int_{r_n}^{r_m} \mathbf{A} \cdot d\mathbf{r}$ is the Peierls phase with $\phi_0 = h/e$ being the magnetic quantum flux, and $\mathbf{A} = (0, Bx, 0)$ is the vector potential taken in the Landau gauge with perpendicular magnetic field B .

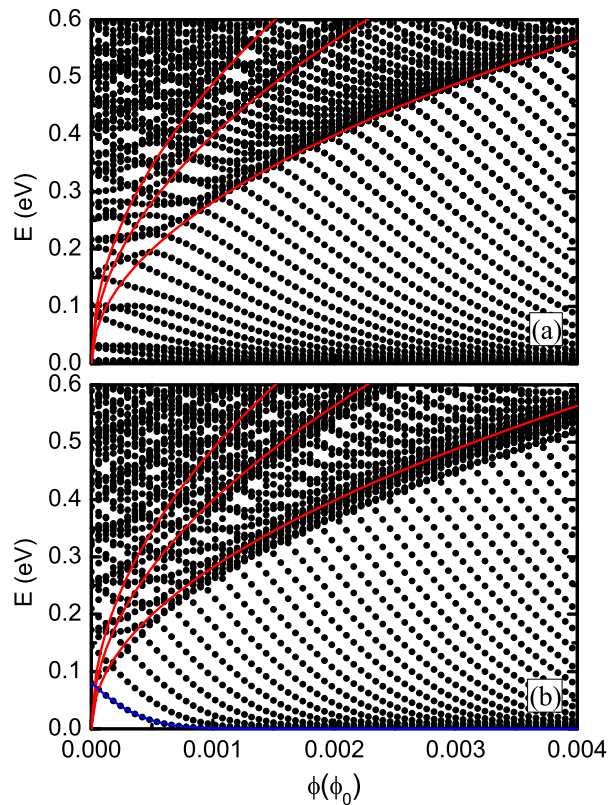


Figure 4.3: Energy spectrum as function of the magnetic field, obtained from the TBM for (a) the cut out graphene dot and (b) the infinite mass defined quantum dot illustrated in Fig. 4.2 with $R = 10$ nm. The red curves represent the Landau levels in graphene. The blue solid curve in panel (b) shows the fitted function to the first energy level.

Let us first analyze the case of a circular dot cut out from a graphene lattice, as shown in Fig. 4.2(a). The energy spectrum in this case, is shown in Fig. 4.3(a) as a function of the magnetic flux through one carbon hexagon $\phi = (3\sqrt{3}a_0^2/2)B$, which looks qualitatively similar to the one shown in Fig. 4.1(b), for a circular dot with ZBC within the continuum model. In both cases, groups of states decrease in energy with increasing magnetic field, eventually converging to the Landau levels, and a zero energy level is observed for any value of magnetic field. On the other hand, some details of the energy spectrum for lower magnetic fields are not captured properly by the continuum model, even for the low energy levels. For instance, in the results for both the continuum and TB models, the first non-zero level decreases with increasing field, whereas the second level starts to increase with the field until it crosses a higher energy level. However, the anti-crossings observed immediately above the described crossing in the TB results are not observed in the continuum model with the ZBC. The IMBC results in Fig. 4.1(a) also do not exhibit such anti-crossings.

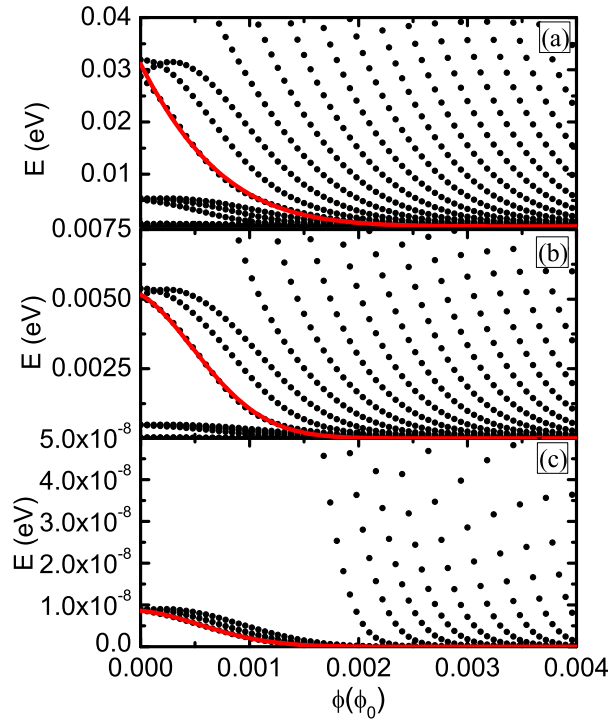


Figure 4.4: Magnification of the results in Fig. 4.3(a) for three different energy scales. The red solid curves display the fitted functions to the several lowest energy states.

There is also a surprising feature in this energy spectrum obtained within the TBM: as we zoom in around the zero-energy region, we realize that it is not really a single $E = 0$ curve, but rather a band of curves, as shown in Fig. 4.4. We considered three different ranges of energy and found curves that exhibit a self-similar-like pattern, which persists until we find the lowest energy levels, which are indeed very close to zero ($\approx 10^{-8}$ eV). The results in Figs. 4.3 and 4.4 were obtained for $R = 10$ nm. As the dot radius is reduced, similar results are observed but the low energy states appear further away from the zero level. For example, for $R = 2$ nm, the lowest level has an energy $E \approx 0.095$ eV, i.e. a 0.190 eV energy gap, even though the dot still exhibits zigzag edge segments. The wavefunction of these small energy states are localized at the zigzag edges of the circular dot (see Fig. 4.5). The lowest energy states consists of wavefunction pockets localized at the largest width zigzag edge regions. (i.e. regions indicated by the red dots in Fig. 4.2(a)). Notice furthermore that for $B \approx 0$ those low energy levels are grouped in three: 1) the two lowest are degenerate for $B = 0$ and their wavefunctions are identical up to a rotation of 60° and 2) the third level has a slightly larger energy with a wavefunction consisting of more pockets localized at the edge with a higher rotational symmetry as compared to the previous two. As the magnetic flux increases, the degeneracy of the two lowest levels is lifted in each group and the second state crosses the third (non-degenerate) state at some value of magnetic flux. For higher flux, all these states decrease and end up forming the zeroth Landau level.

Similar as for the continuum results the first energy levels for both IMBC and ZBC can be fitted to a Gaussian function, i.e. $f(\Phi) = a \exp(-([\Phi - b]/c)^2)$, where $(a, b, c)_{IMBC} = (0.16, -0.0006, 0.0007)$ are the fitting parameters for the IMBC (see the blue sold curve in Fig. 4.3(b)) and $(a, b, c)_{ZBC} = (0.0008, -11, 92) \times 10^{-5}$ are the fitting parameters for the first energy level with ZBC (see the red solid curve in Fig. 4.4(c)). Notice that the upper energy levels (those decreasing with magnetic field) can also be fitted to a Gaussian function as shown by the red curves in Figs. 4.4(a,b) for the ZBC $((a, b, c)_{ZBC}^{(a)} = (0.13, -0.0022, 0.0018)$ and $(a, b, c)_{ZBC}^{(b)} = (0.0053, -0.00018, 0.0001)$ are the fitting parameters respectively for the indicated energy state in Fig. 4.4(a) and Fig. 4.4(b)).

We now analyze the case of a circular dot surrounded by an infinite mass media, as illustrated in Fig. 4.2(b). Although, the sublattice symmetry breaking in epitaxial graphene is still a big challenge in order to realize graphene-based electronic devices, recent experiments demonstrated that by choosing the appropriate substrate [11, 33] this can be realized. Such a symmetry breaking is translated into a mass term in the Dirac-Weyl Hamiltonian for graphene. This suggests that a circular graphene dot embedded in an infinite mass media might be experimentally feasible by means of substrate engineering. This motivated us to study circular GQD surrounded by a staggered potential, as illustrated in Fig. 4.2(b). The results obtained by the TBM for such a system are indeed comparable to those from

the IMBC in the continuum model: both cases have no zero energy levels, and the anti-crossings found for the structure in Fig. 4.3(a) are not present in the energy spectrum for the infinite mass confinement in the TBM, which makes it to agree much better with the IMBC results. On the other hand, a broad energy band is found around the Landau levels in the TB results, which is not observed in the continuum model. Nevertheless, this band occurs for high energy states, which are not expected to be described by the Dirac-Weyl equation, although they follow qualitatively the Landau levels predicted by this equation.

Finally, we investigate how the size of the graphene dot affects their energy spectrum and compare the results from the TB and continuum models. Fig. 4.6(a) shows the energy spectrum as a function of the dot radius obtained by the TBM (symbols) for the mass-confinement dot illustrated in Fig. 4.2(b). The Dirac-Weyl results considering IMBC are shown as red curves, which exhibit very good agreement with the TB results, especially for the lower energy states and larger dots. Some curves in the TB results do not decay monotonically as $\propto 1/R$; instead, they exhibit a fluctuating behavior, which is more pronounced for smaller radii. Such fluctuations can be linked to the fact that the GQDs studied within the TBM are never perfectly circular, as one can verify in the sketch in Fig. 4.2(b). In other words, the microscopical details become important as R decreases, and these de-

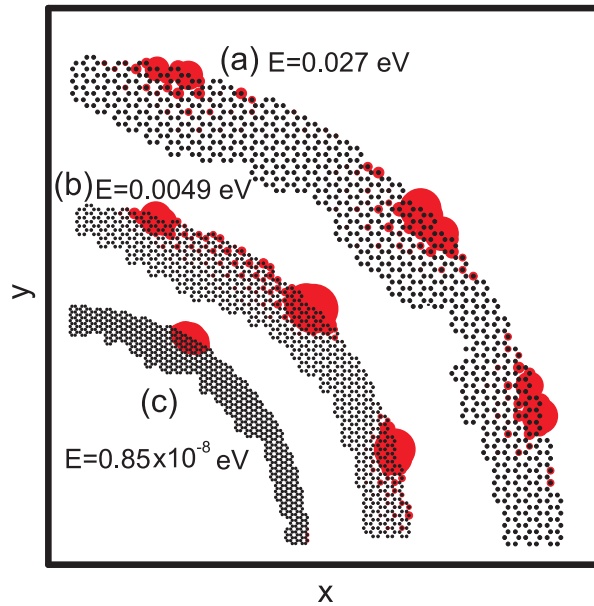


Figure 4.5: Electron densities corresponding to the energy levels shown by the red solid curves in Fig. 4.4 for $\Phi/\Phi_0 = 0$. The black dots are the position of the C-atoms where we showed only a small strip of the quadrant of the circular graphene flake.

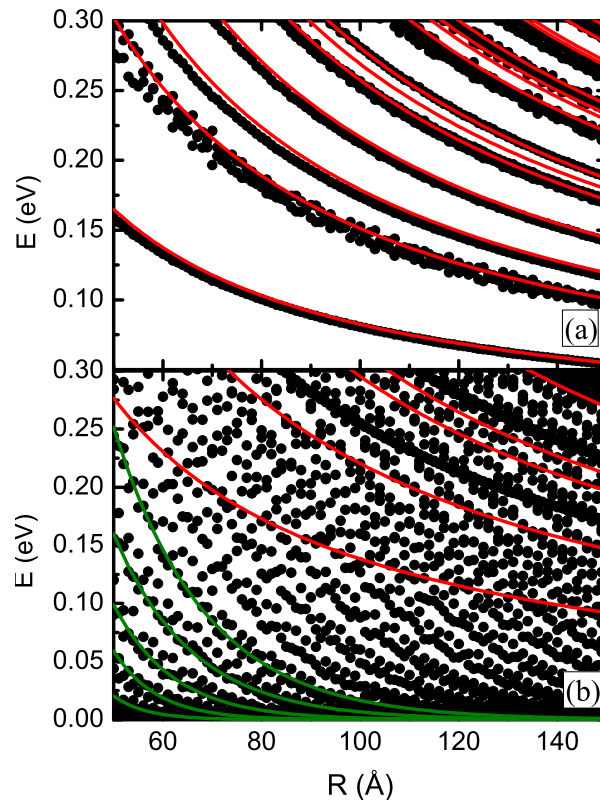


Figure 4.6: Energy spectrum as function of the dot radius, in the absence of a magnetic field, obtained from the continuum (red curves) and TB models (symbols), (a) for the infinite mass defined quantum dot illustrated in Fig. 4.2(b), and (b) for the quantum dot cut out from the graphene layer, illustrated in Fig. 4.2(a).

tails cannot be described properly by the analytical model for circular GQDs, based on the continuum approach. For larger dot radii, these edge imperfections are less important, which explains the less pronounced fluctuations in the energy levels as R increases.

The energy spectrum as function of the radius of the circular dot when cut out from the graphene layer, shown in Fig. 4.6(b), exhibits: i) even larger fluctuations, ii) the energies decrease much faster than $1/R$ with increasing R , and iii) the energy levels are spread out more evenly in the shown energy window. This is due to the fact that, besides the imperfections in the circular shape of the dot, the variations in the number of zigzag and armchair atoms at the edge of the dot also plays a role in the energy spectrum as R increases. We notice that as R increases, lower energy states merge into a very dense $E = 0$ band. This is not expected to be the case in the continuum approximation, where

the zero energy band states are perfectly degenerate with zero energy even for small radius, and higher energy states approach zero only for $R \rightarrow \infty$. Thus, this feature, along with the self-similarity behavior mentioned earlier, are pure manifestations of the microscopical character of such GQDs, which cannot be described by our IMBC and ZBC, or by any analytical model within the continuum approach known to date. Indeed, the results obtained by the ZBC in the continuum model (red curves) give no hint about the energy spectrum, except for the fact that they predict the $1/R$ behavior of some states observed in the TB results. The energy states that decrease much faster than $1/R$, can be fitted to an exponential function, i.e. $E^i = E_0^i e^{-R/R_0^i}$, where E_0^i and R_0^i are fitting parameters and i indicates the eigenstate index. In Fig. 4.6(b) the five lowest energy levels are shown by the green solid curves where $E_0^{i=1,2,\dots,5} = [33.3, 17.96, 6.24, 3.78, 3.82] \text{ eV}$ and $R_0^{i=1,2,\dots,5} = [0.67, 0.87, 1.2, 1.58, 1.84] \text{ nm}$. The parameters R_0^i can be related to each other by $R_0^i \approx 1.3 \times R_0^{i-1}$.

4.4 Conclusion

The electron and hole states in a monolayer graphene circular quantum dot were modeled using the Dirac-Weyl equation. Two distinct types of boundary conditions are employed, namely the infinite-mass and the zigzag boundary conditions. An energy gap near zero energy is only found for the case with infinite-mass boundary condition, whereas the peculiar zero energy state, which is pseudo-spin polarized and localized close to the zigzag boundary, exists when the zigzag boundary condition is imposed. Increase of the magnetic field diminishes the influence of the edge on the electron confinement, and the states merge into Landau levels. The obtained spectra exhibit different symmetries between the electron and hole spectra, and also different inter-valley symmetries.

We found that many features of the more realistic TB quantum dots can be described by simplifications made for the circular dots within the continuum approach. Namely, the energy states in the continuum and TB models converge to the LLs at high magnetic field in a similar way. However, due to their inevitable zigzag edges, circular GQDs cut out from a graphene lattice exhibit a dense quasi-zero energy band, formed by groups of states which exhibit self-similarity. This is a manifestation of the microscopical character of these dots, and can hardly be described by any continuum-based model. Nevertheless, for circular dots based on mass confinement, the TB results and the analytical IMBC results agree very well for lower energies and larger dot radius. Thus, a secondary conclusion comes from the comparison above: the IMBC for the Dirac-Weyl equation, frequently used to simulate electron states in GQDs, can describe only quantum dots created by mass-related confinement, whereas the actual GQDs cut out from a graphene layer obtained in recent

experiments have a much more complex spectrum which, at least in the absence of possible additional potential terms (due to e.g. edge reconstruction, magnetization, etc.), cannot be described either by IMBC or by ZBC when using the continuum model.

CHAPTER 5

Snake states in graphene quantum dots in the presence of a p-n junction

We investigate the magnetic interface states of graphene quantum dots that contain p-n junctions. Within a tight-binding approach, We consider rectangular quantum dots in the presence of a perpendicular magnetic field containing p-n, as well as p-n-p and n-p-n junctions. The results show the interplay between the edge states associated with the zigzag terminations of the sample and the snake states that arise at the p-n junction, due to the overlap between electron and hole states at the potential interface. Remarkable localized states are found at the crossing of the p-n junction with the zigzag edge having a dumb-bell shaped electron distribution. The results are presented as function of the junction parameters and the applied magnetic flux.

5.1 Introduction

The linear gapless electronic spectrum, together with the chirality of carriers in graphene is predicted to allow perfect transmission through potential barriers (Klein paradox) [21]. This transmission has a directional character and is caused by the overlap between electron and hole states across the potential barrier [83, 84]. The effect has been investigated experimentally in p-n junctions of gated graphene samples [85–88].

The results of this chapter were published as
M. Zarenia, J. M. Pereira Jr., F. M. Peeters, and G. A. Farias, Phys. Rev. B **87**, 035426 (2013).

In the presence of an external magnetic field, the electron-hole overlap at the potential barrier (or p-n junction) causes the appearance of states that propagate along the junction interface [25, 89]. These are known as *snake states* since, in a semiclassical view, they arise through the coupling between counter-circling cyclotron orbits on either side of the p-n junction. They may also arise due to the presence of inhomogeneous fields [26] and in warped and folded graphene [90, 91]. The presence of snake states was found to influence the electronic properties of graphene-based samples in the quantum Hall regime [89]. Moreover, the coupling of snake states have been predicted to modify electrical current transport near the interfaces of narrow p-n-p junctions [92]. Recently, experimental evidence was provided of the chaotic coupling of snake states in quantum point contacts [93].

Here we investigate theoretically the interplay between edge and snake states of p-n, p-n-p, and n-p-n junctions imposed on graphene quantum dots (GQDs). We study the character of the different confined states by looking at the probability densities. The electron probability density can be linked to the local density of states (LDOS) which is a quantity that can be measured experimentally using scanning tunneling microscopy (STM). Measurement of the LDOS allows the probing of the spatial structure of the confined energy levels. Such measurements were recently reported for graphene quantum dots [52]. We consider GQDs created by cutting a larger graphene sample in order to obtain electronic confinement in a nanometer-scale structure with well-defined edges. The properties of the confined states of such GQDs in a magnetic field have been studied theoretically [69, 109] as well as experimentally [94]. Note that such p-n junctions (but of irregular shape) are also naturally present in graphene samples when the Fermi energy is located around the Dirac point. They are generally known as puddles and have investigated with scanning tunneling microscopy (STM) [95–97]. In our calculations we neglect disorder which for the considered small sized dots will be of secondary importance.

One important aspect of such graphene-based structures is the possible existence of edge states, for which the wavefunctions are localized at zigzag terminations of the sample [58, 70, 78, 79, 98]. These states have been recently observed by STM [99, 100]. The presence of edge states can be especially relevant for nanometer-scale graphene structures. In particular, depending on the geometry of the GQDs, the edge states can correspond to the ground state of the system [58]. For GQDs of general shape, Wimmer *et al.* have shown that the edge states tend to form a narrow band and are generally robust with regards to perturbations [80]. In the present case we consider the effect of a position-dependent potential profile and an external perpendicular magnetic field on the energy spectrum of rectangular GQDs in the context of the nearest-neighbor tight-binding model. The presence of the potential interface thus introduces additional localized states, i.e. snake states, which can hybridize with the conventional zigzag edge states.

5.2 Model

The nearest-neighbor tight-binding Hamiltonian of the π electrons in the honeycomb graphene lattice can be written as

$$\mathcal{H} = \sum_m \epsilon_m c_m^\dagger c_m + \sum_{lm} (t_{lm} c_l^\dagger c_m + h.c.), \quad (5.1)$$

where ϵ_m is the on-site energy, t_{lm} is the nearest-neighbor coupling parameter and c_j (c_j^\dagger) is the annihilation (creation) operator of the electron at a site with label j . The external magnetic field introduces the Peierls phase in the coupling term $t_{lm} = t \exp(2\pi i \Phi_{l,m})$, where t is the zero-magnetic field coupling parameter, $\Phi_{l,m} = (1/\Phi_0) \int_{r_l}^{r_m} \mathbf{A} \cdot d\mathbf{r}$, and $\Phi_0 = h/e$ is the magnetic quantum flux and \mathbf{A} is the vector potential. For graphene one has $t = 2.7$ eV. The field is given by $\mathbf{B} = B\hat{z}$ and we choose the Landau gauge as $\mathbf{A} = (0, Bx, 0)$. Then, the Peierls phase for a transition between two sites l and m is $\Phi_{l,m} = 0$ in the x direction and $\Phi_{l,m} = \pm(x/3a)\Phi_c/\Phi_0$ along the $\pm y$ direction, where $\Phi_c = 3\sqrt{3}a^2 B/2$ is the magnetic flux threading one carbon hexagon with $a = 0.142$ nm being the C-C distance. The p-n, p-n-p or n-p-n junctions are modeled by assuming a position-dependent on-site energy $\epsilon_m = \epsilon(m)$. Throughout this chapter we assign the values $\epsilon = U_b$ ($\epsilon = -U_b$) for the p (n) regions, whereas at the interfaces between these regions the potential is assumed to vary abruptly. This assumption is expected not to influence the results qualitatively.

5.3 p-n junction: zero magnetic field

We consider an almost square quantum dot because it allows us to investigate the effect of both armchair and zigzag edges in the same sample. We are interested to learn how the confined states are influenced by the relative orientation of the p-n interface with respect to the specific type of edges. Here, the length of the rectangular GQD which is terminated by armchair edges is defined as $L_x = [(3N_a/2) - 1]a$ and the length terminated at the zigzag edges is $L_y = N_z\sqrt{3}a$ where N_a and N_z are the number of C-atoms, respectively at the armchair and zigzag edges. The total number of C-atoms in the rectangular GQD is $N = N_a(2N_z + 1)$. We should notice that the energy spectrum of a rectangular GQD exhibits zero energy states [101] which are confined at the zigzag edges. The number of zero energy states in a rectangular dot depends to the number of both armchair and zigzag atoms [101]. Figure 5.1(a) shows the number of states with *nearly* zero energies (we took the number of states within the energy interval $|E| < 0.1$ meV) as function of N_z and N_a .

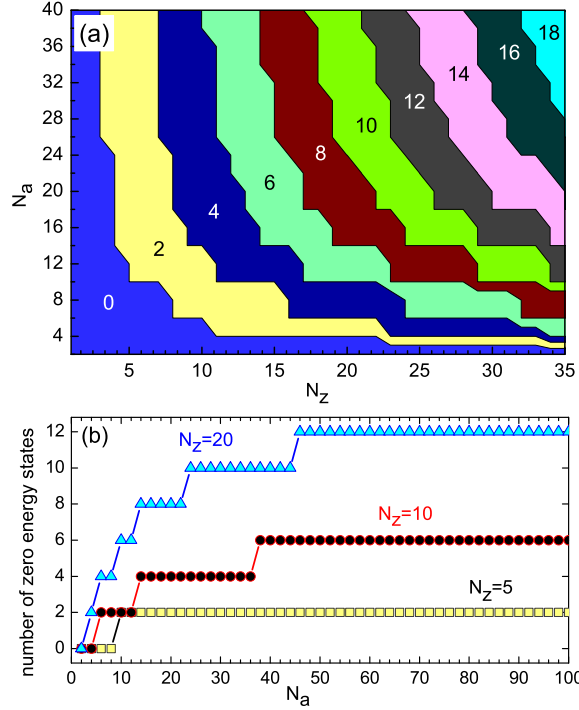


Figure 5.1: (a) Number of nearly zero energy states within the interval $|E| < 0.1$ meV as function of armchair (N_a) and zigzag (N_z) edge atoms. (b) Number of zero energies as function of N_a for $N_z = 5, 10, 20$.

The results show that for a fixed number of zigzag edge atoms the number of zero-energy states increases with increasing the armchair edge atoms (see Fig. 5.1(b)). Notice that the number of zero-energy states can not exceed $2N_z$.

Now We solve the Hamiltonian (5.2) for a system in which a p-n junction is parallel to the zigzag edges of a rectangular GQD (see the inset of Fig. 5.2 where different colors represent the p-type and n-type regions which are respectively subjected to $+U_b$ and $-U_b$ gate voltages). For numerical purposes we take as an example $N_a = 36$ ($L_x = 7.52$ nm) and $N_z = 35$ ($L_y = 8.6$ nm) in all the results of this chapter. The energy levels of this system are shown as function of the gate voltage U_b in Fig. 5.2 for zero magnetic flux $\Phi_c/\Phi_0 = 0$. In the presence of a p-n junction parallel to the zigzag edges the zero energy-degenerate states split into two groups of degenerate states with energy: *i*) $E = +U_b$ and *ii*) $E = -U_b$ where the number of the states in each group is equal. Note that the energy spectrum in Fig. 5.2 exhibits a group of states which on average are almost independent of U_b . Figure 5.3 shows probability density plots for the states indicated by the letters (a-h) in Fig. 5.2. The probability densities in Fig. 5.3(a) and Fig. 5.3(c) exhibit a nodal

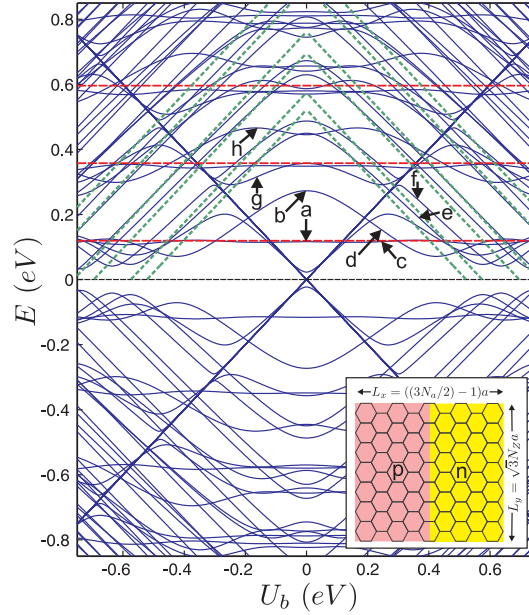


Figure 5.2: Energy levels of a system with a p-n junction parallel to the zigzag edges in a rectangular GQD with $L_x = 7.52$ nm, $L_y = 8.6$ nm and $\Phi_c/\Phi_0 = 0$ as function of applied voltage U_b . The system is illustrated in the inset. The different colors represent the different gate voltages ($+U_b$ for p-type and $-U_b$ for n-type). The red dashed lines correspond to the energy states given by Eq. (5.3) and the green dashed lines represent the energy levels obtained from Eq. (5.4).

character across the zigzag edges and consequently the U_b energy shift from the p- and n-regions cancel out. These levels are similar to confined states in a zigzag *nanoribbon*. The energy levels of a zigzag nanoribbon are described, using the continuum model, by the transcendental equation [74]

$$\frac{k_y - \kappa}{k_y + \kappa} = e^{-2L_x \kappa} \quad (5.2)$$

where $\kappa = \sqrt{k_y^2 - (\epsilon/\hbar v_F)^2}$ with $v_F = 10^6$ m/s being the Fermi velocity. In the low energy limit we take $k_y = 0$ where Eq. (5.3) becomes $\exp(\pm 2iL_x \epsilon/\hbar v_F) = -1$ and results in

$$\epsilon_n = \pm \frac{\pi \hbar v_F}{L_x} \left(n + \frac{1}{2} \right), \quad n = 0, 1, 2, \dots \quad (5.3)$$

The three first electronic levels of the above relation are shown in Fig. 5.2 by red dashed lines which coincide reasonable well with the position of the constant energy levels in the

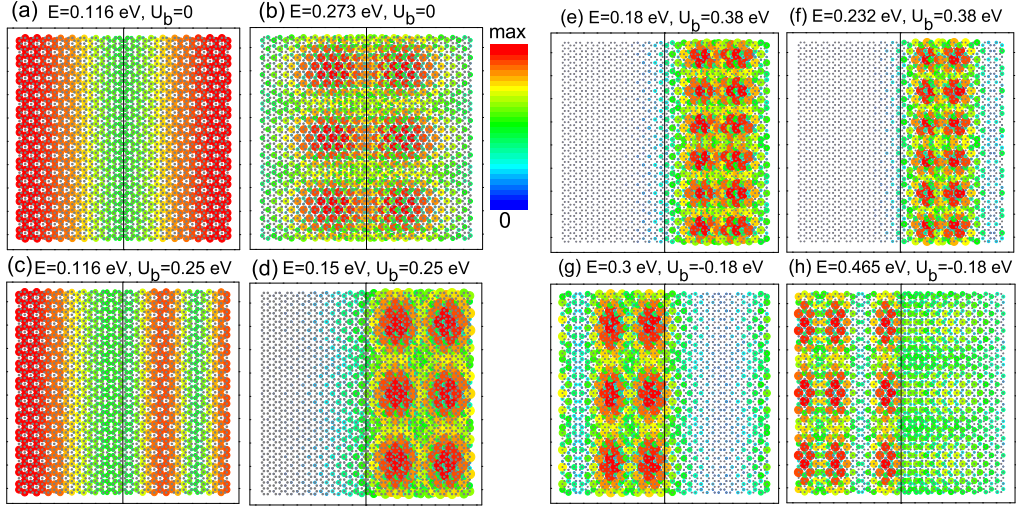


Figure 5.3: Probability densities corresponding to the points indicated by (a-h) in Fig. 5.2. The black vertical line indicates the position of the p-n junction.

spectrum. Note that the agreement is better for low energy where the continuum model is more accurate. For the levels where the wavefunction is spread out inside the dot the energy levels are approximately linear with U_b . As seen in Figs. 5.3(b,d) the probability density corresponding to these levels shows an oscillatory behavior along the y-direction which is due to the confinement by the armchair edges. For armchair nanoribbons the wave vector k_y satisfies the condition $k_y = (n_y\pi/L_y) + (2\pi/3\sqrt{3}a)$ where n_y being an integer [74]. Using Eq. (5.3) we take $k_x = \pi(n_x + 1/2)/L_x$ along the x-direction. Thus the corresponding energies in the presence of $\pm U_b$ are proportional to $\pm(U_b \pm \hbar v_F \sqrt{k_y^2 + k_x^2})$ which results in

$$\epsilon_n = \pm \left[U_b \pm \hbar v_F \sqrt{\left(\frac{n_y\pi}{L_y} + \frac{2\pi}{3\sqrt{3}a} \right)^2 + \left(\frac{\pi(n_x + 1/2)}{L_x} \right)^2} \right] \quad (5.4)$$

These electronic levels described by Eq. (5.4) which are shown by the green dashed lines in Fig. 5.2 for $-26 \leq n_y \leq -20$ and $n_x = 1$. The above arguments describe reasonably well qualitatively most of the energy levels that are found in the numerical spectrum depicted in Fig. 5.2. Because of the finite boundaries those levels may interact leading to anti-crossings. Aside from anti-crossings, the lines describe rather well the low energy levels in the spectrum that decrease linearly with $|U_b|$. Figs. 5.3(e,f) show the electronic density corresponding to the lowest paired levels for $U_b = 0.38$ eV where the electrons are only confined in the n region. Figures 5.3(g,h) show those states that are influenced by both

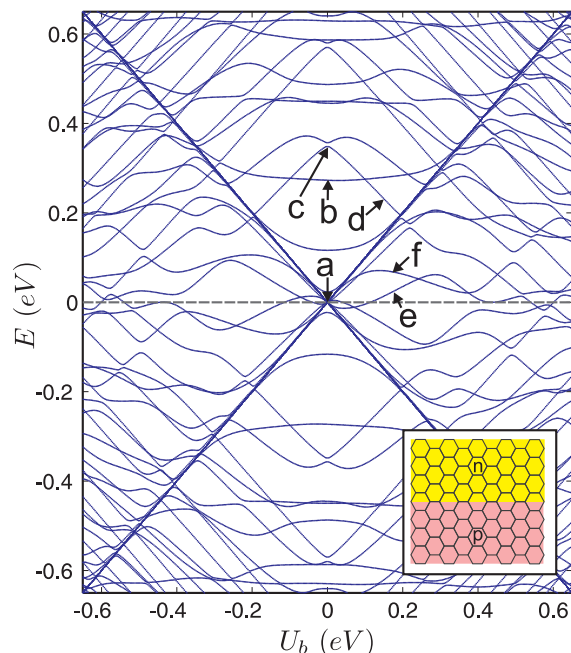


Figure 5.4: Energy levels of a rectangular GQD with a p-n junction parallel to the armchair edges (see the inset of the figure) as function of applied electrostatic potential U_b for $L_x = 7.52$ nm, $L_y = 8.6$ nm and zero magnetic field.

zigzag and armchair edges.

The energy levels of a rectangular GQD subjected to a p-n junction parallel to the armchair edges is shown in Fig. 5.4. The system is depicted in the inset of Fig. 5.4. Since the p-n interface is now located perpendicular to the direction of the edge states (i.e. zigzag edges) the energy spectrum exhibits a complex behavior as function of U_b . In this case the spectrum is not symmetric under switching $U_b \rightarrow -U_b$ for $|E| < U_b$ which is due to the fact that the number of p-type and n-type atoms are unequal. The probability density corresponding to the points indicated by arrows are shown in Fig. 5.5. For $U_b = 0$ and $E = 0$ the carriers are confined at the zigzag edges (see Fig. 5.5(a) and the level is eighteen fold degenerate). Notice that the rectangular GQD with $N_a = 36$ and $N_z = 35$ has 16 zero energy states (see Fig. 5.1(a)). The probability density corresponding to the upper states are spread out over the dot in both x- and y-directions (see Fig. 5.5(b)) or along the zigzag edges (see Fig. 5.5(c)). In the presence of a p-n junction the electrons confine at the p(n)-region when $E > U_b$ and the energy state decrease(increase) with U_b (Fig. 5.5(d)). In contrast with Fig. 5.2, for a p-n junction parallel to the armchair edge several states are found for $E < U_b$. These states, as seen in Figs. 5.5(e,f), present

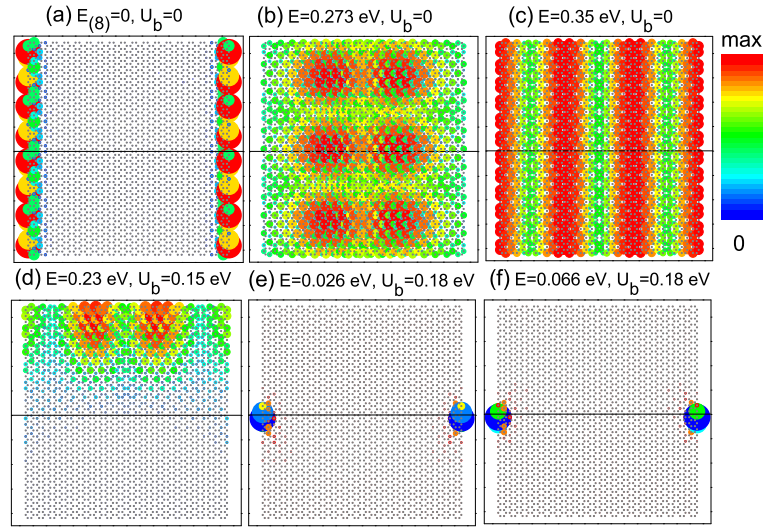


Figure 5.5: Probability densities corresponding to the points indicated by (a-f) in Fig. 5.4. In panel (a) $E_{(8)} = 0$ indicates the eighth degenerate zero energy. The black horizontal line indicates the position of the p-n junction.

an interesting behavior: the probability densities show a significant localization at the intersection of the p-n interface and the zigzag edges. That can be explained as resulting from the hybridization of the zigzag edge states on each side of the p-n junction. This remarkable state appears only when the p-n junction crosses a zigzag edge. Note that the wavefunction of this state consists of both electron and hole components.

5.4 snake states: influence of a perpendicular magnetic field

5.4.1 p-n junction

In the presence of an external magnetic field (see left panel in Fig. 5.6 for $\Phi_c/\Phi_0 = 0.1$) the energy spectrum shows anti-crossings for the energies below the gate voltage amplitude ($E < |U_b|$) which is due to the overlap between the quantum Hall (QH) edge states and the localized states at the p-n interface (i.e. snake states). Because of the smallness of the dot a large magnetic field (i.e. $B = 800$ T for $\Phi_c/\Phi_0 = 0.1$) is required in order to have a significant influence on the energy levels. Nevertheless, as the influence of the magnetic field scales with the magnetic flux through the dot area, similar results will be obtained

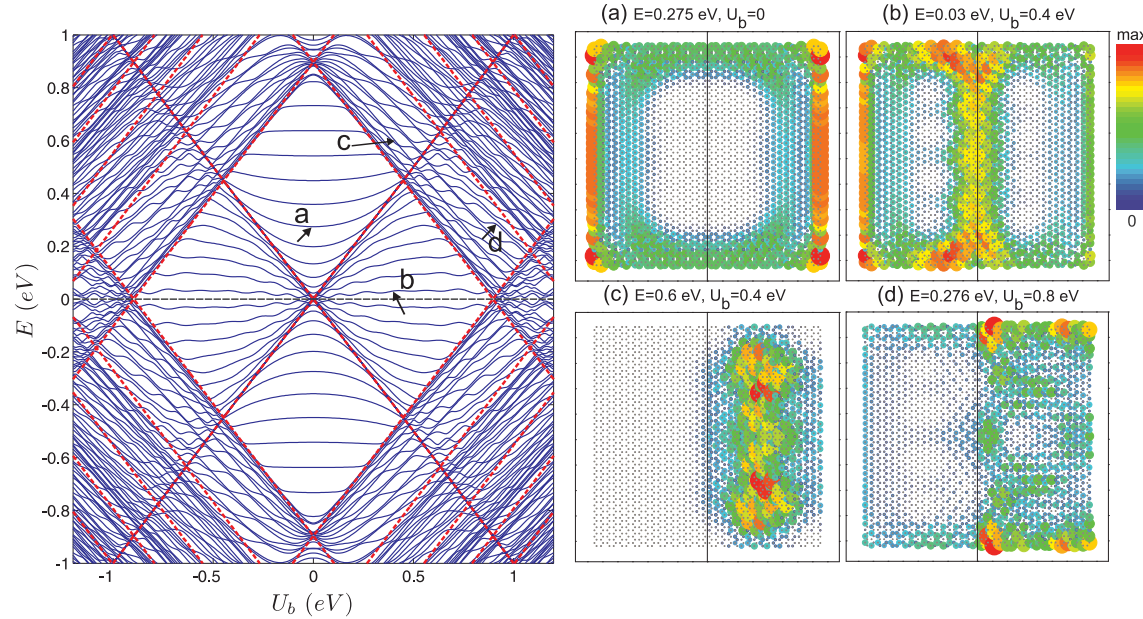


Figure 5.6: Left panel: The same as Fig. 5.2 but with non-zero magnetic flux $\Phi_c/\Phi_0 = 0.1$. The red dashed lines are the LLs of an infinite graphene sheet which are shifted up (down) by $U_b(-U_b)$. Right panels: Probability densities corresponding to the points indicated by (a-d) in the left panel. The black vertical line indicates the position of the p-n junction.

for lower magnetic fields if a larger graphene dot is considered. Notice that the number of degenerate levels with $E = \pm U_b$ ($E = 0$) in the presence (absence) of a p-n junction does not change with magnetic field. The red dashed lines in Fig. 5.6 indicate the Landau levels (LLs) of an infinite graphene sheet that are shifted up(down) in the presence of an external potential $U_b(-U_b)$. The LLs are given by

$$E_n = \text{sgn}(n) \frac{3at}{2l_B} \sqrt{2|n|} \pm U_b \quad (5.5)$$

where $l_B = \sqrt{\hbar/eB}$ is the magnetic length and n is an integer [79]. Left panels in Fig. 5.6 show the probability density corresponding to the states indicated by the arrows in the right panel. Panel (a) shows the confinement due to the QH edge states and zigzag edge states for $U_b = 0$. In the presence of a p-n junction and for $E < U_b$, states can arise due to the overlap of the QH edge states and the snake states (see panel (b)) or due to the overlap with confined states at the p (or n) regions (see panel (d)). For $E > U_b$ the carriers form LLs in the p (or n) potential regions (see panel (c)).

The different types of states become more apparent in Fig. 5.7 where we show the

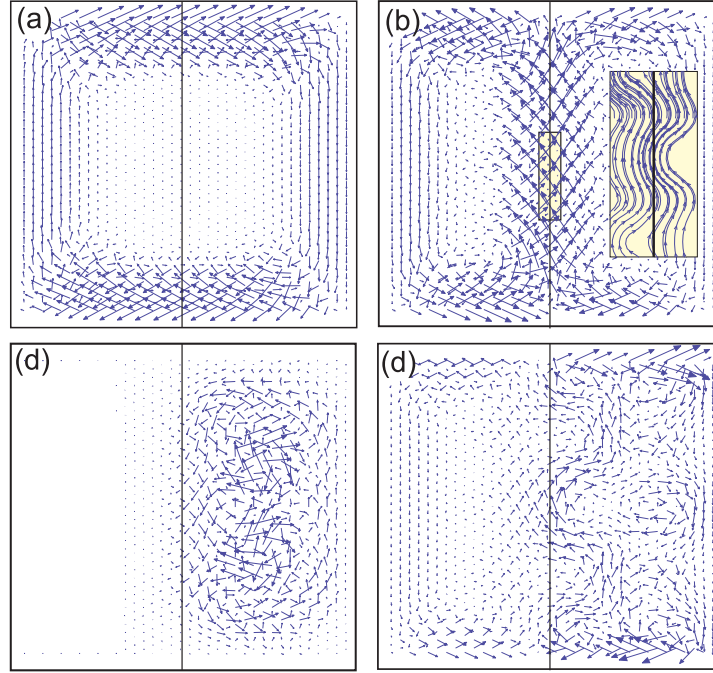


Figure 5.7: Current density profile corresponding to the states indicated by (a-d) in Fig. 5.6. The black line indicates the position of the p-n junction. The inset in (b) shows a streamline plot of the enlargement region.

current density profile corresponding to the states shown in the left panels of Fig. 5.6. The current density vectors are obtained using

$$\mathbf{j}_{l \rightarrow m} = \frac{i}{\hbar} [\langle \psi_l | t_{lm} | \psi_m \rangle - \langle \psi_m | t_{lm}^* | \psi_l \rangle] \quad (5.6)$$

where $\mathbf{j}_{l \rightarrow m}$ is the current flowing out of site l into site m . For clarity we show only the current corresponding to the A sublattice. Figures 5.7(b,d) clearly demonstrate the presence of snake states at the p-n junction where we have clockwise and counterclockwise circling currents, respectively, in the n and p regions. The current profile also reflects the direction of the bonds between the carbon atoms and therefore the arrows around the p-n junction sometimes point away from the interface. The streamline plot in the inset of Fig. 5.7(b) shows the current flow of the snake states more clearly. The vector plot in Fig. 5.7(a) indicates the cyclotron orbit of a quantum Hall edge state, while Fig. 5.7(c) shows the current profile of a LL state that is only very weakly influenced by the p-n junction and the edge of the quantum dot.

The energy levels as function of U_b are shown in Fig. 5.8, in the presence of an external

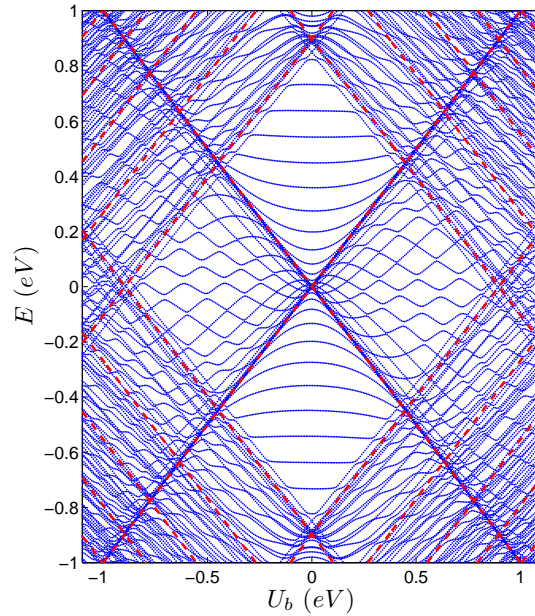


Figure 5.8: The same as Fig. 5.4 but in the presence of magnetic flux $\Phi_c/\Phi_0 = 0.1$. The red dashed lines are the LLs of an infinite graphene sheet which are shifted up (down) by $U_b = 0.25$ eV ($-U_b$).

magnetic flux $\Phi_c/\Phi_0 = 0.1$ for the dot with p-n junction along the armchair edges (see the inset of Fig. 5.4). The red dashed lines are the LLs of a graphene sheet (see Eq. (5.5)). As in Fig. 5.6(a) the energy spectrum exhibits different regimes of states; *i*) The regime of QH edge states where $U_b \leq |E| \leq E_1^{LL}$ and E_1^{LL} is the first LL obtained from Eq. (5.5). *ii*) The $|E| \leq U_b$ and $|E| \leq E_1^{LL}$ regime where there exist snake states. *iii*) The regime of LLs form for $|E| \geq E_{i \geq 1}^{LL}$. Notice that for $U_b > 0$ ($U_b < 0$) the LLs form at p (n) region. *iv*) The last regime that can be seen in Fig. 5.8 (and Fig. 5.6(a)) is due to the overlap of the edge states and LLs that occurs when $E_{i \geq 1}^{LL} \leq |E| \leq U_b$.

Figure 5.9(a) displays the energy levels of the system illustrated in the inset of Fig. 5.2 as function of magnetic flux threading one carbon hexagon Φ_c for $U_b = 0.25$ eV and the same size as Fig. 5.2. Notice that the zeroth Landau level in the absence of a gated voltage is now shifted up(down) by $+U_b(-U_b)$. The green dashed curves are LLs of an infinite graphene sheet (given by Eq. (5.5)). The magnetic levels in the GQD, i.e. the so called Fock Darwin levels, approach the LLs [58, 102] which are shifted by $\pm U_b$. Some of the energy levels approach asymptotically the $E = \pm U_b$ levels. Due to the overlap between the

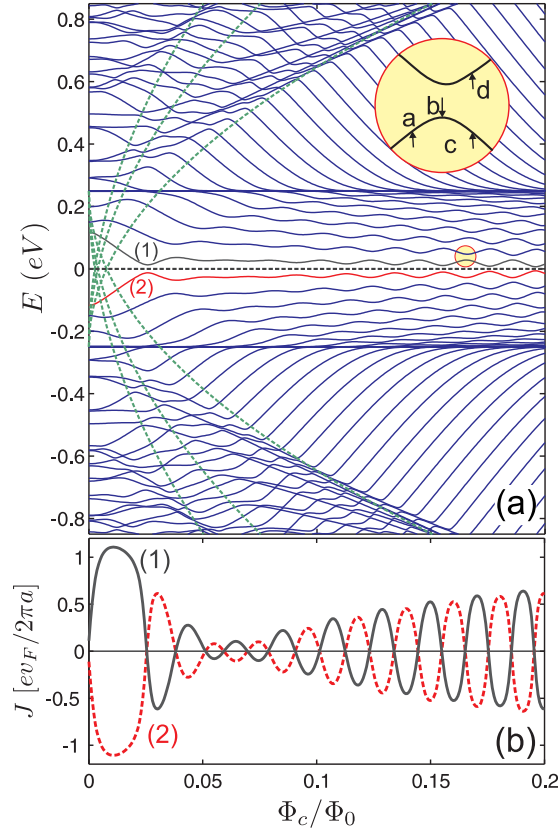


Figure 5.9: (a) Energy levels of a rectangular GQD subjected to a p-n junction parallel to the zigzag edges (see the inset of Fig. 5.2) as function of magnetic flux threading one carbon hexagon Φ_c for $U_b = 0.25$ eV. The green dashed curves are the Landau levels of an infinite graphene sheet which are shifted up (down) by U_b ($-U_b$). (b) Persistent current corresponding to the first electron state (gray solid curve, labeled by (1)) and the first hole state (red dashed curve, labeled by (2)) as function of external magnetic flux Φ_c .

QH edge states and the snake states at the p-n junction, anti-crossings appear in the energy spectrum. An anti-crossing point around $\Phi_c/\Phi_0 = 0.16$ is enlarged in Fig. 5.9(a). In Fig. 5.9(b) the persistent current corresponding to the first electron (solid curve) and the first hole (dashed curve) states is shown as function of magnetic flux. The persistent current J is calculated by taking the derivative of the corresponding energy levels with respect to the flux as $J(\Phi_c) = -\partial E/\partial\Phi_c$. Due to the anti-crossings in the energy spectrum, the persistent current exhibits an oscillatory behavior with respect to the magnetic flux. The current oscillation due to the snake states was recently investigated theoretically for a

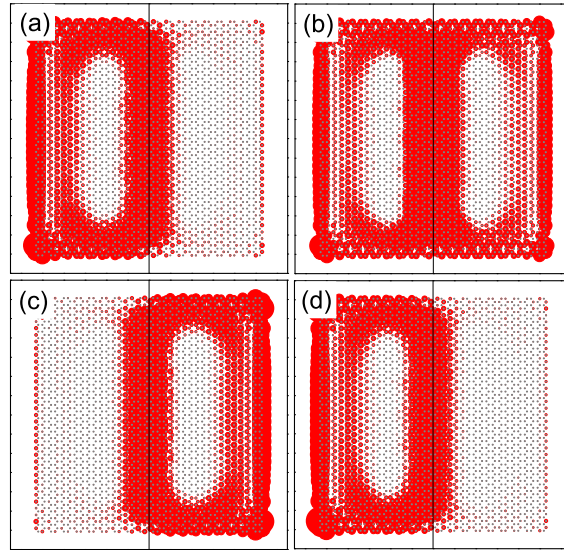


Figure 5.10: Probability densities corresponding to the points indicated by (a-d) in the enlarged circle in Fig. 5.9(a). The black line indicates the position of the p-n junction.

six-terminal graphene nano-ribbon with a p-n junction [103]. Notice that in the presence of the p-n junction the electron QH edge states that are shifted down with $-U_b$ overlap with the hole QH edge states that are shifted up with U_b (they have an opposite circling orbit direction than the electronic QH edge states). This hybridize the states in the region $|E| \leq U_b$ and leads to the current oscillations. Thus, as the magnetic field is adiabatically increased, at each cycle of oscillation the electron becomes predominantly confined either on the p or the n sides of the quantum dot, with the current circulating either clockwise or counterclockwise.

Figure 5.10 shows the electron probability densities corresponding to the points indicated by (a-d) in the enlarged region of Fig. 5.9(a). The results indicate that at the anti-crossing (panel (b)) the carriers are confined by the zigzag edge atoms and the p-n interface which characterizes the overlap between the edge and snake states. The points corresponding to the energy states that increase with respect to the magnetic flux around the anti-crossing (a,d) are due to states that are confined at the p-n junction and the zigzag edges in the n-type region (i.e. left side) while panel (c) displays an electron density that is confined at the right side of the p-n interface.

The energy spectrum of the system depicted in the inset of Fig. 5.4 is shown in Fig. 5.11(a) as function of magnetic flux for $U_b = 0.25$ eV. Since the number of p-type and n-type atoms are unequal here (where their minimum difference is N_a) the energy levels are not symmetric around $E = 0$. Now the confinement due to the p-n junction is along

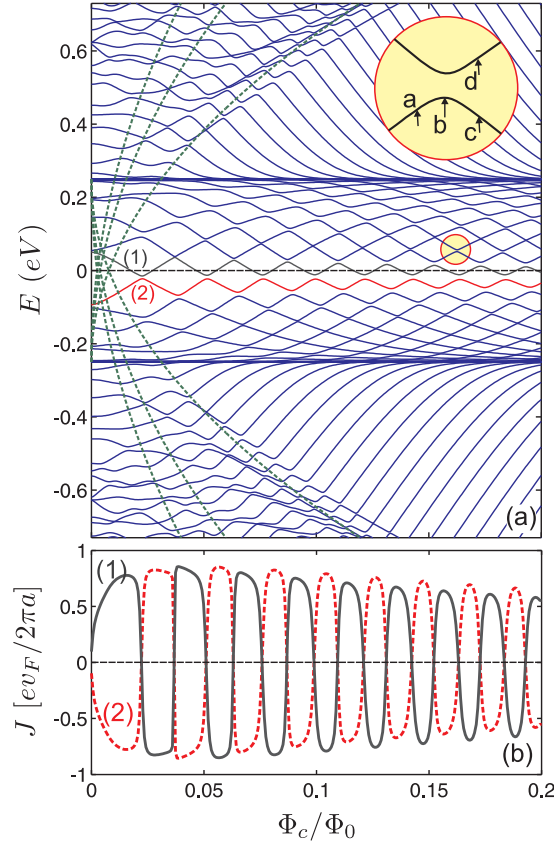


Figure 5.11: The same as Fig. 5.9 but for a rectangular GQD subjected to a p-n junction parallel to the armchair edges (see the inset of Fig. 5.4).

the x-direction which is perpendicular to the edge states (caused by the zigzag edges). Therefore the energy spectrum exhibits a distinct behavior from that of the p-n junction along the zigzag edges.

The persistent current J corresponding to the energy levels indicated by (1) and (2) is shown in Fig. 5.11(b) as function of magnetic flux. Notice that the oscillatory behavior is different from the results in Fig. 5.9(b), now the current amplitude decreases smoothly with increasing magnetic flux. The position of the oscillations are plotted in Fig. 5.12 and compared with the flux through the quantum dot (magenta stars) and half of the quantum dot (blue triangles). Notice that the numerical results are between these two curves. It implies that the effective surface area encircled by the current is larger than the size of the n or p region. The best fit is obtained for flux through a surface area $S = L_x L_y / 1.37$ (see gray squares).

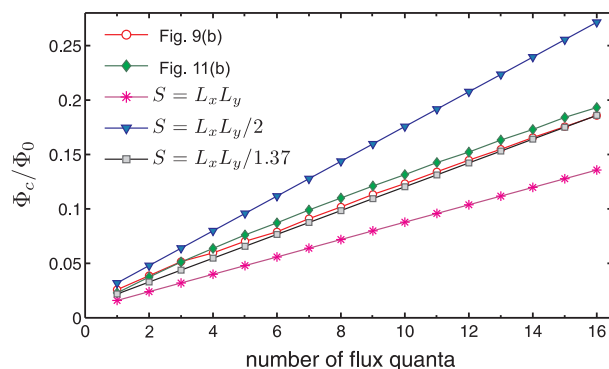


Figure 5.12: The position of the oscillations in Figs. 5.9(b) and 5.11(b) and the number of flux quanta through the surface area $S = L_x L_y$, $L_x L_y/2$, $S = L_x L_y/1.37$ as function of magnetic flux.

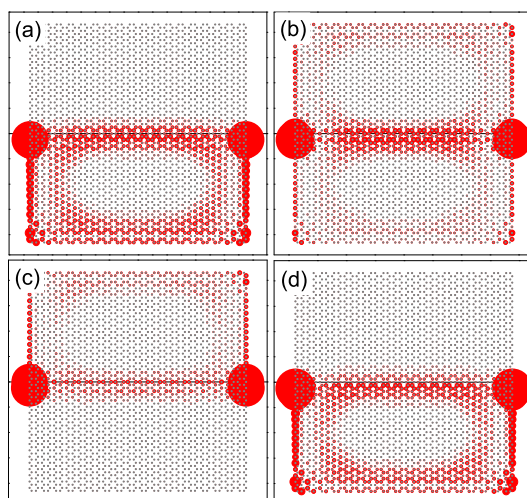


Figure 5.13: Probability densities corresponding to the points indicated by (a-d) in the enlarged circle of Fig. 5.11(a). The black line indicates the position of the p-n junction.

Figure 5.13 shows the electron probability densities corresponding to the indicated points by (a,b,c,d) in the enlarged circle (an anti-crossing point around $\Phi_c/\Phi_0 = 0.16$) of Fig. 5.11(a). We have a superposition of three types of states: *i*) zigzag edge states (modified by the p-n junction), *ii*) QH edge states where we have skipping orbits, and *iii*) snake states. As seen in the figure the overlap of the confined electron in the snake state and the edge states leads to a large density at the intersection of the p-n junction and the zigzag edge. In contrast with the results in Fig. 5.10 only half of the zigzag edge

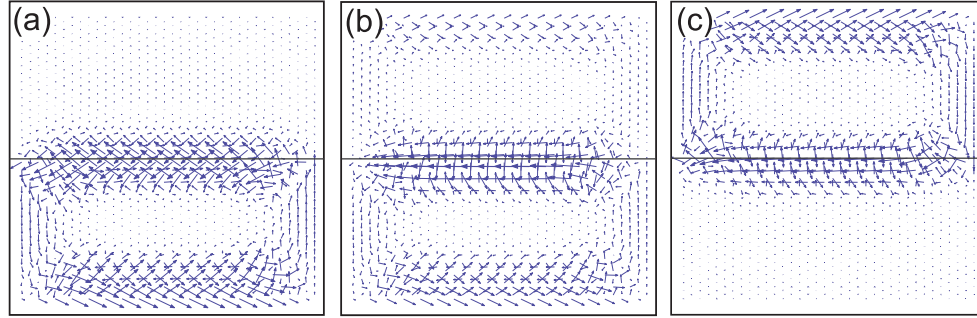


Figure 5.14: Current density profile corresponding to the points indicated by (a-c) in the enlarged circle of Fig. 5.11(a). The black horizontal line indicates the position of the p-n junction.

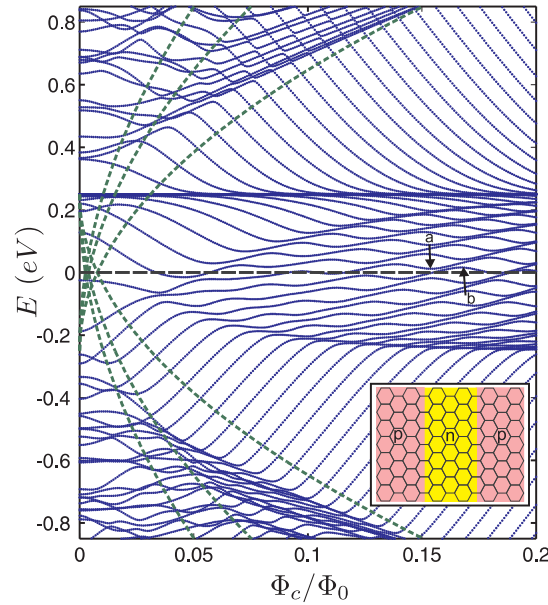


Figure 5.15: Energy levels of a rectangular GQD with a p-n-p junction parallel to the zigzag edges as function of external magnetic flux for $L_x = 7.52$ nm, $L_y = 8.6$ nm and $U_b = 0.25$ eV. The lower inset illustrates the system. The number of p-type atoms is twice larger than the number of n-type atoms. The green dashed curves are the LLs of an infinite graphene sheet which are shifted up (down) by U_b ($-U_b$).

atoms are contributing to the confinement due to the edge states. Therefore the carriers are weakly affected by the edge states in comparison with the confinement due to the snake states. At the anti-crossing (panel (b)) the electrons are mostly confined at the p-n

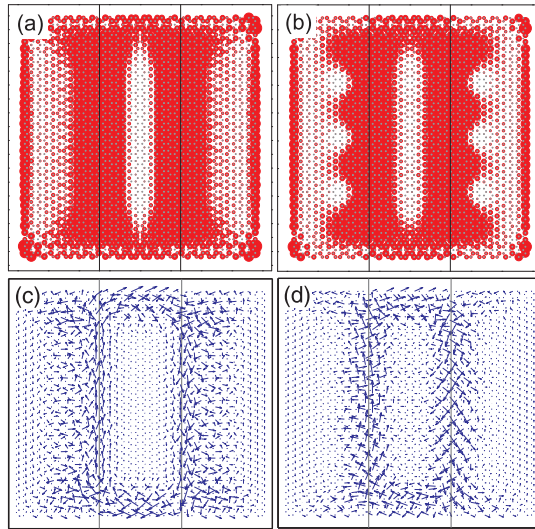


Figure 5.16: (a,b) Electronic probability density and (c,d) the corresponding current profile for the points indicated by (a,b) in Fig. 5.15. The black vertical lines indicate the position of the p-n junctions.

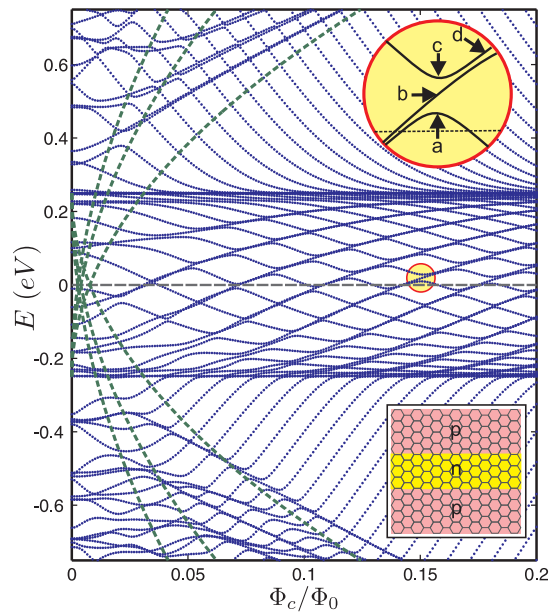


Figure 5.17: The same as Fig. 5.15 but for a rectangular GQD with a p-n-p junction along the armchair edges. The system is illustrated in the lower inset.

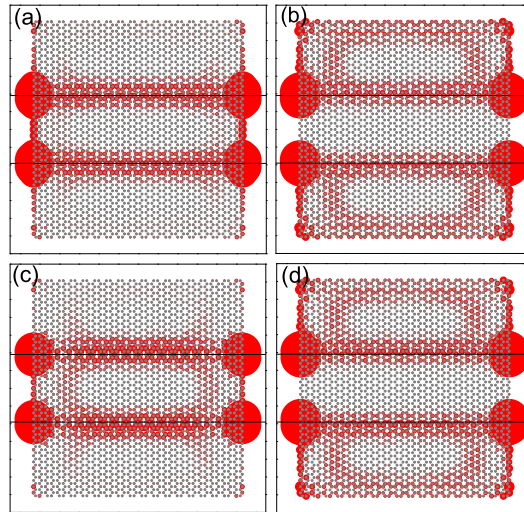


Figure 5.18: Probability densities corresponding to the points indicated by (a-d) in the enlarged region of Fig. 5.17. The black horizontal line indicates the position of the p-n junctions.

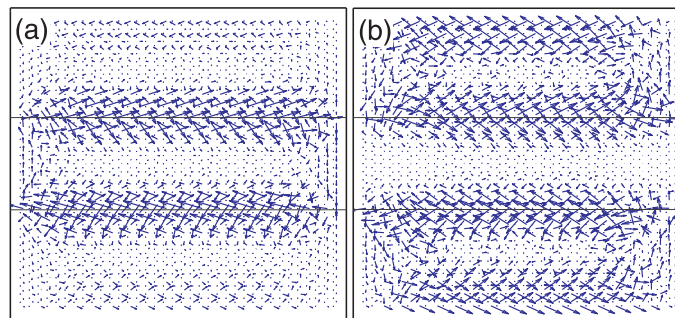


Figure 5.19: Current density profile corresponding to the states shown in Fig. 5.18(a) and Fig. 5.18(b). The black horizontal lines indicate the position of the p-n junctions.

interface and along both lengths of the zigzag edges. The corresponding current profiles of Figs. 5.13(a-c) are shown in Fig. 5.14. Figure 5.14(b) displays the snake states at the p-n interface and Figs. 5.14(a,c) show the cyclotron orbit of QH edge states respectively at the p and n regions.

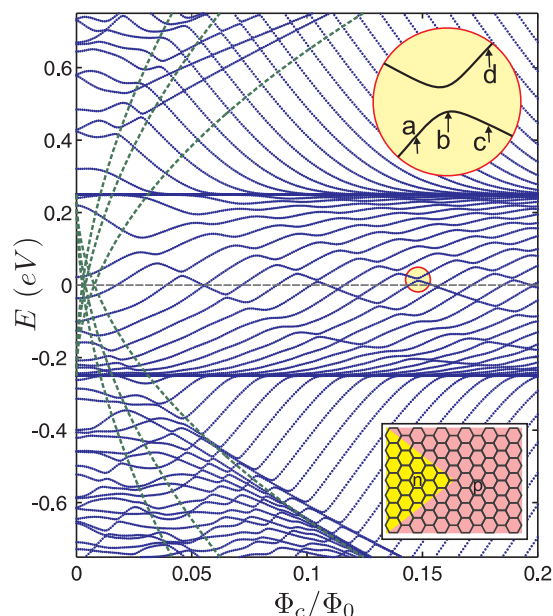


Figure 5.20: Energy levels of a rectangular GQD with triangular shaped p-n junction as function of external magnetic flux for $L_x = 7.52$ nm, $L_y = 8.6$ nm and $U_b = 0.25$ eV. The lower inset shows schematically the system. The green dashed curves are the LLs of an infinite graphene sheet which are shifted up (down) by U_b ($-U_b$).

5.4.2 p-n-p junction

Next we investigate the effect of multiple p-n junctions where I limit ourselves to the example of two junctions. We want to know if there can be any interplay between the two junctions, i.e. can states be confined over the two junctions? Will there be circling currents between the two junctions?

A schematic illustration of a p-n-p junction in a rectangular GQD is depicted in the inset of Fig. 5.15 where the p-n-p junction is parallel to the zigzag edges (along y-direction). The corresponding spectrum in Fig. 5.15 exhibits quite distinct anti-crossings from the case of the p-n junction. On the other hand in low magnetic fields the hole edge states (i.e. those hole states that decrease with respect to the magnetic flux) do not approach the zeroth Landau Level ($E = -U_b$) which is a consequence of the fact that the n-type region does not have a boundary with the zigzag edges. Notice that the hole edge states approach $E = -U_b$ in high magnetic fields. The electron probability densities for the points indicated by (a) and (b) are shown in Figs. 5.16(a,b) where the densities are spread out mostly along the p-n and n-p interfaces. The corresponding current profiles are plotted in Figs. 5.16(c,d). The results show opposite circling currents between the two junctions.

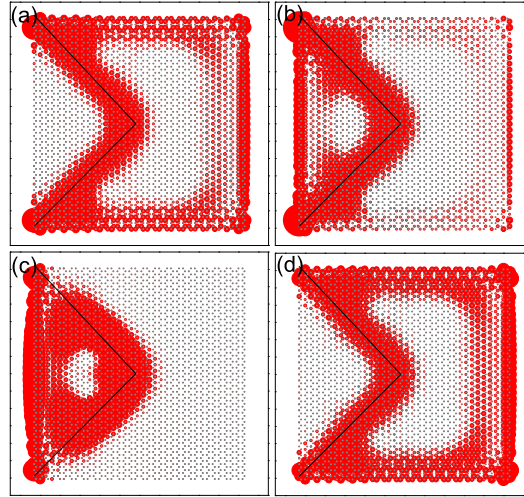


Figure 5.21: Probability densities corresponding to the points indicated by (a-d) in the enlarged region of Fig. 5.20. The black line indicates the position of the p-n junction.

Figure 5.17 displays the energy spectrum for the p-n-p junction parallel to the armchair edges in a rectangular GQD. The system is depicted in the lower inset. Here the n-type region is connected to the zigzag lengths which leads to the convergence of the hole states to $E = -U_b$ even in low magnetic fields. As in previous cases for the region $|E| < U_b$ anti-crossings appear in the spectrum. The electron probability densities corresponding to the points around the enlarged anti-crossing (yellow circle) are shown in Fig. 5.18. Note that the anti-crossing behaviour is qualitative distinct from the previous cases shown in Figs. 5.9(a) and 5.11(a). The results indicate that at the anti-crossing (a,c) the electrons are confined due to the edge states corresponding to the zigzag atoms in the n-type region and the snake states. The points (b,d), correspond to states that are confined at the zigzag edges in the p-type regions and near the p-n-p junction. In all points, the probability density shows strong peaks at the intersection of the p-n junction with the zigzag edges. The density profiles have a dumb-bell shape. As before, these localized states are associated with the hybridization of the zigzag edge states on each side of the junction. However, for non-zero magnetic field these states overlap with snake states that propagate along the potential interfaces. The current profile corresponding to Figs. 5.18(a,b) is shown in Fig. 5.19(a,b) where the counter-circling cyclotron orbits in the n and p regions demonstrate the existence of snake states at the p-n interfaces.

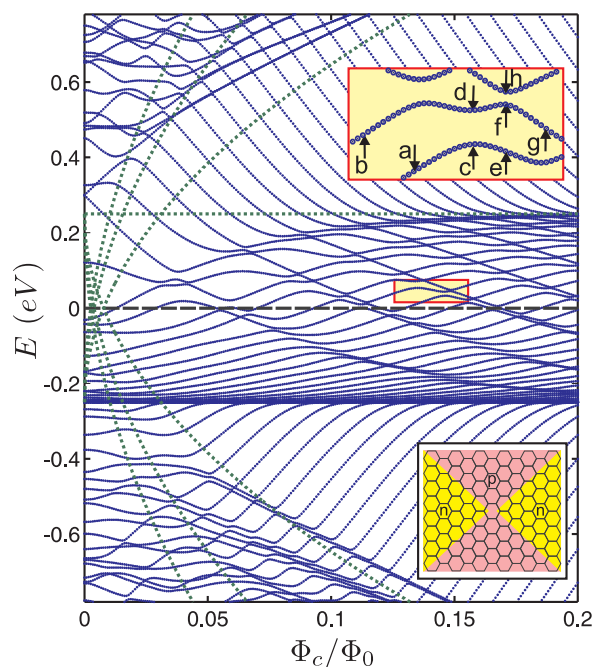


Figure 5.22: Energy levels of a rectangular GQD with triangular shaped p-n-p junction as function of external magnetic flux for $L_x = 7.52$ nm, $L_y = 8.6$ nm and $U_b = 0.25$ eV. The lower inset shows the system schematically where the yellow regions with zigzag edges indicate the n-type atoms. The green dashed curves are the LLs which are shifted up (down) by U_b ($-U_b$).

5.5 Triangular shaped p-n junction

Next we consider the effect of the gate shape on the energy spectrum. Figure 5.20 displays the energy levels for the system illustrated in the lower inset where a triangle-shaped gate voltage is assumed for the n-type region. Notice that here we choose an arbitrary direction for the p-n junction and it not necessarily matched with the zigzag or armchair direction. Since the number of n-type and p-type atoms are unequal the electron and hole energy levels are not symmetric, i.e. $|E_e(\Phi_c)| \neq |E_h(\Phi_c)|$. Due to the confinement by both edge states (at zigzag edges) and snake states (at p-n interface) anti-crossings appear in the energy spectrum. An enlargement around one of the anti-crossings at $\Phi_c/\Phi_0 = 0.15$ is shown in the inset of Fig. 5.11(b). The electron probability densities for the points around this anti-crossing (a,b,c,d) are shown in Fig. 5.21. Panel (b) shows the electron density at the anti-crossing where the electrons confined along the zigzag edge and the p-n interface. For the points whose energy increases with flux (a,d) the electron is localized along the

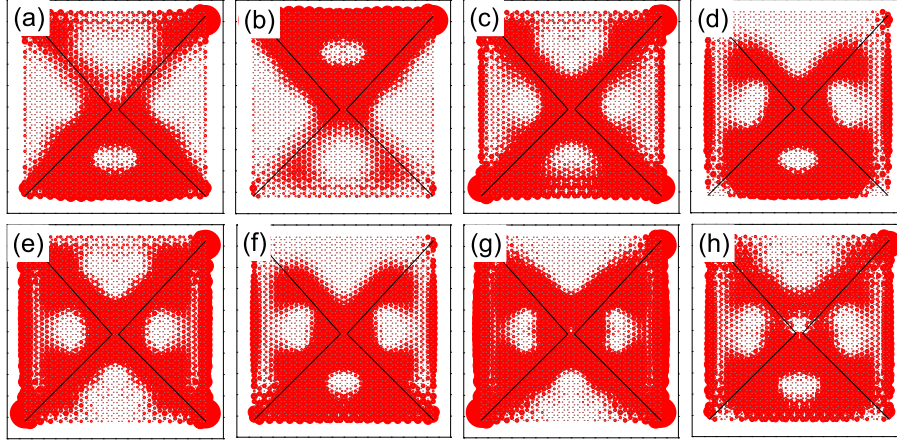


Figure 5.23: Probability densities corresponding to the points indicated by (a-h) in the enlarged region of Fig. 5.22. The black lines indicate the position of p-n junctions.

zigzag edge in the p region and snake states are present along the p-n junction while the probability density for the point (c) is mostly along the zigzag edges in the n region and the p-n interface.

As a last example we investigate the energy spectrum of a system consisting of a point contact in a rectangular GQD (see the lower inset of Fig. 5.22). Recently, transport measurements of such a system were carried out, and it was found that, due to a chaotic mixing of edge channels an unexpected half-integer plateau was observed in the QH resistivity [93]. The spectrum exhibits double anti-crossings between the energy levels in the region $|E| < U_b$. The enlarged rectangle in Fig. 5.22 shows one of these double-anticrossings around $\Phi_c/\Phi_0 \approx 0.15$.

Figure 5.23 shows the electron probability densities corresponding to the points indicated by a-h in Fig. 5.22. The energy levels between $-U_b$ and U_b that increase with magnetic flux are due to the overlap of the QH edge states in the p region and the snake states at the p-n interface (Figs. 5.23(a,b)). Those energy levels that decrease with magnetic flux correspond to the zigzag edge states which hybridize with the QH edge states in the n -region and to snake states (Figs. 5.23(e,g)). Notice that at the anti-crossings, see Figs. 5.23(c,d,f,h), we have an overlap of three types of localized states (i.e. QH edge states, snake states and zigzag edge states).

5.6 Conclusion

We presented numerical results for the energy spectrum and magnetic field dependence of the eigenstates of graphene-based quantum dots, on which p-n junctions create electron and hole-doped regions. The presence of the magnetic field, together with the coupling between electron and hole states across the potential barrier due to Klein tunneling leads to the appearance of localized states at the potential interface, known as snake states. These states, which have previously been investigated for pn junctions on infinite graphene sheets, can influence the transport properties of graphene-based nanodevices. We have obtained results that show that for the case of quantum dots the low energy dynamics of the system is dominated by hybridized states that arise due to the overlap between quantum Hall edge states and the snake states at the p-n junction, with the snake states allowing the superposition of quantum Hall edge states at the p and n sides of the dot. These states are characterized by an energy spectrum that displays an oscillating behavior as function of the electrostatic potential and magnetic field at the vicinity of the Fermi energy. Furthermore, the energy spectrum was shown to depend on the specific alignment of the potential interfaces with regard to the graphene lattice, as well as on the geometry of the gates. The dots were assumed to be defect-free and to have perfect zigzag or armchair edges. Future work will concentrate on the effect of edge disorder, impurities and defects on the electronic properties of these structures. Another aspect that will be considered is the influence of the particular choice of the potential profile and shape of the graphene flake on the confined states.

CHAPTER 6

Electron-electron interaction in bilayer graphene quantum dots

A parabolic quantum dot (QD) as realized by biasing nanostructured gates on bilayer graphene is investigated in the presence of electron-electron interaction. Our studies of the energy spectrum and phase diagram in the presence of magnetic field reveal important and unexpected results. For example, in contrast to semiconductor QDs, we find at low magnetic fields a novel valley transition, rather than the usual singlet-triplet transition and for sufficient large quantum dots the singlet transition can be even absent. This difference is traced back to the valley degree of freedom in bilayer graphene.

6.1 Introduction

The electronic properties of quantum dots (QDs) in graphene, a single layer of carbon atoms arranged in a honeycomb lattice [18, 104, 105], have been studied extensively due to their unique properties and their potential for applications in graphene devices [64, 106–108]. Because of Klein tunneling, electrostatic confinement is not possible in graphene. Therefore one has to rely on direct etching of the graphene sheet. In such systems, controlling the shape and edges of the dot is one of the main challenging issues but the exact configuration of the edges is unknown [23]. The latter is important because the energy spectrum depends strongly on the type of edges [69, 79, 109, 110].

The results of this chapter were submitted to Phys. Rev. Lett. (March 2013).

Two coupled layers of graphene, bilayer graphene (BLG), is known to have quite distinct properties from a single layer. In a pristine BLG the spectrum is gapless and approximately parabolic at low energies around the two nonequivalent points in the Brillouin zone (K and K'). In the presence of a perpendicular electric field, however, the spectrum displays a gap, which can be tuned by varying the bias [40]. It was proposed that nanostructuring the gate allows for a tailoring of the energy gap in BLG which can be used to electrostatically confine QDs [29, 30]. In such confined systems the electrons are displaced from the edge of the sample and consequently edge disorder and the specific type of edges are no longer a problem. Such gate defined QDs in BLG were recently fabricated by two different groups [31, 32]. In these studies, the confinement of electrons and Coulomb blockade effects were demonstrated experimentally.

In this chapter we investigate the energy levels of a parabolic QD in BLG in the presence of Coulomb interaction. Here we solve the two-electron problem as the most simple case to investigate electron-electron correlations. Similar studies have been reported for semiconducting QDs over the last two decades [111, 112] and also recently for graphene QDs [113] and graphene rings [114]. At present no similar study is available for BLG quantum dots. An important issue for graphene structures is the extra valley-index degree of freedom where the electrons have the possibility to be in the same valley or in different valleys [115, 116]. Here we will show that the competition between the valley-index and the spin of the electrons leads to new behaviors for the ground state energy of BLG quantum dots.

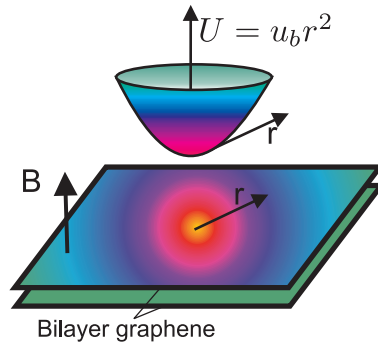


Figure 6.1: Schematic illustration of the potential profile for a parabolic bilayer graphene quantum dot.

6.2 Continuum model

The first step in calculating the interacting electron states is to find the eigenstates of a single electron in a parabolic QD. We employ a two-band continuum model to describe the BLG sheet. In this model, the system is described by a 2×2 Hamiltonian which in the valley-isotropic form is given by [39]

$$H = -\frac{1}{\gamma} \begin{bmatrix} 0 & (\pi^\dagger)^2 \\ (\pi)^2 & 0 \end{bmatrix} + \tau \begin{bmatrix} U(r) & 0 \\ 0 & -U(r) \end{bmatrix} \quad (6.1)$$

where $\pi = -i\hbar v_F e^{i\theta} [\partial_r + i\partial_\theta/r - (eB/2\hbar)r]$ is the momentum operator in polar coordinates and in the presence of an external magnetic field B , $\gamma \approx 400$ meV is the inter-layer coupling term, and $v_F = 10^6$ m/s is the Fermi velocity. The valley index parameter τ distinguishes the energy levels corresponding to the K ($\tau = +1$) and the K' ($\tau = -1$) valleys. The electrostatic potential $U(r)$ is applied to the upper layer while $-U(r)$ corresponds to the lower layer. In order to define a QD profile we consider a parabolic dependence of the potential $U(r) = U_b(r/R)^2$ where the potential U_b and radius R define the size of the dot [Fig. 6.1]. The eigenstates of the Hamiltonian (6.1) are the two-component spinors

$$\psi(r, \theta) = [e^{i(m-1)\theta} \phi_a(r), e^{i(m+1)\theta} \phi_b(r)]^T \quad (6.2)$$

where $\phi_{a,b}$ are the envelope functions associated with the probability amplitudes in uncoupled sublattices A and B in the respective layers of the BLG sheet and m is the angular momentum. The wave function $\psi(r, \theta)$ is an eigenstate of the operator

$$J_z = L_z + [(\hbar/2)\tau_z + (\hbar/2)\sigma_z] \quad (6.3)$$

with eigenvalue m . It should be emphasized that the orbital angular momentum L_z does not commute with the Hamiltonian and is no longer quantized. This is different from two-dimensional semiconductor QDs, where $[H, L_z] = 0$. The matrix τ_z (one of the Pauli matrices) is a layer index operator, which is associated with the behavior of the system under inversion, whereas $\sigma_z \equiv \tau_z$ denotes the pseudo-spin components in each layer.

Solving the Schrödinger equation, $H\Psi = E\Psi$, the radial dependence of the spinor components is described by

$$\left[\frac{d^2}{dr^2} + \frac{\alpha(r) + 2}{r} \frac{d}{dr} + \eta(r) + 4\beta \right] \phi_b = [\epsilon - \tau u(r)] \phi_a, \quad (6.4a)$$

$$\left[\frac{d^2}{dr^2} - \frac{\alpha(r)}{r} \frac{d}{dr} + \eta(r) \right] \phi_a = [\epsilon + \tau u(r)] \phi_b. \quad (6.4b)$$

with $\alpha(r) = (2m - 1 + 2\beta r^2)$ and $\eta(r) = [(m^2 - 1)/r^2] + 2(m - 1)\beta + \beta^2 r^2$, where $\beta = (eB/2\hbar)R^2$ is a dimensionless parameter. The energy and the potential are written

in dimensionless units as $\epsilon = E/E_0$, $u(r) = U(r)/E_0$ with $E_0 = (\hbar v_F/R)^2/\gamma$ being the energy unit and R is the unit of length. The coupled equations (6.4) are solved numerically using the finite element method [72].

6.3 Single-particle energy levels

Figure 6.2(a) shows the lowest single-electron energy levels as a function of the magnetic field for a quantum dot with $U_b = 150$ meV and $R = 50$ nm. The energy levels are labeled by their angular momentum and their valley index (m, τ) . Let us first focus on the $B = 0$ case. Notice that the single particle ground state is not for $m = 0$, in contrast to semiconductors QDs, but in contrast has momentum $m = -1$ at K and $m = 1$ at K' in agreement with Ref. [29]. The lowest $m = 0$ is the second excited state for the dot.

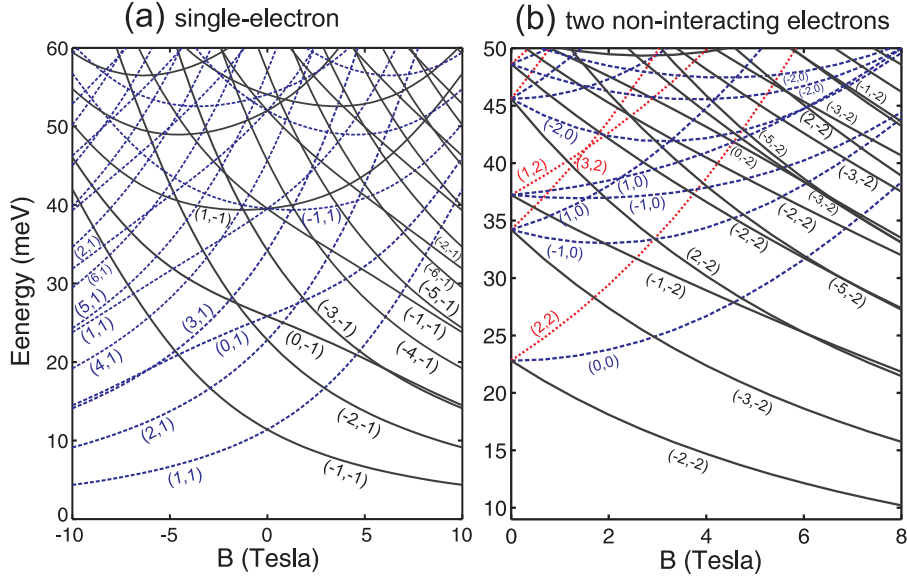


Figure 6.2: Energy spectrum of a parabolic QD in bilayer graphene with $R = 50$ nm and $U_b = 150$ meV as a function of the magnetic field for (a) single-particle and (b) two noninteracting electrons. The energy levels in (a) are labeled by the angular momentum and the valley index (m, τ) . The levels in (b) are labeled by (M, T) , where $M = m_1 + m_2$, is the total angular momentum and $T = \tau_1 + \tau_2$ is the total valley index. Levels having the same valley index are plotted using the same type of curve.

For large magnetic fields the eigenstates become strongly localized at the origin of the dot, where the potential difference between the layers vanishes $\Delta U \rightarrow 0$. Therefore,

the spectrum approaches the Landau levels of an unbiased BLG, and consequently some of the energy levels approach $E = 0$ as the field increases. Notice that this is quite distinct from semiconductor QDs where the zeroth LL is absent and thus the energy of the confined states, i.e. the Fock-Darwin states increase for large magnetic fields. Breaking of the electron-hole symmetry due to the presence of both electric and magnetic fields lifts the valley-degeneracy in non-zero magnetic fields. The energy spectrum also dis-

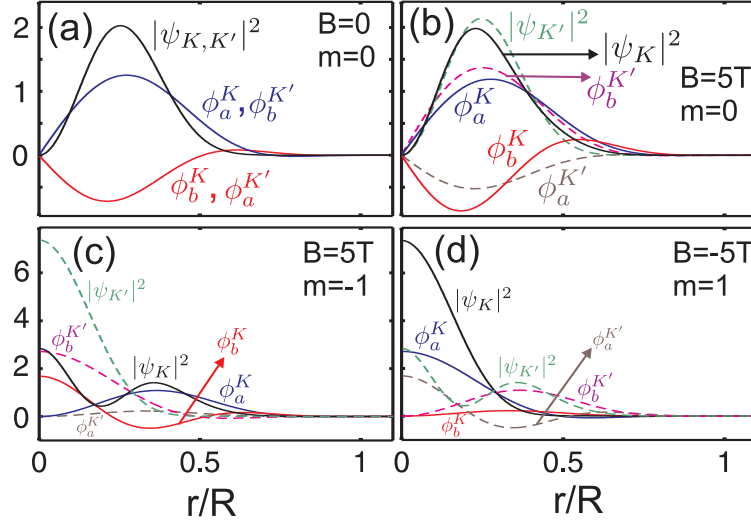


Figure 6.3: Electron probability density and the corresponding wavespinors for the lowest energy levels of K and K' valleys with (a) $m = 0, B = 0$, (b) $m = 0, B = 5\text{T}$, (c) $m = -1, B = 5\text{T}$ and (d) $m = 1, B = -5\text{T}$.

plays $E_K(m, B) = E_{K'}(-m, -B)$ symmetry, which is another feature that is unique to BLG quantum dots. This symmetry is a consequence of the fact that the QD is produced by a gate that introduces an electric field and thus a preferential direction. Inserting the $(m, \beta) \rightarrow (-m, -\beta)$ and $\tau \rightarrow -\tau$ transformations into equations (6.4a) and (6.4b) and using $E_\tau(m, B) = E_{-\tau}(-m, -B)$, one can find the relations $\phi_a^K(m, B) = \phi_b^{K'}(-m, -B)$ and $\phi_b^K(m, B) = \phi_a^{K'}(-m, -B)$ between the wave function components of the K and K' valleys (see Fig. 6.3).

6.4 Two-electron energy spectrum

The Hamiltonian describing the two-electron system is given by

$$H_T = H(\mathbf{r}_1) + H(\mathbf{r}_2) + V_c(\mathbf{r}_1 - \mathbf{r}_2) \quad (6.5)$$

where $V_c = e^2/(4\pi\kappa|\mathbf{r}_1 - \mathbf{r}_2|)$ is the Coulomb interaction between the two electrons with κ being the dielectric constant of BLG. In our calculations we set $\kappa = 3.9$ which is the dielectric constant of gated BLG on top of a hexagonal boron nitride (h-BN) substrate [11]. We carry out an exact diagonalization to obtain the eigenvalues and eigenstates of the two-electron system given by the Hamiltonian (6.5). The two-electron wave function with fixed total angular momentum m and total valley index τ is constructed as linear combinations of the one-electron wave functions:

$$\Psi(\mathbf{r}_1, \mathbf{r}_2) = \sum_i^{N_s} \sum_j^{N_s} C_{ij} \Phi_i(\mathbf{r}_1) \otimes \Phi_j(\mathbf{r}_2) \quad (6.6)$$

where Φ is a four-component wave function which is $\Phi^K = [\psi^K, 0, 0]^T$ corresponding to the K valley and $\Phi^{K'} = [0, 0, \psi^{K'}]^T$ corresponding to the K' valley. The two-component wave function $\psi^{K(K')}$ is given by Eq. (6.2). The subscripts $i \equiv (m_i, \tau_i)$ and $j \equiv (m_j, \tau_j)$ correspond to the one-electron energy levels where the summations in Eq. (6.6) are such that the relations $M = m_i + m_j$ and $T = \tau_i + \tau_j$ are satisfied. N_s is the number of single-particle states which we take into account in constructing the interacting wave function. In our numerical calculations we set $N_s = 30$ in which was found to give sufficient accurate energy levels. In order to avoid the singularity due to the $1/|\mathbf{r}_1 - \mathbf{r}_2|$ term in the matrix elements we use, an alternative expression in terms of the Legendre function of the second kind of half-integer degree [117].

In Figure 6.4, we show two representative spectra for two interacting electrons in a BLG quantum dot: where (a) the radius is $R = 20$ nm, and (b) $R = 50$ nm, and in both cases $U_b = 150$ meV. To clearly see the effect of the electron correlations, the spectra for two non-interacting electrons in a dot with $R = 50$ nm is also shown in Fig. 6.2(b) for comparison. The levels are labeled by (M, T, S) with $M = m_1 + m_2$ the total angular momentum, $T = \tau_1 + \tau_2$ the total valley index, and S the total spin. Energy levels with the same T are drawn using the same type of curve. The two electrons can form a non-degenerate singlet state ($S = 0$) and a threefold degenerate triplet state ($S = 1$). In case the quantum number S is omitted, the singlet and triplet states are degenerate.

While the $(-2, -2)$, $(0, 0)$ and $(2, 2)$ states are degenerate in zero field for non-interacting electrons (see Fig. 6.2(b)), we find that turning on the interaction makes $(0, 0)$ the ground state for small magnetic field values. As $T = 0$ for this state, each electron is located at a different valley. Therefore there is no exchange interaction possible and the singlet and triplet states are degenerate². The main contribution to the $(-2, -2, 0)$ and $(2, 2, 0)$ states comes from the state in which both electrons occupy the same single particle state

²When $T = 0$, the exchange integral is $E_{exc} = \langle \Phi_i^K \otimes \Phi_j^{K'} | V | \Phi_j^{K'} \otimes \Phi_i^K \rangle = 0$.

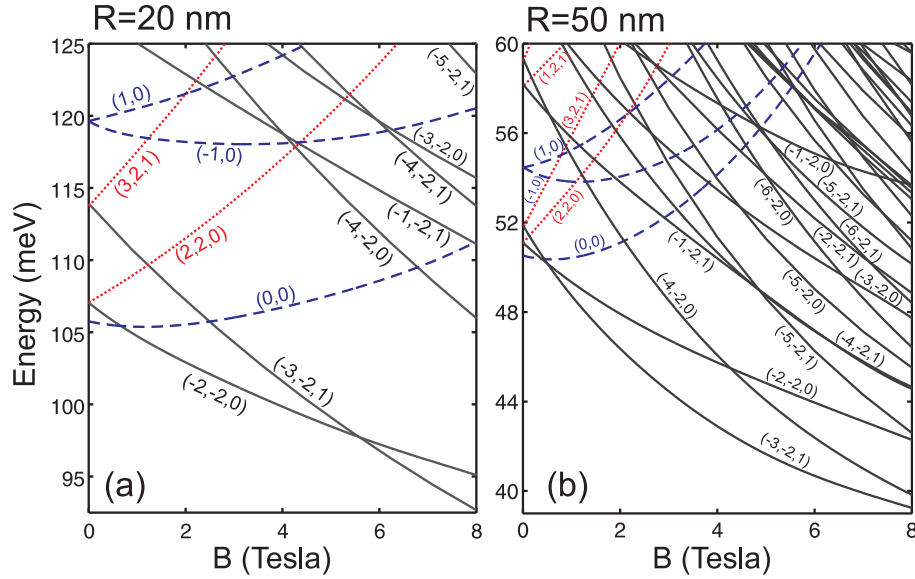


Figure 6.4: The same as Fig. 6.2(b) but in the presence of Coulomb interaction and for (a) $R = 20$ nm and (b) $R = 50$ nm. Here the levels are labeled by (M, T, S) where S is the total spin. The curves with the same total valley index T are shown with the same type of curve.

in the same valley. This indicates that these states are singlets. Thus, although the exchange interaction is absent in all three states, i.e. $(-2, -2, 0)$, $(2, 2, 0)$, and $(0, 0)$, the $(0, 0)$ state has lower energy. To explain this we show in Fig. 6.5 the energy of these states using one, two, and three lowest energy basis functions in expression (6.6). When only the lowest energy single-particle basis function is included, the $(0, 0)$ and $(-2, -2, 0)$ (and thus also $(2, 2, 0)$) states have the same energy expectation value. The next relevant single-particle state for the $(0, 0)$ state is $\Psi_{(0,0)} = \psi_{m=-2, \tau=-1}^{\uparrow} \otimes \psi_{m=2, \tau=1}^{\downarrow}$ while it is $\Psi_{(-2,-2,0)} = \psi_{m=-2, \tau=1}^{\uparrow} \otimes \psi_{m=0, \tau=1}^{\downarrow}$ for the $(-2, -2, 0)$ state. The single-particle energy of the basis-function $\Psi_{(-2,-2,0)}$ is higher in energy than the single-particle energy corresponding to the basis-function $\Psi_{(0,0)}$ (see also Fig. 6.5(b) where we shown the single-particle energies for the lowest angular momentum label m). As a consequence, the state $(0, 0)$ becomes the ground state.

When the magnetic field increases, the $(-2, -2, 0)$ state becomes the ground state because the lowest single-particle states decrease in energy in the K valley, and increase in energy in the K' valley. This results in a transition from a four-fold degenerate state into a singlet state for $B = 0.5$ T in a dot with $R = 20$ nm in Fig. 6.4(a). A further increase of the magnetic field strength will lead to a new transition to another ground state. We

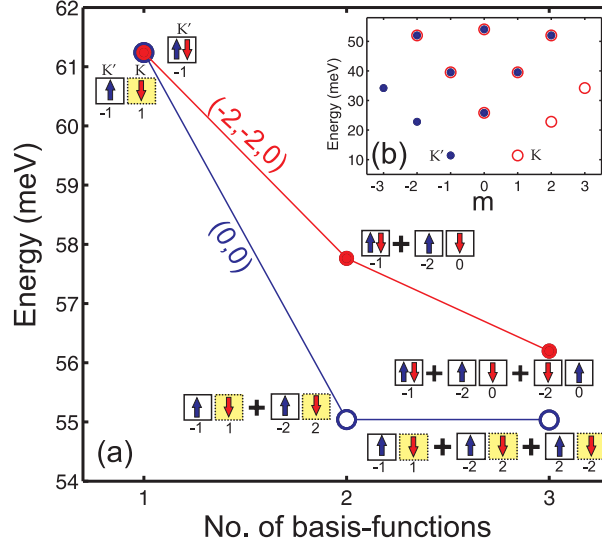


Figure 6.5: (a) Comparison of the energy states $(M, T) \equiv (0, 0)$ and $(M, T, S) \equiv (-2, -2, 0)$ shown in Fig. 6.4(b) at $B = 0$ obtained with 1, 2, and 3 basis functions included in expression (6.6). The insets schematically represent the included basis-functions based on the single particle states. (b) The single-particle energy values as function of angular momentum label m .

find that for the dot with $R = 20$ nm the ground state switches to the state $(-3, -2, 1)$ for $B = 5$ T. While this state is much higher in energy in case of non-interacting particles (see Fig. 6.2(b)), it is stabilized due to the exchange interaction. With an increase of the magnetic field, the splitting between the single-particle energy levels decreases. For a certain magnetic field value, this splitting can be overcome by the exchange energy gain, which results in a transition to the triplet $(-3, -2, 1)$ state.

When increasing the size of the QD it decreases the splitting between the single particle levels. This causes a transition from the singlet $(-2, -2, 0)$ to the triplet $(-3, -2, 1)$ state at smaller magnetic field values with increasing radius of the dot. Therefore for larger R the singlet state is never the ground state, and with increasing B there is immediately a transition from state $(0, 0)$ (the ground state for $B = 0$) to the triplet state $(-3, 2, 1)$, as seen in Fig. 6.4(b). While in conventional semiconductor QDs, the ground state shows a series of singlet to triplet transitions as a function of the magnetic field strength [111, 112], a more complex phase diagram is found for BLG QDs. In Fig. 6.6, we plot this phase diagram for the same U_b and dielectric constant as in Fig. 6.4. As discussed above, for low fields a *valley transition* rather than a singlet-transition occurs.

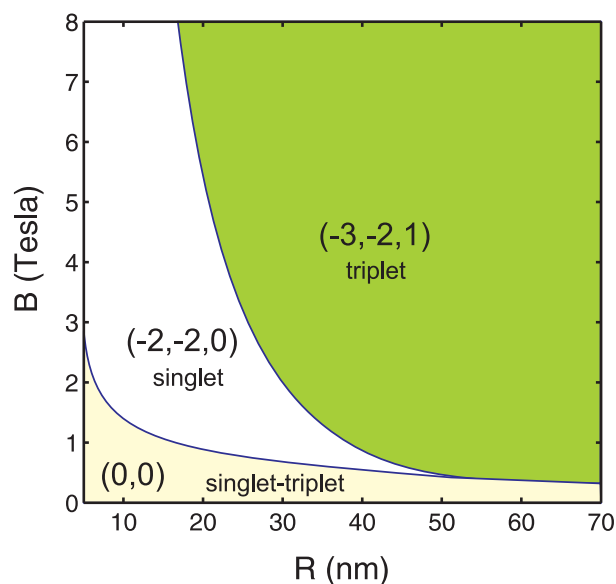


Figure 6.6: The $R - B$ phase diagram of the ground state energy of a two-electron BLG quantum dot.

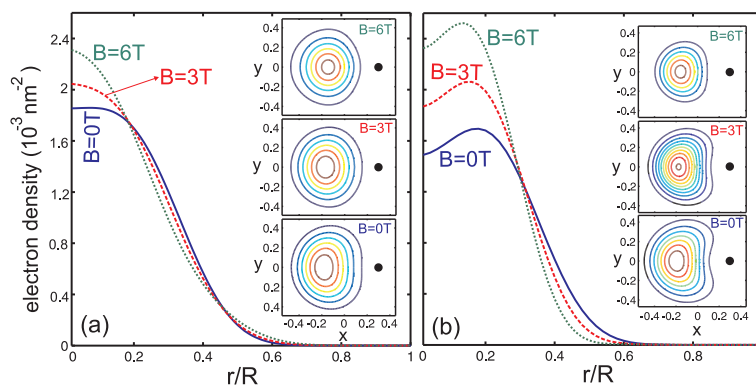


Figure 6.7: The radial electron density for the two-electron QD of Fig. 6.4(b) for (a) $(M, T) \equiv (0, 0)$ and (b) $(M, T, S) \equiv (-3, -2, 1)$ and for three values of the magnetic field $B = 0, 3, 6$ T. The corresponding pair-correlation functions are shown in the insets. The black dot indicates the position of the first electron.

The electron density, which is defined by $\rho(r) = \sum_{i=1}^2 \langle \delta(\mathbf{r} - \mathbf{r}_i) \rangle$ is shown in Figs. 6.7(a) and 6.7(b), respectively for $(0, 0)$ and $(-3, -2, 1)$ states, for a two-electron BLG quantum

dot with $R = 50$ nm, $U_b = 150$ meV, and for three values of the external magnetic field $B = 0, 3, 6$ T. Comparing the density profiles in (a) and (b), the maximum of the density is shifted towards higher radial distance in the state $(-3, -2, 1)$. This is a consequence of the fact that the electrons in the many-particle $(-3, -2, 1)$ state occupy single-particle states with higher angular momentum. When the magnetic field increases the electrons are pulled closer towards the center of the dot. In the inset of Figs. 6.7(a) and 6.7(b) we have shown the corresponding pair-correlation function in which one of the electrons is pinned at $\mathbf{r} = (0.3R, 0)$.

In cyclotron resonance experiments, transitions are induced between the ground state and excited states. In the present case of BLG quantum dot the selection rule on the change of total angular momentum $\Delta m = \pm 1$ is still fulfilled. This is apparent when we calculate

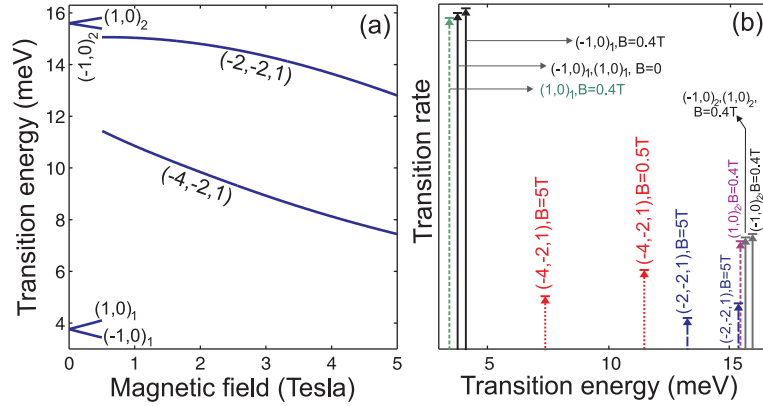


Figure 6.8: (a) The cyclotron transition energies for the dot of Fig. 6.4(b) containing two electrons. The transition energies are labeled by their final states: (M, T, S) for the triplet (or singlet) states and $(M, T)_n$ for the degenerate single-triplet states where n is the principal quantum number. (b) The transition rates corresponding to the transition energies shown in (a) for different values of magnetic field.

the transition energies and the corresponding transition rates for dipole transitions using the relation $|\langle \Psi_i | \sum_{j=1}^2 \frac{1}{2} r_j e^{\pm i \phi_j} | \Psi_f \rangle|^2$. This relation also implies conservation of the total spin, i.e. $\Delta S = 0$. The valley degree of freedom dictates new transition rules for BLG quantum dots, i.e. $\Delta T = 0$ or $\Delta T = \pm 2$. This means that those transitions are possible in which at least one electron remains in the same valley during the transition. The lowest possible transition energies for a two-electron quantum dot are shown in Fig. 6.8(a). The corresponding transition rates are given in Fig. 6.8(b). The possible transitions are labeled by the final states (M, T, S) . When the transition from the degenerate singlet-triplet state

$(0, 0)$ to the single state $(-3, -2, 1)$ occurs, i.e. at $B \approx 0.5$ T in Fig. 6.8(a), the transition energies show a rather high jump that reduces the transition rate (compare the black-solid lines with the red-dotted and the blue-dashed lines in Fig. 6.8(b)).

6.5 Conclusion

In summary, we obtained the energy levels, the electron density, the pair correlation function and the cyclotron transition energies of electrostatically confined QDs containing one or two electrons in BLG. Such QDs can be realized experimentally in BLG using nanostructured gate potentials. In contrast to conventional semiconductor QDs, we found at low magnetic fields that the ground state energy of the two-electron spectrum exhibits a valley transition, rather than a spin singlet-triplet transition. This is due to the extra valley degree of freedom in BLG in which the electrons can be in different valleys and thus allowing for four-degenerate single-triplet states as ground state. Our prediction can be verified by spin susceptibility measurements in low magnetic fields.

CHAPTER 7

Gate defined quantum rings in bilayer graphene

A new system where electron and hole states are electrostatically confined into a quantum ring in bilayer graphene is proposed. These structure can be created by tuning the gap of the graphene bilayer using nanostructured gates or by position-dependent doping. The energy levels have a magnetic field (B_0) dependence that is strikingly distinct from that of usual semiconductor quantum rings. In particular, the eigenvalues are not invariant under a $B_0 \rightarrow -B_0$ transformation and, for a fixed total angular momentum index m , their field dependence is not parabolic, but displays two minima separated by a saddle point. The spectra also display several anti-crossings, which arise due to the overlap of gate-confined and magnetically-confined states.

7.1 Introduction

The striking mechanical and electronic properties of graphene have quickly been recognized and promise to lead to new applications in electronic devices and sensors. These devices will benefit from the large charge carrier mobilities and long mean free paths at room temperature [4, 118–121]. As discussed before, BLG is a very different material from graphene. The spectrum of BLG displays a gap, which can be tuned by varying the bias, or by chemical doping of the surface [39]. This tunable gap can then be exploited

The results of this chapter were published as
M. Zarenia, J. M. Pereira Jr., F. M. Peeters, and G. A. Farias, Nano Lett. **9**, 4088, (2009).

for the development of BG devices. In particular, the possibility of tailoring the energy gap in BG has raised the prospect of the creation of electrostatically defined quantum dots in BLG, discussed in the previous chapter, by means of a position-dependent doping or through the deposition of split gates on the BG surface [29, 30].

A very important class of quantum devices consists of quantum rings. They have generated a lot of interest, especially because they allow the observation of quantum phase coherence effects on carrier transport such as in the Aharonov-Bohm [122] and Aharonov-Casher [123] effects. Semiconductor-based quantum rings have been obtained experimentally [124] and, recently, quantum rings have also been studied on single-layer graphene, both theoretically and experimentally [125, 126]. The latter have been produced by lithographic techniques in which graphene nanoribbons or ring structures are carved from an otherwise defect-free surface. Such techniques permit the production of devices in the nanometer scale, but have the disadvantage of creating defects at the edges of the graphene-based structure which may reduce the overall performance, as well as raise difficulties for the theoretical analysis of the device. These quantum rings can also be described as graphene flakes with a central antidot, and recent calculations indicate that localized edge states strongly affect the spectrum of these systems [63]. Additionally, the specific type of edge (zigzag versus armchair) was also found to influence their electronic properties.

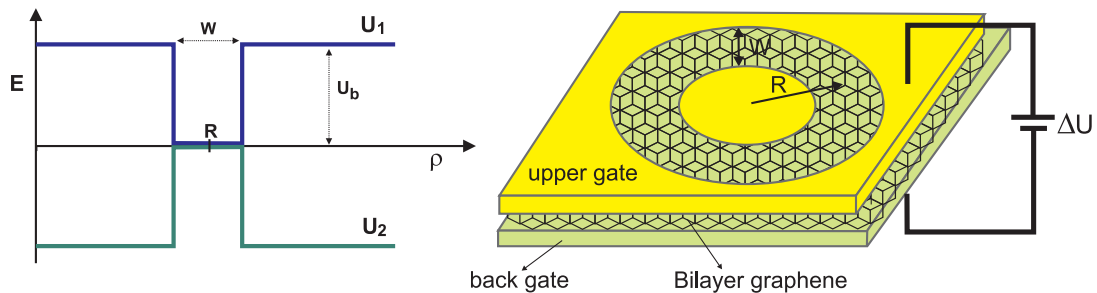


Figure 7.1: Schematic depiction of the potential profile for a bilayer graphene quantum ring

To overcome the problems related to the edges of the quantum ring (i.e. defects and type of edge) we propose here an electrostatically defined graphene-based quantum ring (GQR). In contrast with previous quantum rings on graphene, the system considered here is created by the use of electrostatic potentials which induce a position-dependent gap, such that the low-energy electron and hole states can be confined in a ring-shaped region of an otherwise ideal BLG sheet (see Fig. 7.1). This type of confinement is not possible in single layer graphene, due to the Klein tunneling effect [21]. In our proposed structure, the

effects of the edges are not relevant since the BG sheet is assumed to be defect-free and the confinement is brought about by an external bias. Moreover, in contrast with structures carved by means of lithography, the ring parameters can be tuned by external fields, a feature that can be particularly relevant for the design of field configurable devices. Here, we obtain the energy levels and wavefunctions of the confined electron and hole states by numerically solving the Dirac equation and results are presented as function of ring radius, width and magnetic field.

7.2 Continuum model

Bilayer graphene consists of two weakly, van der Waals coupled honeycomb sheets of covalent-bond carbon atoms in a Bernal AB stacking. The system can be described in terms of four sublattices, labelled A, B (upper layer) and C, D (lower layer). The A and C sites are coupled via a nearest-neighbor interlayer hopping term t . We employ the continuum model based on the Dirac equation, which is known to provide a realistic description of graphene-based structures with dimensions that are much larger than the lattice parameter and that has been shown to give good agreement with experimental data.

The Hamiltonian, in the vicinity of the \mathbf{K} valley and in the presence of a magnetic field normal to the plane of the layer is given by [39]

$$\mathcal{H} = \begin{pmatrix} U_0 + \frac{\Delta U}{2} & \pi & \gamma & 0 \\ \pi^\dagger & U_0 + \frac{\Delta U}{2} & 0 & 0 \\ \gamma & 0 & U_0 - \frac{\Delta U}{2} & \pi^\dagger \\ 0 & 0 & \pi & U_0 - \frac{\Delta U}{2} \end{pmatrix}, \quad (7.1)$$

where $\gamma \approx 400$ meV is the interlayer coupling term, $\pi = v_F[(p_x + eA_x) + i(p_y + eA_y)]$, \mathbf{p} is the momentum operator, \mathbf{A} is the vector potential, $\Delta U = U_1 - U_2$ is the difference of potential between the layers, $U_0 = (U_1 + U_2)/2$ is the average potential, and $v_F \approx 1 \times 10^6$ m/s is the Fermi velocity. In this work we neglect the small Zeeman splitting of the energy levels.

The eigenstates of Eq. (7.1) are four-component spinors $\Psi = [\psi_A, \psi_B, \psi_C, \psi_D]^T$, where ψ_i ($j = A, B, C, D$) are the envelope functions associated with the probability amplitudes at the respective sublattice sites of the upper and lower graphene sheets. For a circular-symmetric, position-dependent potential such as the one described in Ref. [29,30], the spinor components are $\psi_A = \phi_A(\rho)e^{im\theta}$, $\psi_B = \phi_B(\rho)e^{i(m-1)\theta}$, $\psi_C = \phi_C(\rho)e^{im\theta}$, and

$\psi_D = \phi_D(\rho)e^{i(m+1)\theta}$, where m is the angular momentum label. Using the symmetric gauge $\mathbf{A} = (0, B_0\rho/2, 0)$, the radial dependence of the spinor components is described, in dimensionless units, by

$$\begin{aligned} \left[\frac{d}{dr'} + \frac{m}{r'} + \beta r' \right] \phi_A &= -(\alpha - \delta)\phi_B, \\ \left[\frac{d}{dr'} - \frac{(m-1)}{r'} - \beta r' \right] \phi_B &= (\alpha - \delta)\phi_A + \gamma' \phi_C, \\ \left[\frac{d}{dr'} + \frac{(m+1)}{r'} + \beta r' \right] \phi_D &= (\alpha + \delta)\phi_C + \gamma' \phi_A, \\ \left[\frac{d}{dr'} - \frac{m}{r'} - \beta r' \right] \phi_C &= -(\alpha + \delta)\phi_D, \end{aligned} \quad (7.2)$$

where $r' = \rho/R$, $\alpha = \epsilon - u_0$, $u_0 = (u_1 + u_2)/2$, and $\delta = \Delta u/2$, with $\Delta u = u_1 - u_2$. The energy, the potentials and the interlayer coupling strength are written in dimensionless units as $\epsilon = E/E_0$, $u_{1,2} = U_{1,2}/E_0$, $\gamma' = \gamma/E_0$ and $E_0 = \hbar v_F/R$, where ρ is the radial variable and R is the ring radius. The dimensionless parameter $\beta = (eB/2\hbar)R^2$, can be expressed as Φ/Φ_0 , where Φ is the magnetic flux threading the ring and $\Phi_0 = h/e$ is the quantum of magnetic flux.

Here we solve Eq. (7.2) by the finite elements method for the following profile (see Fig. 7.1) :

$$\delta = \begin{cases} 0 & 1 - \frac{w'}{2} \leq r' < 1 + \frac{w'}{2} \\ u_b & 0 < r' < 1 - \frac{w'}{2}, \quad 1 + \frac{w'}{2} \leq r' < \infty \end{cases} \quad (7.3)$$

where $w' = W/R$, with W being the width of the ring. This potential describes a bilayer graphene quantum ring (GQR) of radius R and width W , in which both electron and holes are confined by a tunable potential barrier U_b . As shown in Ref. [29], the wavefunctions given by Eq. (7.2) are eigenstates of the operator

$$J_z = L_z + \frac{\hbar}{2} \begin{pmatrix} -\mathbf{I} & 0 \\ 0 & \mathbf{I} \end{pmatrix} + \frac{\hbar}{2} \begin{pmatrix} \sigma_z & 0 \\ 0 & -\sigma_z \end{pmatrix} \quad (7.4)$$

with eigenvalue m , where \mathbf{I} is the 2×2 identity matrix, L_z is the angular momentum operator and σ_z is one of the Pauli matrices. The above equation can be rewritten as $J_z = L_z + \hbar\tau_z + \hbar S_z$, where the second term in the right hand side is a layer index operator, which is associated with the behavior of the system under inversion, whereas S_z carries the information on the pseudospin components in each layer. It should be emphasized that in this system, L_z does not commute with the Hamiltonian and is no longer quantized.

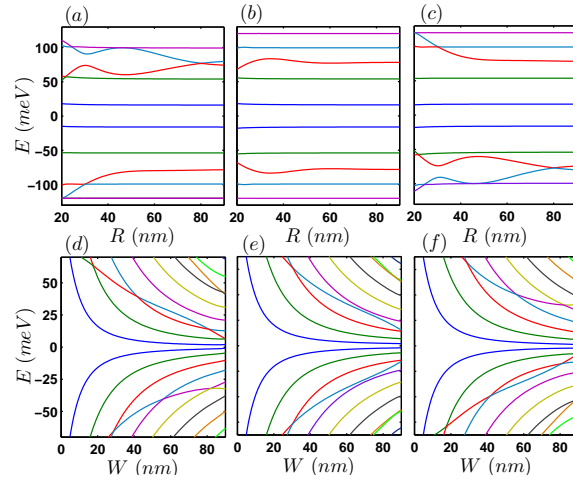


Figure 7.2: Lowest energy levels of a graphene bilayer quantum ring as function of ring radius R (Panels: a, b, c) and width of the ring W (d, e, f). Parameters given in the text.

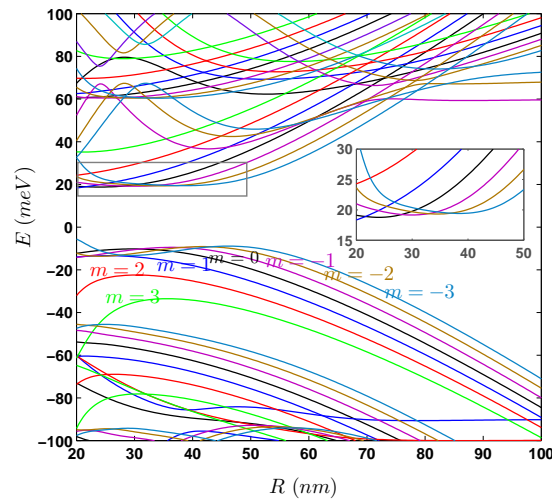


Figure 7.3: Energy levels of a bilayer graphene quantum ring as function of ring radius R . Parameters given in the text.

7.3 Numerical results

Figure 7.2 shows the lowest energy levels of a GQR as function of ring radius R (upper panel), and width W (lower panels), for $m = -1$ (a, d), $m = 0$ (b, e), and $m = 1$ (c, f), for $W = 20$ nm ($a-c$), $R = 50$ nm ($d-f$), $U_b = 150$ meV and $B = 0$. The results show a weak

dependence on the ring radius and an interesting electron-hole asymmetry, which is due to the breaking of the inversion symmetry by the external bias. However, the electron and hole energy levels are invariant under the transformation $E(m) \rightarrow -E(-m)$. In Fig. 7.3,

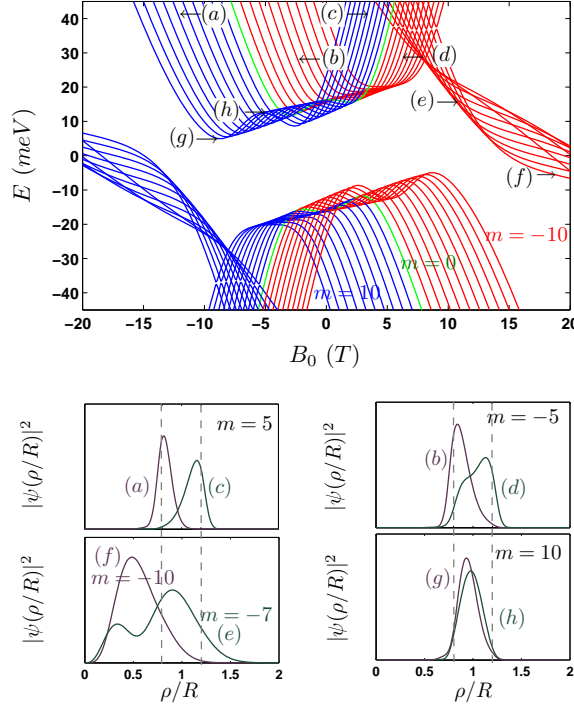


Figure 7.4: Electron and hole energy states of a graphene bilayer ring-shaped quantum dot as function of external magnetic field B_0 . Parameters given in the text.

the lowest energy levels of a QR are shown as function of ring radius in the presence of a non-zero magnetic field, $B_0 = 5$ T, for $-3 \leq m \leq 3$, $W = 20$ nm and $U_b = 150$ meV. In contrast with the zero field case, the results show a strong dependence on the ring radius, with the appearance of several crossings, as shown more clearly in the inset.

The energy levels of electrons and holes for the \mathbf{K} valley in a GQR are presented in Fig. 7.4 as function of external magnetic field B_0 , for $-10 \leq m \leq -1$ (red curves), $m = 0$ (green curves) and $1 \leq m \leq 10$ (blue curves) with $R = 50$ nm, $W = 20$ nm and $U_b = 150$ meV. In contrast with the results obtained from the Schrödinger equation, the spectra are not invariant under the transformation $B_0 \rightarrow -B_0$. Moreover, the individual branches display two local minima. The figures also show a set of branches with energies that decay as the field increases. These states correspond to Landau levels of the biased bilayer, for which the carrier confinement is mainly due to the magnetic field. By making

a small gap in the confinement region of the ring it can be evidenced that those branches are only weakly affected by a variation of the gap. We found that the electron and hole energies are related by $E_e(m, B_0) = -E_h(-m, -B_0)$. The spectrum for the \mathbf{K}' valley can be obtained by setting $B_0 \rightarrow -B_0$, which shows that, as in the case of the graphene bilayer quantum dot [29, 30], the valley degeneracy is lifted. The four lower panels show the probability density of the points on the spectrum which are labeled by (a), (b), ... in the upper panel. The vertical dashed lines indicate the edges of the ring. As seen, for the (e) and (f) points the probability density has peaks in the internal region of the ring structure ($\rho < R - W/2$), whereas for the remaining points the carriers are mainly confined inside the ring. The (e) and (f) states belong to energy states that in the limit $B_0 \rightarrow \infty$ approach the zero Landau level are shifted from $E = 0$ due to the presence of the ring potential.

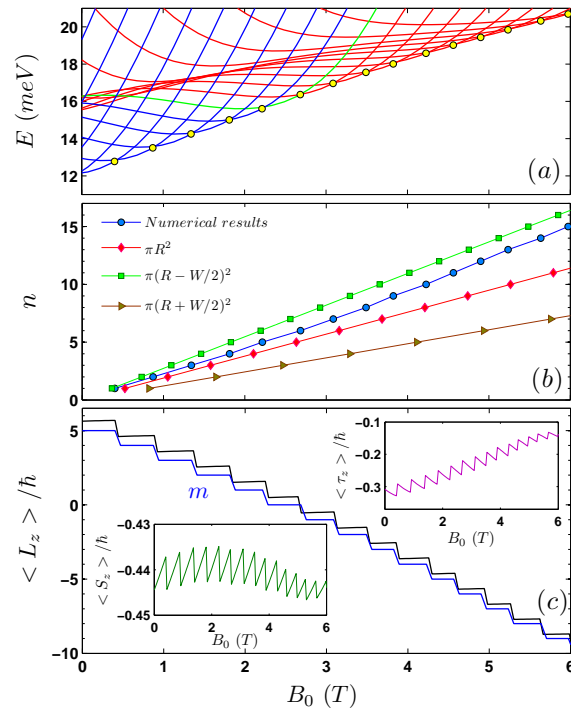


Figure 7.5: (a) Enlargement of the electron spectrum of Fig 7.4. (b) Number of transitions between the levels (circles) and AB oscillations for a ring with radius R and surface $S = \pi R^2$, $S = \pi(R \pm W/2)^2$. (c) Ground state expectation values of L_z/\hbar , τ_z/\hbar and S_z/\hbar as function of the magnetic field.

An enlargement of the region of the spectrum is shown in Fig. 7.5(a). The yellow dots correspond to the location of the transitions of the ground state between the levels

which is related to the number of AB oscillations $n = \Phi/\Phi_0$. Figure 7.5(b) shows the number of transitions between the levels (circles) and the AB oscillations for a zero-width ring with radius R and surface $S = \pi R^2, S = \pi(R \pm W/2)^2$. Notice that the numerical results obtained for the finite width ring follow closely the AB oscillations as expected for an ideal ring with radius equal to the one of the inner ring.

The ground state expectation values of the $L_z/\hbar, \tau_z/\hbar$ and S_z/\hbar operators are shown as function of the magnetic field in Fig. 7.5(c). The figure shows that the values of $\langle L_z \rangle / \hbar$ (black curve), $\langle \tau_z \rangle / \hbar$ (upper inset) and $\langle S_z \rangle / \hbar$ (lower inset) are not quantized, but, their sum, as in Eq. (7.4) (blue curve) is given by the m quantum number. Very different from the Schrödinger case we find that for $B_0 \approx 0$ the quantum number m and the average $\langle L_z \rangle$ are non-zero.

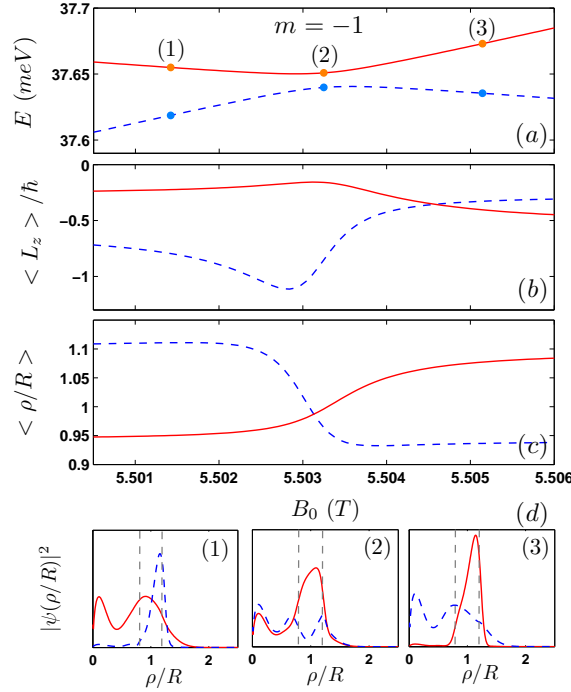


Figure 7.6: (a) Enlargement around an anti-crossing point in the energy spectrum. (b) Expectation value of angular momentum $\langle L_z \rangle / \hbar$ and (c) radial average position $\langle \rho/R \rangle$ around the anti-crossing point shown in (a). (d) Probability density for the points (1), (2) and (3) shown in (a).

The spectrum in Fig. 7.4 exhibits several anticrossings between different branches. An enlargement of one particular anticrossing (between the first and second level of $m = -1$) is displayed in Fig. 7.5(a). The corresponding values of $\langle L_z \rangle$, the average radial

position $\langle \rho/R \rangle$, as well as the probability density for the points (1), (2) and (3) are shown in panels (b), (c) and (d), respectively. The figure indicates that at the anti-crossing the eigenstate evolves from a configuration in which the electron is mainly confined in the center of the ring by the magnetic field, to a state in which the confinement is mainly caused by the electrostatic potential U_b . At the anti-crossing (2), the probability density plot shows peaks both in the central part of the structure, as well as in the ring, which characterizes the overlap of the magnetically and electrostatically confined states.

In Fig. 7.6(a), the energy spectrum of a GQR is shown as function of the external magnetic field, for $-15 \leq m \leq 5$, $R = 25 \text{ nm}$, $W = 10 \text{ nm}$, $U_b = 150 \text{ meV}$ and $U_w = 0 \text{ meV}$. Panel (b) displays the ground state energy as function of magnetic field, whereas panel (c) shows the expectation value of the operator $\langle L_z \rangle / \hbar$, for the first energy levels of different values of m shown in panel (a). The black line follows expectation value of angular momentum of the ground state energy, which shows the eigenvalues of $\langle L_z \rangle / \hbar$ are field-dependent. That behavior is related to the lack of inversion symmetry of the biased bilayer graphene.

7.4 Conclusion

In summary, we obtained the eigenstates and energy levels of electrostatically confined quantum rings in graphene bilayers. This new approach differs from previous studies of graphene-based quantum rings which were realized through a lithographic cutting of the sample. The advantage of the present approach is that the confinement can be tuned by varying the profile and depth of the confining potential, preventing issues as edge disorder and the specific edge type. Numerical results were presented for a step-like confining potential, which can be expected to provide a good approximation of actual potential barriers, because of the large screening in bilayer graphene. We predict that the energy levels display a dependence on the magnetic field that is quite distinct from that of a conventional 2D electron gas. Moreover, the energy levels are not invariant under a $B_0 \rightarrow -B_0$ transformation, in contrast with usual ring structures. This is a consequence of the fact that the ring structure is produced by a gate that introduces an electric field and thus a preferential direction. On the other hand, the spectrum is found to be invariant under the transformation $B_0 \rightarrow -B_0$, together with $U_b \rightarrow -U_b$ and $m \rightarrow -m$. Alternatively, $B_0 \rightarrow -B_0$ and $E \rightarrow -E$ transforms electron states into hole states and vice-versa. The spectra also present several anti-crossings at low energies, which arise due to the overlap of gate-confined and magnetically-confined states. For a fixed total angular momentum index m , the $E(B_0)$ curves are no longer parabola, but show two minima separated by a saddle point. The existence of Aharonov-Bohm oscillations for both electrons and holes

are still linked with flux quantization through the ring. Throughout the calculation, we considered single electron states. However, the inclusion of Coulomb interaction between carriers may introduce interesting modifications in the spectrum [114]. The system can be realized experimentally by a suitable choice of nanostructured doping levels or with the application of nanostructured gates. The spectra may be investigated by, e.g. cyclotron resonance methods [127] and quantum transport measurements.

CHAPTER 8

Energy levels of an ideal quantum ring in monolayer and bilayer graphene

Within a minimal model, we present analytical expressions for the eigenstates and eigenvalues of carriers confined in quantum rings in monolayer and bilayer graphene. The calculations were performed in the context of the continuum model, by solving the Dirac equation for a zero width ring geometry, i.e. by freezing out the carrier radial motion. We include the effect of an external magnetic field and show the appearance of Aharonov-Bohm oscillations and of a non-zero gap in the spectrum. Our minimal model gives insight in the energy spectrum of graphene-based quantum rings and models different aspects of finite width rings.

8.1 Introduction

In this chapter we present analytical results for the eigenstates and energy levels of ideal quantum rings with zero-width created with graphene and bilayer graphene. Recently, graphene-based quantum rings produced by lithographic techniques have been investigated on single-layer graphene [125, 126]. These systems have been studied theoretically

The results of this chapter were published as
M. Zarenia, J. Milton Pereira, A. Chaves, F. M. Peeters, and G. A. Farias, Phys. Rev. B **81**, 045431 (2010);
Erratum: Phys. Rev. B **82**, 119906 (2010).

by means of a tight-binding model, which does not provide straightforward analytical solutions for the eigenstates and eigenvalues [63, 76, 128–130]. For bilayer graphene it is possible to electrostatically confine quantum rings with a finite width [131] as we shown in the previous chapter. The energy spectrum was obtained by solving the Dirac equation numerically.

In this chapter we present a toy model that allows for analytical expressions for the energy levels of quantum rings in single layer and bilayer graphene. This model permits the description of several aspects of the physics of graphene quantum rings without the additional complications of edge effects and finite width of the quantum ring. We are able to obtain analytical expressions for the energy spectrum and the corresponding wavefunctions, the persistent current, and the orbital momentum as function of ring radius, total momentum and magnetic field, which can be related to the numerical results obtained by other methods.

8.2 Single layer graphene

8.2.1 Model

The dynamics of carriers in the honeycomb lattice of covalent-bond carbon atoms of single layer graphene can be described by the Dirac Hamiltonian (valid for $E < 0.8$ eV). In the presence of a uniform magnetic field $\mathbf{B} = B_0 \mathbf{e}_z$ perpendicular to the plane and finite mass term Δ , which might be caused by an interaction with the underlying substrate [11] The Hamiltonian in the valley isotropic form is given by [76]:

$$H = v_F(\mathbf{p} + e\mathbf{A}) \cdot \boldsymbol{\sigma} + \tau \Delta \sigma_z \quad (8.1)$$

where $\tau = +1$ corresponds to the K point and $\tau = -1$ to the K' point. \mathbf{p} is the in-plane momentum operator, \mathbf{A} is the vector potential and $v_F \approx 1.0 \times 10^6$ m/s is the Fermi velocity, and $\boldsymbol{\sigma} = (\sigma_x, \sigma_y, \sigma_z)$ is the pseudospin operator with components given by Pauli matrices. The eigenstates of Eq. (8.1) are two-component spinors which, in polar coordinates is given by

$$\Psi(\rho, \phi) = \begin{pmatrix} \phi_A(\rho) e^{im\phi} \\ i\phi_B(\rho) e^{i(m+1)\phi} \end{pmatrix}. \quad (8.2)$$

where m is the angular momentum label. We follow the earlier very successful approach [132, 133] of ideal one-dimensional (1D) quantum rings in semiconductors with spin-orbit interaction where the Schrödinger equation was simplified by discarding the radial variation of the electron wave function. Thus, in the case of an ideal ring with radius

R , the momentum of the carriers in the radial direction is zero. We treat the radial parts of the spinors in Eq. (8.2) as a constant

$$\Psi(R, \phi) = \begin{pmatrix} \phi_A(R)e^{im\phi} \\ i\phi_B(R)e^{i(m+1)\phi} \end{pmatrix}. \quad (8.3)$$

Because the radial motion is frozen in our model there will be no radial current and the persistent current will be purely in the angular direction. By solving $H\Psi(R, \phi) = E\Psi(R, \phi)$ and using the symmetric gauge $\mathbf{A} = (0, B_0\rho/2, 0)$, we obtain

$$\begin{aligned} (m + \beta + 1/2)\phi_B(R) &= (\epsilon - \tau\delta)\phi_A(R), \\ (m + \beta + 1/2)\phi_A(R) &= (\epsilon + \tau\delta)\phi_B(R), \end{aligned} \quad (8.4)$$

where the energy and mass terms are written in dimensionless units as $\epsilon = E/E_0$, $\delta = \Delta/E_0$ with $E_0 = \hbar v_F/R$. The parameter $\beta = (eB_0/2\hbar)R^2$ can be expressed as $\beta = \Phi/\Phi_0$ with $\Phi = \pi R^2 B_0$ being the magnetic flux threading the ring and $\Phi_0 = h/e$ the quantum of magnetic flux. The homogeneous set of equations (8.4) is solvable for the energies

$$\epsilon = \pm \sqrt{(m + \beta + 1)(m + \beta) + \delta^2 + 1/4}. \quad (8.5)$$

The wavefunctions are eigenfunctions of the total angular momentum operator given by the sum of orbital angular momentum L_z and a term describing the pseudo-spin S_z

$$J_z = L_z + \hbar S_z, \quad (8.6)$$

where $S_z = (1/2)\sigma_z$, with σ_z being one of the Pauli matrices and the eigenvalues of J_z operator become $[m + (1/2)]\hbar$.

The current is obtained using $j_{x,y} = v_F[\psi^\dagger \sigma_{x,y} \psi]$. The total angular current $j = v_F[\psi^\dagger \sigma_\phi \psi]$ can be calculated using the fact that $\sigma_\phi = \xi(\phi)\sigma_y$, where

$$\xi(\phi) = \begin{pmatrix} e^{-i\phi} & 0 \\ 0 & e^{i\phi} \end{pmatrix}. \quad (8.7)$$

The current for the electrons in the K-valley becomes

$$j_K = v_F(\phi_A^* \phi_B + \phi_B^* \phi_A). \quad (8.8)$$

The total current is then given by $j = j_K + j_{K'}$. The radial part of the two spinor components are

$$\phi_A(R) = 1, \quad \phi_B(R) = \frac{m + \beta + 1/2}{\epsilon + \tau\delta}. \quad (8.9)$$

Notice that the radial current can be calculated using $j_r = v_F[\psi^\dagger \xi(\phi) \sigma_x \psi]$ which leads to the following relation,

$$j_r = iv_F(\phi_A^* \phi_B - \phi_B^* \phi_A), \quad (8.10)$$

where, in the case of our ideal ring we have $j_r = 0$. From Eqs. (8.8) and (8.9), one can find the following expression for the total angular current of a single layer quantum ring

$$j = \frac{4v_F \epsilon (m + \beta + 1/2)}{\epsilon^2 - \delta^2}. \quad (8.11)$$

One can rewrite Eq. (8.11) in the following form

$$\frac{j}{v_F} = \left(\frac{\partial \epsilon}{\partial \beta}\right)_K + \left(\frac{\partial \epsilon}{\partial \beta}\right)_{K'} + \frac{[2(m + \beta) + 1](\epsilon^2 + \delta^2)}{\epsilon(\epsilon^2 - \delta^2)}. \quad (8.12)$$

Since for the ground state energy $m + \beta = -1/2$ where $\partial \epsilon / \partial \beta = 0$ the last term in Eq. (8.12) is zero and the total current oscillates around zero. Note that in 1D semiconductor rings the current is exactly given by $\partial E / \partial \Phi$, which is thus different from graphene where we have approximately

$$\frac{j}{v_F} \simeq \left(\frac{\partial \epsilon}{\partial \beta}\right)_K + \left(\frac{\partial \epsilon}{\partial \beta}\right)_{K'}. \quad (8.13)$$

with $\beta = \Phi / \Phi_0$.

8.2.2 Results

The energies as function of ring radius R are shown in Fig. 8.1, for $\Delta = 50$ meV, with $-10 \leq m \leq -1$ (magenta curves), $1 \leq m \leq 10$ (blue curves), and $m = 0$ (green curves). In the absence of an external magnetic field, the energy is given by $E = \pm \sqrt{[(m + 1/2)(\hbar v_F / R)]^2 + \Delta^2}$ and the energy branches have a $1/R$ dependence and approach $E \rightarrow \pm \Delta$ for very large radii. For non-zero magnetic field ($B_0 = 3$ T), the right panel shows that the branches have an approximately linear dependence on the ring radius for large R , in particular we have $E \simeq \pm \sqrt{(\alpha R)^2 + \Delta^2}$, with $\alpha = v_F e B_0 / 2$. For small radii, $E \simeq \pm \hbar v_F |m + 1/2| / R$ and all branches diverge as $1/R$. Figure 8.2 presents results for the energy as function of total angular momentum index m , for $\Delta = 50$ meV, $R = 50$ nm and for three different values of magnetic field, namely $B_0 = -5$ T (diamonds), $B_0 = 0$ T (circles) and $B_0 = 5$ T (triangles). Notice that for a given B_0 the electron energy obtains a minimum for a particular m , i.e. for $B_0 = 0$ (5 T, -5 T) it is $m = 0$ (9, -10). In fact it is given by $m = -(\Phi / \Phi_0 + 1/2)$ and is independent of Δ .

The energy levels as function of the external magnetic field are shown in Fig. 8.3, for a quantum ring with (a) $\delta = 1/2$ and (b) $\delta = 0$ with $R = 50$ nm for $-10 \leq m \leq -1$

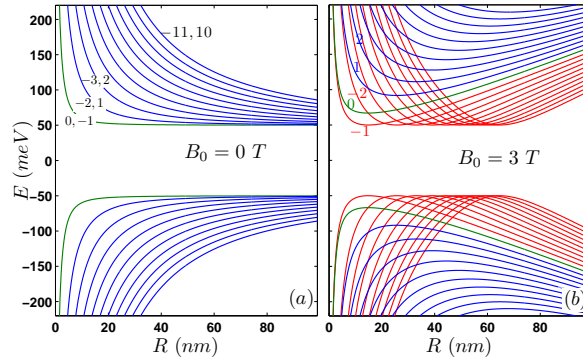


Figure 8.1: Energy levels with $m = -10, \dots, 10$ of a single layer graphene quantum ring as function of ring radius R for $B_0 = 0$ T (left panel) and $B_0 = 3$ T (right panel) when the mass term is $\Delta = 50$ meV.

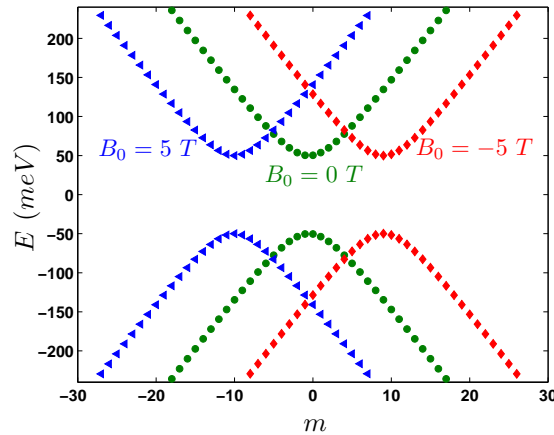


Figure 8.2: Energy levels of a single layer graphene quantum ring as function of the quantum number m for $B_0 = -5, 0, 5$ T with $\Delta = 50$ meV and $R = 50$ nm.

(red curves), $1 \leq m \leq 10$ (blue curves), and $m = 0$ (green curves). The magnetic field dependence of the spectrum becomes evident if one rewrites Eq. (8.5) as $\epsilon^2 - [(m + \Phi/\Phi_0) + 1/2]^2 = \delta^2$. Thus, for the special case of $\delta = \Delta/E_0 = 0$ the gap is zero and the energy levels are straight lines given by $\epsilon = \pm(m + 1/2 + \Phi/\Phi_0)$. The energy spectra for $\delta > 0$ shows an energy gap and resemble those found earlier by Recher *et al.* [76] in the case of a finite width graphene ring with infinite mass boundary conditions. For $\delta = 0$ the double degeneracy is restored at $E = 0$. This behavior can be easily illustrated by considering $m = 0$. The energy in this case is $\epsilon = \pm\sqrt{\beta(\beta + 1) + \delta^2 + 1/4}$ which for

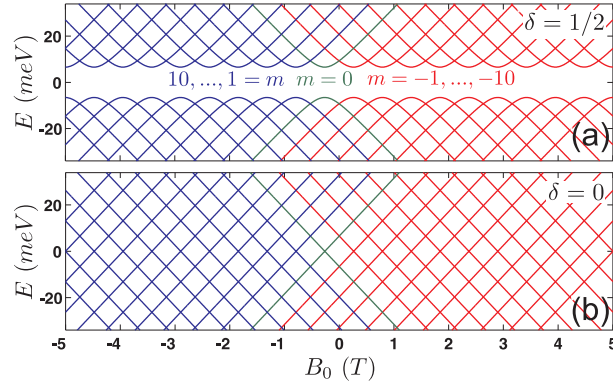


Figure 8.3: Electron and hole energy levels of a single layer graphene quantum ring as function of external magnetic field B_0 for (a) $\delta = 1/2$ and (b) $\delta = 0$ with $R = 50$ nm, and total angular quantum number $-10 \leq m \leq -1$ (red curves), $1 \leq m \leq 10$ (blue curves) and $m = 0$ (green curves).

$\delta = 0$ becomes $\epsilon = \pm|\beta + 1/2|$.

In Fig. 8.4(a) the energy spectrum is plotted vs magnetic field for $\delta = 2$. Where, the energy has a hyperbolic dependence on the applied magnetic field with minima at $\Phi/\Phi_0 = -m - 1/2$ and a gap of $\Delta\epsilon = 2\delta$. The exact location of the transitions (orange dots) and the location of the minima points (yellow dots) in the energy spectrum is clarified in Fig. 8.4(b). The dependence of the energy levels on the gap parameter Δ is shown in Fig. 8.5, for zero magnetic field (left panels) and $B_0 = 1$ T (right panels). When $m \geq 0$ (upper panels) and $m < 0$ (lower panels). For $B_0 = 0$ T the energy levels are two fold degenerate where $E(m) = -E(-m - 1)$. When a magnetic field is applied an energy gap is opened (see right-bottom panel).

The corresponding ground state expectation values for the operators in Eq. (8.16) are plotted as function of the magnetic field in Fig. 8.6(b) for both K (black dashed curve) and K' valley (black dash-dotted curve). Notice that for the K -valley $\langle L_z \rangle \simeq m\hbar$ and $\langle S_z \rangle \simeq \hbar/2$ whereas in the K' -valley $\langle L_z \rangle \simeq (m + 1)\hbar$ and $\langle S_z \rangle \simeq -\hbar/2$. Thus for both the K valley and the K' valley $\langle J_z \rangle \simeq [m + (1/2)]\hbar$ which is approximately quantized and on the average its value decreases linearly with the applied magnetic field.

The angular current density for a single layer graphene quantum ring is shown in Fig. 8.7(c). Note that the contribution from the K -valley j_K (Fig. 8.7(a)) and the K' -valley $j_{K'}$ (Fig. 8.7(b)) are the same and they oscillate around zero. The reason is that if for given energy we have electrons in the K -valley, the corresponding particles in the K' -valley will behave as holes. The persistent current is a sawtooth shaped oscillating function of the magnetic field with period $\Delta B_0 = \Phi_0/\pi R^2$. This behavior is quantitatively very similar to

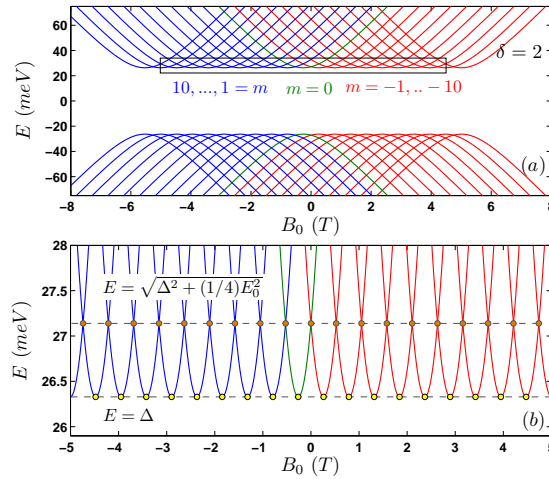


Figure 8.4: (a) Electron and hole energy levels of a single layer graphene quantum ring as function of external magnetic field B_0 for $\delta = 2$ and $R = 50$ nm. (b) An enlargement of the region which is shown in (a) by a rectangle.

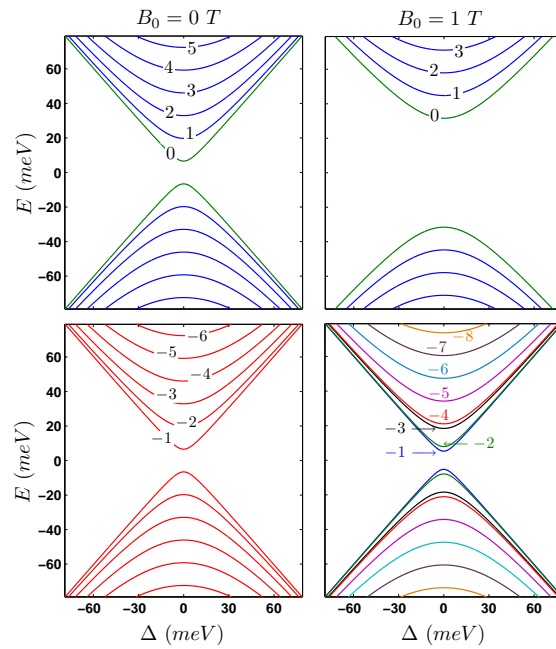


Figure 8.5: Lowest energy levels of a single layer graphene quantum ring as function of the mass term Δ with $B_0 = 0$ T (left panels) and $B_0 = 1$ T (right panels) for $m \geq 0$ (upper panels) and $m < 0$ (lower panels) with $R = 50$ nm.

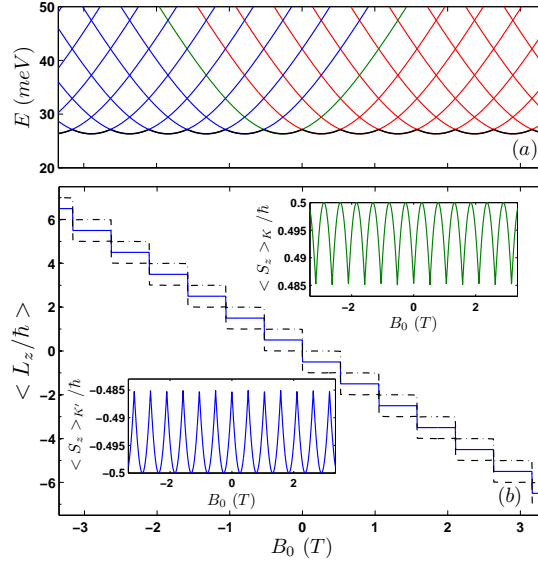


Figure 8.6: (a) Electron energy levels of a graphene single layer quantum ring as function of external magnetic field B_0 for $R = 50$ nm and $\delta = 2$. Black curve shows the ground state energy (b) Ground state expectation value of L_z/\hbar as function of magnetic field for both K (black dashed curve) and K' valley (black dash-dotted curve). Expectation value of S_z/\hbar versus magnetic field is plotted in upper inset for K -valley and in lower inset for K' -valley. Blue solid curve shows the expectation value $\langle J_z \rangle$ which is the same for both valleys.

those found for the standard Aharonov-Bohm oscillations in metallic and semiconductor quantum rings.

8.3 Bilayer graphene

8.3.1 Model

In the case of bilayer graphene the Hamiltonian in the vicinity of the K point, is given by [39]

$$H = \begin{pmatrix} \tau U_1 & \pi & \gamma & 0 \\ \pi^\dagger & \tau U_1 & 0 & 0 \\ \gamma & 0 & \tau U_2 & \pi^\dagger \\ 0 & 0 & \pi & \tau U_2 \end{pmatrix} \quad (8.14)$$

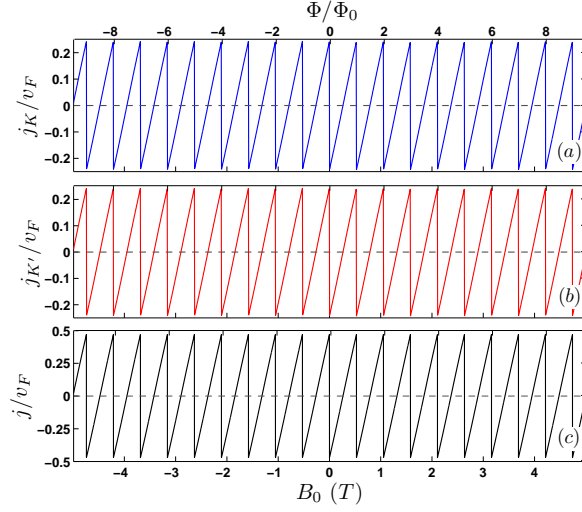


Figure 8.7: The angular current density in the (a) K -valley, (b) K' -valley and (c) the total current density of a monolayer graphene quantum ring as function of external magnetic field B_0 for the ground state energy shown by the black curve in Fig. 8.6(a).

where $\tau = \pm 1$ distinguishes the two K and K' valleys. $\gamma \simeq 400$ meV is the inter-layer coupling term, $\pi = v_F[(p_x + eA_x) + i(p_y + eA_y)]$, U_1 and U_2 are the potentials, respectively, at the two graphene layers. Here we do not include any mass term because the gate potential across the bilayer is able to open an energy gap in the spectrum [39]. The eigenstates of the Hamiltonian (8.14), are four-component spinors $\Psi(r, \phi) = [\phi_A(\rho)e^{im\phi}, i\phi_B(\rho)e^{i(m-1)\phi}, \phi_C(\rho)e^{im\phi}, i\phi_D(\rho)e^{i(m+1)\phi}]^T$ (see Ref. [29]). Following our earlier approach for an ideal ring with radius R , the wave function becomes:

$$\Psi = \begin{pmatrix} \phi_A(R)e^{im\phi} \\ i\phi_B(R)e^{i(m-1)\phi} \\ \phi_C(R)e^{im\phi} \\ i\phi_D(R)e^{i(m+1)\phi} \end{pmatrix}. \quad (8.15)$$

We use the symmetric gauge and obtain the following set of coupled algebraic equations

$$-(\epsilon - \tau u_1)\phi_A(R) - (m + \beta - 1/2)\phi_B(R) + \gamma'\phi_C(R) = 0,$$

$$(m + \beta - 1/2)\phi_A(R) + (\epsilon - \tau u_1)\phi_B(R) = 0,$$

$$\gamma'\phi_A(R) - (\epsilon - \tau u_2)\phi_C(R) + (m + \beta + 1/2)\phi_D(R) = 0,$$

$$(m + \beta + 1/2)\phi_C(R) - (\epsilon - \tau u_2)\phi_D(R) = 0, \quad (8.16)$$

where, $\gamma' = \gamma/E_0$ and $u_{1,2} = U_{1,2}/E_0$ are in dimensionless units. After some straightforward algebra we obtain the following polynomial equation that determines the energy spectrum

$$\begin{aligned} & [(\epsilon - \tau u_1)^2 + (m + \beta - 1/2)^2][(\epsilon - \tau u_2)^2 - (m + \beta + 1/2)^2] - \\ & (\epsilon - \tau u_1)(\epsilon - \tau u_2)\gamma'^2 = 0. \end{aligned} \quad (8.17)$$

After introducing the average potential $u = (u_1 + u_2)/2$ and half the potential difference $\delta = (u_1 - u_2)/2$ we can rewrite this quartic algebraic equation in a more comprehensive form:

$$\begin{aligned} & s^4 - 2s^2[(m + \beta)^2 + \delta^2 + (\gamma')^2/2 + 1/4] + 4s\tau\delta(m + \beta) + \\ & [(m + \beta)^2 - 1/4]^2 - 2\delta^2[(m + \beta)^2 - (\gamma')^2/2 + 1/4] + \delta^4 = 0, \end{aligned} \quad (8.18)$$

where $s = \epsilon - \tau u$ is the energy shifted by the average potential. In the next section we report the results for the case of $U_1 = -U_2 = U_b$ where, the average potential u is zero. In the limit $\delta \rightarrow 0$, the quartic equation is reduced to a quadratic equation in s^2 and we obtain the real solutions

$$s_{\pm}^2 = (m + \beta)^2 + (\gamma')^2/2 + 1/4 \pm \sqrt{1/4[(\gamma')^4 + (\gamma')^2] + (m + \beta)^2[(\gamma')^2 + 1/2]} \quad (8.19)$$

which results in four solutions for the energy. In the limit of $\gamma' \gg m + \beta$ we obtain $s_{-}^2 = [(m + \beta)^2 - 1/4]^2/[(\gamma')^2 + 1/2]$ and thus the low energy solutions are given by

$$s \simeq \pm[(m + \beta)^2 - 1/4]/\sqrt{(\gamma')^2 + 1/2}. \quad (8.20)$$

For bilayer graphene, the wavefunctions are eigenfunctions of the following operator:

$$J_z = L_z + \hbar\tau_z + \hbar S_z, \quad (8.21)$$

where now

$$\tau_z = \frac{1}{2} \begin{pmatrix} -\mathbf{I} & 0 \\ 0 & \mathbf{I} \end{pmatrix}, \quad S_z = \frac{1}{2} \begin{pmatrix} \sigma_z & 0 \\ 0 & -\sigma_z \end{pmatrix}, \quad (8.22)$$

are 4×4 matrices.

In bilayer graphene the components of the current density are given by

$$j_x = v_F \left[\psi^\dagger \begin{pmatrix} \sigma_x & 0 \\ 0 & \sigma_x \end{pmatrix} \psi \right], \quad j_y = v_F \left[\psi^\dagger \begin{pmatrix} -\sigma_y & 0 \\ 0 & \sigma_y \end{pmatrix} \psi \right]. \quad (8.23)$$

The angular current can be calculated from the following relation,

$$j = v_F \left[\psi^\dagger \begin{pmatrix} \sigma_y^* \xi(\phi) & 0 \\ 0 & \xi(\phi) \sigma_y \end{pmatrix} \psi \right]. \quad (8.24)$$

Where, $\xi(\phi)$ is given by Eq. (8.7). We obtain for the angular current in the K-valley,

$$j_K = v_F (\phi_C^* \phi_D + \phi_D^* \phi_C - \phi_A^* \phi_B - \phi_B^* \phi_A), \quad (8.25)$$

and the total angular current is given by $j = j_K + j_{K'}$, where, the four spinor components are:

$$\begin{aligned} \phi_A(R) &= 1, \\ \phi_B(R) &= -\frac{m + \beta - 1/2}{\epsilon - \tau u_1}, \\ \phi_C(R) &= \frac{(\epsilon - \tau u_1)^2 - (m + \beta - 1/2)^2}{\gamma'(\epsilon - \tau u_1)}, \\ \phi_D(R) &= \frac{(m + \beta + 1/2)[(\epsilon - \tau u_1)^2 - (m + \beta - 1/2)^2]}{\gamma'(\epsilon - \tau u_1)(\epsilon - \tau u_2)}. \end{aligned} \quad (8.26)$$

Note that the radial current can be calculated through

$$j_r = v_F \left[\psi^\dagger \begin{pmatrix} \sigma_x \xi(\phi) & 0 \\ 0 & \xi(\phi) \sigma_x \end{pmatrix} \psi \right], \quad (8.27)$$

where, $j_r = i v_F (\phi_A^* \phi_B - \phi_B^* \phi_A + \phi_C^* \phi_D - \phi_D^* \phi_C) = 0$ for the case of an ideal ring. Using Eq. (8.25), the total current density becomes,

$$j = \sum_{\tau=\pm 1} \frac{2v_F}{\epsilon - \tau u_1} \left[(m + \beta - 1/2) + \frac{(m + \beta + 1/2)[(\epsilon - \tau u_1)^2 - (m + \beta - 1/2)^2]}{\gamma'^2(\epsilon - \tau u_1)(\epsilon - \tau u_2)} \right]. \quad (8.28)$$

8.3.2 Results

The dependence of the spectrum on the ring radius, for $B_0 = 0$ T (upper panel) and $B_0 = 5$ T (lower panel) is shown in Fig. 8.8, for a gate potential $U_b = 100$ meV, which for

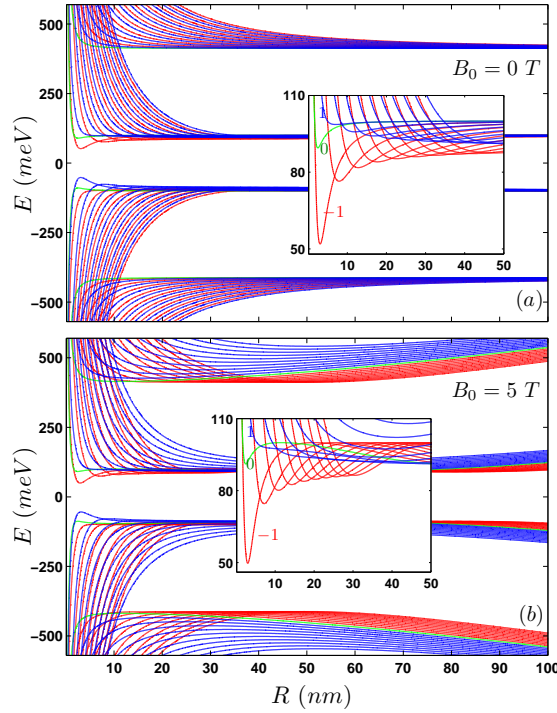


Figure 8.8: Lowest energy levels of a bilayer graphene quantum ring as function of ring radius R with (a) $B_0 = 0$ T and (b) $B_0 = 5$ T for $U_b = 100$ meV and total angular quantum number $-10 \leq m \leq -1$ (red curves), $1 \leq m \leq 10$ (blue curves) and $m = 0$ (green curves). The insets are an enlargement of the small energy and small R region.

$B = 0$ T opens up a gap in the energy spectrum. As compared to the single layer quantum ring results of Fig. 8.1, we find that we have a second set of levels that for large R are displaced in energy by t . In the limit $R \rightarrow 0$ the most important term in the dispersion relation is $[(m + \beta)^2 - 1/4]^2$. Previously, we found that for rings with finite width [131] the spectrum exhibits anti-crossing points which arise due to the overlap of gate-confined and magnetically-confined states. In the present model the carrier motion along the radial direction is neglected and consequently we have level crossings instead of anti-crossing points in the spectrum.

The dependence of the energy eigenstates on the angular momentum index m is displayed in Fig. 8.9 for $U_b = 100$ meV, $R = 50$ nm, with $B_0 = -5$ T (diamonds), 0 T (circles) and 5 T (triangles). Due to the finite bias in this case, the fourth-order character of the dispersion Eq. (8.17) causes the curves to exhibit a Mexican hat shape. The energy minima for $B_0 = -5, 0, 5$ T are respectively given by $m = -1, -10, -20$.

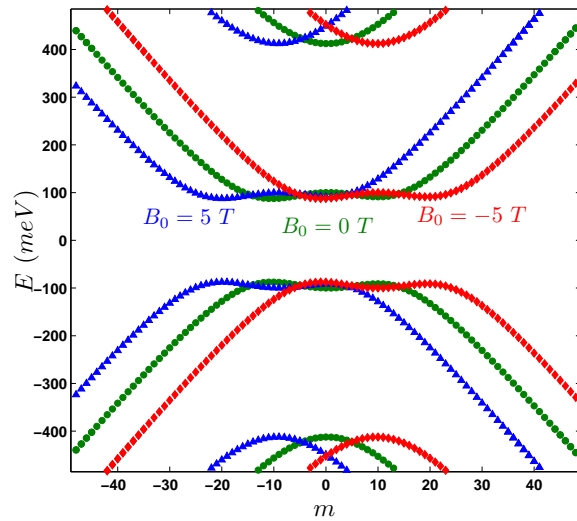


Figure 8.9: Lowest energy levels of a graphene bilayer quantum ring as function of total angular momentum label m for $B_0 = -5, 0, 5$ T with $U_b = 100$ meV and $R = 50$ nm.

In Fig. 8.10 the energy levels are plotted as function of magnetic field, for a quantum ring with $U_b = 100$ meV, $R = 50$ nm, and for $-10 \leq m \leq -1$ (red curves), $1 \leq m \leq 10$ (blue curves), and $m = 0$ (green curves). These results are very similar to those found for a finite width ring and exhibit two local minima that are separated by a saddle point. In the case of finite width quantum rings there are additional energy levels that correspond with states that are partly localized outside the ring. Figs. 8.10(a,b) show the asymmetry between the electron and hole states, caused by the bias. It is seen that the electron and hole energies are related by $E_h(m, B_0) = -E_e(-m, -B_0)$, where the indices $h(e)$ refer to holes (electrons). In the absence of bias, the electron-hole symmetry is restored, as shown in Fig. 8.11, for a ring with $R = 50$ nm and a parabolic energy spectrum is recovered with zero energy gap.

In Fig. 8.12, the energy branches are plotted as function of the bias, for both the zero field case (left panels) and for $B_0 = 1$ T (right panels), with $m \geq 0$ (upper panels) and $m < 0$ (lower panels). Notice that the figures are quantitatively similar to those found previously for a quantum ring made of a single layer of graphene where the gate potential U_b has a similar effect as the mass term Δ . The differences are that for $B_0 = 0$ T the degeneracies are now: *i*) $E(0) \approx E(1) \approx E(-1)$ and *ii*) $E(m) = E(-m)$ for $|m| > 1$. In the presence of the magnetic field a gap is opened even for $U_b = 0$ meV, which is more clearly illustrated in the inset of the right-bottom panel of Fig. 8.12.

Figures 8.13(b,c) shows the ground state expectation value of the angular momentum

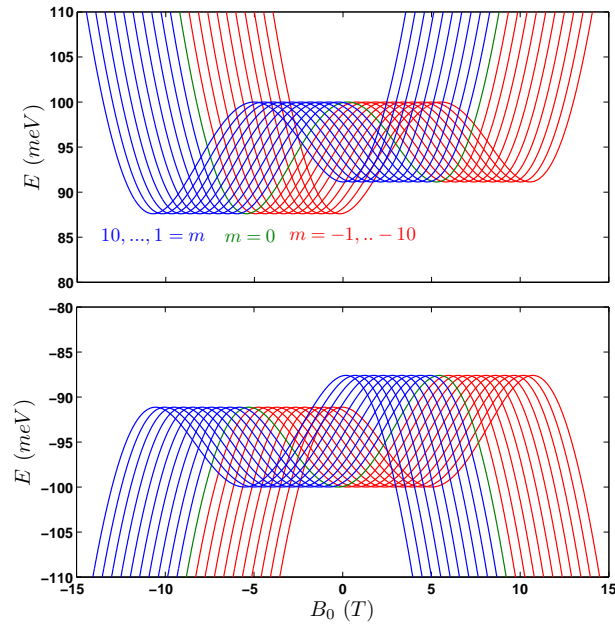


Figure 8.10: Electron and hole energy states of a graphene bilayer quantum ring as function of external magnetic field B_0 for $U_b = 100$ meV and $R = 50$ nm. The energy levels are shown for the quantum numbers $-10 \leq m \leq -1$ (red curves), $1 \leq m \leq 10$ (blue curves) and $m = 0$ (green curves).

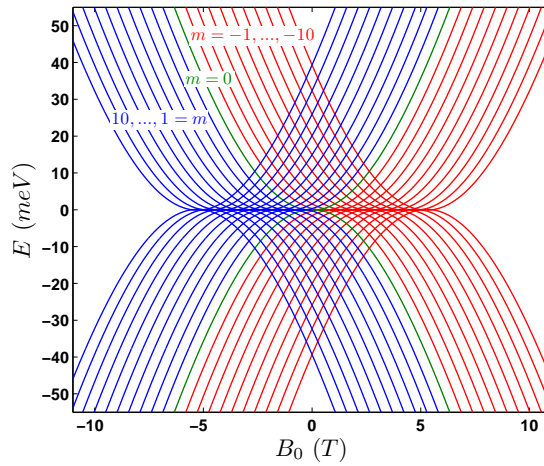


Figure 8.11: The same as Fig. 8.10, but for $U_b = 0$ meV.

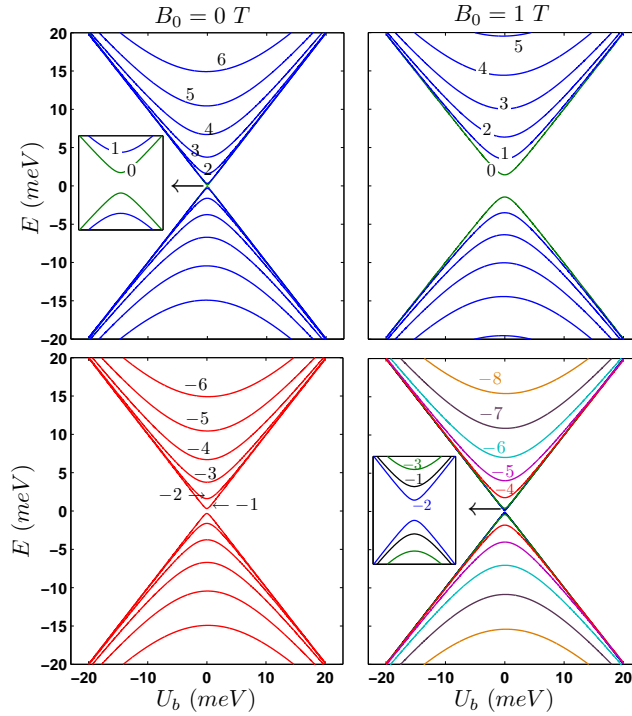


Figure 8.12: Lowest energy levels of a bilayer graphene quantum ring as function of the gate potential U_b when $B_0 = 0$ T (left panels) and $B_0 = 1$ T (right panels) for $m \geq 0$ (upper panels) and $m < 0$ (lower panels) with $R = 50$ nm.

versus the magnetic field together with the quantum number m (blue solid curve) which is an eigenvalue of the total momentum operator J_z . Notice that the expectation value of J_z , i.e. m , is different in the K and K' valley which was not the case for monolayer graphene. The energy levels for the K (solid red curves) and K' (dashed blue curves) valleys are depicted in Fig. 8.13(a). Black curve (gray curve) shows the ground state energy for the K -valley (K' -valley). Notice that in the considered case we find that the difference between $\langle J_z \rangle = m\hbar$ and $\langle L_z \rangle$ is about $(0.7 - 0.8)\hbar$ for both the K and K' valleys.

The ground state angular current of a bilayer graphene as function of magnetic field B_0 in the K -valley j_K , the K' -valley $j_{K'}$ and the total angular current j is shown, respectively, in Figs. 8.14(a), (b) and (c). In the case of a bilayer graphene quantum ring, the energy levels in the vicinity of the K and K' points are different because of the valley splitting and consequently the total angular current versus magnetic field is a more complicated sawtooth function. Notice that the angular current for the K or K' valley is not zero at $B_0 = 0$ which is due to the valley polarization whereas the total current is zero at $B_0 = 0$.

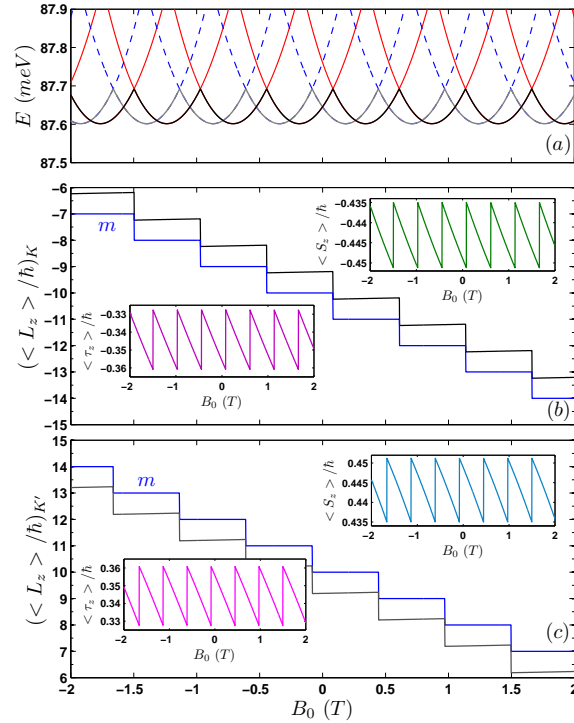


Figure 8.13: (a) Electron energy levels of a bilayer graphene quantum ring as function of external magnetic field B_0 for a quantum ring of radius $R = 50$ nm and with $U_b = 100$ meV for both the K -valley (solid curves) and the K' -valley (dashed curves). Black curve shows the ground state energy of the energy spectrum in the K -valley whereas the gray curve gives the corresponding ground state energy of the K' -valley (b) Ground state expectation values of L_z/\hbar , S_z/\hbar , τ_z/\hbar as function of magnetic field in the K -valley. Blue solid curve shows the expectation value of the J_z/\hbar operator. (c) The same as (b) but for the K' -valley.

8.4 Conclusion

In summary we considered the behavior of carriers in single and bilayer graphene quantum rings within a toy model. Our approach leads to analytic expressions for the energy spectrum. In our simple model we are not faced with the disadvantages of the nature of edge effects which appears in quantum rings created by cutting the layer of graphene (or lithography defined quantum rings).

We found an interesting behavior in the presence of a perpendicular magnetic field, which has no analogue in semiconductor-based quantum rings. In single layer graphene

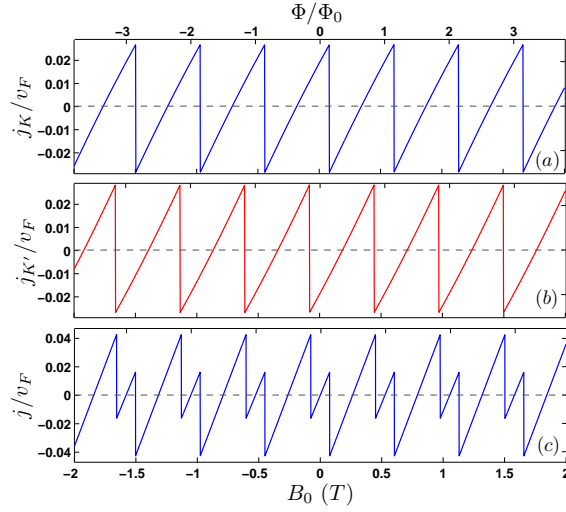


Figure 8.14: The ground state angular current density in the (a) K -valley, (b) K' -valley and (c) the total current density of a bilayer graphene quantum ring as function of external magnetic field B_0 with $U_b = 100$ meV and $R = 50$ nm.

quantum rings only for $\Delta > 0$ we found the opening of a gap in the energy spectrum between the electron and hole states. For both single layer and bilayer graphene quantum rings the eigenvalues are not invariant under a $B_0 \rightarrow -B_0$ transformation. For bilayer graphene the spectra for a fixed total angular momentum index m is not parabolic as function of the magnetic field but exhibit two minima separated by a saddle point. The persistent current exhibits oscillations as function of the magnetic field with period $\Phi_0/\pi R^2$ which are the well-known Aharonov-Bohm oscillations. Because of the valley splitting in the energy spectrum of bilayer graphene the total current density versus magnetic field is a more complicated sawtooth function.

CHAPTER 9

Chiral states in monolayer graphene

Uni-directional chiral states are predicted in single layer graphene which originate from the breaking of the sublattice symmetry due to an asymmetric mass potential. The latter can be created experimentally using boron nitride (BN) substrates with a line defect (B-B or N-N) that changes the induced mass potential in graphene. Solving the Dirac-Weyl equation, the obtained energy spectrum is compared with the one calculated using ab initio density functional calculations. We found that these one-dimensional chiral states are very robust and they can even exist in the presence of a small gap between the mass regions. In the latter case additional bound states are found that are topologically different from those chiral states.

9.1 Introduction

A pristine layer of graphene shows a gapless linear energy spectrum at the two inequivalent points, i.e. K and K' , in its Brillouin zone. This gapless behavior is a consequence of the sublattice (chiral) and time reversal symmetries of graphene. It was recently found that the application of appropriate substrates can break the sublattice symmetry and induce a gap in the spectrum [11, 33]. The hexagonal boron nitride (h-BN) substrate is such an example, and recent magnetotransport measurement of graphene on top of h-BN were

The results of this chapter were published as
M. Zarenia, O. Leenaerts, B. Partoens, and F. M. Peeters, Phys. Rev. B **86**, 085451 (2012).

very promising for high quality electronic devices [11]. Furthermore, *ab initio* density functional calculations (DFT) demonstrated that the energy spectrum of graphene exhibits a gap when placed on top of h-BN substrates [134, 135]. Such a breaking of the sublattice symmetry in graphene can be translated into a mass term in the Dirac-Weyl Hamiltonian [65]. The spatial variation of such a mass term will be useful for the creation of quantum devices where a tunable energy gap allows the observation of confined states [69, 109, 131, 136].

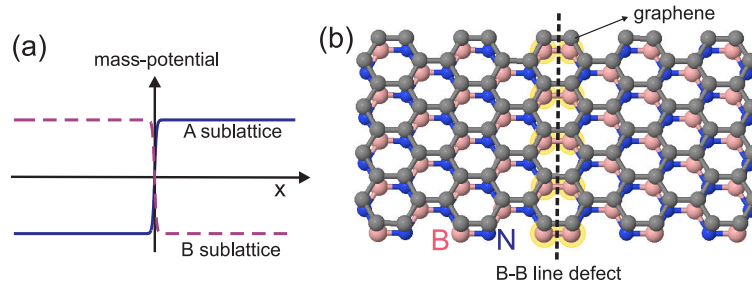


Figure 9.1: (a) The induced mass potential profile in single layer graphene in the presence of a Boron-Nitride (BN) substrate with a line defect. (b) A schematic picture of graphene on top of BN substrate. The dashed line indicates the position of the line defect (i.e. B-B)

Surface states have been investigated in topological insulator materials over the last three decades. Such materials are insulating in the bulk while on their boundaries topologically protected surface (edge) states are found [137]. In this chapter we propose one-dimensional (1D) chiral state in single layer graphene that relies on the creation of an asymmetric mass profile (i.e. a kink potential) (see Fig. 9.1(a)). A similar electrostatic kink potential profile has been recently investigated in bilayer graphene (BLG), that can be realized using nanostructured double gates placed respectively on the bottom and top of the BLG layers [34, 138–140]. At the interface of the kink potential, 1D chiral states appear in the energy gap with unidirectional motion of the electrons. Recently, it was also found that these states are robust even in the presence of a perpendicular external magnetic field [141–143]. In contrast to these early proposals our system can be realized with a *single layer* of graphene without using gate potentials. We show that these new chiral states can be induced by a line defect in the h-BN substrate that results in a kink in the effective mass profile. Other types of line defects or vacancies can induce a mass profile different from the present kink-antikink structure which even may open an energy gap due to the coupling between the K and K' valleys.

Here, we will solve the Dirac-Weyl Hamiltonian analytically, for the kink-antikink mass profile and obtain the dispersion relation explicitly. We complemented our results with DFT calculations. In our plane-wave base DFT calculations it is necessary to apply

periodic boundary conditions. We use a rectangular graphene supercell containing 32 carbon atoms and place it on top of a boron nitride substrate with a topological defect line (see Fig. 9.1(b)). Different ways of stacking are possible but AA-stacking, i.e. all carbon atoms are on top of boron or nitrogen atoms, maximizes the graphene-substrate interaction [134]. The DFT results support our analytical results and show that the line defect in h-BN results in the disappearance of the band gap which is normally induced by a homogeneous h-BN substrate [134].

9.2 Kink-shaped mass profile

We employ the continuum model based on the Dirac equation, which in the valley isotropic form is described by

$$H = -i\hbar v_F \begin{bmatrix} 0 & \partial_x - i\partial_y \\ \partial_x + i\partial_y & 0 \end{bmatrix} + \tau \begin{bmatrix} \Delta(x) & 0 \\ 0 & -\Delta(x) \end{bmatrix} \quad (9.1)$$

where, $v_F = 10^6$ m/s is the Fermi velocity, $\tau = 1$ ($\tau = -1$) corresponds to the K (K') valley, and $+\Delta(-\Delta)$ is the mass term induced by the BN substrate to the A(B) sublattice. The mass term breaks the sublattice symmetry and a gap 2Δ opens in the graphene energy spectrum.

The eigenstates of Eq. (9.1) are two-component spinors $\psi = [\phi_a(x, y), i\phi_b(x, y)]^T$ where $\phi_{a,b}$ are the envelope functions associated with the A and B sublattices. Since $[H, -i\partial_y] = 0$, the momentum along the y -direction is a conserved quantity and we have $\psi = e^{ik_y y} [\varphi_a(x), i\varphi_b(x)]^T$, where k_y is the wavevector along the y -direction. Solving the Schrödinger equation $H\psi(x, y) = E\psi(x, y)$ we obtain the two coupled differential equations as

$$[\partial_x + k_y]\varphi_b = [\epsilon - \zeta(x)]\varphi_a, \quad (9.2a)$$

$$-[\partial_x - k_y]\varphi_a = [\epsilon + \zeta(x)]\varphi_b. \quad (9.2b)$$

where, $\epsilon = El/\hbar v_F$, $\zeta(x) = \Delta(x)l/\hbar v_F$ and $(x, y) \rightarrow (x, y)/l$ are dimensionless with $l = 1$ nm taken as the length unit. For convenience we consider a step-like kink profile for the mass term which is modeled by $\zeta(x) = \zeta_0 x/|x|$. We decouple Eqs. (9.2) and obtain

$$[\partial_x^2 - \gamma^2]\varphi_a = 0, \quad (9.3)$$

where $\gamma = \sqrt{\zeta_0^2 + k_y^2 - \epsilon^2}$ is real when $|\epsilon| < \sqrt{\zeta_0^2 + k_y^2}$ (i.e. the region where bound states exist). The solutions of Eq. (9.3) for $x > 0$ and $x \leq 0$ regions are, respectively,

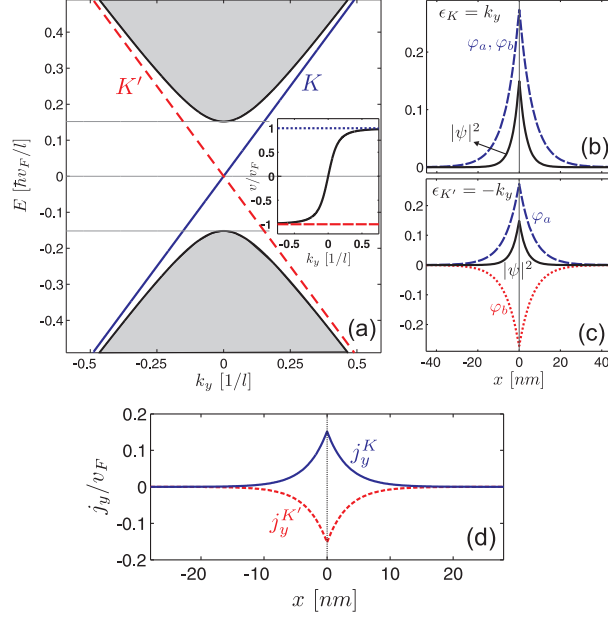


Figure 9.2: (a) Energy levels for a kink-shaped mass profile in single graphene. The curves and parameters are explained in the text. (b,c) The wave spinors and probability density respectively for $\epsilon_K = k_y$ and $\epsilon_{K'} = -k_y$. (d) y-component of the persistent current corresponding to the chiral state for the K (blue solid curve) and the K' (red dashed curve) valleys as a function of the x-direction.

given by

$$\psi(x < 0) = Ae^{\gamma x} [1, (k_y - \gamma)/(\epsilon - \zeta_0)]^T, \quad (9.4a)$$

$$\psi(x > 0) = Be^{-\gamma x} [1, (k_y + \gamma)/(\epsilon + \zeta_0)]^T, \quad (9.4b)$$

where φ_b is obtained using Eq. (9.2b). Matching the solution at $x = 0$ leads to,

$$\epsilon\gamma = \zeta_0 k_y. \quad (9.5)$$

Eq. (9.5) can be written as $\epsilon^4 - (\zeta_0^2 + k_y^2)\epsilon^2 + \zeta_0^2 k_y^2 = 0$ which results in four bands $\epsilon = \pm k_y$ and $\epsilon = \pm \zeta_0$. From Eq. (9.5) we notice that these solutions must satisfy $\text{sgn}(k_y \epsilon) > 0$ in addition to the $|\epsilon| < \sqrt{\zeta_0^2 + k_y^2}$ condition. Notice that the flat bands at $\epsilon = -\zeta_0$ (for $k_y < 0$) and $\epsilon = \zeta_0$ (for $k_y > 0$) are not a solution for all k_y values and should be discarded. From Eqs. (9.2) one can simply obtain the valid solution as, $k_y = \zeta_0$ for $\epsilon = \zeta_0$ and $k_y = -\zeta_0$ for $\epsilon = -\zeta_0$. The equations for the K' valley, can be obtained using the $\zeta(x) \rightarrow -\zeta(x)$ transformation in Eqs. (9.2) where it leads to the $\epsilon_{K'} = -k_y$ solution, for the K' valley.

Figure 9.2(a) shows the spectrum for a kink-like mass potential as function of the wavevector along the kink. The shaded region corresponds to the continuum of free states. The solid black curves correspond to the energy levels of a single layer graphene in the presence of an uniform mass potential ζ_0 which can be obtained from Eq. (9.1) as, $\epsilon = \pm\sqrt{k_y^2 + \zeta_0^2}$. The gray dotted horizontal lines correspond to $\epsilon = \pm\zeta_0 = \pm 0.152 = (100 \text{ meV})$ and $\epsilon = 0$. The solid blue line $\epsilon_K = k_y$ and the red dashed line ($\epsilon_{K'} = -k_y$) show the chiral states corresponding to the K and K' valleys, respectively. Notice that these states have an unidirectional character of propagation, i.e. they are chiral states, with positive (negative) group velocity for the K (K') valley. These states are related to the edge states of 2D electrons that are realized in the presence of a perpendicular magnetic field and that are responsible for the quantum Hall effect (QHE). Notice that here these states are realized without a magnetic field. The inset of Fig. 9.2(a) shows the velocity of the carriers for the chiral state which is $+v_F$ for the K valley (blue dotted curve) and $-v_F$ for the K' valley (red dashed curve). The black solid curve displays the velocity of the electrons for a gapped single layer graphene, $\epsilon = \sqrt{k_y^2 + \zeta_0^2}$, and results in the velocity $v/v_F = k_y/\sqrt{k_y^2 + \zeta_0^2}$. Figs. 9.2(b) and 9.2(c) present the real parts of the spinor components and the probability density for (a) $\epsilon_K = k_y$ and (b) $\epsilon_K = -k_y$. These electron states are localized at the position of the kink. Notice that the solutions corresponding to the K and K' valleys are related by the transformations $\varphi_a^{K'} \rightarrow -\varphi_b^K$, $\varphi_b^{K'} \rightarrow \varphi_a^K$ and $k'_y \rightarrow -k'_y$. These uni-directional states move in the opposite direction when they belong to the K and K' valley and therefore are very promising for electronic devices based on *valleytronics* [35, 144]. These chiral states exhibit persistent currents in the y-direction $j_y = \psi^\dagger \sigma_y \psi$ (σ_y is the y-component of the Pauli matrices). In Fig. 9.2(d), the y-component of the persistent current for the K (blue solid curve) and K' (red dashed curve) valleys is shown as function of the x-direction. Notice that the current is localized at the position of the kink interface and the K and K' valleys carry the opposite currents.

9.3 Effect of a small gap between two mass regions

. In order to investigate the stability of these chiral states we consider the effect of a small gap between the two mass regions. We checked numerically that such a gap has qualitatively the same effect as smoothing the step profile of Fig. 9.1(a). We modelled the mass term by, $\zeta(|x| > d/2) = \zeta_0 x/|x|$ and $\zeta(|x| \leq d/2) = 0$. The eigenstates of Eq. (9.3) in the regions $I(x < -d/2)$ and $III(x > d/2)$ are given by Eqs. (9.4a) and (9.4b) respectively and in the gap distance is $\psi_{II} = C e^{i\lambda x} [1, (k_y - i\lambda)/\epsilon]^T + D e^{-i\lambda x} [1, (k_y +$

$i\lambda)/\epsilon]^T$, where $\lambda = \sqrt{\epsilon^2 - k_y^2}$ and d denotes the gap distance between the two mass regions. Matching the solutions at $x = \pm d/2$ and setting the matrix of the coefficients to zero leads to the following equation,

$$[\epsilon\gamma - \zeta_0 k_y][\gamma \sin(d\lambda) + \lambda \cos(d\lambda)] = 0. \quad (9.6)$$

The first part in Eq. (9.6) is the same as Eq. (9.5) (i.e. for the case of $d = 0$) that leads to the above chiral states (i.e. $\epsilon_K = k_y$ and $\epsilon_{K'} = -k_y$). Setting the second part between brackets to zero leads to a transcendental equation that results in extra localized states when $\epsilon > k_y$. These extra bound states for the K' valley can be obtained using the $\zeta_0 \rightarrow -\zeta_0$ transformation in the second part of Eq. (9.6) which results in the same states as for the K valley (i.e. $\epsilon_K = \epsilon_{K'}$ for the extra localized states).

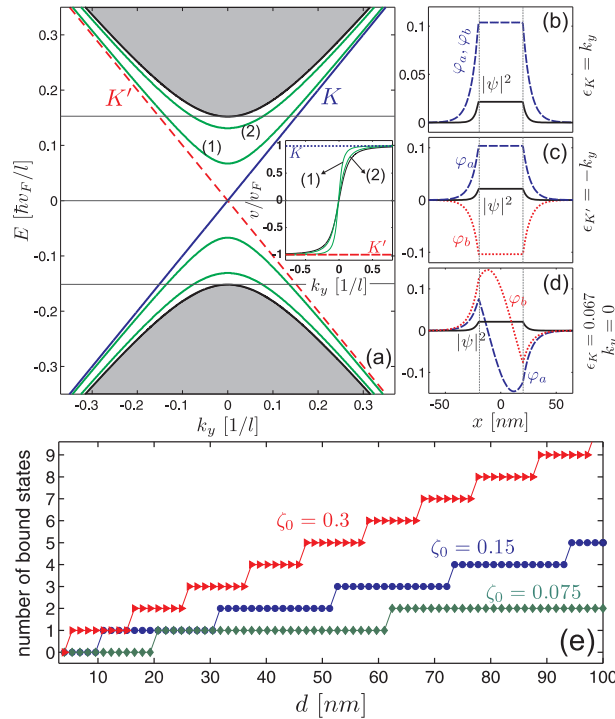


Figure 9.3: (a) Energy levels for a kink mass-potential with a gap distance $d = 40$ nm. (b,c,d) The wave spinors and corresponding probability density. (e) Number of additional bound states as a function of the gap distance. The curves and the parameters are explained in the text.

In Fig. 9.3(a) the energy levels as a function of k_y are shown for the kink profile with a gap of $d = 40$ nm between the two mass regions. Notice that now in addition to

the chiral states several branches (solid green curves) are seen which are split off from the continuum. Increasing the gap distance increases the number of those states that are confined near the kink. The number of these bound states can be related to the height of the mass potential ζ_0 . Figure. 9.3(e) shows the number of these extra bound states for three different ζ_0 values as function of the gap distance d . The first bound state for $\zeta_0 = 0.075, 0.15, 0.3$ appears, respectively, at $d \approx 20, 11, 5$ nm. Notice that the chiral states $\epsilon_K = k_y$ (blue solid line) and $\epsilon_{K'} = -k_y$ (red dashed line) are robust with regard to the smoothing of the step profile (here modeled by the gap distance). The velocity of the carriers corresponding to the chiral states (i.e. $v_K = v_F$ and $v_{K'} = -v_F$) and the additional localized levels (labeled by (1) and (2)) are shown in the inset of Fig. 9.3. The extra bound states have a zero velocity at $k_y = 0$ which is a consequence of the symmetric energy dispersion around $k_y = 0$. The wavefunctions for $\epsilon_K = k_y$ and $\epsilon_{K'} = -k_y$ are respectively shown in the panels (b) and (c). In comparison with the sharp kink mass potential ($d = 0$) the probability density is now uniformly spread out over the distance d . Figure 9.3(d) shows the wavefunction for the first additional bound state (labeled by (1) in Fig. 9.3(a)) at $k_y = 0$ and $\epsilon_K = 0.067$ which is also bound along the x-direction with a probability distribution very similar to the one of the chiral states but where the wavespinors exhibit now a nodal character in the $-d/2 \leq x \leq d/2$ region.

9.4 Superlattice

Now we extend our results to a superlattice (SL) of mass-kinks. Here we use periodic boundary conditions $\psi(0) = e^{ik_x L} \psi(L)$ where L is the periodicity and k_x denotes the wavevector along the x-direction. The kink mass interface is located at $x = L/2$ which is repeated periodically. The solutions ψ_I and ψ_{II} respectively for $x < L/2$ and $x \geq L/2$ regions are given by

$$\psi_I = Ae^{\gamma x} \left[1, \frac{k_y - \gamma}{\epsilon - \zeta_0} \right]^T + Be^{-\gamma x} \left[1, \frac{k_y + \gamma}{\epsilon - \zeta_0} \right]^T, \quad (9.7a)$$

$$\psi_{II} = Ce^{\gamma x} \left[1, \frac{k_y - \gamma}{\epsilon + \zeta_0} \right]^T + De^{-\gamma x} \left[1, \frac{k_y + \gamma}{\epsilon + \zeta_0} \right]^T. \quad (9.7b)$$

where $\gamma = \sqrt{\zeta_0^2 + k_y^2 - \epsilon^2}$. Matching the solutions at $x = L/2$ and imposing the periodic boundary condition we find a set of four algebraic equations that have a solution if

$$[(\epsilon^2 - k_y^2) \cosh(\gamma L) - \zeta_0^2] + \gamma^2 \cos(k_x L) = 0. \quad (9.8)$$

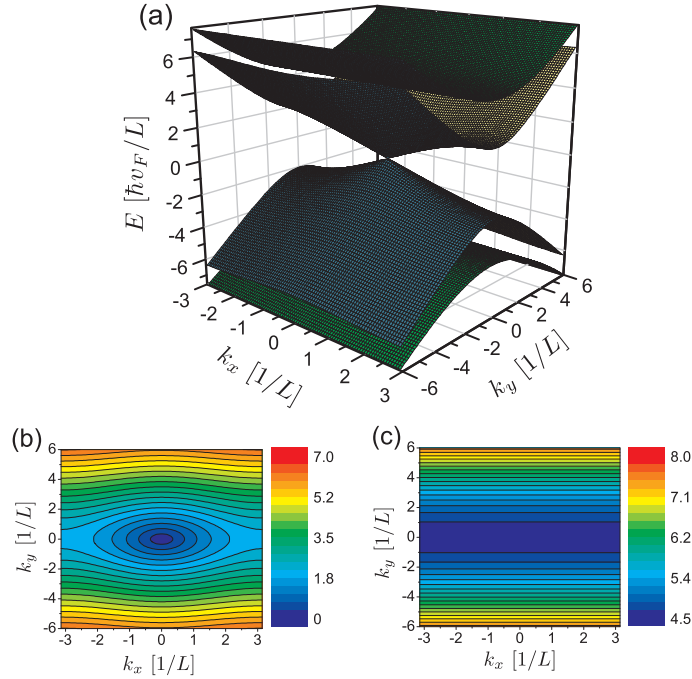


Figure 9.4: (a) 3D plot of the energy bands in the presence of a superlattice of kink mass potentials in single layer graphene with $\zeta_0 = 4.55$ ($= 100$ meV) and $L = 30$ nm. Panels (b) and (c) respectively display the contourplots corresponding to the first and the second conduction bands.

Figure 9.4(a) shows a 3D plot of the energy bands resulting from Eq. (9.8) as function of k_x and k_y near the K point. Panels (b) and (c) are contourplots of $\epsilon_K(k_x, k_y)$ for the first and the second conduction bands, respectively. Two solutions to Eq. (9.8) are $\epsilon_K = \pm\sqrt{k_y^2 + \zeta_0^2}$ (see the upper and lower bands in Fig. 9.4(a)) which denotes the energy bands of gapped graphene with a uniform mass potential. Another solution results in a Dirac cone at $(k_x, k_y) = 0$ which is a consequence of the additional states brought by the antikink steps in the SL system (see intermediate bands in Fig. 9.4(a)). Expanding Eq. (9.8) for $k_x, k_y \rightarrow 0$ and $\epsilon \ll \sqrt{k_y^2 + \zeta_0^2}$ we obtain $\epsilon_k = \pm\sqrt{k_x^2 + k_y^2}$ which demonstrates the linearity of the dispersion relation around the Dirac cone. Such Dirac cones have also been found in graphene superlattices [145].

9.4.1 Ab-initio verification

We supplemented our theoretical treatment with *ab initio* DFT simulations. We used the ABINIT software package [146] to calculate the electronic band structure of graphene on top of a boron nitride substrate with and without the line defect. These calculations were done within the local density approximation (LDA) to obtain a reasonable description of the graphene-BN interlayer interaction [147] and the specific parameters for the the DFT calculations were the same as given in Ref. [147]. The specific model structure that we

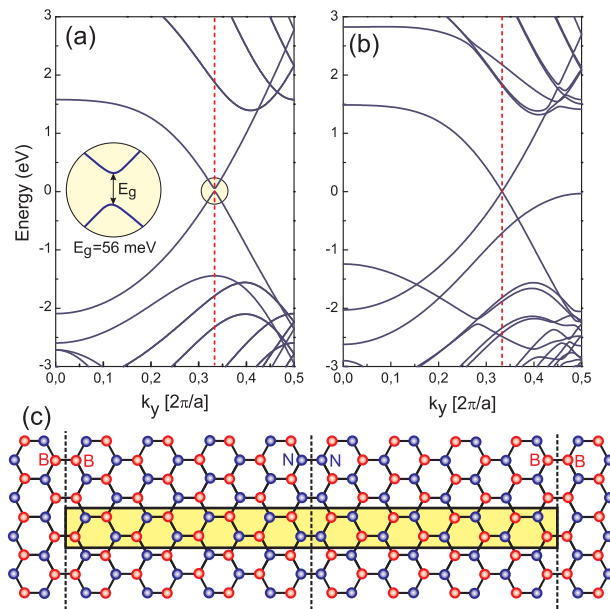


Figure 9.5: The band structure obtained within DFT for (a) graphene on top of an uniform layer of a BN substrate and (b) graphene on top of a BN substrate with a periodic area of line defects. The vertical dashed line indicates the position of the K point. The structure that is simulated is shown in (c): the supercell is indicated by the yellow rectangle and the dashed vertical lines indicate the position of the line defects.

used consists of a rectangular graphene supercell containing 32 C atoms on top of a BN substrate where the relaxed distance between the BN substrate and graphene is set to 3.24 (see Fig. 9.5(c)). The line of defects are taken along the zigzag direction and consists of alternating B-B and N-N defect lines separated by defect-free h-BN regions with a width of approximately 2 nm. In Fig. 9.5(a,b), the electronic band structure of the investigated systems, calculated along the k_y -direction and through the Γ -point, is shown. As can be seen from Fig. 9.5(a), a band gap, i.e. ≈ 56 meV, is opened when graphene is placed on top of a perfect BN substrate. When the line of defects, corresponding to a kink in the

mass potential, is added, the band gap closes and the linear spectrum at the K -point is recovered (see Fig. 9.5(b)). This is in agreement with the analytical results derived before. Note that there are some differences between the band spectra as obtained with DFT and the analytical result for a superlattice (Fig. 9.5(b) and Fig. 9.4, respectively): (i) There are additional bands in the DFT spectrum because of the explicit incorporation of the boron nitride substrate in the calculations. (ii) The parabolic bands are shifted to larger k_y -point (i.e. away from the K -point) and are situated farther away from the Fermi-level. This can be attributed to the relatively small size of the supercell in the DFT calculations as compared to the continuum model.

9.5 Conclusion

In summary, we predicted new chiral states in the presence of an asymmetric (kink profile) mass-potential in *single* layer graphene. Our study showed that these states are robust even when a small gap is located between the two mass regions. The system can be realized experimentally using a boron-nitride substrate with a line defect that induces an asymmetric mass potential in graphene. These 1D chiral states were also investigated within *ab-initio* calculations for a superlattice of line defects. Throughout our calculations we showed that the chiral states corresponding to the K and K' valleys exhibit opposite direction of propagation which is a consequence of their chiral nature. Nano-structuring of such line defects in the h-BN substrate can be very promising for the fabrication of electronic devices for *valleytronics*. Graphene dots with perfect zigzag edges, were earlier proposed for valleytronics applications [35]. The realization of perfect zigzag edges is very challenging and this disadvantage does not arise in our case, where the asymmetric mass potential is induced by a line of defects in the h-BN substrate.

CHAPTER 10

Chiral states in bilayer graphene

At the interface of electrostatic potential kink profiles one dimensional chiral states are found in bilayer graphene (BLG). Such structures can be created by applying an asymmetric potential to the upper and the lower layer of BLG. We found that: i) due to the strong confinement by the single kink profile the uni-directional states are only weakly affected by a magnetic field, ii) increasing the smoothness of the kink potential results in additional bound states which are topologically different from those chiral states, and iii) in the presence of a kink-antikink potential the overlap between the oppositely moving chiral states results in the appearance of crossing and anti-crossing points in the energy spectrum. This leads to the opening of tunable minigaps in the spectrum of the uni-directional chiral states.

10.1 Introduction

It was recently recognized that a tunable energy gap in BLG can allow the observation of new confined electronic states, which could be obtained by applying a spatially varying potential profile to create a position-dependent gap analogous to semiconductor heterojunctions [29, 131].

The results of this chapter were published as
M. Zarenia, J. M. Pereira Jr., G. A. Farias, and F. M. Peeters, Phys. Rev. B **84**, 125451 (2011), and
M. Zarenia, J. M. Pereira Jr., F. M. Peeters, and G. A. Farias, Nanoscale Research Letters **6**, 452 (2011).

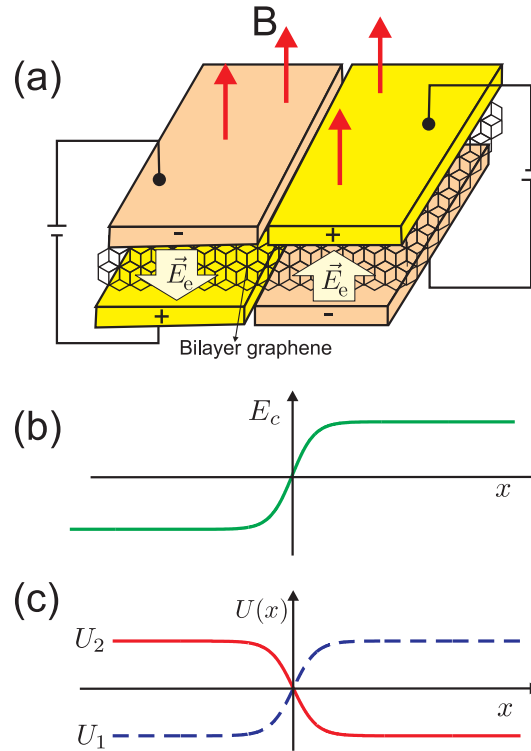


Figure 10.1: (a) Schematic illustration of the non-uniformly gated bilayer graphene device for the creation of a kink potential. Applied gated voltage to the upper and lower layers with opposite sign induces an electric field \vec{E}_e , with preferential direction. An external magnetic field $\mathbf{B} = B \hat{z}$, is applied perpendicular to the bilayer graphene sheets. (b) Electric field between the two graphene layers. (c) Potential on layer 1 (U_1) and layer 2 (U_2).

An alternative way to create one dimensional localized states in BLG has recently been suggested by Martin *et al.* [34] and relies on the creation of a potential *kink* by an asymmetric potential profile (see Fig. 10.1). Such kink potential can also be realized in p-n junctions [110] or in a graphene sheet on top of a substrate with a line defect [148]. They showed that localized chiral states arise at the location of the kink, with energies inside the energy gap. These states correspond to unidirectional motion of electrons which are analogous to the edge states in a quantum Hall system. From a practical standpoint, the kinks may be envisaged as configurable metallic nanowires embedded in a semiconductor medium. Moreover, the carrier states in this system are expected to be robust with regards to scattering and may display Luttinger liquid behavior [138].

An additional tool for the manipulation of charged states in BLG is the use of magnetic

fields. The application of an external magnetic field perpendicular to the BLG sheet causes the appearance of Landau levels which can be significantly modified by the induced gap, leading to effects such as the lifting of valley degeneracy caused by the breaking of the inversion symmetry by the electrostatic bias [149, 150]. Recently the transport properties of p-n-p junctions in bilayer graphene were experimentally investigated in the presence of a perpendicular magnetic field [139].

Here we generalize previous work on topological confinement in bilayer graphene [34] on three levels: *i*) we investigate the effect of smoothing the kink potential on the topological states, *ii*) the effect of a perpendicular magnetic field is studied, and *iii*) we investigate a new system that consists of a coupled kink-antikink structure. We demonstrate that the latter opens a gap in the 1D electron states.

10.2 Model

We employ a two-band continuum model to describe the BLG sheet. In this model, the system is described by four sublattices, two in the upper (A , B) and two in the lower (A' and B') layer [39]. The interlayer coupling is given by the hopping parameter $\gamma \approx 400 \text{ meV}$ between sites A and B' . The Hamiltonian around the K valley of the first Brillouin zone can be written as

$$H = -\frac{1}{\gamma} \begin{bmatrix} 0 & (\pi^\dagger)^2 \\ (\pi)^2 & 0 \end{bmatrix} + \begin{bmatrix} U(x) & 0 \\ 0 & -U(x) \end{bmatrix} \quad (10.1)$$

where $\pi = v_F(p_x + ip_y)$, $p_{x,y} = -i\hbar\partial_{x,y} + eA_{x,y}$ is the momentum operator in the presence of an external magnetic field with $A_{x,y}$ being the components of the vector potential \mathbf{A} , $v_F = 10^6 \text{ m/s}$ is the Fermi velocity, $U(x)$ and $-U(x)$ is the electrostatic potential respectively applied to the upper and lower layers. The eigenstates of the Hamiltonian Eq. (10.1) are two-component spinors $\Psi(x, y) = [\psi_a(x, y), \psi_b(x, y)]^T$, where $\psi_{a,b}$ are the envelope functions associated with the probability amplitudes at sublattices A and B' at the respective layers of the BLG sheet. Since $[H, p_y] = 0$ the momentum along the y -direction is a conserved quantity and therefore we can write:

$$\psi(x, y) = e^{ik_y y} [\varphi_a(x), \varphi_b(x)]^T \quad (10.2)$$

where, k_y is the wave vector along the y direction.

In order to apply a perpendicular magnetic field to the bilayer sheet we employ the Landau gauge for the vector potential $\mathbf{A} = (0, Bx, 0)$. The Hamiltonian (10.1) acts on the wave function of Eq. (10.2) which leads to the following coupled second-order differential

equations,

$$\left[\frac{\partial}{\partial x'} + (k'_y + \beta x')\right]^2 \varphi_b = [\epsilon - u(x')] \varphi_a, \quad (10.3a)$$

$$\left[\frac{\partial}{\partial x'} - (k'_y + \beta x')\right]^2 \varphi_a = [\epsilon + u(x')] \varphi_b. \quad (10.3b)$$

where, in the above equations we used dimensionless units $x' = x/l$, $k'_y = k_y l$, $\epsilon = E/\gamma$, and $u(x') = U(x)/\gamma$ where $l = \hbar v_F/\gamma = 1.6455 \text{ nm}$, $\beta = (eB/\hbar)l^2$ ($= 0.0041$ for $B = 1 \text{ T}$). The step-like kink (see Fig. 10.1(c)) is modeled by

$$u(x') = u_b \tanh(x'/\delta), \quad (10.4)$$

where u_b is the maximum value of the gate voltage, in dimensionless unit, in each BLG layer. Here, δ denotes the width of the region in which the potential switches its sign in each layer. This parameter is determined by the distance between the gates used to create the gap. Next, we numerically solve Eqs. (3) to obtain the dependence of the energy levels on the magnetic field and potential parameters. For the case of a sharp kink potential $\delta \rightarrow 0$ and in the absence of a magnetic field, i.e. $B = 0$, Eqs. (10.3) reduces to

$$\left[\frac{\partial}{\partial x'} + k'_y\right]^2 \varphi_b = [\epsilon - u(x')] \varphi_a, \quad (10.5a)$$

$$\left[\frac{\partial}{\partial x'} - k'_y\right]^2 \varphi_a = [\epsilon + u(x')] \varphi_b. \quad (10.5b)$$

where $u(x') = u_b[\Theta(x') - \Theta(-x')]$. We simply decouple Eqs. (10.5) and obtain

$$\left[\frac{\partial^2}{\partial x'^2} + \lambda_{\pm}^2\right] \varphi_a = 0 \quad (10.6)$$

where, $\lambda_{\pm} = [-k_y'^2 \pm \sqrt{\epsilon^2 - u_b^2}]^{1/2}$ which can be a complex quantity. The solution for $x' < 0$ ($\psi^<$) and $x' \geq 0$ ($\psi^>$) are given by

$$\psi(x')_{\pm}^< = \begin{pmatrix} e^{i\lambda_{\pm} x'} \\ f_{\pm} e^{i\lambda_{\pm} x'} \end{pmatrix}, \quad (10.7a)$$

$$\psi(x')_{\pm}^> = \begin{pmatrix} e^{-i\lambda_{\pm} x'} \\ g_{\pm} e^{-i\lambda_{\pm} x'} \end{pmatrix} \quad (10.7b)$$

where, $f_{\pm} = (i\lambda_{\pm} - k'_y)^2/(\epsilon - u_b)$, and $g_{\pm} = (i\lambda_{\pm} + k'_y)^2/(\epsilon + u_b)$. The above solutions should satisfy the asymptotics $\varphi_{a,b}^>(x' \rightarrow \infty) = 0$ and $\varphi_{a,b}^<(x' \rightarrow -\infty) = 0$. Matching the

solutions and the first derivatives at $x' = 0$ gives a homogeneous set of algebraic equations which in matrix form becomes

$$\begin{pmatrix} 1 & 1 & -1 & -1 \\ f_+ & f_- & -g_+ & -g_- \\ \lambda_+ & \lambda_- & \lambda_+ & \lambda_- \\ f_+\lambda_+ & f_-\lambda_- & g_+\lambda_+ & g_-\lambda_- \end{pmatrix} \begin{pmatrix} C_1 \\ C_2 \\ C_3 \\ C_4 \end{pmatrix} = 0. \quad (10.8)$$

Solutions are found when the determinant of the matrix is set to zero from which we obtain the energy spectrum. Notice that Eq. (10.8) leads to four solutions, of which two of them, i.e. $\pm u_b$, do not satisfy Eqs. (10.5) and are not acceptable. In the limiting case $\epsilon \ll u_b$ we are able to obtain an analytical expression for the energy,

$$\begin{aligned} \epsilon_{\pm} = \frac{u_b}{\alpha} \times \left\{ 4k'_y \sqrt{\epsilon_0} [u_b \sin(\theta/2) + k'_y{}^2 \cos(\theta/2)] \right. \\ \left. \pm [56k'_y{}^8 + 14u_b^4 + 70u_b^2 k'_y{}^4 - k'_y{}^2 \epsilon_0 (40k'_y{}^4 + 46u_b^2)]^{1/2} \right\}. \end{aligned} \quad (10.9)$$

where, $\epsilon_0 = \sqrt{k'_y{}^4 + u_b^2}$, $\alpha = 6k'_y{}^4 + 7u_b^2 - 6k'_y{}^2 \epsilon_0$ and $\theta = \tan^{-1}(u_b/k'_y{}^2)$. Solving the above equation for $\epsilon = 0$ we find that $k'_y = \pm \sqrt{u_b/\sqrt{8}}$ (≈ 0.3 for $u_b = 0.25$).

Next we consider a sharp kink potential in parallel with an antikink potential which are located at $x' = -d$ and $x' = +d$. In this case we have to consider three regions, i.e. $x' > d$ ($\psi_I(x')$), $-d \leq x' \leq -d$ ($\psi_{II}(x')$) and $x' < -d$ ($\psi_{III}(x')$) and the solutions are given by

$$\psi_I(x')_{\pm} = \begin{pmatrix} e^{i\lambda_{\pm} x'} \\ g_{\pm} e^{i\lambda_{\pm} x'} \end{pmatrix}, \quad (10.10a)$$

$$\psi_{II}(x')_{\pm} = \begin{pmatrix} e^{\pm i\lambda_{\pm} x'} \\ f_{\pm} e^{i\lambda_{\pm} x'} \end{pmatrix}, \quad (10.10b)$$

$$\psi_{III}(x')_{\pm} = \begin{pmatrix} e^{-i\lambda_{\pm} x'} \\ g_{\pm} e^{-i\lambda_{\pm} x'} \end{pmatrix} \quad (10.10c)$$

Matching the solutions and their first derivatives at $x' = \pm d$ leads to a set of eight algebraic

equations which in matrix form becomes $\mathbf{FC} = \mathbf{0}$ where

$$F = \begin{pmatrix} \kappa_+^- & \kappa_-^- & -\kappa_+^- & -\kappa_-^- & -\kappa_+^+ & -\kappa_-^- & 0 & 0 \\ g_+\kappa_+^- & g_-\kappa_-^- & -f_+\kappa_+^- & -f_-\kappa_-^- & -f_+\kappa_+^+ & -f_-\kappa_-^- & 0 & 0 \\ \lambda_+\kappa_+^- & \lambda_-\kappa_-^- & -\lambda_+\kappa_+^- & -\lambda_-\kappa_-^- & \lambda_+\kappa_+^+ & \lambda_-\kappa_-^- & 0 & 0 \\ g_+\lambda_+\kappa_+^-g_-\lambda_-\kappa_-^- - f_+\lambda_+\kappa_+^- - f_-\lambda_-\kappa_-^- & f_+\lambda_+\kappa_+^+ & f_-\lambda_-\kappa_-^- & 0 & 0 \\ 0 & 0 & \kappa_+^+ & \kappa_-^+ & \kappa_+^- & \kappa_-^- & -\kappa_+^- & -\kappa_-^- \\ 0 & 0 & f_+\kappa_+^+ & f_-\kappa_-^+ & f_+\kappa_+^- & f_-\kappa_-^- & -g_+\kappa_+^- & -g_-\kappa_-^- \\ 0 & 0 & \lambda_+\kappa_+^- & \lambda_-\kappa_-^- & -\lambda_+\kappa_+^- & -\lambda_-\kappa_-^- & \lambda_+\kappa_+^- & \lambda_-\kappa_-^- \\ 0 & 0 & f_+\lambda_+\kappa_+^+ & f_-\lambda_-\kappa_-^+ & -f_+\lambda_+\kappa_+^- & -f_-\lambda_-\kappa_-^- & g_+\lambda_+\kappa_+^- & g_-\lambda_-\kappa_-^- \end{pmatrix} \quad (10.11)$$

and $\mathbf{C} = [C_1, C_2, \dots, C_8]^T$. $\kappa_\pm^+ = \exp(i\lambda_\pm d)$ and $\kappa_\pm^- = \exp(-i\lambda_\pm d)$. Setting the determinant to zero gives the energy spectrum.

10.3 Single kink

10.3.1 Influence of the smoothness of the kink profile

In the general case of $\delta \neq 0$ we solve the set of second order differential Eqs. 10.3(a,b) numerically, using the finite difference technique. Figure 10.2(a) shows the spectrum for a single potential kink as function of the wavevector along the kink for zero magnetic field. We consider a relatively sharp kink, i.e. $\delta = 1$, and compare the numerical results with the analytical solution (dashed black curves) from Eq. (10.8) for the case of a sharp profile ($\delta = 0$). The shaded region corresponds to the continuum of free states. The solid red curves correspond to the energy levels of a biased BLG which can be obtained using Eq. (10.1) as,

$$\epsilon = \pm \sqrt{k_y'^4 + u_b^2} \quad (10.12)$$

The dotted horizontal lines correspond to $\epsilon = \pm u_b = \pm 0.25$ and $\epsilon = 0$. These results are valid in the vicinity of a single valley (K) and show that the topological states have a unidirectional character of propagation, i.e. they are chiral states [34], with positive group velocity. The topological levels can be fitted to $\epsilon = a\sqrt{(k_y' - k_0)^4 + (u_b/a)^2} - 1/2$ with $a = 0.5$ and $k_0 = -0.65$ being the fitting parameters (see green solid curve). For localized states around the K' valley, we have $E_{K'}(k_y) = -E_K(k_y)$ and the charge carriers move in the opposite direction. In order to consider the energy levels for the K' valley, $u(x)$ in Eqs. (3) should be replaced with $-u(x)$. Then using the transformations $\epsilon \rightarrow -\epsilon$ and $\varphi_a \rightarrow -\varphi_a$ (or $\varphi_b \rightarrow -\varphi_b$) leads to the same equation as for the K valley. Thus the $E_K(k) = -E_{K'}(k)$ symmetry remains even in the presence of an uniform perpendicular

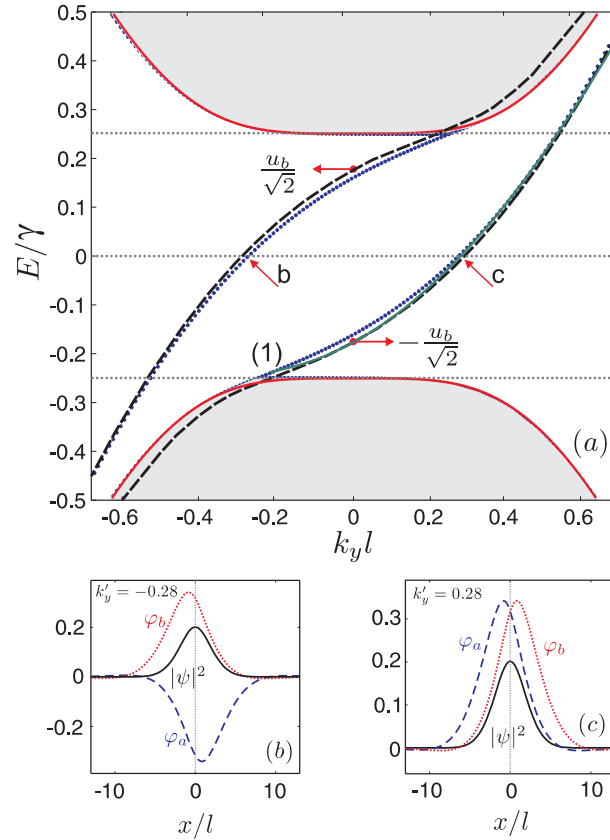


Figure 10.2: (a) Energy levels for a single kink profile on bilayer graphene with $u_b = 0.25$. Dotted curves are the numerical results for $\delta = 1$ and dashed curves are the analytical results for $\delta = 0$ using Eq. (10.8). The solid red curves are the energy levels of a biased BLG. The solid green curve (indicated by the symbol (1)) shows a fitted function to the numerical results. The lower panels show the wave spinors and probability density corresponding to the states that are indicated by the arrows (b) and (c) in panel (a).

magnetic field (i.e. $\beta \neq 0$). Notice that the wavespinors corresponding to the K and the K' valleys are related to each other by $\varphi_a^K \rightarrow -\varphi_a^{K'}$ (or $\varphi_b^K \rightarrow -\varphi_b^{K'}$) while the sign of the other component does not change.

Panels (b) and (c) of Fig. 10.2 present the real parts of the spinor components and the probability density for the states indicated by the arrows (b) and (a) in panel (a), corresponding to $k'_y = -0.28$ (b) and $k'_y = 0.28$ (c). These electron states are localized at the position of the potential kink. Notice that the solutions of Eqs. (3) are related by the transformations $\varphi_a \rightarrow -\varphi_b$, $\varphi_b \rightarrow \varphi_a$, $k'_y \rightarrow -k'_y$ and $\epsilon \rightarrow -\epsilon$ and consequently for $\epsilon = 0$

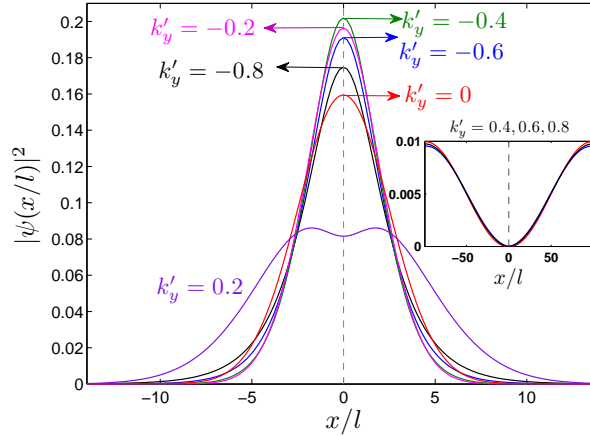


Figure 10.3: The probability densities of the left topological state in Fig. 10.2(a), i.e. including point b, for $k'_y = -0.8, -0.6, -0.4, -0.2, 0.2$. The inset shows the probability density for $k'_y = 0.4, 0.6, 0.8$

the solutions in Figs. 10.2(b) and 10.2(c) have the same probability distribution. For the case of $k'_y = 0$ the solutions of Eq. (10.8) are $\epsilon_{\pm} = \pm u_b / \sqrt{2}$ which result in the following wavespinors,

$$\varphi_a^< = (1 \mp \sqrt{2}) [e^{-i(\lambda_+ x' + \frac{\pi}{4})} \mp e^{i(\lambda_- x' + \frac{\pi}{2})}], \quad (10.13a)$$

$$\varphi_a^> = e^{i(\lambda_+ x' + \frac{\pi}{4})} \mp e^{-i\lambda_- x'}, \quad (10.13b)$$

$$\varphi_b^< = -\frac{(1 \mp \sqrt{2})}{(\epsilon_{\pm} - u_b)} [\lambda_+^2 e^{-i(\lambda_+ x' + \frac{\pi}{4})} \mp \lambda_-^2 e^{i(\lambda_- x' + \frac{\pi}{2})}], \quad (10.13c)$$

$$\varphi_b^> = \frac{-1}{\epsilon_{\pm} + u_b} [\lambda_+^2 e^{i(\lambda_+ x' + \frac{\pi}{4})} \mp \lambda_-^2 e^{-i\lambda_- x'}]. \quad (10.13d)$$

where, $\lambda_{\pm} = (1 \pm i)\sqrt{u_b/8}$. Notice that in the above equations $e^{\pm i\lambda_{\pm} x'}$ leads to an oscillating contribution $e^{\pm i\Re(\lambda_{\pm})x'}$ with an evanescent $e^{\mp \Im(\lambda_{\pm})x'}$ part. The oscillating part is strongly damped and therefore Eqs. (10.13) corresponds to localized wavespinors. Expanding Eqs. (10.13) around $x' = 0$ we obtain for the second derivative of the wavespinors,

$$\frac{\partial^2}{\partial x'^2} \Re[\varphi_a^<(x' \rightarrow 0)] = (1 \pm \sqrt{2})(2 + \sqrt{2})(u_b/8)^{1/2}, \quad (10.14a)$$

$$\frac{\partial^2}{\partial x'^2} \Re[\varphi_b^<(x' \rightarrow 0)] = \frac{(4 - 2\sqrt{2})(u_b/8)^{3/2}}{\epsilon_{\pm} - u_b} < 0. \quad (10.14b)$$

This indicates that $\Re[\varphi_a](\Re[\varphi_b])$ has its maximum value located at $x' < 0(x' > 0)$ for $\epsilon_+ = u_b/\sqrt{2}$ while the opposite is found for $\epsilon_- = -u_b/\sqrt{2}$ which is also evident from Figs. 10.2(b,c).

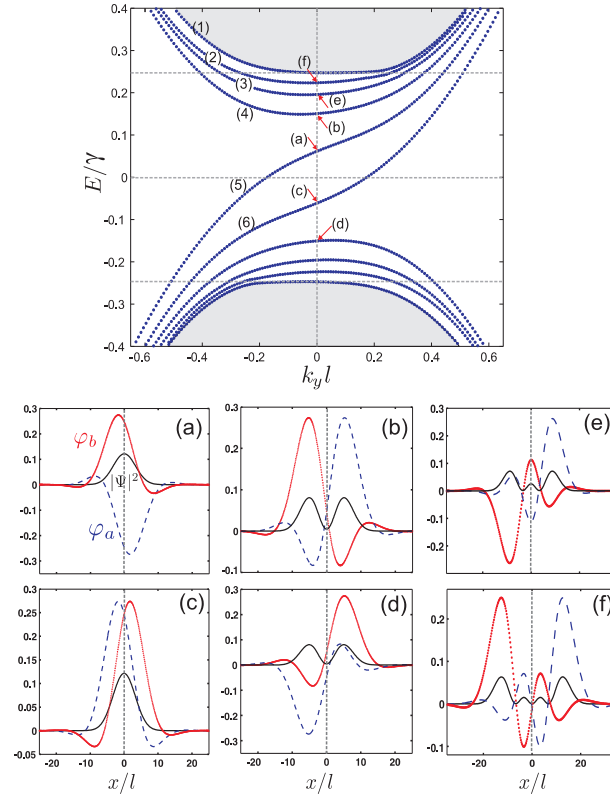


Figure 10.4: Upper panel: Energy levels for a single kink profile in bilayer graphene with $u_b = 0.25$ and $\delta = 10$. The energy states indicated by (a) and (c) are chiral states and those indicated by (b),(d),(e) and (f) are the extra-bound states. Lower panels: Real parts of the wave spinors and the corresponding probability density for the two first electron and hole energy levels at $k'_y = 0$ as indicated in the upper panel.

In Fig. 10.3 we show the probability densities corresponding to one of the topological branches (for the state which includes point b in Fig. 10.2(a)) at several k'_y values. As shown in the inset of Fig. 10.3 for those k'_y values where the topological state merged with the continuum spectrum the carriers are no longer confined by the kink potential.

Next we increase the smoothness of the kink potential and investigate how the energy spectrum changes. In Fig. 10.4 the energy levels as function of k_y are shown for the smooth kink profile $\delta = 10$, where in addition to the chiral states several branches are seen

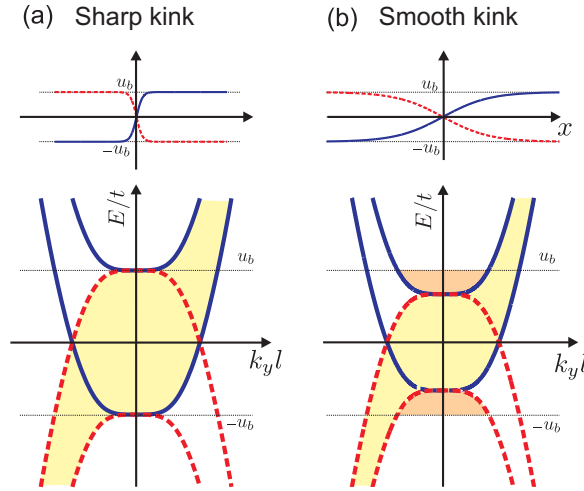


Figure 10.5: Upper panels: applied potential profile $u(x)$ to the upper (solid blue curve) and the lower layer (red dashed curve) for (a) sharp and (b) smooth kink profiles. Lower panel: schematic representation of the energy spectrum in (E, k_y) space, corresponding to the blue and red dashed potential profiles near the kink region. Topological states can be found in the yellow region. For the smooth profile (b), extra bound states can be found in the orange region.

which are split off from the continuum. In order to understand the physical origin of those new states we show in the lower panels of Fig. 10.5 a cartoon of the low energy spectra for the (a) sharp and (b) smooth profiles where, the chiral states appear in the yellow regions and those additional states are found in the orange region. Increasing the smoothness of the kink potential leads to the creation of a region below the energy gap which allows for carriers to be confined near the kink. Therefore, extra bound states can be created in the orange region (lower panel in Fig. 10.5(b)). The wavefunctions for $k_y = 0$ of the two chiral states and the new bound states are shown in the lower panels of Fig. 10.4. The new bound states are also bound in the x -direction near $x = 0$ but the electron states are more extended and have a clear nodal character near $x = 0$.

Figure 10.6 shows the velocity of the carriers for the states which are indicated by (1), (2), ..., (6) in Fig. 10.4. The chiral states ((5),(6)) are only shown for the K valley and they have positive velocity. The curves (5),(6) can be fitted to $v/v_F \approx a\sqrt{(k'_y - k'_0)^2 + b^2}$ (see the solid gray curves) with $a = 1.8, b = 0.15$ being the fitting parameters and $k'_0 = \pm 0.08$ corresponds to the minimum point in the curves (5) and (6). Notice that the extra bound states ((2), (3), (4)) have a slightly nonzero velocity at $k'_y = 0$ which is a

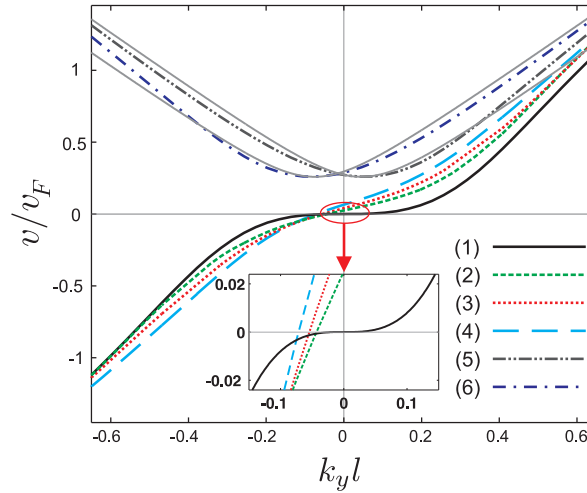


Figure 10.6: The carrier velocity in the single kink profile for the energy levels which are indicated by (1), (2), ..., (6) in Fig. 10.4. The gray solid curves are the fitted functions to curve (5) and (6).

consequence of the asymmetric energy dispersion as seen in Fig. 10.4. Curve (1) corresponds to the energy spectrum of a biased BLG which is given by Eq. (10.12) and results in the velocity $v/v_F = [\partial\epsilon/\partial k'_y] = 2k'_y{}^3/\sqrt{k'_y{}^4 + u_b^2}$ which is zero for $k'_y = 0$ in a biased BLG (black solid curve in Fig. 10.6).

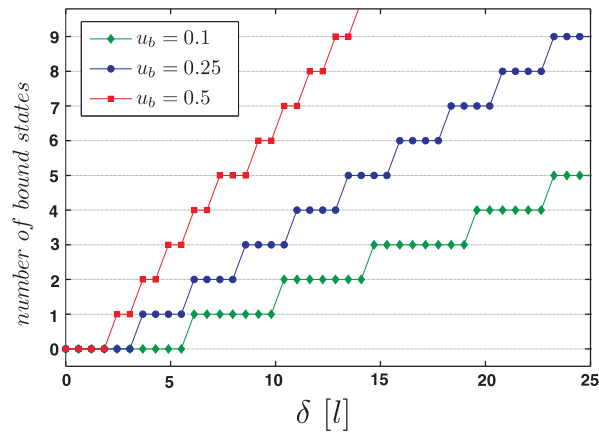


Figure 10.7: Number of additional bound states as function of the width of the interface δ for $u_b = 0.1, 0.25$ and 0.5 .

As mentioned before for smooth kink potentials additional 1D bound states appear and the number of these bound states can be related to the height of the gate voltage u_b and the smoothness(δ) at the interface. Figure 10.7 shows the number of these extra bound states for three different u_b values as function of the width δ . The first bound state for $u_b = 0.1, 0.25, 0.5$ appears respectively at $\delta \approx 6, 4, 2$ in the absence of magnetic field. Notice also that for fixed δ the number of extra bound states increases with u_b in agreement with the qualitative picture shown in Fig. 10.5(b).

We also calculate the transmission of an electron through the kink structure in a system of size $-L_x/2 < x < L_x/2$ and $-L_y/2 < y < L_y/2$. No bias nor magnetic field is assumed in the $x < -L_x/2$ and $x > L_x/2$ regions. We assume that $L_y \gg L_x$ and the electrons are free to move in the y -direction whereas, they are confined in the x -direction. Associated with each real λ_{\pm} there are two right(left) propagating modes, $\psi_{\pm}^>(\psi_{\pm}^<)$ which are given by Eqs. (10.7). In the region I ($x < -L_x/2$) two incident right-traveling modes $\psi_{\pm}^>$ can be reflected into two left-traveling modes $\psi_{\pm}^<$,

$$\Psi_{\pm}^I = \psi_{\pm}^> + r_{\pm}^+ \psi_{+}^< + r_{\pm}^- \psi_{-}^<. \quad (10.15)$$

where, t_{\pm}^{\pm} (r_{\pm}^{\pm}) are the transmission (reflection) amplitudes. The propagating modes in region I can also be transmitted to region III ($x > L_x/2$) in the right-traveling modes,

$$\Psi_{\pm}^{III} = t_{\pm}^+ \psi_{+}^> + t_{\pm}^- \psi_{-}^>. \quad (10.16)$$

The wevefunctions in regions I and III can be connected by the transfer matrix M where at the kink-potential boundaries we have

$$\Psi_{\pm}^I(-L_x/2) = M \Psi_{\pm}^{III}(L_x/2). \quad (10.17)$$

The transmission (or reflection) amplitude can be found by substituting Eqs. (10.15) and (10.16) in the above equation. The four transmission amplitudes t_{\pm} for given ϵ and k_y can be combined in the transmission matrix

$$t(\epsilon, k_y) = \begin{pmatrix} t_{+}^+ & t_{-}^+ \\ t_{+}^- & t_{-}^- \end{pmatrix}. \quad (10.18)$$

The total transmission amplitude T is given by [151] $T = Tr(tt^{\dagger})$. The two-terminal conductance of such an asymmetric potential profile in bilayer graphene can be calculated using the Landauer formula which is given by [152, 153]

$$G = G_0 \int T(E_F, k'_y) dk'_y \quad (10.19)$$

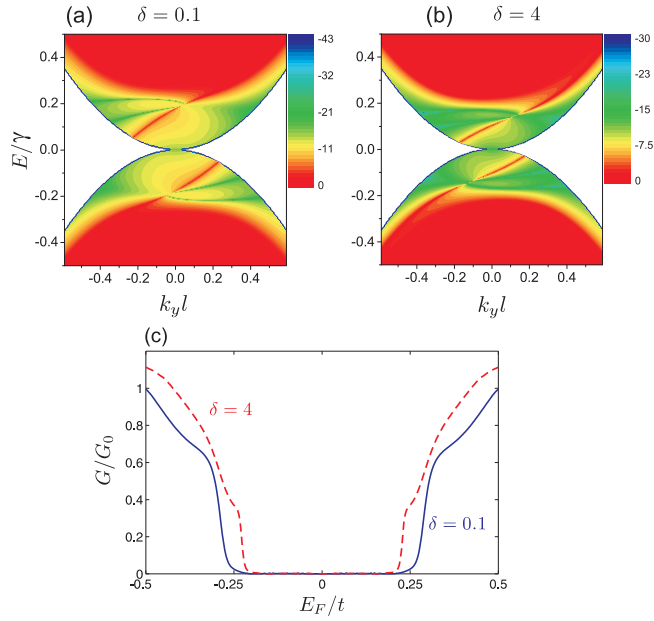


Figure 10.8: (a,b) Contour plot of the transmission T (in logarithmic scale) through a single kink structure with $L_x = 20$ (≈ 32 nm), $u_b = 0.25$ for (a) $\delta = 0.1$ and (b) $\delta = 4$. (c) Conductance G/G_0 vs Fermi energy of a single kink profile for the same parameters as (a,b).

Here, $G_0 = (2e^2/h)(L_y|E_F|/\pi\hbar v_F)$ is the conductance unit per valley and per spin. In Figs. 10.8(a,b) we show a contour plot of the transmission probability in logarithmic scale for the kink structure with $L_x = 20$ (in dimensionless unit). The transmission probability has the symmetry $T(k_y, E) = T(-k_y, -E)$. The conductance as function of the Fermi energy for the single kink profile is shown in panel (c) for $\delta = 0.1$ (blue solid curve) and $\delta = 4$ (red dashed curve). For the case $\delta = 4$ the smoothness of the potential at $x = 0$ leads to a higher transmittance and consequently a higher conductance around $\epsilon \approx u_b$ (see panel (b) and the dashed curve in panel (c)).

10.3.2 Magnetic field dependence

Dependence of the energies of the 1D bound states on an external magnetic field is shown in Fig. 10.9 for (a) $k'_y = 0$ and (b) $k'_y = 0.15$. In order to show the effect of a magnetic field on the chiral states (blue solid curves) and the other localized bound states (red dashed curves) we present the results for a smooth potential (i.e. $\delta = 10$). It is seen that the chiral states are very weakly influenced by the magnetic field. This is a consequence of the

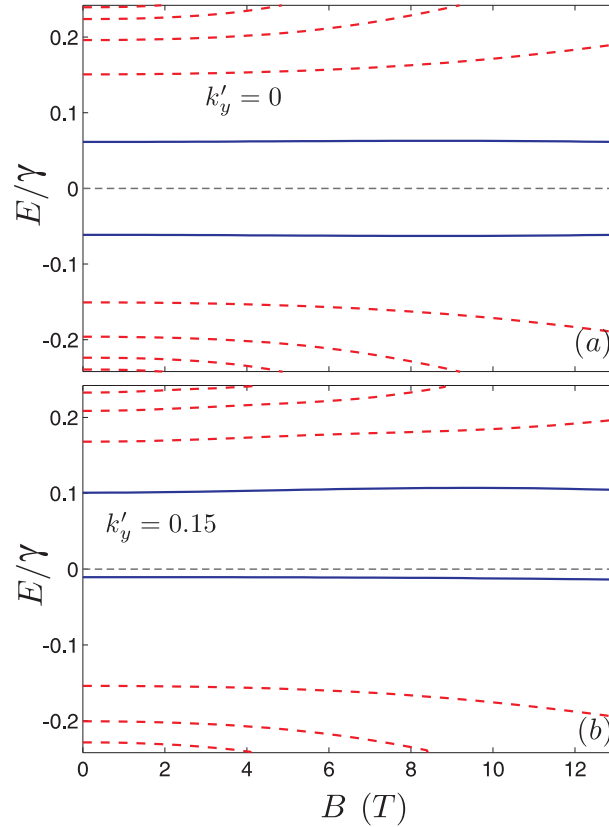


Figure 10.9: Energy levels of a single potential kink profile as function of the external magnetic field with $u_b = 0.25$ and $\delta = 10$ for (a) $k_y l = 0$ and (b) $k_y l = 0.15$. The full blue curves are the topological states and the dashed red curves are the extra bound states.

strong confinement of these states in the kink potential (see Fig. 10.3 and Fig. 10.4(a,c)). In a semiclassical view, the movement of the carriers is constrained by the kink potential and that together with the unidirectional propagation, prevents the formation of cyclotron orbits. For the energy levels above the chiral states, the energy values increase as the magnetic field increases, because of the weaker confinement of these states as is apparent from Figs. 10.4(b,d,e,f).

Figure 10.10 shows the spectrum of a sharp ($\delta = 1$) single kink potential in the presence of an external magnetic field $B = 7 T$ as function of the orbit center $X_c = k_y l_B^2 / l$ where $l_B = \sqrt{\hbar / eB}$ is the magnetic length. The solid lines represent the applied kink potential to upper (black) and lower (green) layer. The results show that the topological states are practically not affected by the magnetic field. The free energy region (i.e. $|\epsilon| > u_b$) in the absence of magnetic field now is replaced with Landau levels (the solid red

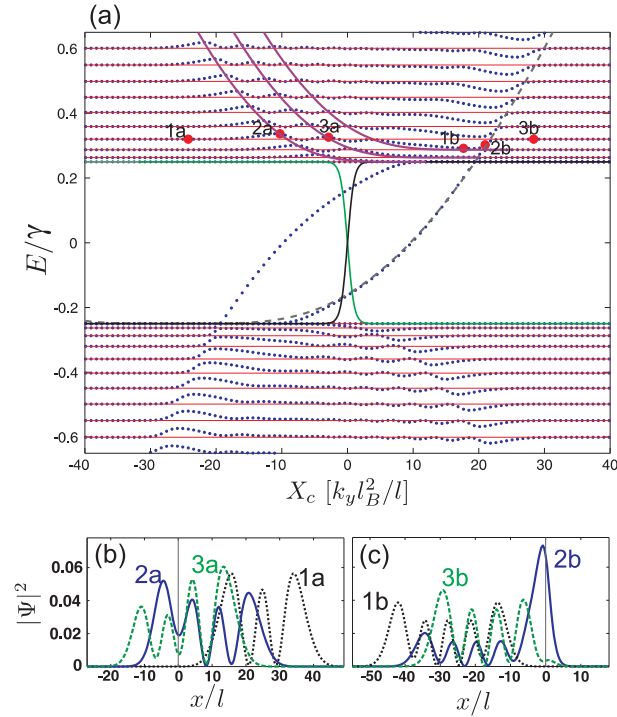


Figure 10.10: (a) Energy spectrum of a single kink profile in bilayer graphene as function of the cyclotron orbit coordinate X_c for $B = 7 T$, $u_b = 0.25$ and $\delta = 1$. The dashed gray curve shows a fitted function to the numerical results. The solid black and green curves are respectively the potential in the upper and lower layer. Solid red lines corresponds to the Landau levels of a biased BLG. The solid purple curves show fitted functions (given in the text) to the position of the resonances. (b,c) The probability densities for the indicated points by red full circles in the spectrum.

lines are the Landau levels of a biased bilayer graphene). In some region the Landau levels are influenced by the kink potential and anti-crossings appear in the low energy spectrum. Some of these anti-crossings are situated along the extension of the topological states into the $|\epsilon| > u_b$ region. In addition of these anti-crossings the Landau levels display some resonances along the energy levels of a biased BLG (red solid curves in Fig. 10.2(a)) which can be linked to the edge effects of the potential profile. The position of the resonances can be fitted to $\epsilon = a\sqrt{(X_c - X_0)^4 + (\epsilon_n/a)^2}$ where $a = 0.0006$ and $X_0 = 9.25$ are fitting parameters and ϵ_n indicates the n th Landau level of a biased BLG (see solid purple curves). Also the topological levels can be fitted to $\epsilon = a\sqrt{(X_c - X_0)^4 + (u_b/a)^2}$ (dashed gray curve) with $a = 0.0003$ and $X_0 = -26$. Panels (b,c) show the probability densities

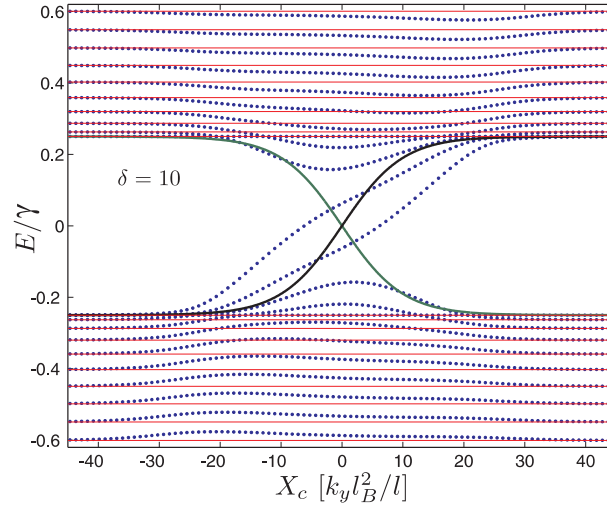


Figure 10.11: The same as Fig. 10.10 but for $\delta = 10$. The solid black and green curves are the potential, respectively, in the upper and lower layer.

for the points that are indicated by full red circles in the energy spectrum. For the points on the purple solid curves (2a,3a) the distribution of the carriers by the magnetic field is influenced by the small confinement by the interface potential (see solid and dashed curves in panel b). The probability density for the point on the fitted curve along the topological level (2b) shows a higher peak at the kink interface ($x = 0$) indicating that the kink potential acts as an attractive potential (solid curve in panel (c)). The other probabilities are clearly those of free electron LL. The result for a smooth kink potential $\delta = 10$ is shown in Fig. 10.11 where the energy value of the extra bound states are increased by the magnetic field and the topological levels are practically not affected by the magnetic field.

The localization of the states is reflected in the position dependence of the current. The current in the y -direction is obtained using

$$j_y = iv_F [\Psi^\dagger (\partial_x \sigma_y - \partial_y \sigma_x) \Psi + \Psi^T (\partial_x \sigma_y + \partial_y \sigma_x) \Psi^*] \quad (10.20)$$

where $\Psi = [\psi_a(x, y), \psi_b(x, y)]^T$. By substituting $\Psi(x, y) = e^{ik_y y} [\varphi_a(x), \varphi_b(x)]^T$ we have

$$j_y = 2v_F [Re\{\varphi_a^* \partial_x \varphi_b - \varphi_b^* \partial_x \varphi_a\} + 2k_y Re\{\varphi_a^* \varphi_b\}]. \quad (10.21)$$

The x -component of the current vanishes for the confined states. In Fig. 10.12, the y -component of the persistent current for a sharp (blue curves) and smooth (black curves) single potential kink profile is shown as function of the x direction without magnetic field (solid curves) and in the presence of the magnetic field (dashed curves). In the absence of

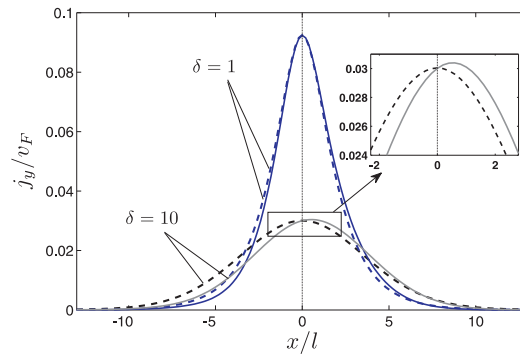


Figure 10.12: y -component of the persistent current corresponding to the topological state of a single kink potential as function of the x direction for zero magnetic field (dashed curves) and $B = 5 T$ (solid curves) with $k_y' = 0$ and $u_b = 0.25$. Blue curves display the current density for $\delta = 1$ and black curves are the corresponding results for $\delta = 10$.

a magnetic field the current is localized around $x = 0$ for both sharp ($\delta = 1$) and smooth ($\delta = 10$) potentials. For a smooth profile the wavefunction of the topological states and consequently also the current density profile is broadened (compare Figs. 10.2(b,c) with Figs. 10.4(a,c)). A magnetic field shifts the density profile slightly to the right (see the inset of Fig. 10.12) due to the Lorentz force and there is also a very small narrowing of the current distribution.

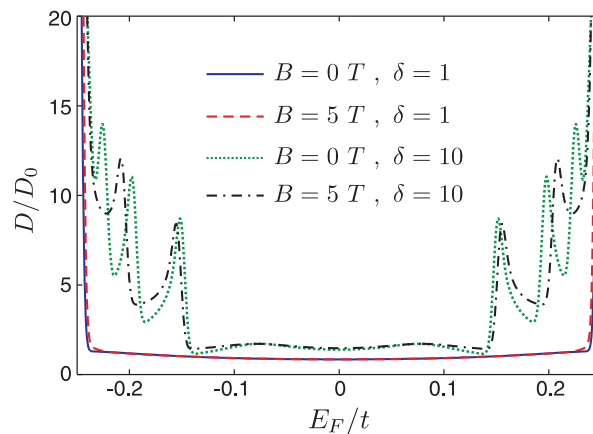


Figure 10.13: Density of states (DOS) of a single kink potential for $\delta = 1$ (solid and dashed curves) and $\delta = 10$ (dotted and dashed-dotted curves) with $u_b = 0.25$ for two different magnetic field values.

Next we consider the density of states (DOS) for the kink potential. The number of k -states per unit energy is given by

$$D(E) = \frac{D_0}{2\pi} \sum_n \int dk_y \delta(\epsilon - \epsilon_{n,k_y}). \quad (10.22)$$

where $D_0 = (\hbar v_F)^{-1}$. To calculate the DOS numerically we introduce a Gaussian broadening,

$$\delta(\epsilon - \epsilon_{n,k_y}) \rightarrow \frac{1}{\Gamma\sqrt{\pi}} \exp\left[-\frac{(\epsilon - \epsilon_{n,k_y})^2}{\Gamma^2}\right], \quad (10.23)$$

where Γ is the broadening which is taken as $\Gamma = 0.005$ in our calculations. Figure 10.13 shows the DOS as function of Fermi energy E_F in the absence and presence of an external magnetic field for sharp ($\delta = 1$) and smooth ($\delta = 10$) kink potentials. For a sharp profile the topological levels contribute an almost constant value to the DOS for $|\epsilon| < u_b$ even in the presence of an external magnetic field. For the smooth profile, peaks corresponding to the non-topological levels appear in the DOS and note that only these peaks are shifted in the presence of a magnetic field while the DOS of the topological states are not affected by the magnetic field.

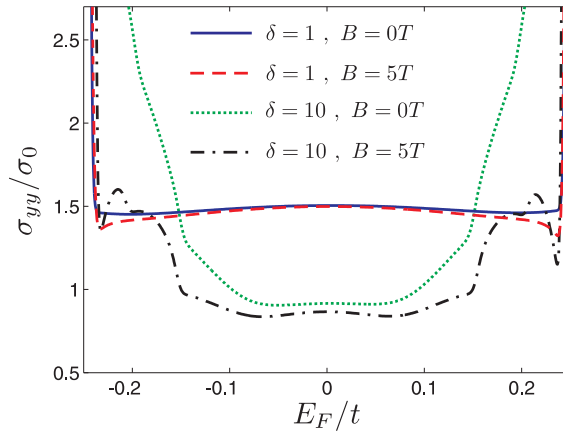


Figure 10.14: Conductivity σ_{yy} as function of the Fermi energy E_F for a single kink potential with $u_b = 0.25$. Other parameters are indicated in the figure.

We now turn to the transport properties of a kink potential and look at the influence of the topological states on the conductivity in the y -direction (σ_{yy}). For elastic scattering

the diffusive conductivity σ_{yy} is given by [154],

$$\sigma_{yy} = \frac{e^2 v_F}{2\pi \hbar k_B T} \sum_n \int dk'_y \tau v_{n,y}^2 f_{n,k'_y} (1 - f_{n,k'_y}). \quad (10.24)$$

Here T is the temperature, $v_{n,y} = \partial \epsilon_n / \partial k'_y$ is the electron velocity, $f_{n,k} = 1 / [\exp((E_F - E_{n,k'_y}) / K_B T) + 1]$ is the equilibrium Fermi-Dirac distribution function, and τ is the momentum relaxation time. For low temperatures we assume that τ is approximately constant, evaluated at the Fermi level ($\tau \approx \tau_F$), and replace the product $f_{n,k'_y} (1 - f_{n,k'_y}) / k_B T$ by the delta function given in Eq. (10.23). The results are presented as function of E_F in Fig. 10.14 in the units of $\sigma_0 = e^2 v_F \tau_F / \hbar L_y$ for both sharp ($\delta = 1$) and smooth ($\delta = 10$) potentials with $B = 0 T$ and $B = 5 T$. Due to the robust confinement of the topological levels the conductivity is constant in the energy gap even for a non-zero magnetic field (solid blue curve for $B = 0 T$ and red dashed curve for $B = 5 T$). The extra localized levels in the case of $\delta = 10$ lead to an increasing conductivity as function of E_F . Note that in the presence of an external magnetic field some of the additional electron(hole) states are shifted up(down) in energy (see Figs. 10.4 and 10.11) which results in smaller σ_{yy} at the $|\epsilon_F| < u_b$ region compared to the conductivity in the absence of magnetic field (black dotted-dashed curve).

10.4 Kink-antikink

10.4.1 Zero magnetic field

Next we consider a potential profile with a pair kink-antikink. The kink-antikink potential is modeled by,

$$u(x') = u_b \left[\tanh\left(\frac{x' - d}{\delta}\right) - \tanh\left(\frac{x' + d}{\delta}\right) + 1 \right] \quad (10.25)$$

where, d is the distance between the kink and the antikink in units of l . The spectrum of the localized states in the absence of a magnetic field is shown in Fig. 10.15(a) for $u_b = 0.25$, $\delta = 1$ and $d = 15$. The black dashed curves are the analytical results for $\delta = 0$ which are obtained using Eqs. (10.11). Note that there are only two chiral states per kink which leads to the appearance of crossing points in the energy spectrum (at $E = 0$ and $k'_y = 0$). The spinor components and probability densities associated with the points indicated inside the circle in Figs. 10.15(a) are shown in the panels (1a, 2a,3a,4a,5a). In the absence of a magnetic field and for the points around the energy level crossing the carriers are strongly confined at either the position of the kink or antikink. The wavefunction corresponding to an energy at the crossing point (panel 5a) is localized at both the kink and antikink.

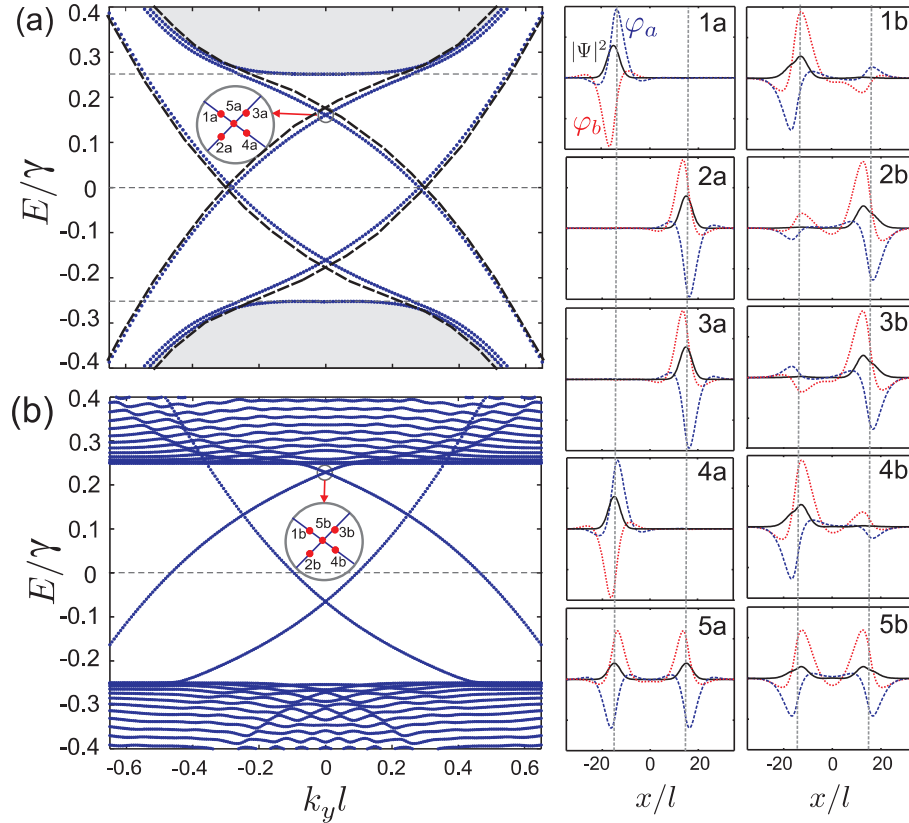


Figure 10.15: Left panels: Energy levels of a kink-antikink profile in bilayer graphene with $u_b = 0.25$, $\delta = 1$, $d = 15$ for (a) $B = 0 T$ and (b) $B = 3 T$. The black dashed curves display analytical results as obtained from Eq. (10.11). Right panels: Real part of the wavepinors and the corresponding probability density for the points that are indicated in the panels (a,b).

Next we investigate smooth potential kink profiles. In Figure 10.16(a) the energy spectrum of a smooth kink-antikink profile (i.e. $\delta = 10$) is presented for zero magnetic field. As in the case of the single kink profile additional bound states appear in the energy spectrum. The overlap between these states leads to the appearance of crossing points in the energy spectrum. The wavepinors and the corresponding probability density for the points indicated by arrows in panel (a) are shown in panels (1a,2a,3a,4a). In the absence of a magnetic field and for $k'_y = 0$ the states are localized at both kink and antikink (panels 1a, 2a and 4a) whereas, panel 3a shows that the confinement tends to the kink or antikink at $k'_y \neq 0$.

Decreasing the distance between the kink and antikink generate an unperfect kink-

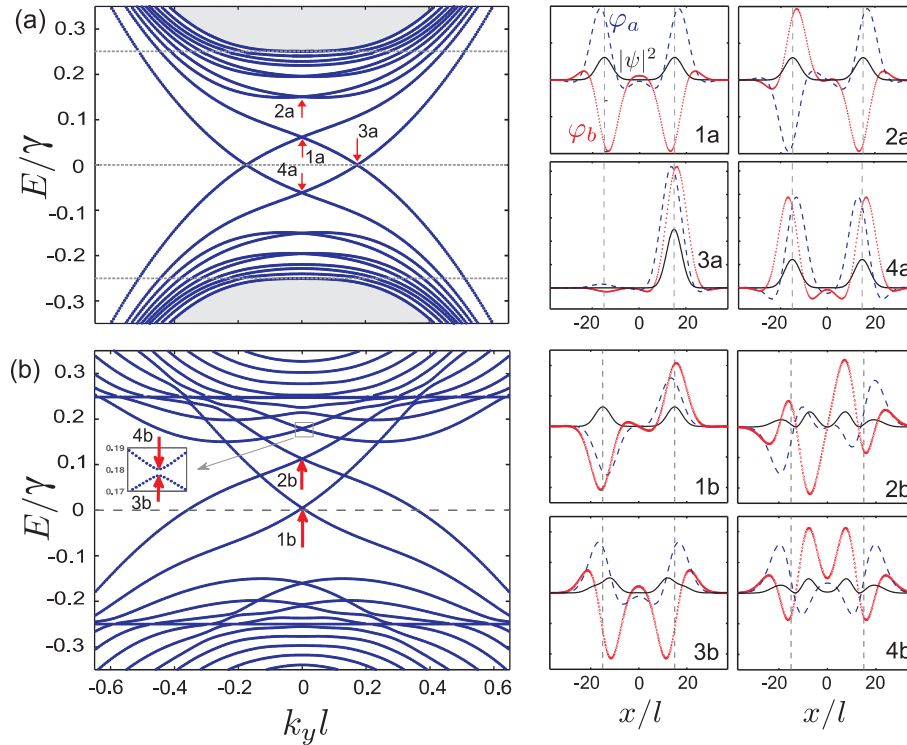


Figure 10.16: The same as Fig. 10.15 but for a smooth kink-antikink profile with $\delta = 10$.

antikink profile². This profile is illustrated in Fig. 10.17(a). The energy spectrum of such a profile is shown in Fig. 10.17(b) for $B = 0 T$, $\delta = 1$ and $d = 3 (\approx 5 \text{ nm})$. The analytical results (obtained from Eq. (10.11)) for $\delta = 0$ are shown by the black dashed curves. Now the crossing points in the energy spectrum for the case of $d = 15$ (see Fig. 10.15(a)) are replaced with anticrossings and an energy gap E_g appears in the energy spectrum. The positions of these minigaps move when we increase the magnetic field as in apparent from Fig. 10.17(c). The panels (1b,2b,3b,4b) show the real parts of the wavefunctions and corresponding probability density for the indicated points in Fig. 10.17(b) by red arrows. Note that due to the decreasing distance of the kink and antikink the carriers can be localized between the kink and antikink.

Figure 10.18(a) displays the energy spectrum of a smooth ($\delta = 10$) kink-antikink potential with $d = 3$ for $B = 0 T$. Now the kink and antikink are close to each other and the smoothness of the potential leads to extra localized levels. Therefore the crossing and anticrossing points between the additional bound states are seen to disappear and the

²Since the kink and antikink are close to each other the height of the applied voltage to the layers is less than u_b in the $|x'| \leq d$ region and we call the profile *imperfect* kink-antikink.

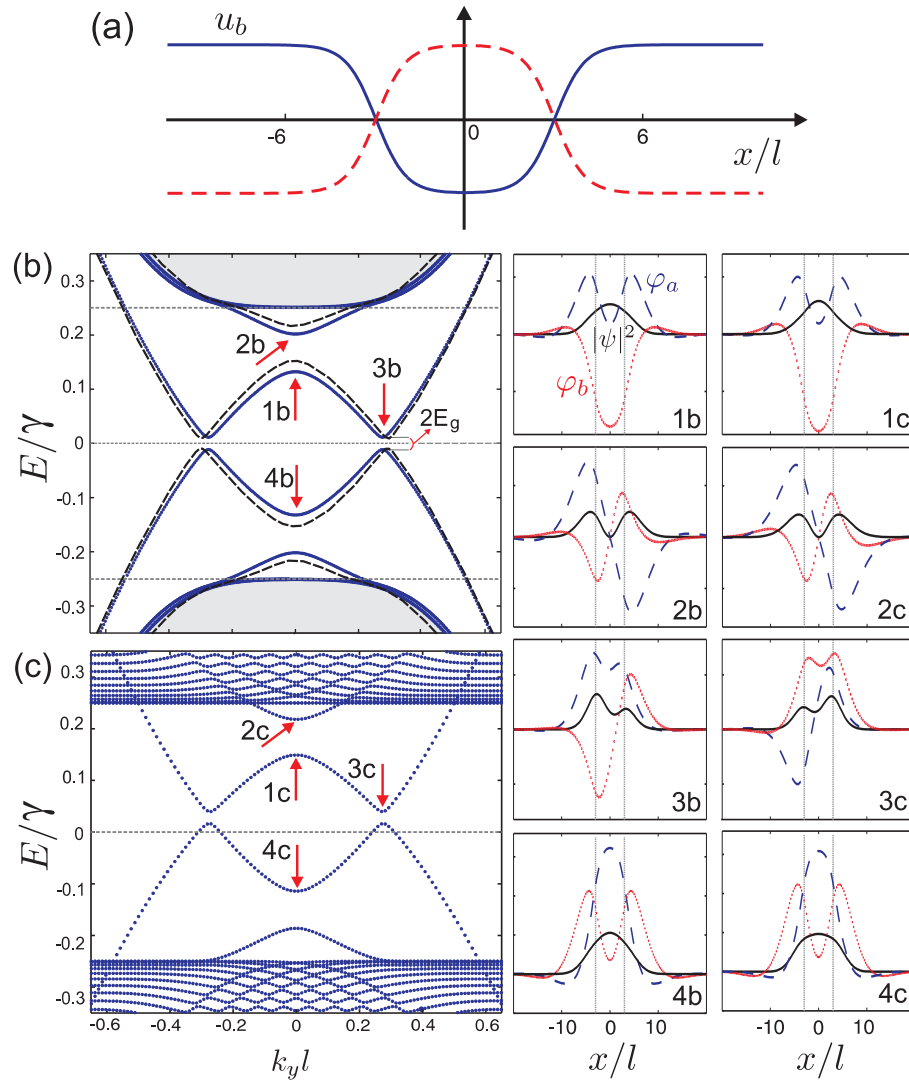


Figure 10.17: Energy levels of a sharp kink-antikink profile with $u_b = 0.25$, $d = 3$ ($\approx 5 \text{ nm}$) and $\delta = 1$ (the profile is depicted in (a)) for (b) $B = 0 T$ and (c) $B = 3 T$. The black dashed curves in panel (b) display analytical results as obtained from Eq. (10.11). Right panels show the real part of the wavefunctions and the corresponding probability density for the points at the energy spectrum that are indicated by arrows in panels (b,c).

energy gap between the topological levels is increased. The magnitude of the energy gap E_g depends on the width of the interface region δ , the maximum value of the potential u_b and the distance between the kink and antikink. This is shown in Fig. 10.19, where E_g is

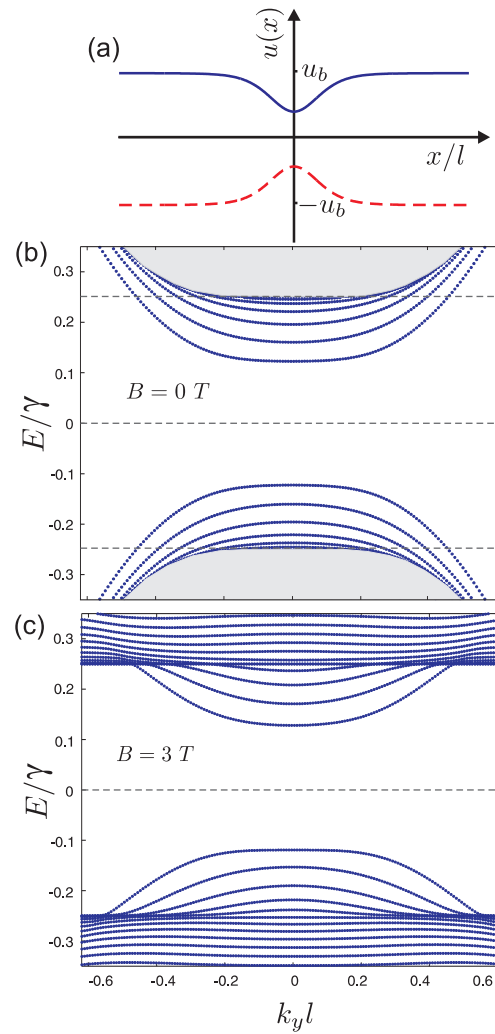


Figure 10.18: Energy levels of a smooth kink-antikink profile on bilayer graphene with $u_b = 0.25$, $d = 3$ and $\delta = 10$ for (a) $B = 0 T$ and (b) $B = 3 T$.

plotted as function of u_b , δ and d respectively in panels (a), (b) and (c) in the absence of magnetic field (blue solid curves). As shown in panels (a,b) the energy gap is an increasing function of u_b and δ . When δ increases the first energy level at the spectrum changes from a Mexican hat shape to a parabola. Therefore, E_g increases with increasing δ (compare the potentials illustrated in Figs. 10.17(a) and 10.18(a)). Increasing the distance of the kink and antikink results in perfect unidirectional states and the gap disappears (panel 10.19(c)).

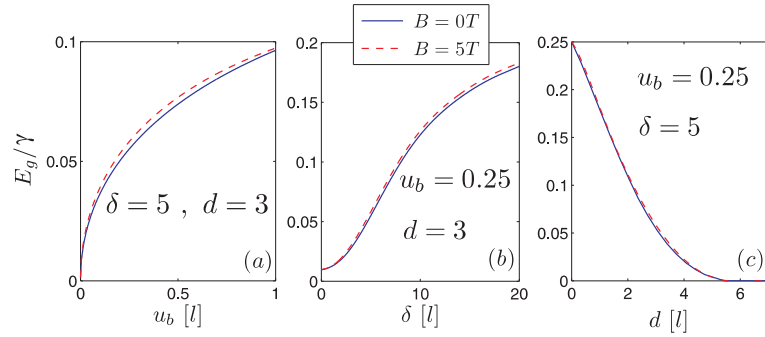


Figure 10.19: The energy gap E_g (indicated in Fig. 10.17(b)) as function of (a) maximum amplitude of the gate voltage u_b , (b) the width of kink profile δ and (c) the position of the kink and antikink d . Other parameters are shown in the figures.

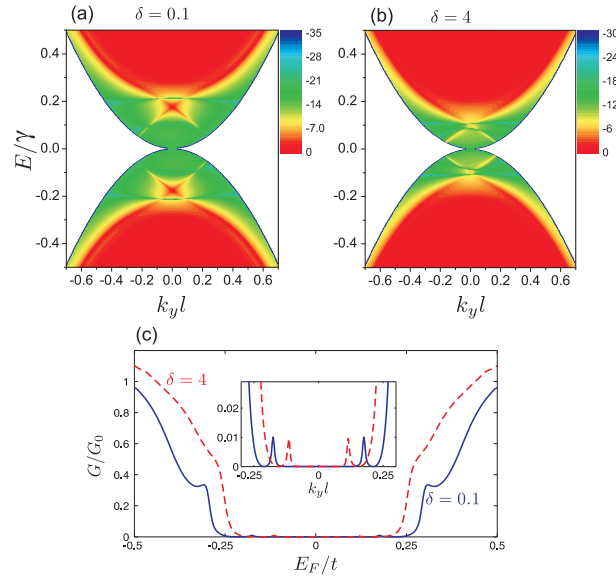


Figure 10.20: (a,b) Contour plot of the transmission T (in logarithmic scale) through a kink-antikink structure with the length $L = 24$ (≈ 40 nm) for $u_b = 0.25$ and $d = 6$ with (a) $\delta = 0.1$ and (b) $\delta = 4$. (c) Conductance G/G_0 vs Fermi energy of a kink-antikink potential for the same parameters as (a,b).

Next we consider the transmittance of a kink-antikink potential. In Fig. 10.20 we show a contour plot of the transmission probability (in logarithmic scale) for the kink-antikink structure with $L_x = 24$ for (a) $\delta = 0.1$ (sharp) and (b) $\delta = 4$ (smooth) potentials. The results show a nonzero region for the transmittance below the gap where the topological

levels corresponding to the kink and antikink cross each other. The conductance as function of Fermi energy is plotted in Fig. 10.20(b). A small region of transmittance appears in the energy gap due to the chiral states that appears as small peaks in the conductance (see the inset of panel (c)).

10.4.2 Magnetic field dependence

Figure 10.15(b) shows the kink-antikink energy levels in the presence of an external magnetic field ($B = 3 T$). The results show a shift of the four intra-gap energy branches as the magnetic field increases. In addition, the continuum of free states at zero magnetic field (shadowed region in Fig. 10.15(a) is replaced by a set of Landau levels. The spinor components and probability densities associated with the points indicated inside the circle in Figs. 10.15(b) are shown in the panels (1b,2b,...5b). For non-zero magnetic field the states show a shift of the probability density towards the region between the kink and the antikink. This is caused by the additional confinement due to the magnetic field.

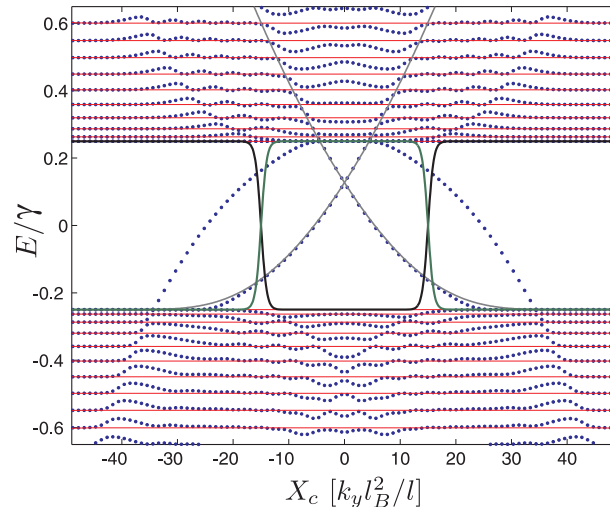


Figure 10.21: Energy spectrum of a kink-antikink profile in bilayer graphene as function of the cyclotron orbit center X_c with $u_b = 0.25$, $d = 15$, $B = 7 T$ and $\delta = 1$. Solid red lines correspond to the Landau levels of a biased BLG. The gray solid curves show fitted functions (given in the text) to the numerical results. The solid black and green curves describe the potential, respectively, in the upper and lower layer.

The energy levels of a smooth kink-antikink profile (i.e. $\delta = 10$) in the presence of a perpendicular magnetic field is presented in Fig. 10.16(b). Now the crossings points (in the case of $B = 0 T$) changed into anticrossings. In the inset of Fig. 10.16(b) an anti-crossing

is enlarged. Due to the strong confinement of the potential the magnetic field can only lead to a shift up in energy of the localized chiral states. The wavenumbers and the corresponding probability density for the points indicated by arrows in panel (b) are shown in the panels (1b,2b,3b,4b). In the presence of an external magnetic field and at the crossing points of the topological states (panels 1b, 2b) due to the strong confinement by the potential the magnetic field can only affect weakly the electrons. At the first anticrossing (panels 3b and 4b) which arises from the overlap of the first bound states in the kink and antikink potentials, the electrons are confined closer to the center of the potential.

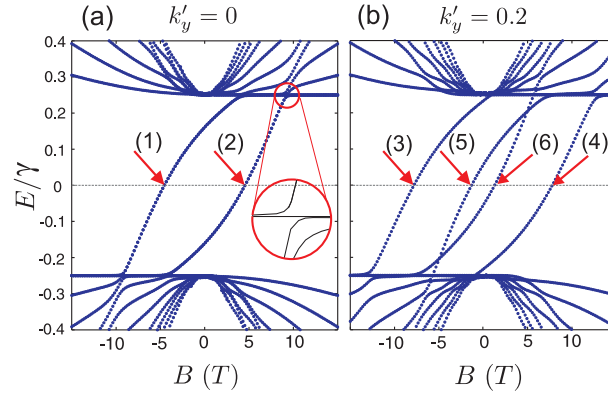


Figure 10.22: Energy levels of a sharp kink-antikink profile ($\delta = 1$) as function of external magnetic field for $u_b = 0.25$ with (a) $k'_y = 0$ and (b) $k'_y = 0.2$.

The energy levels for a sharp ($\delta = 1$) kink- antikink potential with $d = 3$ is presented in Fig. 10.17(c). The crossings which appeared in the energy spectrum due to the overlap of the extra bound states in the absence of magnetic field (see Fig. 10.17(b)) now are replaced with anti-crossings and the energy gap E_g between the kink and antikink states is shifted up in energy due to the confinement by the magnetic field. Panels (1c,2c,3c,4c) show the wavenumbers and probability density for the points indicated by arrows in panel (c). The energy spectrum of a smooth kink-antikink potential with $d = 3$, $\delta = 10$ and in the presence of an external magnetic field $B = 3 T$ is shown in Fig. 10.18(b). In the presence of a magnetic field the energy gap is shifted and the symmetry of the spectrum around $E = 0$ for $B = 0 T$ is broken (see panel (a)). The energy gap in the presence of a magnetic field ($B = 5 T$) is shown in Fig. 10.19 as red dashed curves. Notice that an external magnetic field only shifts up the energy gap and the gap size remains constant.

The energy spectrum of a kink-antikink potential is shown in Fig. 10.21 as function of orbit center X_c for $\delta = 1$, $u_b = 0.25$ and $d = 15$. The kink-antikink potential is depicted in the figure by the dashed curves. Such as for the single kink potential the topological levels can be fitted to $\epsilon_{\pm} \approx a\sqrt{(X_c \pm X_0)^4 + (u_b/a)^2}$ (see gray solid curves)

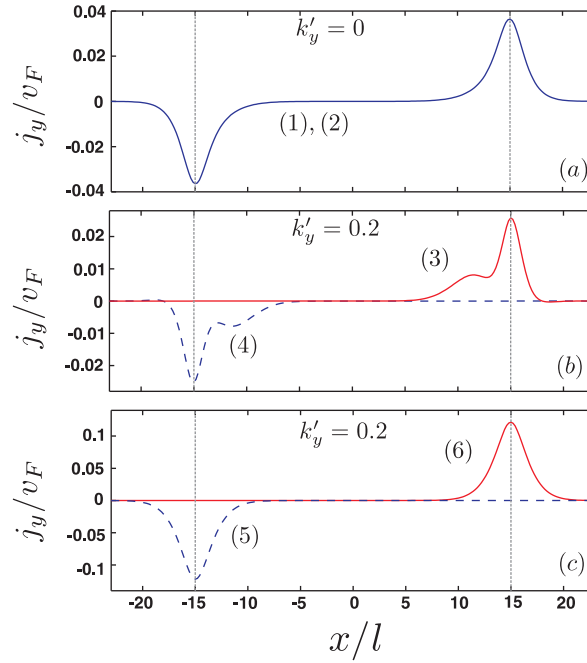


Figure 10.23: y -component of the persistent current of a kink-antikink profile in bilayer graphene as function of the x -direction for $E = E_F$ and for values of the magnetic field that are indicated by (1), (2), ... in Figs. 10.22(a,b).

where $-(+)$ corresponds to the kink(antikink) branches ($a = 0.003$ and $X_0 = 41$ are the fitting parameters). Now the Landau levels above the gap are affected by the kink-antikink potential where anti-crossing points appear along the topological levels. The solid red lines are the Landau levels in a biased BLG.

Figure 10.22 shows the dependence of the energies on the external magnetic field for (a) $k'_y = 0$ and (b) $k'_y = 0.2$. The branches that appear for $|\epsilon| > 0.25$ correspond to Landau levels that arise from the continuum of free states. For the kink-antikink case, however, the overlap between the states associated with each confinement region allows the formation of Landau orbits. Therefore, the proximity of an antikink induces a strong dependence of the states on the external field.

Figure 10.23 shows plots of the y -component of the current density as function of x for the states labeled (1) to (6) in panels (a) and (b) of Fig. 10.22. It should be noticed that a non-zero current can be found for $E = 0$ and $k'_y \neq 0$, as can be deduced from the dispersion relations. For $k'_y = 0$ the results presented in Fig. 10.23(a) show a persistent current carried by electrons localized at each kink region, irrespective of the direction of \mathbf{B} , as exemplified by the states (1) and (2) which correspond to opposite directions of

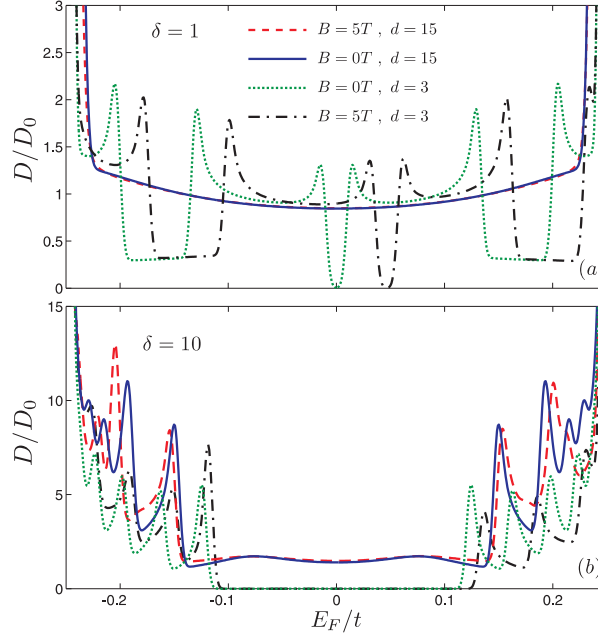


Figure 10.24: Density of states (DOS) of kink-antikink potentials for (a) $\delta = 1$ and (b) $\delta = 10$ with $u_b = 0.25$. The results are presented for $d = 3$ and $d = 15$ with $B = 0 T$ and $B = 5 T$.

the magnetic field. For non-zero wave vector, however, as shown in panels (b) and (c), the current is strongly localized around one of the potential kinks. In Fig. 10.23(b), the current density curve shows an additional smaller peak caused by the strong magnetic field ($B \approx 7.5 T$) where, the carriers can also be confined closer to the center.

The density of states of the topological states for (a) $\delta = 1$ and (b) $\delta = 10$ kink-antikink potential is shown in Fig. 10.24 with $d = 3$ and $d = 15$. The results show additional peaks for a sharp kink-antikink with $d = 3$ which is due to the splitting of the topological levels. Note that the energy gap leads to a zero density at $E_F = 0$ for zero magnetic field (blue circles in (a)) while shifting the gap in the presence of a magnetic field results in a non-zero DOS at $E_F = 0$ (red diamonds in (a)). For the smooth profiles the non-topological 1D states lead to the appearance of additional peaks in the DOS (panel (b)) that shift with the magnetic field.

10.5 Conclusion

In summary we obtained the energy spectrum, the density of states, the transmission and conductivity for carriers moving in BLG in the presence of asymmetric potentials (i.e. kink and kink-antikink profiles) in each layer of the BLG. Uni-directional chiral states are localized at the location of the kink (or antikink). By controlling the gate voltages and/or the smoothness of the kink profile the number of one-dimensional metallic channels and their subsequent magnetic response can be configured. The effect of an external magnetic field perpendicular to the bilayer sheet was investigated. We found that the influence of the magnetic field is very different for single and double kinks. Due to the strong confinement by the kink potential, the topological states are weakly affected by the magnetic field in the case of a single kink profile.

Changing the sign of the kink potential smoothly (i.e. broadening the kink potential) leads to extra bound states which have a very different behavior as compared to the uni-directional topological states. First, these states are no longer uni-directional and they have a quasi-1D free electron-type of spectrum which is asymmetric around $k_y = 0$. Second, they are less strongly localized at the kink of the potential as compared to the chiral states and their probability distribution appears as those of excited states of the chiral state. In the case of parallel kink-antikink profiles apparent crossings of the energy levels are found in the spectrum. Decreasing the distance between (and/or smoothing) the kink-antikink profiles turns into anti-crossings. It opens a gap in the topological state spectrum. This allows for a robust 1D system having a tunable minigap.

CHAPTER 11

Summary and future prospects

In the last chapter of my thesis I summarize and highlight the remarkable results I have achieved within the presented studies on monolayer and bilayer graphene nanostructures. Subsequently, I present two possible proposals for future research.

11.1 Concluding remarks of the thesis

In the present thesis, we theoretically investigated the electronic properties of monolayer and bilayer graphene nanostructures. Confined states in these systems are of particular interest. Within our study we employed the continuum model, i.e. by solving the Dirac-Weyl equation for monolayer and bilayer graphene, and the tight-binding approach.

In chapter 3, we have obtained the energy levels of triangular and hexagonal GQDs and compared the results obtained with the tight-binding approach with those calculated using the continuum model. In the latter model, the Dirac-Weyl equation is solved numerically for armchair, zigzag and infinite-mass boundary conditions. We found that the energy levels of GQDs sensitively depend to the boundaries. For example, the zigzag GQDs exhibit zero energy while the energy spectrum of GQDs with armchair boundaries shows an energy gap. Our results show a qualitative agreement between the two models, in which the continuum model overestimates the energy gap in comparison with TBM, for small graphene dots. Such agreement becomes better, when the size of the dot increases. For zigzag hexagonal and triangular dots, the DOS at zero energy is overestimated in the continuum approach. In the presence of infinite-mass boundary conditions the energy

spectrum of GQDs, obtained by the continuum model, do not exhibit the same properties as the case of armchair or zigzag boundaries (in both TBM and continuum models), which shows that this type of boundary condition may not give a good description of GQDs. In the presence of an external magnetic field the energy gap of hexagonal GQDs reduces quickly as the magnetic flux increases whereas the energy gap of the triangular GQDs reduces slowly with increasing the magnetic flux.

In chapter 4, the energy spectrum of a circular graphene quantum dot as a function of a perpendicular magnetic field was studied analytically. We examined the effect of both zigzag and infinite-mass boundary conditions and compared the results with those obtained with the Dirac-Weyl Hamiltonian and with the tight-binding approach. In contrast to the continuum model where we found only one zeroth-LL for zigzag boundary, the energy spectrum in TBM shows a degenerate zero-energies which are linked to the number of zigzag atoms. In the presence of a mass-term the TB results and the analytical results with infinite-mass boundary condition agree very well for lower energies and larger dot radius.

In chapter 5, we presented numerical results within a tight-binding study, for the energy spectrum and magnetic field dependence of the eigenstates of graphene quantum dots, on which a p-n junction creates electron and hole-doped regions. The presence of the magnetic field, together with the coupling between electron and hole states across the potential barrier due to Klein tunneling leads to the appearance of localized states at the potential interface, known as snake states. These states, which have previously been investigated for p-n junctions on infinite graphene sheets, can influence the transport properties of graphene-based nanodevices. We have obtained results that show that for the case of quantum dots the low energy dynamics of the system is dominated by hybridized states that arise due to the overlap between quantum Hall edge states and the snake states at the p-n junction, with the snake states allowing the superposition of quantum Hall edge states at the p and n sides of the dot. These states are characterized by an energy spectrum that displays an oscillating behavior as function of the electrostatic potential and magnetic field at the vicinity of the Fermi energy. Furthermore, the energy spectrum was shown to depend on the specific alignment of the potential interfaces with regard to the graphene lattice, as well as on the geometry of the gates.

In chapter 6, the energy levels, the electron density, the pair correlation function and the cyclotron transition energies of electrostatically confined QDs in BLG containing one or two electrons are investigated. Such QDs can be realized experimentally in BLG using nanostructured gate potentials. In contrast to conventional semiconductor QDs, we found at low magnetic fields that the ground state energy of the two-electron spectrum exhibits a valley transition, rather than a spin singlet-triplet transition. This is due to the extra valley degree of freedom in BLG in which the electrons can be in different valleys and thus

allowing for four-degenerate single-triplet states as ground state. Our prediction can be verified by spin susceptibility measurements in low magnetic fields.

In chapter 7, we proposed electrostatically confined quantum rings in BLG. In contrast to the monolayer graphene QDs, edge disorder and specific type of edges is no longer important in BLG quantum dots. Our results display interesting new behaviors in the presence of a perpendicular magnetic field (B), which have no analogue either in semiconductor-based or in lithography-based graphene quantum rings. In particular, the eigenvalues are not invariant under a $B \rightarrow -B$ transformation and, for a fixed total angular momentum m , their field dependence is not parabolic, but displays two minima separated by a saddle point. This is a consequence of the fact that the ring structure is produced by a gate that introduces an electric field and thus a preferential direction. The existence of Aharonov-Bohm oscillations for both electrons and holes are still linked with flux quantization through the ring. The system can be realized experimentally by a suitable choice of nanostructured doping levels or with the application of nanostructured gates.

In chapter 8, we considered the behavior of carriers in single and bilayer graphene quantum rings within a toy model where the ring has zero-width. Our approach leads to analytical expressions for the energy spectrum and current densities through the rings.

In chapter 9, we predicted new chiral states in the presence of an asymmetric (kink profile) mass-potential in monolayer graphene. Within a continuum model, we obtained analytic expressions for the energy spectrum. Our study showed that these states are robust even when a small gap is located between the two mass regions. The system can be realized experimentally using a boron-nitride substrate with a line defect that induces an asymmetric mass potential in graphene. Nanostructuring of such line defects in the h-BN substrate can be very promising for the fabrication of electronic devices for valleytronics.

In chapter 10, we studied the energy spectrum, the density of states, the transmission and conductivity for carriers moving in BLG in the presence of asymmetric potentials (i.e. kink and kink-antikink profiles). Uni-directional chiral states are localized at the location of the kink (or antikink). By controlling the gate voltages and/or the smoothness of the kink profile the number of one-dimensional metallic channels and their subsequent magnetic response can be configured. The effect of an external magnetic field perpendicular to the bilayer sheet was investigated. We found that the influence of the magnetic field is very different for single and double kinks. Due to the strong confinement by the kink potential, the chiral states are weakly affected by the magnetic field in the case of a single kink profile. Changing the sign of the kink potential smoothly (i.e. broadening the kink potential) leads to extra bound states which have a very different behavior as compared to the uni-directional topological states. In the case of parallel kink-antikink profiles apparent crossings of the energy levels are found in the spectrum. Decreasing the distance between (and/or smoothing) the kink-antikink profiles turns into anti-crossings. It opens

a gap in the chiral state spectrum. This allows for a robust 1D system having a tunable minigap.

11.2 Future prospects

In chapter 6, we found energy levels of BLG quantum dots containing two interacting electrons. Extending this problem to few electrons may provide a prospect to the experimental observation of many-body aspects of BLG quantum dots, such as Coulomb blockade [31, 32]. Of particular interest will be the investigation of different physical phenomena in BLG quantum dots (QDs) such as Wigner molecules and the maximum density droplet state which have been predicted and observed in semiconductor QDs [155, 156].

In chapter 10 we investigated the influence of a perpendicular magnetic field on the chiral states in BLG. In the studied system, the carriers are confined in one direction under a kink (or kink-antikink) potential profile while in the other direction were free to move. Future work will concentrate on the effect of a perpendicular magnetic field on the chiral states which are induced by a 2D kink potential profile, e.g. chess-board like profile, rather than a 1D profile. In analogy with 2D topological insulators I expect to find Aharonov-Bohm oscillations in this system. Another interesting aspect in this system would be the study of the effect of interaction on the chiral states. Previous results for a 1D kink-profile demonstrate that the zero modes in BLG, behave as a strongly interacting Tomonaga-Luttinger liquid [138]. Similar to BLG, one can investigate the effect of an asymmetric gate potential profile in trilayer graphene. I expect that this system exhibits new chiral states which are different from those in BLG and monolayer graphene (chapter 7).

CHAPTER 12

Overzicht en toekomstperspectieven

In het laatste hoofdstuk van mijn thesis worden de opmerkelijke resultaten die ik bereikt heb binnen de studie van mono- en bilaag grafeen nanostructuren, benadrukt en samengevat. Vervolgens geef ik verscheidene mogelijke voorstellen voor toekomstig onderzoek.

12.1 Overzicht van de thesis

In deze thesis heb ik een theoretische studie gemaakt van de elektronische eigenschappen van mono- en bilaag grafeen nanostructuren. Van bijzonder belang in deze thesis, is de zoektocht naar gebonden toestanden in deze systemen. Voor mijn onderzoek heb ik zowel het continuüm model gebruikt, i.e. het oplossen van de Dirac-Weyl vergelijking voor mono- en bilaag grafeen, alsook de tight-binding benadering.

In hoofdstuk 3, heb ik de energie niveaus van driehoekige en hexagonale grafeen kwantum stippen berekend, binnen een vergelijkende studie tussen het tight-binding en het continuüm model. In het continuüm model, werd de Dirac-Weyl vergelijking numeriek opgelost voor armchair, zigzag en gesloten randvoorwaarden. De resultaten tonen een kwalitatieve overeenkomst tussen beide modellen. Met name wordt de energie kloof overschat voor kleine stippen in het continuüm model, in vergelijking met tight-binding. De overeenkomst wordt beter, naarmate de grootte van de stip toeneemt. In de aanwezigheid van een extern loodrecht magnetisch veld, neemt de energie kloof van zeer kleine hexagonale stippen zeer snel af met toenemende magnetische flux, terwijl de kloof voor driehoekige stippen zeer geleidelijk toeneemt.

In hoofdstuk 4, wordt het energie spectrum van een cirkelvormige kwantum stip als functie van een loodrecht magnetisch veld, analytisch bestudeerd. Het effect van zigzag en gesloten randvoorwaarden werd onderzocht, en de resultaten bekomen met de Dirac-Weyl Hamiltoniaan werden vergeleken met de tight-binding resultaten. In tegenstelling met het continuüm model, waar er alleen één nulde Landau level gevonden werd, toont de energie in tight-binding, een ontaard energie niveau, waarbij de ontaarding gegeven wordt door het aantal zigzag atomen. In de aanwezigheid van een massa term, komen de tight-binding resultaten en de analytische resultaten met gesloten randvoorwaarden zeer goed overeen voor lage energie en grote kwantum stippen.

In hoofdstuk 5, geef ik numerieke resultaten van een tight-binding studie, voor het energie spectrum en de magneetveld afhankelijkheid van de eigentoestanden van grafeen kwantum stippen waarop een p-n junctie zorgt voor elektron en holte gedoteerde gebieden. Het magnetisch veld, samen met de koppeling tussen de elektron en holte toestanden over de potentiaal barrière dankzij Klein tunneling, leidt tot zogenaamde ‘snake states’, die gelokaliseerd zijn aan het potentiaal tussenvlak. Deze toestanden, die reeds eerder onderzocht werden voor p-n juncties op een oneindig vlak grafeen, kunnen de transport eigenschappen van grafeen gebaseerde nanodevices beïnvloeden. De resultaten tonen aan dat de dynamica van een kwantum-stip, bij lage energie gedomineerd wordt door gehybridiseerde toestanden die ontstaan door overlap tussen kwantum Hall rand toestanden en ‘snake states’ aan de p-n junctie. De ‘snake states’ laten zo een superpositie toe van kwantum Hall rand toestanden aan de p en n kant van de stip. Deze toestanden worden gekarakteriseerd door een energie spectrum dat oscilleert rond de Fermi energie als functie van de elektrostatische potentiaal en het magnetisch veld. Bovendien werd er aangetoond dat de energie afhankelijk is van de richting van het potentiaal tussenvlak ten aanzien van het grafeen-rooster, en ook van de gate opstelling.

In hoofdstuk 6, worden de energie niveaus, de elektronendichtheid, de paar-correlatie functie en de cyclotron transitie energie van elektrostatisch opgesloten kwantum-stippen die één of twee elektronen bevatten, bestudeerd in bilaag grafeen. Zulke kwantum-stippen kunnen experimenteel gerealiseerd worden, aan de hand van nanogestructureerde gate potentialen. In tegenstelling tot conventionele halfgeleider kwantum-stippen, vonden we, dat bij kleine magnetische velden, de grondtoestand van het twee-elektron systeem, een ‘valley’ transitie ondergaat, in plaats van een spin singlet-triplet transitie. Dit is een gevolg van de extra ‘valley’ vrijheidsgraad in bilaag grafeen, waardoor de elektronen verschillende ‘valley’ toestanden bezetten zodat de grondtoestand gegeven wordt door vier ontaarde singlet-triplet toestanden. Deze voorspelling kan experimenteel bevestigd worden door een meting van de spin susceptibiliteit bij kleine magnetische velden.

In hoofdstuk 7, stel ik een elektrostatisch opgesloten kwantum-ring voor in bilaag grafeen. De wanorde op de rand en het soort van rand zijn niet belangrijk in bilaag

kwantum-stippen, in tegenstelling tot monolaag grafeen. Onze resultaten vertonen een interessant nieuw gedrag in de aanwezigheid van een loodrecht magnetisch veld B , dat geen analoog heeft in kwantum-ringen gebaseerd op halfgeleiders of lithografisch grafeen. In het bijzonder zijn de eigenwaarden niet invariant onder de transformatie $B \rightarrow -B$, en voor een vast draaimoment m , is de afhankelijkheid van het magneetveld niet parabolisch, maar vertoont het twee minima gescheiden door een zadelpunt. Dit is een gevolg van het feit dat de ring structuur gemaakt wordt door een gate dat een elektrisch veld introduceert, en dus een voorkeursrichting. Het bestaan van Aharonov-Bohm oscillaties voor elektronen en holten, heeft te maken met de kwantisatie van de flux door de ring. Dit systeem kan experimenteel gerealiseerd worden door een gepaste keuze van nanogestructureerde doping, of door het gebruik van nanogestructureerde gates.

In hoofdstuk 8, bestudeer ik het gedrag van ladingsdragers in mono- en bilaag grafeen kwantum-ringen met een model waar de ring geen dikte heeft. Deze aanpak leidt tot analytische uitdrukkingen voor de energie en de stroomdichtheid doorheen de ring.

In hoofdstuk 9, worden er nieuwe chirale toestanden voorspeld in de aanwezigheid van een asymmetrische (kink profiel) massa potentiaal in monolaag grafeen. Aan de hand van het continuüm model, heb ik analytische uitdrukkingen bekomen voor het energie spectrum. Mijn studie heeft aangetoond dat deze toestanden robust zijn, ook als er een kleine scheiding is tussen de twee massa gebieden. Dit systeem kan experimenteel gerealiseerd worden aan de hand van een boron nitride substraat met een lijn defect, dat een asymmetrische massa potentiaal induceert in het grafeen. Nano structurering van zulke lijn defecten in het h-BN substraat kan veelbelovend zijn voor de vervaardiging van elektronische devices voor ‘valleytronics’. Het effect van wanorde aan het defect vormt geen probleem in dit systeem, omdat de asymmetrische massa potentiaal veroorzaakt wordt door een lijn defect in het h-BN substraat.

In hoofdstuk 10, heb ik het energie spectrum, de toestandsdichtheid, de transmissie en geleidbaarheid van ladingsdragers in bilaag grafeen bestudeerd in de aanwezigheid van asymmetrische potentialen (kink en kink-antikink profielen). Eenrichtings chirale toestanden zijn gelokaliseerd rond de positie van de (anti)kink. Door de controle van gate voltages en/of de gladheid van het kink profiel, kan het aantal eendimensionale metallische kanalen en de daarvan afhankelijke magnetische respons ingesteld worden. Het effect van een extern magnetisch veld, loodrecht op het bilaag grafeen vlak, werd ook onderzocht. We vonden dat de invloed van het magneetveld heel verschillend is voor enkele en dubbele kinken. Dankzij de sterke opsluiting van de kink potentiaal, worden de chirale toestanden enkel zwak beïnvloed door het magneetveld in het geval van één enkel kink profiel. Als het teken van de kink potentiaal geleidelijk veranderd wordt, i.e. een verbreding van de kink potentiaal, vinden we extra gebonden toestanden die een heel verschillend gedrag vertonen in vergelijking met de eenrichtings topologische toestanden. In

het geval van evenwijdige kink-antikink profielen, worden er duidelijke kruisingen van de energie-niveaus gevonden in het spectrum. Door de afstand tussen (en/of gladder maken) de kink-antikink profielen te verkleinen, verandert dit in een vermijde kruising. Hierdoor ontstaat er een energie kloof in het spectrum van de chirale toestanden. Dit maakt een robust 1D systeem met een regelbare minikloof mogelijk.

Bibliography

- [1] P. R. Wallace, Phys. Rev. **71**, 622 (1947).
 - [2] H. P. Boehm, A. Clauss, G. O. Fischer, and U. Hofmann, Z. Naturforsch **17**, 150 (1962).
 - [3] J. W. May, Surf. Sci. **17**, 267 (1969).
 - [4] K. S. Novoselov, A. K. Geim, S. V. Morozov, D. Jiang, Y. Zhang, S. V. Dubonos, I. V. Grigorieva, and A. A. Firsov, Science **306**, 666 (2004).
 - [5] M. I. Katsnelson, Materials Today **10**, 20 (Jan-Feb. 2007).
 - [6] ISI web of knowledge service (www.wokinfo.com).
 - [7] The official website of the Nobel prize (www.nobelprize.org)
 - [8] M. I. Katsnelson, *Graphene: Carbon in Two Dimensions*, (Cambridge University press, New York, 2012).
 - [9] A. K. Geim and A. H. MacDonald, Phys. Today **60**, 35 (August 2007).
 - [10] M. P. Ramuz, M. Vosgueritchian, P. Wei, Ch. Wang, Y. Gao, Y. Wu, Y. Chen, and Zh. Bao, ACS Nano **6**, 10384 (2012).
 - [11] C. R. Dean, A. F. Young, I. Meric, C. Lee, L. Wang, S. Sorgenfrei, K. Watanabe, T. Taniguchi, P. Kim, K. L. Shepard, and J. Hone, Nat. Nanotech. **5**, 722 (2010).
-

-
- [12] K. I. Bolotin, K. J. Sikes, J. Hone, H. L. Stormer, and P. Kim, *Phys. Rev. Lett.* **101**, 096802 (2008).
- [13] X. Du, I. Skachko, A. Barker, and E. Y. Andrei, *Nat. Nanotech.* **3**, 491 (2008).
- [14] F. Schwierz, *Nature Nanotech.* **5**, 487 (2010).
- [15] Y. M. Lin, C. Dimitrakopoulos, K. A. Jenkins, D. B. Farmer, H. Y. Chiu, A. Grill, and Ph. Avouris, *Science* **327**, 662 (2010).
- [16] F. Bonaccorso, Z. Sun, T. Hasan, and A. C. Ferrari, *Nat. Photon.* **4**, 611 (2010).
- [17] S. Bae, H. Kim, Y. Lee, X. Xu, J. S. Park, Y. Zheng, J. Balakrishnan, T. Lei, H. R. Kim, Y. I. Song, Y. J. Kim, K. S. Kim, B. Ozyilmaz, J. H. Ahn, B. H. Hong, and S. Iijima, *Nat. Nanotech.* **5**, 574 (2010).
- [18] A. H. Castro Neto, F. Guinea, N. M. R. Peres, K. S. Novoselov, and A. K. Geim, *Rev. Mod. Phys.* **81**, 109 (2009).
- [19] M. O. Goerbig, *Rev. Mod. Phys.* **83**, 1193 (2011).
- [20] C. W. J. Beenakker, *Rev. Mod. Phys.* **80**, 1337 (2008).
- [21] M. I. Katsnelson, K. S. Novoselov, and A. K. Geim, *Nat. Phys.* **2**, 620 (2006).
- [22] L. A. Ponomarenko, F. Schedin, M. I. Katsnelson, R. Yang, E. W. Hill, K. S. Novoselov, and A. K. Geim, *Science* **320**, 356 (2008).
- [23] K. A. Ritter and J. W. Lyding, *Nature Materials* **8**, 235 (2009).
- [24] J. S. Bunch, Y. Yaish, M. Brink, K. Bolotin, and P. L. McEuen, *Nano Lett.* **5**, 287 (2005).
- [25] J. M. Pereira Jr., F. M. Peeters, and P. Vasilopoulos, *Phys. Rev. B* **75**, 125433 (2007).
- [26] L. Oroszlány, P. Rakytá, A. Kormányos, C. J. Lambert, and J. Cserti, *Phys. Rev. B* **77**, 081403 (2008); T. K. Ghosh, A. De Martino, W. Häusler, L. Dell'Anna, and R. Egger, *ibid.* **77**, 081404 (2008).
- [27] E. McCann, *Phys. Rev. B* **74**, 161403 (2006).
- [28] E. V. Castro, K. S. Novoselov, S. V. Morozov, N. M. R. Peres, J. M. B. Lopes dos Santos, J. Nilsson, F. Guinea, A. K. Geim, and A. H. Castro Neto, *Phys. Rev. Lett.* **99**, 216802 (2007).
-

-
- [29] J. M. Pereira Jr., P. Vasilopoulos, and F. M. Peeters, *Nano Lett.* **7**, 946 (2007).
- [30] J. M. Pereira Jr., F. M. Peeters, P. Vasilopoulos, R. N. Costa Filho, and G. A. Farias, *Phys. Rev. B* **79**, 195403 (2009).
- [31] M. T. Allen, J. Martin, and A. Yacoby, *Nature Comm.* **3**, 934 (2012).
- [32] A. M. Goossens, S. C. M. Driessen, T. A. Baart, K. Watanabe, T. Taniguchi, and L. M. K. Vandersypen, *Nano Lett.* **12**, 4656 (2012).
- [33] S. Y. Zhou, G. H. Gweon, A. V. Fedorov, P. N. First, W. A. de Heer, D. H. Lee, F. Guinea, A. H. Castro Neto, and A. Lanzara, *Nat. Mater.* **6**, 770 (2007).
- [34] I. Martin, Ya. M. Blanter, and A. F. Morpurgo, *Phys. Rev. Lett.* **100**, 036804 (2008).
- [35] A. Rycerz, J. Tworzydo, and C. W. J. Beenakker, *Nature Physics* **3**, 172 (2007).
- [36] A. V. Rozhkov and F. Nori, *Phys. Rev. B* **81**, 155401 (2010).
- [37] P. A. M. Dirac, *Phil. Trans. R. Soc. A* **117**, 610 (1928).
- [38] A. Bostwick, T. Ohta, Th. Seyller, K. Horn, and E. Rotenberg, *Nature Physics* **3**, 36 (2007).
- [39] E. McCann and V. I. Fal'ko, *Phys. Rev. Lett.* **96**, 086805 (2006).
- [40] Y. Zhang, T. T. Tang, C. Girit, Z. Hao, M. C. Martin, A. Zettl, M. F. Crommie, Y. R. Shen, and F. Wang, *Nature (London)* **459**, 820 (2009).
- [41] E. McCann, D. S. L. Abergel, and V. I. Fal'ko, *Solid State Communications* **143**, 110 (2007).
- [42] M. Ramezani Masir, P. Vasilopoulos, A. Matulis, and F. M. Peeters, *Phys. Rev. B* **77**, 235443 (2008).
- [43] G. Li and E. Y. Andrei, *Nature Physics* **3**, 623 (2007).
- [44] M. L. Sadowski, G. Martinez, M. Potemski, C. Berger, and W. A. de Heer, *Phys. Rev. Lett.* **97**, 266405 (2006).
- [45] Z. Jiang, E. A. Henriksen, L. C. Tung, Y. J. Wang, M. E. Schwartz, M. Y. Han, P. Kim, and H. L. Stormer, *Phys. Rev. Lett.* **98**, 197403 (2007).
- [46] O. Klein, *Z. Phys.* **53**, 157 (1929).
-

-
- [47] A. F. Young and Ph. Kim, *Nature Physics* **5**, 222 (2009).
- [48] T. Chakraborty, *Quantum Dots: A Survey of the Properties of Artificial Atoms*, (Elsevier Science, Amsterdam, 1999); L. Jacak, P. Hawrylak, and A. Wójs, *Quantum dots*, (Springer-Verlag, Berlin, 1998).
- [49] S. M. Reimann and M. Manninen, *Rev. Mod. Phys.* **74**, 1283 (2002).
- [50] F. Molitor, J. Güttinger, C. Stampfer, S. Dröscher, A. Jacobsen, T. Ihn, and K. Ensslin, *J. Phys.: Condens. Matter* **23**, 243201 (2011).
- [51] L. C. Campos, V. R. Manfrinato, J. D. Sanchez-Yamagishi, J. Kong, and P. Jarillo-Herrero, *Nano Lett.* **9**, 2600 (2009).
- [52] S. K. Hämäläinen, Zh. Sun, M. P. Boneschanscher, A. Uppstu, M. Ijäs, A. Harju, D. Vanmaekelbergh, and P. Liljeroth, *Phys. Rev. Lett.* **107**, 236803 (2011).
- [53] D. Subramaniam, F. Libisch, Y. Li, C. Pauly, V. Geringer, R. Reiter, T. Mashoff, M. Liebmann, J. Burgdörfer, C. Busse, T. Michely, R. Mazzarello, M. Pratzer, and M. Morgenstern, *Phys. Rev. Lett.* **108**, 046801 (2012).
- [54] Soo-hyon Phark, J. Borme, A. L. Vanegas, M. Corbetta, D. Sander, and J. Kirschner, *ACS Nano* **5**, 8162 (2011).
- [55] H. P. Heiskanen, M. Manninen, and J. Akola, *New J. Phys.* **10**, 103015 (2008).
- [56] M. Ezawa, *Phys. Rev. B* **76**, 245415 (2007).
- [57] P. Potasz, A. D. Güclü, and P. Hawrylak, *Phys. Rev. B* **81**, 033403 (2010).
- [58] Z. Z. Zhang, K. Chang, and F. M. Peeters, *Phys. Rev. B* **77**, 235411 (2008).
- [59] J. Wu, W. Pisula, and K. Müllen, *Chem. Rev.* **107**, 718 (2007).
- [60] H. Hiura, *Appl. Surf. Sci.* **222**, 374 (2004).
- [61] J. Akola, H. P. Heiskanen, and M. Manninen, *Phys. Rev. B* **77**, 193410 (2008).
- [62] D. P. Kosimov, A. A. Dzhurakhalov, and F. M. Peeters, *Phys. Rev. B* **81**, 195414 (2010).
- [63] D. A. Bahamon, A. L. C. Pereira, and P. A. Schulz, *Phys. Rev. B* **79**, 125414 (2009).
- [64] A. Matulis and F. M. Peeters, *Phys. Rev. B* **77**, 115423 (2008).
-

-
- [65] P. Recher, J. Nilsson, G. Burkard, and B. Trauzettel, *Phys. Rev. B* **79**, 085407 (2009).
- [66] G. Giavaras and F. Nori, *Phys. Rev. B* **83**, 165427 (2011).
- [67] G. Giavaras and F. Nori, *App. Phys. Lett.* **97**, 243106 (2010).
- [68] G. Giavaras, P. A. Maksym and M. Roy, *J. Phys.: Condens. Matter* **21**, 102201 (2009).
- [69] S. Schnez, K. Ensslin, M. Sigrist, and T. Ihn, *Phys. Rev. B* **78**, 195427 (2008);
- [70] C. Tang, W. Yan, Y. Zheng, G. Li, and L. Li, *Nanotechnology* **19**, 435401 (2008).
- [71] A. L. Pereira and P. A. Schulz, *Phys. Rev. B* **78**, 125402 (2008).
- [72] For more details see the COMSOL Multiphysics website: www.comsol.com
- [73] A. R. Akhmerov and C. W. J. Beenakker, *Phys. Rev. B* **77**, 085423 (2008).
- [74] L. Brey and H. A. Fertig, *Phys. Rev. B* **73**, 235411 (2006).
- [75] M. V. Berry and R. J. Mondragon, *Proc. R. Soc. London, Ser. A* **412**, 53 (1987).
- [76] P. Recher, B. Trauzettel, A. Rycerz, Ya. M. Blanter, C. W. J. Beenakker, and A. F. Morpurgo, *Phys. Rev. B* **76**, 235404 (2007).
- [77] N. M. R. Peres, J. N. B. Rodrigues, T. Stauber, and J. M. B. Lopes dos Santos, *J. Phys.: Condens. Matter* **21**, 344202 (2009).
- [78] K. Nakada, M. Fujita, G. Dresselhaus, and M. S. Dresselhaus, *Phys. Rev. B* **54**, 17954 (1996).
- [79] M. Zarenia, A. Chaves, G. A. Farias, and F. M. Peeters, *Phys. Rev. B* **84**, 245403 (2011).
- [80] M. Wimmer, A. R. Akhmerov, and F. Guinea, *Phys. Rev. B* **82**, 045409 (2010).
- [81] D. P. DiVincenzo and E. J. Mele, *Phys. Rev. B* **29**, 1685 (1984).
- [82] C. S. Lent, *Phys. Rev. B* **43**, 4179 (1991).
- [83] J. Milton Pereira Jr., V. Mlinar, F. M. Peeters, and P. Vasilopoulos, *Phys. Rev. B* **74**, 045424 (2006).
- [84] V. V. Cheianov and V. I. Fal'ko, *Phys. Rev. B* **74**, 041403(R) (2006).
-

-
- [85] B. Huard, J. A. Sulpizio, N. Stander, K. Todd, B. Yang, and D. Goldhaber-Gordon, *Phys. Rev. Lett.* **98**, 236803 (2007).
- [86] J. R. Williams, L. DiCarlo, and C. M. Marcus, *Science* **317**, 638 (2007).
- [87] B. Özyilmaz, P. Jarillo-Herrero¹, D. Efetov, D. A. Abanin, L. S. Levitov, and Philip Kim, *Phys. Rev. Lett.* **99**, 166804 (2007).
- [88] N. Stander, B. Huard, and D. Goldhaber-Gordon, *Phys. Rev. Lett.* **102**, 026807 (2009).
- [89] J. R. Williams and C. M. Marcus, *Phys. Rev. Lett.* **107**, 046602 (2011).
- [90] E. Prada, P. San-Jose, and L. Brey, *Phys. Rev. Lett.* **105**, 106802 (2010).
- [91] D. Rainis, F. Taddei, M. Polini, G. León, F. Guinea, and V. I. Fal'ko, *Phys. Rev. B* **83**, 165403 (2011).
- [92] D. A. Abanin and L. S. Levitov, *Science* **317**, 641 (2007).
- [93] S. Nakaharai, J. R. Williams, and C. M. Marcus, *Phys. Rev. Lett.* **107**, 036602 (2011).
- [94] J. Güttinger, C. Stampfer, F. Libisch, T. Frey, J. Burgdörfer, T. Ihn, and K. Ensslin, *Phys. Rev. Lett.* **103**, 046810 (2009).
- [95] J. Martin, N. Akerman, G. Ulbricht, T. Lohmann, J. H. Smet, K. von Klitzing, and A. Yacoby, *Nat. Phys.* **4**, 144 (2008).
- [96] A. Deshpande, W. Bao, F. Miao, C. N. Lau, and B. J. LeRoy, *Phys. Rev. B* **79**, 205411 (2009).
- [97] Y. Zhang, V. W. Brar, C. Girit, A. Zettl, and M. F. Crommie, *Nat. Phys.* **5**, 722 (2009).
- [98] M. Kohomoto and Y. Hasegawa, *Phys. Rev. B* **76**, 205402 (2007).
- [99] Y. Kobayashi, K. Fukui, T. Enoki, K. Kusakabe, and Y. Kaburagi, *Phys. Rev. B* **71**, 193406 (2005).
- [100] Y. Niimi, T. Matsui, H. Kambara, K. Tagami, M. Tsukada, and H. Fukuyama, *Phys. Rev. B* **73**, 085421 (2006).
- [101] S. C. Kim, P. S. Park, and S. R. Eric Yang, *Phys. Rev. B* **81**, 085432 (2010).
-

-
- [102] F. Libisch, S. Rotter, J. Güttinger, C. Stampfer, and J. Burgdörfer, *Phys. Rev. B* **81**, 245411 (2010).
- [103] Jiang-chai Chen, X. C. Xie, and Qing-Feng Sun, *Phys. Rev. B* **86**, 035429 (2012).
- [104] D. S. L. Abergel, V. Apalkov, J. Berashevich, K. Ziegler, and T. Chakraborty, *Adv. Phys.* **59**, 261 (2010).
- [105] S. Das Sarma, Sh. Adam, E. H. Hwang, and E. Rossi, *Rev. Mod. Phys.* **83**, 407 (2011).
- [106] J. Güttinger, F. Molitor, C. Stampfer, S. Schnez, A. Jacobsen, S. Dröscher, T. Ihn, and K. Ensslin, *Rep. Prog. Phys.* **75**, 126502 (2012).
- [107] A. V. Rozhkov, G. Giavaras, Y. P. Bliokh, V. Freilikher, and F. Nori, *Phys. Rep.* **503**, 77 (2011).
- [108] Wei-dong Sheng, M. Korkusinski, A. D. Güçlü, M. Zielinski, P. Potasz, E. S. Kadantsev, O. Voznyy, and P. Hawrylak, *Front. Phys.* **7**, 328 (2012).
- [109] M. Grujić, M. Zarenia, A. Chaves, M. Tadić, G. A. Farias, and F. M. Peeters, *Phys. Rev. B* **84**, 205441 (2011).
- [110] M. Zarenia, J. M. Pereira Jr., F. M. Peeters, and G. A. Farias, *Phys. Rev. B* **87**, 035426 (2013).
- [111] M. Wagner, U. Merkt and A. V. Chaplik, *Phys. Rev. B* **45**, 1951 (1992).
- [112] P. A. Maksym and T. Chakraborty, *Phys. Rev. Lett.* **65**, 108 (1990); F. M. Peeters and V. A. Schweigert, *Phys. Rev. B* **53**, 1468 (1996).
- [113] B. Wunsch, T. Stauber, and F. Guinea, *Phys. Rev. B* **77**, 035316 (2008).
- [114] D. S. L. Abergel, V. M. Apalkov, and T. Chakraborty, *Phys. Rev. B* **78**, 193405 (2008).
- [115] V. N. Kotov, B. Uchoa, V. M. Pereira, F. Guinea, and A. H. Castro Neto, *Rev. Mod. Phys.* **84**, 1067 (2012).
- [116] J. Sabio, F. Sols, and F. Guinea, *Phys. Rev. B* **81**, 045428 (2010).
- [117] H. S. Cohl, A. R. P. Rau, Joel E. Tohline, D. A. Browne, J. E. Cazes, and E. I. Barnes, *Phys. Rev. A* **64**, 052509 (2001).
-

-
- [118] Y. Zheng and T. Ando, *Phys. Rev. B* **65**, 245420 (2002).
- [119] V. P. Gusynin and S. G. Sharapov, *Phys. Rev. Lett.* **95**, 146801 (2005).
- [120] K. S. Novoselov, A. K. Geim, S. V. Morozov, D. Jiang, M. I. Katsnelson, I. V. Grigorieva, S. V. Dubonos, and A. A. Firsov, *Nature (London)* **438**, 197 (2005).
- [121] Y. Zhang, Y. W. Tan, H. L. Stormer, and P. Kim, *Nature (London)* **438**, 201 (2005).
- [122] Y. Aharonov and D. Bohm, *Phys. Rev.* **115**, 485 (1959).
- [123] Y. Aharonov and A. Casher, *Phys. Rev. Lett.* **53**, 319 (1984).
- [124] A. Fuhrer, S. Lüscher, T. Ihn, T. Heinzel, K. Ensslin, W. Wegscheider, and M. Bichler, *Nature* **413**, 822 (2001).
- [125] S. Russo, J. B. Oostinga, D. Wehenkel, H. B. Heersche, S. S. Sobhani, L. M. K. Vandersypen, and A. F. Morpurgo, *Phys. Rev. B* **77**, 085413 (2008).
- [126] F. Molitor, M. Huefner, A. Jacobsen, A. Pioda, C. Stampfer, K. Ensslin, and T. Ihn, *New J. Phys.* **12**, 043054 (2010).
- [127] E. A. Henriksen, Z. Jiang, L.-C. Tung, M. E. Schwartz, M. Takita, Y. -J. Wang, P. Kim, and H. L. Stormer, *Phys. Rev. Lett.* **100**, 087403 (2008).
- [128] J. Wurm, M. Wimmer, H. U. Baranger, and K. Richter, *Semicond. Sci. Technol.* **25**, 034003 (2010)
- [129] T. Luo, A. P. Iyengar, H. A. Fertig, and L. Brey, *Phys. Rev. B* **80**, 165310 (2009).
- [130] A. Rycerz, *Act. Phys. Pol.* **115**, 322 (2009).
- [131] M. Zarenia, J. M. Pereira Jr., F. M. Peeters, and G. A. Farias, *Nano Lett.* **9**, 4088, (2009).
- [132] F. E. Meijer, A. F. Morpurgo, and T. M. Klapwijk, *Phys. Rev. B* **66**, 033107 (2002).
- [133] B. Molnár, F. M. Peeters, and P. Vasilopoulos, *Phys. Rev. B* **69**, 155335 (2004).
- [134] G. Giovannetti, P. A. Khomyakov, G. Brocks, P. J. Kelly, and J. van den Brink, *Phys. Rev. B* **76**, 073103 (2007).
- [135] B. Sachs, T. O. Wehling, M. I. Katsnelson, and A. I. Lichtenstein, *Phys. Rev. B* **84**, 195414 (2011).
-

- [136] M. Zarenia, J. Milton Pereira, A. Chaves, F. M. Peeters, and G. A. Farias, *Phys. Rev. B* **81**, 045431 (2010); Erratum: *Phys. Rev. B* **82**, 119906 (2010).
- [137] B. A. Volkov and O. A. Pankratov, *JETP Lett.* **42**, 178 (1985).
- [138] M. Killi, T. -C. Wei, I. Affleck, and A. Paramekanti, *Phys. Rev. Lett.* **104**, 216406 (2010).
- [139] L. Jing, J. Velasco Jr., P. Kratz, G. Liu, W. Bao, M. Bockrath, and C. N. Lau, *Nano Lett.* **10**, 4775 (2010).
- [140] Zh. Qiao, J. Jung, Q. Niu, and A. H. MacDonald, *Nano Lett.* **11**, 3453 (2011).
- [141] M. Zarenia, J. M. Pereira Jr., G. A. Farias, and F. M. Peeters, *Phys. Rev. B* **84**, 125451 (2011).
- [142] M. Zarenia, J. M. Pereira Jr., F. M. Peeters, and G. A. Farias, *Nanoscale Research Letters* **6**, 452 (2011).
- [143] M. Killi, S. Wu, and A. Paramekanti, *Int. J. Mod. Phys. B* **26**, 1242007 (2012).
- [144] J. Jung, F. Zhang, Zh. Qiao, and A. H. MacDonald, *Phys. Rev. B* **84**, 075418 (2011).
- [145] M. Barbier, P. Vasilopoulos, and F. M. Peeters, *Phys. Rev. B* **81**, 075438 (2010).
- [146] X. Gonze, J.-M. Beuken, R. Caracas, F. Detraux, M. Fuchs, G.-M. Rignanese, L. Sindic, M. Verstraete, G. Zerah, F. Jollet, M. Torrent, A. Roy, M. Mikami, P. Ghosez, J.-Y. Raty, and D. C. Allan, *Comp. Mat. Science* **25**, 478 (2002).
- [147] O. Leenaerts, B. Partoens, and F. M. Peeters, *Phys. Rev. B* **80**, 245422 (2009).
- [148] M. Zarenia, O. Leenaerts, B. Partoens, and F. M. Peeters, *Phys. Rev. B* **86**, 085451 (2012).
- [149] J. M. Pereira, F. M. Peeters, and P. Vasilopoulos, *Phys. Rev. B* **76**, 115419 (2007).
- [150] V. I. Fal'ko, *Phil. Trans. R. Soc. A* **366**, 205 (2008).
- [151] I. Snyman and C. W. J. Beenakker, *Phys. Rev. B* **75**, 045322 (2007).
- [152] M. Ramezani Masir, P. Vasilopoulos, and F. M. Peeters, *Phys. Rev. B* **79**, 035409 (2009).
-

- [153] M. Barbier, P. Vasilopoulos and F. M. Peeters, *Phil. Trans. R. Soc. A* **368**, 5499 (2010).
- [154] M. Charbonneau, K. M. van Vliet, and P. Vasilopoulos, *J. Math. Phys.* **23**, 318 (1982).
- [155] M. B. Tavernier, E. Anisimovas, F. M. Peeters, B. Szafran, J. Adamowski, and S. Bednarek, *Phys. Rev. B* **68**, 205305 (2004).
- [156] T. H. Oosterkamp, J. W. Janssen, L. P. Kouwenhoven, D. G. Austing, T. Honda, and S. Tarucha, *Phys. Rev. Lett.* **82**, 2931 (1999).
-

- 2009
 - Belgium Physical Society meeting (BPS), 1 April 2009, Hasselt University, Belgium.
 - 32nd International Symposium on Dynamical Properties of Solids (DyProSo), 13th-17th Sep. 2009, University of Antwerp, Belgium.
- 2010
 - FYSICA 2010 conference, 23 April 2010, Utrecht University, Netherlands.
 - International spring collage on computational nanoscience, 17th-28th May 2010, ICTP, Trieste, Italy.
 - EuroMagNET summer school: *Science in High Magnetic Fields*, 5th-11th Sep. 2010, Ameland, Netherlands.
- 2011
 - Belgium Physical Society meeting (BPS), 25th May 2011, University of Namur, Belgium.
- 2012
 - *Graphene2012* international conference, 1st-13th April 2012, Brussels, Belgium.
 - *Graphene Week 2012* international conference, 4th-8th June 2012, University of Delft, Netherlands.
 - CECAM workshop: *Graphene: from band structure to many-body physics*, 3rd-7th Sep. 2012, University of Bremen, Germany.

Publications

- [1] M. Zarenia, J. M. Pereira Jr., F. M. Peeters, and G. A. Farias, *Electrostatically confined quantum rings in bilayer graphene*, Nano Letters **9**, 4088 (2009).
- [2] M. Zarenia, J. Milton Pereira, A. Chaves, F. M. Peeters, and G. A. Farias, *Simplified model for the energy levels of quantum rings in single layer and bilayer graphene*, Phys. Rev. B **81**, 045431 (2010); Erratum: Phys. Rev. B **82**, 119906 (2010).
- [3] M. Ebrahim Fouladvand, M. Zarenia, *Optimization of quantum Monte Carlo wave function: steepest descent method*, Int. J. Mod. Phys. C **21**, 523 (2010).
- [4] M. Zarenia, J. M. Pereira, Jr., G. A. Farias, and F. M. Peeters, *Chiral states in bilayer graphene: Magnetic field dependence and gap opening*, Phys. Rev. B **84**, 125451 (2011).
- [5] M. Grujić, M. Zarenia, A. Chaves, M. Tadić, G. A. Farias, and F. M. Peeters, *Electronic and optical properties of a circular graphene quantum dot in a magnetic field: Influence of the boundary conditions*, Phys. Rev. B **84**, 205441 (2011).
- [6] M. Zarenia, A. Chaves, G. A. Farias, and F. M. Peeters, *Energy levels of triangular and hexagonal graphene quantum dots: A comparative study between the tight-binding and Dirac equation approach*, Phys. Rev. B **84**, 245403 (2011).
- [7] M. Zarenia, J. M. Pereira, Jr., G. A. Farias, and F. M. Peeters, *Topological confinement in an antisymmetric potential in bilayer graphene in the presence of a magnetic field*, Nanoscale Research Letters **6**, 452 (2011).
- [8] M. Grujić, M. Zarenia, M. Tadić, and F. M. Peeters, *Interband optical absorption in a circular graphene quantum dot*, PHYSICA SCRIPTA **T149**, 014056 (2012).
- [9] M. Zarenia, P. Vasilopoulos, and F. M. Peeters, *Magnetotransport in periodically modulated bilayer graphene*, Phys. Rev. B **85**, 245426 (2012).

- [10] M. Zarenia, O. Leenaerts, B. Partoens, and F. M. Peeters, *Substrate-induced chiral states in graphene*, Phys. Rev. B **86**, 085451 (2012).
- [11] M. Zarenia, P. Vasilopoulos, N. Pourtolami, and F. M. Peeters, *Landau-level dispersion and the quantum Hall plateaus in bilayer graphene*, Accepted in Journal of Applied Physics (July 2012).
- [12] M. Zarenia, J. M. Pereira, Jr., F. M. Peeters, and G. A. Farias, *snake states in graphene quantum dots in the presence of a p-n junction*, Phys. Rev. B **87**, 035426 (2013).
- [13] M. Zarenia, B. Partoens, T. Chakraborty, and F. M. Peeters, *Electron-electron interaction in bilayer graphene quantum dots*, submitted to Phys. Rev. Lett. (2013).

Research interests

- Electronic properties of graphene
- Quantum dots and quantum rings
- Graphene nanostructures
- Electron-electron correlation in quantum nanostructures

Awards and Honors

- Award of top graduate student, Physics department of Tarbiat Modares University, Tehran, Iran (2008).
- Workshop grant awarded by Fonds Wetenschappelijk Onderzoek (FWO), (Sep. 2012).
- One figure of my paper in *Phys. Rev. B* **84**, 245403 (2011) has been selected for the Phys. Rev. B Kaleidoscope (Dec. 2011).